TWO-FLUID MODELLING OF HETEROGENEOUS COARSE PARTICLE SLURRY FLOWS

A Thesis Submitted to the

College of Graduate Studies and Research

in Partial Fulfilment of the Requirements for the Degree of

Doctor of Philosophy

in the Department of Mechanical Engineering

University of Saskatchewan

Saskatoon, Saskatchewan

by

Franklin Norvisi Krampa

Your file Votre référence
ISBN: 978-0-494-62631-3
Our file Notre référence
ISBN: 978-0-494-62631-3

PERMISSION TO USE

In presenting this thesis in partial fulfilment of the requirements for a Postgraduate degree from the University of Saskatchewan, I agree that the Libraries of this University may make it freely available for inspection. Copying of this thesis in any manner, in whole or in part, for scholarly purposes may be granted by Professor D.J. Bergstrom and/or Professor J.D. Bugg who supervised my thesis work or, in their absence, by the Head of the Department of Mechanical Engineering or the Dean of the College of Engineering. It is understood that any copying or publication or use of this thesis or parts thereof for financial gain shall not be allowed without my written permission. It is also understood that due recognition shall be given to me and to the University of Saskatchewan in any scholarly use which may be made of any material in my thesis.

Requests for permission to copy or to make other use of material in this thesis in whole or part should be addressed to:

Head of the Department of Mechanical Engineering
University of Saskatchewan
Saskatoon, Saskatchewan, Canada
S7N 5A9

ABSTRACT

In this dissertation, an experimental and numerical study of dense coarse solids-liquid flows has been performed. The experimental work mainly involved pressure drop measurements in a vertical flow loop. A limited number of measurements of solids velocity profiles were also obtained in the upward flow section of the flow loop. The numerical work involved simulations of coarse particles-in-water flows in vertical and horizontal pipes. The vertical flow simulations were performed using the commercial CFD software, ANSYS CFX-4.4, while ANSYS CFX-10 was used to simulate the flows in the horizontal pipes. The simulations were performed to investigate the applicability of current physically-based models to very dense coarse-particle flows.

In the experimental study, measurements of pressure drop and local solids velocity profiles were obtained. The experiments were conducted in a 53 mm diameter vertical flow loop using glass beads of 0.5 mm and 2.0 mm diameter solids for concentration up to 45%. The liquid phase was water. The measured pressure drop exhibited the expected dependence on bulk velocity and solids mean concentration. The wall shear stress was determined by subtracting the gravitational contribution from the measured pressure drop. For flow with the 0.5 mm particles at high bulk velocities, the values of the wall shear stress were essentially similar for each concentration in the upward flow sections but more variation, indicating the effect of concentration, was noted in the downward flow section. At lower bulk velocities, the wall shear stresses with the 0.5 mm glass beads-water flow showed a dependence on concentration in both test sections. This was attributed to an increase in the slip velocity. For the large particle (2.0 mm glass beads), similar observations were made but the effect of concentration was much less in the upward test section. In the downward test section, the wall shear stress for the flow of the 2.0 mm glass beads increased by almost a constant value for the bulk velocities investigated. The solids velocity

profiles showed that the solids velocity gradient is large close to the wall. In addition, the solids velocity profiles indicated that the slip velocity increased at lower velocities due to increase in the bulk concentration in the upward flow section.

For the vertical flow simulations, different physical models based on the kinetic theory of granular flows were programmed and implemented in ANSYS CFX-4.4. These models, referred to as the $k_{\mathrm{f}} - \varepsilon_{\mathrm{f}} - k_{\mathrm{s}} - \varepsilon_{\mathrm{s}}$, $k_{\mathrm{f}} - \varepsilon_{\mathrm{f}} - k_{\mathrm{s}} - \varepsilon_{\mathrm{s}} - T_{\mathrm{s}}$, and $k_{\mathrm{f}} - \varepsilon_{\mathrm{f}} - k_{\mathrm{s}} - k_{\mathrm{fs}}$ models, were investigated by focusing on the closure laws for the solids-phase stress. The treatment of the granular temperature T_{s} depends on whether small- or large-scale fluctuating motion of the particles is considered. The models were implemented via user-Fortran routines. The predicted results were compared with available experimental results. The predicted solids-phase velocity profiles matched the measured data close to the pipe wall but were higher it in the core region. The solids concentration, on the other hand, was significantly under-predicted for concentrations higher than 10%. Variations in the predictions of the phasic turbulent kinetic energy and the eddy viscosity were noted; the effect of solids concentration on them was mixed. A general conclusion drawn from the work is that a more accurate model is required for accurate and consistent prediction of coarse particle flows at high concentrations (less than 10%). In a related study, attention was given to wall boundary conditions again focusing on the effect of the solids-phase models at the wall. Comparison between numerical predictions, using some of the existing wall boundary condition models for the solids phase in particulate flows, with experimental results indicated that the physical understanding of the influence of the fluid and solids-phase on each other and their effect on frictional head loss is far from complete. The models investigated failed to reproduce the experimental results. At high solids concentration, it was apparent from the present study that the no-slip and free-slip wall boundary conditions are not appropriate for liquid-solid flows.

For the horizontal flow case, three-dimensional simulations were performed with a focus on the velocity and concentration distributions. Medium and coarse sand-in-water flows in three pipe diameters were considered to investigate the default solids stress models in

ANSYS CFX-10. Simulations were performed for three cases by considering: 1) no additional solids-phase stress, i.e. no model for T_s; 2) a zero equation, and 3) an algebraic equilibrium model for the granular temperature. The model predictions were compared to experimental results. The effect of particle size, solids-phase concentration, and pipe diameter was explored using the algebraic equilibrium model. All the cases for the models considered exhibited the characteristic features of horizontal coarse particle slurry flows. The zero equation and the algebraic equilibrium model for the granular temperature produced similar results that were not significantly different from the prediction obtained when no solids-phase stress was considered. The comparison with experimental results was mixed. Locally, the measured solids-phase velocity distributions were over-predicted, whereas the solids concentration was reasonably reproduced in the core of all the pipes. The concentration at the bottom and top walls were over-, and under-predicted, respectively. This was attributed to the inappropriate phasic wall boundary condition models available.

ACKNOWLEDGEMENT

I would like to express my sincere appreciation to my supervisors, Professor Donald J. Bergstrom and Professor James D. Bugg. I thank them for the thoughtful insights, guidance, advice, and for generously making time for me to discuss various aspects of this interesting research. I am also grateful that they allowed me to continue with the research when I had to take on a contract to begin my career.

My sincere thanks go to my advisory committee members: Professors R.D. Sanders, R. Sumner, and Dr. R. Gillies, as well as the late Professor C.A. Shook, for their invaluable suggestions. I am very grateful to my external examiner Professor Jennifer Sinclair-Curtis for her interesting comments and suggestions most of which have been reflected in the final version of the thesis. I and very grateful to the Professors whose classes I have taken as a course, audited or just sat in; all of them have something special and unique to offer and at University of Saskatchewan for me it is an honour to have had contact with them and also to learn as a student and to acquire the tools for teaching. Advice on the profession of teaching during my earlier days of the program by the Professor S. Yannacopoulos is not forgotten and I am thankful to have met him.

Technical assistance, among others, provided by Mr. D. Deutscher, Mr. D. Pavier, Mr. D.V. Bitner and the staff at Saskatchewan Research Council Pipe Flow Technology Centre is gratefully acknowledged. My appreciation also goes to the secretaries in the Department of Mechanical Engineering for their various help and support.

Special thanks go to Dr. and Mrs. Afeti, Mr. Adim Morkporkpor, Dr. L.E. Ansong, and Dr. Tachie for their motivation. I am also very grateful for the exceptional support and help by Mr. and Mrs. Pavier; words can never describe my appreciation for your graciousness. To my numerous well-wishers, thank you all so much. I would also like to thank all my colleagues and friends for their moral support and prayers. A special thank you to Samuel Adaramola; Olajide Akinlade; Mr. and Mrs. Ahiahonu, Botchwey, Dzaka, Gana, Mawuli,

Nketia, and Udemgha, to mention a few. I really appreciate your friendship and support. And thanks to the late Mr. and Mrs. Dan and Joan Peters. I would also like to thank the management of SINTEF Petroleum Research in Norway for allowing me to take time off to complete the thesis work.

It is my pleasure to acknowledge the encouragement and support received from my family who helped in many ways to make this program a success. A special thank you to my wonderful wife, Bridgette Krampa. Thank you for being in my life and always being supportive. To my son Jayden and daughter Iyanna, all I can say is that you have been a source of inspiration and encouragement.

Financial supports in the form of research grants from Syncrude Canada Limited and the Collaborative Research Development Fund (CRD) of the Natural Science and Engineering Research Council of Canada (NSERC) are gratefully acknowledged. Also financial support from the university in the forms of devolved scholarship, Graduate Teaching fellowships, travel awards, all of which help in attaining various accomplishments are graciously acknowledged.

DEDICATION

To

My wonderful father Felix, uncles Julius and Peter;

to wife; Bridgette, and to Jayden and Iyanna,

my two wonderful kids for enriching my life in ways unimaginable;

and to the memory of my late Mother, Monica

TABLE OF CONTENTS

LIST OF TABLES

LIST OF FIGURES

LIST OF SYMBOLS

Acronyms

CFD	Computational Fluid Dynamics
CRD	Collaborative Research Development
DEM	Discrete Element Simulation
DNS	Direct Numerical Simulation
DPM	Discrete Particle Method
LES	Large Eddy Simulation
LDV	Laser Doppler Velocimetry
PDPA	Phase Doppler Particle Analyser
PDF	Probability Density Function
EMFM	Electromagnetic Flow Meter
NSERC	Natural Sciences and Engineering Research Council
NMR	Nuclear Magnetic Resonance
RANS	Reynolds Averaged Navier-Stokes
SRC	Saskatchewan Research Council

Roman Symbols

A	Cross-sectional area of pipe
A_1, A_2	Sectional areas of pipe cross-section in layer model
c	Concentration
c_1, c_2	Constants in turbulence model
c_f	Liquid phase concentration
c_s	Solids phase concentration
c_μ	Turbulence constant
C_1, C_2	sectional concentration in layer model
C_lim	Concentration limit
C_max	Solids maximum concentration

C_{s}	Solids mean concentration
C_{r}	In-situ solids mean concentration
C_{D}	Drag coefficient
C_{M}	Compaction modulus
C_{T}	Coefficient of fluid phase turbulence time scale
C_{β}	Model coefficient
$C_{\varepsilon 1}, C_{\varepsilon 2}, C_{\varepsilon 3}$	Turbulence constants
d_{50}	Median particle diameter, m
d_{p}	Particle diameter, m
D	Pipe diameter, m
$D_{\mathrm{fs}ij}$	Particle diffusion tensor
e	Coefficient of restitution
E	Constant in wall function formulation
E_{l}	Voltage drop in mixture
E_{m}	Voltage drop in carrier fluid
g	Gravitational acceleration, ms^{-2}
g_k	Functional relations related to kinetic theory models, k = 1,2,3,4
g_{o}	Radial distribution function
G_{o}	Reference elasticity modulus, Pa
f_{12}	Interfacial friction factor
f_{drag}	Drag force, N
f_{f}	Fluid phase friction factor
f_{s}	Solids phase friction factor
F_{i}	External force on particle per unit mass, Nkg^{-1}
F_2	Coulombic force
h	Height of fluid column, m
H	Channel height, m
i_{m}	Frictional head loss
J	Molecular flux
k	Turbulence kinetic energy, $\mathrm{m}^2\mathrm{s}^{-2}$

k	Roughness height, m
k_{fs}	Covariance correlation, $\mathrm{m^2 s^{-2}}$
K_{i}	Bagnold's grain-inertial model coefficient
K_{v}	Bagnold's macro-viscous model coefficient
K_{sc}	Collisional coefficient of diffusion
K_{st}	Kinetic diffusivity
l_{12}	Relative distance between two particles, m
l_{c}	Particle mean free path, m
l_{f}	Eulerian integral length scale of the fluid phase, m
l_{fs}	Distance between two particles, m
L	Characteristic length of pipe, m
m	Mass, $\mathrm{kgm^{-3}}$
$M_{\mathrm{fs}i}$	Momentum inter-phase drag transfer
n	Outward pointing normal
P	Pressure, Pa
P_{f}	Production term due to shear in fluid phase, $\mathrm{Nm^{-2} s^{-1}}$
$s = \rho_s/\rho_{\mathrm{f}}$	Density ratio
S_1, S_2, S_{12}	Sectional perimeters of the pipe cross-section
$S_{\alpha ij}$	Phasic strain rate tensor, $\mathrm{s^{-1}}$
$S_{\mathrm{fs}ij}$	Fluid-solids strain rate tensor, $\mathrm{s^{-1}}$
t	Time, s
t_{c}	Particle-particle collision time, s
t_{fs}	Particle-fluid interaction time, s
t_{p}	Particle relaxation time-scale, s
t_{T}	Fluid phase turbulence time-scale, s
$\mathfrak{T}_{\mathrm{f}ij}$	Fluid phase effective stress tensor, $\mathrm{kgm^{-3} s^{-1}}$
TI	Turbulence Intensity
T_{s}	Granular temperature, $\mathrm{kgm^{-3} s^{-1}}$
$\mathfrak{T}_{\mathrm{s}ij}$	Solids phase effective stress tensor, $\mathrm{kgm^{-3} s^{-1}}$
u	Velocity field, $\mathrm{ms^{-1}}$

u'	Velocity fluctuation, ms^{-1}
$u''_{\mathrm{s}\,i}$	Small-scale solids velocity fluctuation, ms^{-1}
u_τ	Friction velocity, ms^{-1}
U	Velocity field, ms^{-1}
U_{d}	Drift velocity, ms^{-1}
U_{ir}	Characteristic mean relative velocity, ms^{-1}
U_{plus}	Mean velocity in inner units, U/u_τ
v_∞	Particle settling velocity, ms^{-1}
V	Bulk velocity, ms^{-1}
$\mathcal{V}$	Characteristic control volume, m^3
$\mathcal{W}$	Weighting factor
x, y, z	Cartesian coordinate in the streamwise, wall-normal or cross-stream direction, m
$X_{\mathrm{fs}i}$	Two-phase flow loading
$X_\alpha(r,t)$	Phase indicator function

Greek Symbols

α	Constituent phase
β	Inter-phase drag function
β_{ha}	Half angle
γ	Dissipation rate of granular temperature, $\mathrm{Nm}^{-2}\mathrm{s}^{-2}$
γ_{cr}	Crossing trajectory coefficient
$\Gamma_{\Theta_{\mathrm{s}}}$	Diffusion coefficient of the granular temperature
δ_{ij}	Kroneker delta
ε	Dissipation rate of turbulent kinetic energy, $\mathrm{m}^2\mathrm{s}^{-3}$
η_{s}	Coefficient of Coulombic friction
κ	Log-law constant
λ_{L}	Linear concentration
λ_{slip}	Wall slip parameter

$\mu_{\alpha t}$	Phasic turbulence (eddy) viscosity, Pa·s
μ_{α}	Phasic dynamic viscosity, Pa·s
ν_{α}	Phasic kimenatic viscosity
ξ_{s}	Bulk viscosity of solid phase, Pa·s
ρ_{m}	Mixture density, kgm^{-3}
ρ_{α}	Phasic density, kgm^{-3}
σ_2	Normal stress in layer model, Ns^{-2}
$\sigma_{\mathrm{k}}, \sigma_{\varepsilon}$	Prandtl number
$\tau_1, \tau_2, \tau_{12}$	Shear stresses in layer model, Pa
τ_{ij}	Viscous stress tensor, Pa
τ_{w}	Wall shear stress, Pa
ϕ	Specularity coefficient
φ	Angle of friction
ψ	Flow field variable
Ω	Generic source quantity

Subscripts

coll	Related to collision
d	Downward flow section
dil	Related to dilute regime
f	Fluid phase
fn	First computational node from a solid boundary
ha	Half-angle
l	Liquid phase
m	Mixture
mixin	related to inlet mixture variable
p	Particle
s	Solid phase
sin	Inlet solids phase variable

t	Turbulent
u	Upward flow section
w	Wall

Superscripts

$+$	Dimensionless indicator
$'$	Fluctuating component of a quantity
f	Solids phase friction
int	Fluid-solid interface parameter indicator
pif	Phase induced fluctuations

Dimensionless Groups

Ba	Bagnold number
Re	Reynolds number
St	Stokes number

Operators and special notations

$\langle\rangle$	Ensemble average operator
$\partial/\partial t$	Partial derivative
D/Dt	Material derivative
Δ	Difference

CHAPTER 1

INTRODUCTION

A two-phase mixture is made up of two distinct phases such as gas-liquid, gas-solid, or liquid-solid that co-exist in an arbitrary space. The phases are separated by interfaces and interact dynamically across these interfaces. For most particulate two-phase flows (i.e. liquid-solid or gas-solid flows), the fluid phase (also known as the carrier phase) is continuously connected and the solids phase (often referred to as the dispersed or particle phase) exists as discrete particles. The study of particulate two-phase flows is not only important from a fundamental viewpoint, but also from the viewpoint of practical applications (e.g. hydrotransport and pneumatic transport of particles in pipes and channels) and natural flow phenomena (e.g. atmospheric dispersion, sediment transport in water bodies, and biological/biomedical flows). Flows which include granular materials are found in the mining, chemical, petrochemical, pharmaceutical, and food industries.

Due to the dispersed phase, the physics of two-phase flow is generally more complex than for single-phase flow. Further complications, which are sometimes difficult to elucidate, arise when the flow is affected by turbulence, and/or when the dispersed phase undergoes either a fluctuating or continuous contact motion with other particles. In this case, the solids phase does not follow the flow but interacts and modifies the fluid phase flow features. The motion of particles in two-phase flow mixtures affects the structure of fluid-phase turbulence and influences the momentum balance in the flow. Turbulence modulation in two-phase turbulent flows is also of importance for industrial applications. These turbulent flows continue to provide a challenge to engineers and physicists in developing an analytical description and predictive model from first principles. Furthermore, the design

of conveying systems requires fundamental understanding of the transport mechanisms of the mixtures.

The analysis of single-phase flows using computational fluid dynamics (CFD) has steadily advanced in sophistication. Although there are various methods for solving the Navier-Stokes equation (e.g. Direct Numerical Simulation (DNS), Large Eddy Simulation (LES)), the so-called Reynolds Averaged Navier-Stokes (RANS) approach is often preferred due to its reduced computation cost. One of the most widely used turbulence closure models based on the RANS approach is the two-equation $k-\varepsilon$ model (e.g. see Pope, 2000); k is the turbulence kinetic energy and ε is the dissipation rate of k. The turbulence kinetic energy and its dissipation rate are obtained by solving their respective transport equations. In this model, the Reynolds stress is approximated by the product of the turbulent viscosity and the mean strain rate. The turbulent viscosity is assumed to be a function of the turbulence kinetic energy and its dissipation rate. Being an isotropic model, the $k-\varepsilon$ model has the limitation of not predicting highly anisotropic and rotational flows well. Nonetheless, it is the most widely used turbulence model for industrial processes. The simplicity of the $k-\varepsilon$ model makes it amenable to the simulation of complex two-phase flow.

1.1 Motivation for the Present Study

The hydrotransport of solid particles occurs in many natural and industrial processes. Pipelining of oil sands by means of hydrotransport not only reduces material handling costs, but also provides some initial processing (Lipsett, 2004). During its hydrotransport, the slurry undergoes a process known as oil sands conditioning where the bitumen separates from the oil sands matrix. This initial conditioning process facilitates the aeration of the bitumen droplets prior to entering the separation unit. The transported oil sands slurry overall forms a complex multiphase system made up of water, bitumen, solids, air, and chemicals. The interaction forces in this complex multiphase system govern the conditioning and separation as well as tailings handling and disposal.

The development of better mechanistic models requires an understanding of the flow physics. Other challenges include the effect of large particles on pump performance and the pipeline itself. Presently, existing mechanistic models can only predict the pipeline friction with some success using either empirical or *ad hoc* models. A few detailed studies have been performed to investigate the local phasic velocity and concentration distributions (Hsu et al., 1989; Roco, 1990). However, such studies were limited to one-dimensional analysis and the constitutive relations for the closure terms were empirical. In this thesis, the two-fluid model is used to model pipe flow of coarse-particle liquid-solid mixtures. The two-fluid model treats both the liquid and the solids phase as individual fluids which are considered to form an inter-penetrating continuum. This allows the pertinent flow physics of each phase as well as the interaction between the phases to be considered.

1.2 Classification of Flow Regimes

Two-phase pipe flow regimes depend on the phasic materials, flow rates, and pipe orientation. For liquid-solid flows, the particle diameter and the solids mean concentration are often used to classify the nature of the mixture and flow regimes. The particle diameter is often used to determine whether the flow exhibits Newtonian or non-Newtonian behaviour, or possesses homogeneous or heterogeneous characteristics. The solids mean concentration is generally used to delineate dilute or dense flows. Before discussing in detail the flow regimes, illustrative examples for dispersed vertical and horizontal slurry pipe flows are given in Figures 1.1 and 1.2, respectively, as reproduced from Brennen (2005).

In Figure 1.1, the flow regime is vertical and the constituents are well-mixed; the mean velocity and concentration fields are symmetric about the centreline. Particle size and concentration effects cause the flow to exhibit heterogeneous characteristics (see Sumner et al., 1990). For the horizontal flow case shown in Figure 1.2, the phasic field variable distributions in the vertical plane vary from symmetric (homogeneous regime) to asymmetric (heterogeneous regime) forms depending on several factors, including particle size, solids phase concentration, and the total flow rate. The homogeneous flow regime illustrated by

Figure 1.1: A sketch of two-phase flow in a vertical pipe. *Reproduced with permission from Fundamentals of Multiphase Flow, Brennen, C.E., page 169, Copyright (2005), Cambridge University Press.*

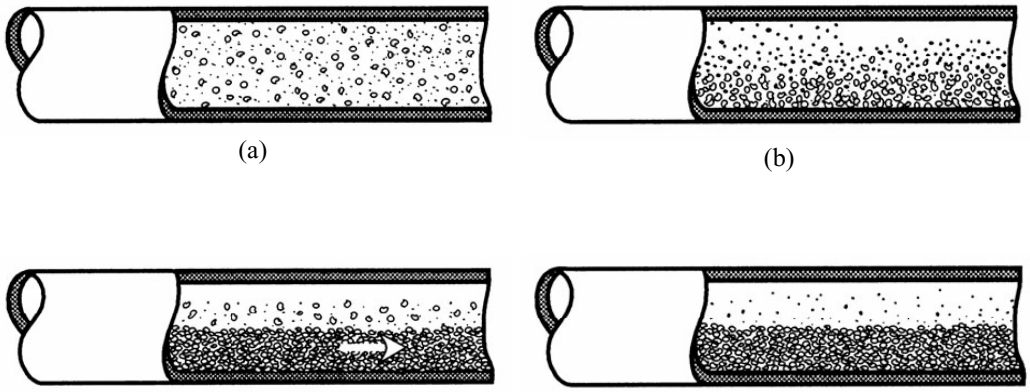

Figure 1.2: Flow regimes for slurry flow in a horizontal pipeline. (a) Homogeneous flow, (b) Heterogeneous flow, (c) Flow with moving bed, and (d) Flow over a stationary bed. *Reproduced with permission from Fundamentals of Multiphase Flow, Brennen, C.E., page 170, Copyright (2005), Cambridge University Press.*

Figure 1.2a occurs at low or moderate solids concentration and when the fluid phase turbulence velocity scale is much larger that the settling velocity of the particles. In the presence of large particles, concentration gradients in the vertical direction often exist leading to a heterogeneous flow regime, e.g. Figure 1.2b. Occasionally, a limiting case where particles form a bed in the bottom of the pipe occurs and this phenomenon is termed saltation flow. Two scenarios can occur in saltation flow, a moving bed (Figure 1.2c), where the bulk of

the packed bed formed at the bottom of the wall moves or a stationary bed (Figure 1.2d) where the solids phase above a static bed is transported by the fluid phase.

1.2.1 Classification based on particle size

Particle size has been used to classify liquid-solid flow regimes in industrial horizontal pipelines in some studies. Durand and Condolios (1952) proposed that a slurry flow is homogeneous when the particle size in the mixture is less than 50 μm; heterogeneous when it lies between 50 μm and 2000 μm; and a sliding bed flow is encountered when the particle size is greater than 2000 μm. Roco (1990), on the other hand, indicated that for industrial pipelines, the flow of mixtures with particle size less than 10 μm corresponds to a non-Newtonian flow; between 10 μm and 200 μm is quasi-homogeneous flow, and over 200 μm is considered heterogeneous. One of the leading research institutes conducting slurry flow research, the Saskatchewan Research Council (SRC) in Saskatoon, Saskatchewan, Canada, characterizes heterogeneous slurry flow as one with median particle diameter greater than $50 \sim 100$ μm and a sufficiently small content of flocculated fines such that the viscosity of the carrier mixture (water + fine particles) is not high (Shook et al., 2002). The particle density and flow conditions also play a role in determining the flow regimes; large particles that are positively or neutrally buoyant could result in homogeneous flow.

1.2.2 Classification based on solids concentration

For Newtonian heterogeneous flows, the solids concentration is often used as a criterion to determine when the flow is dilute or dense. If the motion of the particles is controlled by local hydrodynamic forces then the mixture is said to be dilute. In this case, the effects of particle-particle interactions may be neglected. For the case where the flow is controlled by both the local hydrodynamic forces and particle-particle interactions, the mixture is considered to be a dense mixture.

There is no universal criterion for distinguishing between dilute and dense flows on the basis of concentration. The criterion varies from study to study and depends on the type of mixture and the flow structure under investigation. Using the solids concentration C_s and

the ratio of the inter-particle distance (l_{fs}) to the particle diameter (d_{p}), Elghobashi (1991) classified dense suspensions for $C_{\mathrm{s}} \geq 0.1\%$ and $l_{\mathrm{fs}}/d_{\mathrm{p}} \leq 10$. In slurry flows, dense flow is generally assumed for $C_{\mathrm{s}} \geq 5\%$ (e.g. McKibben, 1992), while in fluidized bed research, a value of $C_{\mathrm{s}} > 20\%$ is generally considered to be dense (e.g. Gidaspow, 1994). The physical characteristics of whether the flow is dilute or dense have been broadly classified into three categories on the basis of inter-particle collisions (Tsuji, 2000), namely: 1) collision-free flow or dilute flow; 2) collision-dominated flow or medium concentration flow; and 3) contact-dominated flow or dense flow.

1.3 Numerical Techniques for Two-Phase Flows

Over the past five decades, mathematical modelling of particulate two-phase flows has been the focus of many research studies. In general, two distinct methods are used: the Eulerian-Lagrangian and the Eulerian-Eulerian methods.

1.3.1 Eulerian-Lagrangian method

In the Eulerian-Lagrangian approach, the fluid phase continuity and momentum conservation equations are solved in the Eulerian framework using the Navier-Stokes equation with or without additional coupling terms; that is the Direct Numerical Simulation (DNS), Large Eddy Simulation (LES), and the Reynolds Averaged Navier-Stokes (RANS) formulations. For the solids phase, the trajectories of the individual particles in the mixture are solved in the Lagrangian framework using Newton's second law. The two frameworks are coupled through interaction forces implemented by considering the coupling mechanisms between the fluid and the particles. In recent years more complex situations such as particle-particle interactions have been accounted for using the so-called Discrete Element Method (DEM). Briefly, the DEM, also called the Discrete Particle Method (DPM), is an extension of Newton's second law to explicitly include inter-particle forces. These forces, expressed in terms of contact and damping force terms resulting from particle-particle interaction, are derived from the Hertzian contact theory (see for example, Cundall and Strack, 1979). The implementation of boundary conditions and the robustness in handling poly-dispersed particle

size distributions makes the Lagrangian formulation attractive. However, the solids phase concentration does not explicitly appear in this formulation and requires special treatment. Nonetheless, the rapid development in the DEM approaches appears to provide a solution for this drawback in the Eulerian-Lagrangian method, *albeit* with severe computational limitations.

1.3.2 Eulerian-Eulerian method

The Eulerian-Eulerian formulation is essentially obtained from some sort of averaging technique. The averaging techniques often consist of one of the following approaches: 1) Reynolds Averaged Navier-Stokes (RANS) type modelling, or 2) Probability Density Function (PDF) modelling. These approaches result in continuum-like governing equations for the statistical properties of the dispersed phase. In the RANS approach, the equations are derived using one of several methods. The common methods include: 1) ensemble, 2) volume, 3) local mass and local time, 4) space/time, and 5) double-time averaging. While a vast body of literature on the topic exists, the work of Anderson and Jackson (1967); Drew (1983); Elghobashi and Abou-Arab (1983); Ishii (1975); Jackson (1997); and Whitaker (1973) are among the most cited. The resulting averaged equations are often similar, but different modelling and treatment of closure laws have been suggested (see for example, van Wachem and Almstedt, 2003).

The Eulerian-Eulerian equations for two-phase flows are obtained either by considering each phase separately using the Eulerian-Eulerian method or by considering the mixture as a single continuum. For the mixture model, averaged phasic equations for each phase are added together to obtain a single transport equation for the mixture. For example, for isothermal flows, the mixture model consists of one continuity equation, one momentum equation, and one diffusion equation representing the concentration gradient. For sediment transport and in some slurry flow studies, the Rouse-Smith equation or an extended form, formally derived from the momentum equation (Greimann and Holly, 2001; Roco and Shook, 1985) is employed. Bartosik and Shook (1991) and Bartosik and Shook (1995), used a different approach. Known concentration distributions were supplied to the

transport equations of the mixture to predict the pressure gradient of slurry flows in a pipe using single-phase, two-equation turbulence models.

The Eulerian-Eulerian method (commonly known as the two-fluid model) considers both the fluid and solids phase as two inter-penetrating continua, and the RANS form of the continuity and momentum equations are solved for both phases. In the two-fluid model, the solids concentration appears in the transport equations of each phase. Furthermore, it is possible to account for particle-particle interaction in the two-fluid model at high solids concentrations. Thus, the solids phase is treated as a 'fluid', but the modelling of the solids phase stresses continues to be a challenge for researchers.

The constitutive models for the solid stresses and the inter-phase momentum transfer are partially empirical. Single-phase flow closures are normally adopted for the fluid phase with concentration taken into account. For the solids phase, several approaches have been used to model the stresses in the averaged equations. The momentum equation contains both a solids pressure term and a solids molecular or laminar viscosity term. The solids pressure is either accounted for using an empirical correlation (Gidaspow, 1994), the theory of powder compaction (Bouillard et al., 1989) or the kinetic theory of dense gasses (Chapman and Cowling, 1970). Implementation of the correct solids laminar viscosity is critical. The development of constitutive relations for the solids viscosity is still a major area of research in the two-phase flow community. A variety of approaches including a constant value (e.g. Sun and Gidaspow, 1999; Gómez and Milioli, 2001), empirical correlations (e.g. Enwald et al., 1996) and theoretical formulations (e.g. Sinclair and Jackson, 1989; Enwald et al., 1996) have been used to specify the solids viscosity. Empirical correlations of the solids viscosity are usually determined from the mixture viscosity (measured experimentally), the carrier fluid viscosity, and the solids concentration. In many gas-solid flows relating to fluidization, the application of granular kinetic theory provides models for the solids pressure and viscosity of the solids phase (Gidaspow, 1994; van Wachem et al., 2001). The modelling issues become complicated when turbulence in the solids phase has to be considered and solids concentration fluctuations are also taken into account. Often the

solids phase turbulence is modelled in terms of the fluid phase turbulence through an eddy viscosity expression. In some studies which employ the kinetic theory, the solids phase turbulent stress is expressed in terms of the granular temperature. Second-order scalar moments resulting from solids concentration fluctuations are usually modelled using a gradient diffusion model.

1.3.3 Typical governing equations

As noted in the preceding section, the governing equations for the two-fluid model are similar irrespective of the averaging process employed. However, the interpretation of the terms - particularly the unclosed ones - is often different. With this in mind, a general set of phasic governing equations for isothermal flow are presented.

Continuity equations

Liquid phase

$$\frac{\partial}{\partial t}(\, c_{\mathrm{f}}\rho_{\mathrm{f}}) + \frac{\partial}{\partial x_i}\left(c_{\mathrm{f}}\rho_{\mathrm{f}}\, U_{\mathrm{f}i}\right) = 0, \tag{1.1}$$

Solids phase

$$\frac{\partial}{\partial t}(\, c_{\mathrm{s}}\rho_{\mathrm{s}}) + \frac{\partial}{\partial x_i}\left(c_{\mathrm{s}}\rho_{\mathrm{s}}\, U_{\mathrm{s}\,i}\right) = 0, \tag{1.2}$$

with the additional constraint of

$$c_{\mathrm{f}} + c_{\mathrm{s}} = 1. \tag{1.3}$$

The subscripts f and s denote the fluid and solids phases, respectively; c is the volume fraction or concentration; ρ is the material density; U_i is a component of the velocity field; and x_i denotes a coordinate direction.

Momentum equations

Liquid phase

$$\frac{\partial}{\partial t}(c_{\mathrm{f}}\rho_{\mathrm{f}}U_{\mathrm{f}i}) + \frac{\partial}{\partial x_j}(c_{\mathrm{f}}\rho_{\mathrm{f}}U_{\mathrm{f}i}U_{\mathrm{f}j}) = -c_{\mathrm{f}}\frac{\partial P}{\partial x_i} + \frac{\partial}{\partial x_j}\left(\mathfrak{T}_{\mathrm{f}ij}\right) - \beta\left(U_{\mathrm{f}i} - U_{\mathrm{s}i}\right) + c_{\mathrm{f}}\rho_{\mathrm{f}}g_i. \tag{1.4}$$

Solids phase

$$\frac{\partial}{\partial t}(c_{\mathrm{s}}\rho_{\mathrm{s}}U_{\mathrm{s}i}) + \frac{\partial}{\partial x_j}(c_{\mathrm{s}}\rho_{\mathrm{s}}U_{\mathrm{s}\,i}U_{\mathrm{s}j}) = -c_{\mathrm{s}}\frac{\partial P}{\partial x_i} + \frac{\partial}{\partial x_j}\left(\mathfrak{T}_{\mathrm{s}\,ij}\right) + \beta\left(U_{\mathrm{f}i} - U_{\mathrm{s}i}\right) + c_{\mathrm{s}}\rho_{\mathrm{s}}g_i. \quad (1.5)$$

where P is the mean fluid pressure; $\mathfrak{T}_{\mathrm{f}ij}$ and $\mathfrak{T}_{\mathrm{s}\,ij}$ are the effective stress tensors for the fluid and solids phase, respectively; β is the inter-phase drag correlation; and g is the gravitational acceleration.

1.4 Experimental Techniques for Slurry Flows

Most experimental studies of slurry flows have been limited to measurements of bulk parameters due to the inherent problems associated with detailed measurements of local field variables such as velocity and concentration in two-phase mixtures. For liquid-solid mixture flows, the pressure drop, deposition velocity, and in-situ concentration have been measured. These measurements cover a wide range of particle types and sizes as well as solids mean concentrations and mean velocities. In most of the studies where local field variables have been measured, conductivity probes and gamma-ray densitometers are usually used extensively (Sumner, 1992; Gillies, 1993). The conductivity probe is very sensitive to flow chemistry and, like the pitot-tube and other intrusive devices, cannot be used to obtain near-wall measurements due to its poor spatial resolution. While the conductivity probe can be used to measure local solids phase velocity and concentration, the gamma-ray densitometer is often used to measure chordal average concentration distribution to supplement velocity data measured with the conductivity probe. In general, local measurements have been hindered by instrument limitations.

The application of non-intrusive devices to measure flow quantities has been extended to two-phase particulate flows (Tsuji et al., 1984). The use of gamma ray and laser Doppler measurement techniques have enabled local flow field mean and fluctuating quantities to be measured in two-phase particulate flows (Alajbegovic et al., 1994; Fessler and Eaton, 1999; Liljegren and Vlachos, 1983). However, because slurry flows are generally opaque, the use of the common non-intrusive devices is limited to simple flows at low solids con-

centrations. Nevertheless, application of techniques such as Nuclear Magnetic Resonance (NMR) and Ultrasonic Doppler Techniques are emerging and showing promise for slurry data measurement. Presently, the NMR is not applied extensively for turbulent flows and the ultrasonic technique is only effective for obtaining solids velocity data. Recent studies employing imaging techniques are also emerging (for example, Kiger and Pan, 2000). For most multiphase flow data, particularly two-phase liquid-solids flow, only velocity and concentration profiles are available, while turbulence and higher order statistics are inconceivably difficult to measure. A detailed review of the experimental techniques is provided in Chapter 2.

1.5 Objectives and Organization of the Thesis

1.5.1 Objectives

In the hydrotransport of slurries with large particles in pipelines, the pipeline friction and the preconditioning of the slurries are important for the efficient operation of the transport system. The present work is part of a larger collaborative research program between the University of Saskatchewan and Syncrude Canada Limited in association with the Saskatchewan Research Council (SRC) to investigate coarse particle slurry flows in pipes. The project was funded by the Natural Sciences and Engineering Research Council of Canada (NSERC) through a Collaborative Research Development (CRD) grant supported by Syncrude Canada Limited. The project involved both experimental and numerical work.

The overall objective of this study was to simulate coarse particle liquid-solid flows in vertical and horizontal pipes, and to experimentally investigate these flows in a vertical pipe. The experimental work was conducted at the SRC Pipe Flow Technology Centre. A vertical flow loop was constructed for the project. The study involved measurement of radial distributions of solids velocity as well as pressure drop measurements. The numerical activity was performed at University of Saskatchewan. The numerical study involved the use of the commercial CFD package ANSYS CFX. The specific objectives are outlined below:

1. Investigate friction effects by obtaining pressure drop measurements of coarse particle in water slurry flows in a vertical flow loop using spherical glass beads as the solids phase.

2. Investigate particulate two-phase flow closure models, with special attention to the solids stress closure, for the prediction of coarse-particle liquid-solid flows in a vertical pipe using the two-fluid model in ANSYS CFX-4.4. The predicted radial profiles of solids velocity and concentration were compared with experimental data of Sumner et al. (1990).

3. Investigate solids-phase boundary conditions and their contribution to the total pressure drop of liquid-solid flows in vertical pipes. Comparisons between the predictions and the experimental results of Shook and Bartosik (1994) were made.

4. Predictions of solids velocity and concentration distributions in horizontal pipe flows of coarse-particle liquid-solids mixtures. The solids stress models implemented in ANSYS CFX-10 for the two-fluid model were tested. The predictions were compared with the solids velocity and concentration distributions from the benchmark experimental data from Gillies (1993).

1.5.2 Organization of the thesis

In Chapter 2, theoretical models for pressure drop predictions of liquid-solid flows in vertical and horizontal pipes as well as the effects of solids concentration and particle size on pipeline friction are reviewed. In addition, the two-fluid model is reviewed in terms of averaging techniques, closure problems, and formulation of boundary conditions. The chapter ends with a review of previous relevant experimental studies on vertical and horizontal flows. In Chapter 3, a vertical pipe flow loop facility and an experimental procedure for solids velocity and concentration measurements as well as pressure drop measurements are described. The solids velocity measured in the upward flow section of the flow loop are discussed in Chapter 3. The discussion of the pressure drop data analysis and results in upward and downward flow sections in a 53 mm diameter vertical pipe is also presented.

The transport equations for the phasic mass and momentum are derived in Chapter 4 by employing a so-called double averaging technique. Closure equations, as well as additional auxiliary equations and phasic boundary conditions are also discussed in a general context. In Chapter 5, liquid-solid flows in a vertical pipe were simulated using three approaches for the two-fluid model in ANSYS CFX-4.4. The effect of particle diameter and solids mean concentration on the predicted results is discussed. As well, a comparative study of five solids boundary condition formulations and their effect on the total frictional head loss for vertical flows of liquid-solid mixtures is reported. The simulation of coarse particle liquid-solid flows in horizontal pipes is discussed in Chapter 6, where the effect of the solids phase stresses implemented in ANSYS CFX-10 on the flow field variables is investigated. The simulations focused on the solids velocity and concentration results. A summary, conclusions, contributions, and recommendations for future work are provided in Chapter 7.

CHAPTER 2

LITERATURE REVIEW

In this chapter, theoretical, numerical and experimental studies of liquid-solid slurry flows are reviewed. The theoretical part considers methods for frictional head loss prediction and continuum modelling in the context of the two-fluid model. In the case of the frictional head loss, pressure drop analysis for vertical flows is considered followed by a discussion of the two-layer model for horizontal flows. The continuum modelling begins with a review of averaging techniques for the two-fluid model. Next, modelling techniques used to obtain closure for the two-phase momentum and auxiliary transport equations are considered. Finally, a brief survey of particulate flow experiments is provided. Experimental distributions of phasic concentration and velocity, as well as turbulence field variables, are reviewed. In addition, recent developments in measurement techniques and their limitations are highlighted.

2.1 Predictive Models for Liquid-Solid Flows

> *Because of its complexity, particulate and multiphase processing was treated with empiricism in the past decades, while other areas such as single fluid and solid mechanics attracted most of the scientific attention and relative progress. Currently, we are witnessing a significant shift of fortune that offers an outstanding challenge and opportunity to the particulate community. The methods of investigation for particulate and multiphase processes are rapidly moving from macroscopic (bulk) to microscopic and mesoscopic (particle-scale) analysis. The connection between the flow microstructure and macroscopic behaviour is a central research issue, and can provide a rational approach for predictive methods and new design in various industrial processes.*
>
> M.C. Roco, *Particulate Science and Technology: A New Beginning,*
> Particulate Science and Technology, Vol. 15, 81-83, 1997.

The observation of Roco (1997) cited above is particularly true for gas-solid flows and fluidized beds. However, studies of liquid-solid mixtures such as slurries still rely heavily on empiricism. This is not surprising because the physics of slurries is further complicated by the fact that the constituents of most practical slurries vary in physical composition and properties. Analytical methods using bulk parameters have been used for many years and have had a specific focus on pipeline friction prediction. For example, the two- (Gillies et al., 1991) or three-layer model (Doron and Barnea, 1993) are used to predict pressure drops in slurry pipelines. However, to predict local flow variables, the transport equations for the variables must be solved. That is the case of the mixture model (for example, Roco and Balakrishnan, 1985; Roco and Shook, 1984) and the two-fluid model (for example, Hadinoto and Curtis, 2004; Ling et al., 2002), which are methods used to predict local field variables of liquid-solid slurry flows. An additional drawback has been the fact that slurries are opaque, which makes local measurements more difficult. This opacity is a major setback for modern non-intrusive experimental instrumentation (Crowe, 1993). Significant advances (e.g. Dudukovic, 2000) have been made in recent years with specific attention on the measurement of higher-order moments in turbulent fluidized bed experiments for CFD model validation. For gas-solid flows, the experimental data of Tsuji et al. (1984) have contributed significantly to the development of microscopic models.

Prior to discussion of the theoretical aspects of liquid-solid (or slurry) flows, it is worth noting some significant earlier work on slurry transport in pipelines. Slurry pipeline design parameters include flow quantities such as the bulk velocity, the input or delivered concentration, and pressure drop. Several empirical correlations for pressure drop have evolved since the early part of the twentieth century (Howard, 1939; Wilson, 1942). The extensive work by Durand and co-workers (for example, Durand and Condolios, 1952) on pressure drop measurements for slurry flows was later improved by Wasp and co-workers (cf. Wasp et al., 1977). Newitt et al. (1955) noted that the contribution of the solids phase to the frictional head loss is the result of the particles immersed weight being transmitted to the wall of the pipe. This significant observation forms the basis of pipeline friction calculations in slurry flow research. Notable correlations can be found in the studies of Charles

(1970) and Turian and Yuan (1977), which aimed to provide pressure drop information for different flow regimes. As indicated in the review by Wani et al. (1982, 1983), extrapolation of the results to flow conditions outside the range of the database used to develop them must be done cautiously. In the following sections, frictional head loss analyses for vertical and horizontal flows, and a detailed review of the two-fluid model are discussed.

2.2 Liquid-Solid Flow Pressure Drop

Considering the flow mixture as a single fluid, the mixture momentum equation can be obtained by the summation of equations (1.4) and (1.5). For a fully developed flow, integration of the axial momentum equation over the pipe cross-section (assumed constant) for a constant density mixture yields the following expression for the pressure drop

$$-\frac{\mathrm{d}P}{\mathrm{d}z} = \frac{4\tau_{\mathrm{w}}}{D} + \rho_{\mathrm{m}} g \frac{\mathrm{d}h}{\mathrm{d}z}, \tag{2.1}$$

where P is the static pressure; z is the pipe axis along the flow direction; g is the acceleration due to gravity; D is the pipe diameter; τ_{w} is the total wall shear stress $\mathrm{d}h/\mathrm{d}z$ is the pipe inclination; and ρ_{m} is the mixture density:

$$\rho_{\mathrm{m}} = C_{\mathrm{s}}\rho_{\mathrm{s}} + (1 - C_{\mathrm{s}})\rho_{\mathrm{f}}. \tag{2.2}$$

2.2.1 Frictional head loss in vertical flows

In a vertical upward flow, the pressure drop $(P_1 - P_2)$ measured over a pipe section of length L is given by

$$\frac{(P_1 - P_2)}{L} = \frac{4\tau_{\mathrm{w}}}{D} + \rho_{\mathrm{m}} g. \tag{2.3}$$

The frictional pressure drop is typically expressed in the form

$$i_{\mathrm{m}}\rho_{\mathrm{f}} g = \frac{4\tau_{\mathrm{w}}}{D}, \tag{2.4}$$

where ρ_f is the liquid density and i_m is the frictional head loss of the liquid-solid mixture. The total shear stress τ_w is treated as the sum of the fluid and particle shear stresses:

$$\tau_\mathrm{w} = \tau_\mathrm{fw} + \tau_\mathrm{sw}. \tag{2.5}$$

For Newtonian fluids, the fluid phase wall shear stress is calculated from the linear stress-strain relationship

$$\tau_\mathrm{fw} = \mu_\mathrm{f} \left(\frac{\mathrm{d}U_\mathrm{f}}{\mathrm{d}y} \right)_\mathrm{w}, \tag{2.6}$$

where μ_f and U_f are the dynamic viscosity and the mean velocity of the liquid phase, and y is the distance normal to the wall of the pipe. A similar argument can be made for the solids phase if it is considered to exhibit Newtonian behaviour.

For the dispersion of large solids in a Newtonian fluid under shear, Bagnold (1954) characterised the stresses between the solids as 'macro-viscous' and 'grain-inertia' regimes, between which a transitional regime exists. The shear stress at the wall can be written for the 'macro-viscous' and 'grain-inertia' regimes as (cf. Shook and Bartosik, 1994)

$$\tau_\mathrm{sw} = \begin{cases} K_\mathrm{v} \mu_\mathrm{f} \lambda_\mathrm{L}^{3/2} \left(\dfrac{\mathrm{d}U_\mathrm{s}}{\mathrm{d}y} \right) \Bigg|_\mathrm{w} & Ba < 40 \\ K_\mathrm{i} \rho_\mathrm{s} d_\mathrm{p}^2 \lambda_\mathrm{L}^2 \left(\dfrac{\mathrm{d}U_\mathrm{s}}{\mathrm{d}y} \right)^2 \Bigg|_\mathrm{w} & Ba > 450. \end{cases} \tag{2.7}$$

In equation (2.7),

$$Ba = \frac{\rho_\mathrm{s} \lambda_\mathrm{L}^{1/2} d_\mathrm{p}^2 (\mathrm{d}U_\mathrm{s}/\mathrm{d}y)}{\mu_\mathrm{f}} \tag{2.8}$$

is the Bagnold number, where $\mathrm{d}U_\mathrm{s}/\mathrm{d}y$ is the shear rate of the solids phase at the wall, and λ_L is the linear concentration (e.g. Bagnold, 1954; Shook and Roco, 1991) given by

$$\lambda_\mathrm{L} = \left[\left(\frac{C_\mathrm{max}}{C_\mathrm{s}} \right)^{\frac{1}{3}} - 1 \right]^{-1}. \tag{2.9}$$

In general, the Bagnold number indicates whether the source of granular (i.e. the

solids phase) stresses is from inter-particle collisions or from the interstitial fluid. In his study of fluid-particle flows in a shear cell, Bagnold concluded that when the value of Ba is less than 40, the viscous interstitial fluid dominates and the mixture exhibits a Newtonian rheology (that is the solids phase stress and strain are linearly related) meaning that the solids phase stress is due to the viscous effect of the interstitial fluid. This regime is called the macro-viscous regime. When Ba greater than 450, direct collision between particles and particle-wall collisions dominate and the stress becomes proportional to the square of the strain rate; this regime is called the grain-inertia regime. The grain-inertia regime can be related to the rapid granular flow regime where the stresses are entirely attributed to kinetic and collisional effects. It should be noted that the concept of a rapid granular flow regime also extends to dilute regions where it is expected that the contribution of the kinetic stress will be higher compare to the collisional contribution. The coefficients determined for K_{i} and K_{v} in the work by Bagnold (1954) are approximately 2.25 and 0.013, respectively. In the study of Shook and Bartosik (1994), it was assumed the velocity gradient at the wall was equal for both phases since velocity information for both phases is not always readily available. The same approach was adopted by Bartosik (1996) who modified equation (2.7) to the form

$$\tau_{\mathrm{sw}} = \frac{8.3018 \times 10^7}{Re_{\mathrm{f}}^{2.317}} D^2 \rho_{\mathrm{s}} d_{\mathrm{p}}^2 \lambda_{\mathrm{L}}^{3/2} \left(\frac{\mathrm{d}U_{\mathrm{l}}}{\mathrm{d}y} \right)^2 \Bigg|_{\mathrm{w}}, \tag{2.10}$$

where Re_{f} is the liquid phase Reynolds number, and D represents the diameter of the pipe. Recently, Matousek (2002) evaluated the effect of the modified Bagnold stress at the wall given by equation (2.10). It was observed that equation (2.10) predicted a much smaller value for the solids effect than that measured in a vertical pipe for both medium and coarse sand slurries.

Using the friction factors for the fluid phase and solids phase, and equation (2.5) it can be shown that the wall shear stress for vertical flows is

$$\tau_{\mathrm{w}} = 0.5 V^2 \left(f_{\mathrm{f}} \rho_{\mathrm{f}} + f_{\mathrm{s}} \rho_{\mathrm{s}} \right), \tag{2.11}$$

where V is the bulk velocity, and f_{f} and f_{s} are the friction factors of the liquid and solids-

phases, respectively. The fluid phase wall stress is determined by estimating the fluid phase friction factor f_{f} for the pipe using the Reynolds number ($Re = DV\rho_{\mathrm{L}}/\mu_{\mathrm{f}}$) and the roughness ($k$) from the correlation of Churchill (1977). The correlation of Churchill (1977), which can used for both laminar and turbulent flows over smooth or rough surfaces is often applied to estimate f_{f} in the slurry flow community:

$$f_{\mathrm{f}} = 2\left[\left(\frac{8}{Re}\right)^{12} + (A+B)^{-1.5}\right]^{\frac{1}{12}}, \tag{2.12}$$

with A and B given by

$$A = \left\{-2.457\ \ln\left[\left(\frac{7}{Re}\right)^{0.9} + 0.27\left(\frac{k}{D}\right)\right]\right\}^{16} \quad \text{and} \quad B = \left(\frac{37530}{Re}\right)^{16}. \tag{2.13}$$

For the solids-phase, different correlations for f_{s} have been used for different flow conditions and for various d_{p}/D values. Shook and Bartosik (1994) proposed a correlation of the form

$$f_{\mathrm{s}} = \mathrm{A}\left(\frac{d_{\mathrm{p}}V\rho_{\mathrm{s}}}{\mu_{\mathrm{f}}}\right)^{\mathrm{I1}}\left(\frac{d_{\mathrm{p}}}{D}\right)^{\mathrm{I2}}\lambda_{\mathrm{L}}^{\mathrm{I3}}, \tag{2.14}$$

where A = 0.0153, I1 = -0.15, I2 = 1.53, and I3 = 1.69. In the study of Ferré and Shook (1998), the coefficient and indices in equation (2.14) were modified as A = 0.0428, I1 = -0.36, I2 = 0.99, and I3 = 1.31 to closely match the experimental results.

2.2.2 Frictional head loss in horizontal flows: The Two-Layer Model

The two-layer model concept began with the initial studies of Wilson et al. (1972). The two-layer model consists of force and mass balances coupled together using the two layers shown in Figure 2.1. In Figure 2.1, A_1 and A_2 are the cross-sectional areas of layers 1 and 2, respectively, and $A = A_1 + A_2$; C_1 and V_1 are the concentration and velocity in layer 1; V_2 is the velocity in layer 2, and C_2 is the incremental concentration in layer 2. The quantity C_{lim} is assumed to be the total coarse particle concentration in layer 2 including C_1, (i.e. $C_{\mathrm{lim}} = C_1 + C_2$) (see Gillies, 1993). The quantities S_1, S_2, S_{12} are the perimeters bounded by the surface of the pipe in layers 1 and 2, and of the interface, respectively.

Also, β_{ha} is the half-angle subtended by the interface. The stresses at the boundaries and at the interface are calculated independently. The upper layer is usually assumed to contain particles whose immersed weight is balanced by lift forces due to the fluid so that the fluid and particles (i.e. fines) together form the carrier fluid.

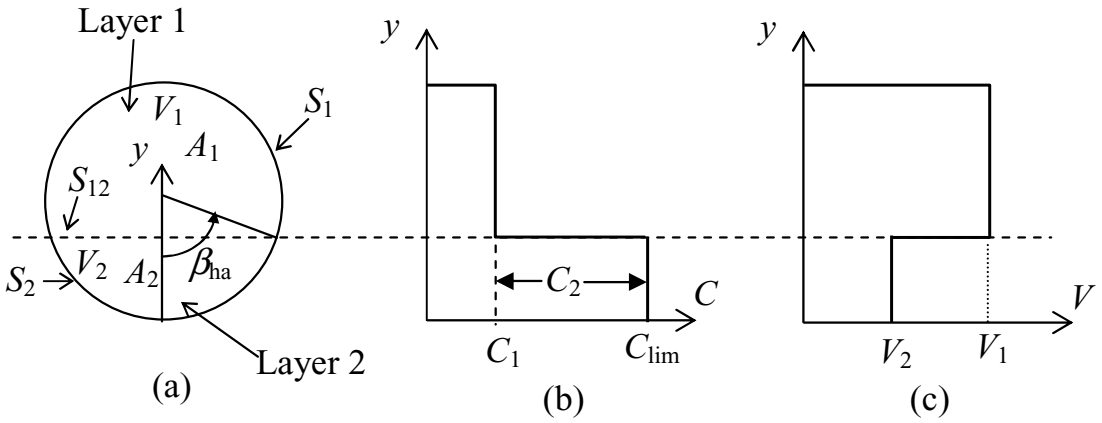

Figure 2.1: Idealized concentration and velocity distributions used in the SRC two-layer model; (a) cross-section of pipe, (b) step profile for concentration distribution, and (c) step profile for velocity.

The force balance includes contributions from the fluid wall friction in each layer and particle-wall friction in the lower layer. The initial two-layer model was developed using the coefficient of Coulombic friction, η_s, and a friction coefficient that is dependent on velocity and constituent properties. The research group at the Pipe Flow Technology Centre of SRC extended the model to coarse particle slurry flows (Gillies et al., 1985) with several improved versions over the past two decades (Gillies et al., 1991; Gillies and Shook, 2000; Gillies et al., 2004). Recent versions of the two-layer model for slurry flows in horizontal or inclined pipes (Gillies et al., 1991; Shook et al., 2002) are based on the concept that the concentration and velocity distributions at any cross section consisting of the two layers separated by a hypothetical interface (Figure 2.1).

In horizontal flows, the frictional head loss can be directly determined from the mea-

sured pressure gradient

$$-\frac{\mathrm{d}P}{\mathrm{d}z} = \frac{(P_1 - P_2)}{L} = \frac{4\tau_{\mathrm{w}}}{D} = i_{\mathrm{m}}\rho_{\mathrm{f}}g, \tag{2.15}$$

In the two-layer model for a horizontal slurry flow, the frictional head losses for the upper and lower layers are given by

$$i_{\mathrm{m}}\rho_{\mathrm{f}}g = \frac{\tau_1 S_1 + \tau_{12} S_{12}}{A_1} \tag{2.16}$$

and

$$i_{\mathrm{m}}\rho_{\mathrm{f}}g = \frac{\tau_2 S_2 - \tau_{12} S_{12} + F_2}{A_2}, \tag{2.17}$$

respectively, where the stresses τ_1 and τ_2 are stresses which act on the pipe wall in the upper and lower layers, respectively; τ_1 opposes the motion in Layer 1, while τ_2 opposes the motion in Layer 2; F_2 is the Coulombic force which opposes the motion of layer 2. Equations (2.16) and (2.17) constitute the two-layer model.

2.2.3 Frictional stresses

The frictional stresses in layers 1 and 2, τ_1 and τ_2, are velocity-dependent and are calculated from the velocities in the respective layers:

$$\tau_{\mathrm{L}} = 0.5 V_{\mathrm{L}}^2 \left(f_{\mathrm{f_L}}\rho_{\mathrm{f}} + f_{\mathrm{s_L}}\rho_{\mathrm{s}}\right), \quad \mathrm{L} = \mathrm{Layer}\ \ 1, \mathrm{Layer}\ \ 2. \tag{2.18}$$

In equation (2.18), $f_{\alpha_{\mathrm{L}}}$ is the friction factor of each phase α. The equation shows that in each layer the frictional stress is produced by fluid ($\alpha \equiv \mathrm{f}$) and solids ($\alpha \equiv \mathrm{s}$) effects. The fluid contribution to the frictional stress is determined by estimating the fluid friction factor from equation (2.12). The solid contribution to the frictional stress is determined by estimating the solids friction factor f_{s}. The current correlation for the solids friction factor (Gillies et al., 2004) is

$$f_{\mathrm{s}} = \lambda_{\mathrm{L}}^{1.25}\left[0.00005 + 0.00033\exp\left(-0.10\, d^{+}\right)\right], \tag{2.19}$$

where d^+ is the dimensionless particle diameter:

$$d^+ = d_\mathrm{p}\frac{\rho_\mathrm{f}}{\mu_\mathrm{f}}u_\tau = d_\mathrm{p}\frac{\rho_\mathrm{f}}{\mu_\mathrm{f}}V_\mathrm{L}\left(\frac{f_{\mathrm{f_L}}}{2}\right)^{0.5`}; \tag{2.20}$$

and u_τ is the friction velocity.

The stress τ_{12} at the interface between the layers is computed from the velocity difference $V_1 - V_2$ and the density of the upper layer ρ_1 using a fanning friction factor characteristic of the interface f_{12}:

$$\tau_{12} = 0.5 f_{12}\left(V_1 - V_2\right)^2 \rho_1, \tag{2.21}$$

where $\rho_1 = C_1\rho_\mathrm{s} + (1 - C_1)\,\rho_\mathrm{f}$.For highly stratified flows Wilson and Pugh (1995) (cf. Shook et al., 2002) proposed an interfacial friction factor given by

$$f_{12} = 0.2175\left[\frac{i_\mathrm{m}}{(\rho_\mathrm{s}/\rho_\mathrm{f}) - 1}\right]^{0.78}. \tag{2.22}$$

For flows with less stratification, Gillies et al. (1991) proposed the following relation for the interfacial friction factor:

$$f_{12} = \begin{cases} 2\dfrac{1}{\left[3.36 + 4\log_{10}(d_\mathrm{p}/D)\right]^2}, & d_\mathrm{p}/D < 0.002 \\ 2\dfrac{\left[1 + 5 + 1.86\log_{10}(d_\mathrm{p}/D)\right]}{\left[3.36 + 4\log_{10}(d_\mathrm{p}/D)\right]^2}, & d_\mathrm{p}/D \geq 0.002 \end{cases} \tag{2.23}$$

2.2.4 Coulombic stresses

The Coulombic and frictional stresses (τ_1 and τ_2) are modelled using empirical and semi-empirical correlations that are based on physically sound theories and experimental evidence. The friction due to the particles at the boundary is due to Coulombic effects and interaction with other particles (Gillies, 1993). The Coulombic friction force F_2 is the resisting force exerted by the wall on the particles and creates a normal inter-particle stress gradient:

$$\frac{\mathrm{d}\sigma_{_2}}{\mathrm{d}y} = \left(\rho_\mathrm{s} - \rho_\mathrm{f}\right) g C_\mathrm{lim}, \tag{2.24}$$

where σ_2 is the normal inter-particle stress in Layer 2. Estimation of $C_{\rm lim}$ has been a major issue in the development of the SRC two-layer model. In the study of Gillies et al. (1985) a constant value of $C_{\rm lim}$ was used. Taking the solids concentration into account, Gillies et al. (1991) used a correlation for $C_{\rm lim}$ that depends on the in-situ concentration $C_{\rm r}$, mean flow velocity V, and the terminal falling velocity v_∞ for particles with a mass median particle diameter d_{50} greater than 74μm :

$$\frac{C_{\rm max}-C_{\rm lim}}{C_{\rm max}-C_{\rm r}} = 0.074\left(\frac{V}{v_\infty}\right)^{0.44}(1-C_{\rm r})^{0.189}, \tag{2.25}$$

where $C_{\rm max}$ is the maximum packing concentration of the solids, $C_{\rm r}$ is the mean spatial volume fraction of the coarse particles, and v_∞ is the particle settling velocity at infinite dilution. A method for estimating the solids mean concentration based on physical arguments and experimental observations was later proposed in the work of Gillies and Shook (1994) who also postulated a semi-empirical approach for calculating $C_{\rm lim}$. In the earlier two-layer models, the interfacial stress was considered to produce a normal stress in the solids in layer 2, i.e. $\sigma_2 = \tau_{12}/\tan\varphi$, where φ is the angle of internal frictional of the particles. Gillies et al. (1991) integrated equation (2.24) and obtained an equation for the solids shear stress that, in addition to the stress in Layer 2, also depends on the stress at the interface between the two layers. Later, Gillies and Shook (2000) obtained a Coulombic shear stress relation that is independent of the stress at the interface between Layer 1 and Layer 2. The result, expressed as a Coulombic force, is

$$F_2 = \frac{0.5\left(\rho_{\rm s}-\rho_{\rm f}\right)gD^2\eta_{\rm s}\left(\sin\beta_{\rm ha}-\beta_{\rm ha}\cos\beta_{\rm ha}\right)\left(C_{\rm lim}-C_1\right)\left(1-C_{\rm lim}\right)}{1-C_{\rm lim}+C_1}. \tag{2.26}$$

To estimate the frictional head loss using the two-layer model, the slurry flow pipeline designer must determine the stresses τ_1 and τ_2 in layers 1 and 2, respectively as well as the Coulombic force F_2. To do that V, $C_{\rm t}$, $C_{\rm max}$, D, $\rho_{\rm f}$, $\rho_{\rm s}$, $\mu_{\rm f}$, and k must be specified. In addition, the particle size distribution, the relationship between viscosity and concentration for the fine particles and the particle drag coefficients must be known. The steps to be taken leading to the estimation of i_m are detailed in the works of Gillies (1993) and Gillies et al.

(2004).

2.3 Particle Size and Concentration Effects on Pipeline Friction

The effect of the particle diameter d_{p} on the fluid phase friction factor is often considered negligible. It is, however, worth noting that fine particles can change the rheological properties of the carrier fluid and consequently affect the friction factor. The dependence of the fluid phase friction factor on concentration is influenced by the concentration of the fines in the mixture.

The effect of particle diameter on the solids-phase friction factor friction f_{s} is physically based on the particle-fluid interaction in the near-wall region of the flow. For a particular flow condition, Wilson et al. (2000) and Wilson and Sellgren (2003) proposed a Kutta-Joukowski lift force on the particles in the near-wall region that can drive them away from the wall provided the particles are large enough not to be trapped in the viscous sub-layer. For small particles trapped in the viscous sub-layer, the lift force is not able to repel them away from the wall. The resulting effect is either a combined effect of kinematic and Coulombic friction, if the particles form a moving bed, or a Coulombic friction due mainly to a stationary bed. In either case, the solids friction would be high. For larger particles with diameter greater than the thickness of the viscous sub-layer, the recent theory of Wilson et al. (2000) predicts that the lift force will repel the particles from the wall and this will decrease the friction factor. This has been supported by the experimental results of Gillies et al. (2004). At higher velocities, the lift force also reduces the Coulombic friction, significant especially for finer particles.

At low velocities, the friction factor increases rapidly as the concentration is increased beyond a certain level; Gillies and Shook (2000) noted that this concentration is typically between 30% and 35%. As shown in their horizontal flow experiments for high concentration slurries, this indicates that the Coulombic friction will increase at low velocities due to a high concentration at the bottom of the pipe.

2.4 Two-Fluid Models

The development of the two-fluid model consists of three fundamentally important steps: the averaging process, the development of constitutive relations, and the boundary condition formulation.

2.4.1 Averaging techniques

The ergodic theorem of averaging often assumed for stationary and homogeneous single-phase turbulence (Kleinstreuer, 2003; Monin and Yaglom, 1971; Wilcox, 2002) is usually adopted to derive the two-phase mass and momentum transport equations. Prior to performing an averaging process, a number of assumptions regarding the flow physics are often made (e.g. Ahmadi and Ma, 1990; Elghobashi and Abou-Arab, 1983). Different averaging techniques have also been related to particular types of two-phase flows (Roco and Shook, 1985). Over the past three decades, several extensive studies on averaging techniques for two-phase flows have appeared in the literature. The types of averaging include volume averaging (e.g. Soo, 1967; Whitaker, 1969, 1973), local mass and local time averaging (e.g. Roco, 1990), and ensemble averaging (e.g. Drew, 1983; Drew and Lahey, 1993; Drew and Passman, 1999; Joseph and Lundgren, 1990). Others include local spatial averaging (e.g. Anderson and Jackson, 1967; Jackson, 1997, 1998), space-time averaging (e.g. Elghobashi and Abou-Arab, 1983; Roco and Shook, 1985), and double-time averaging (e.g. Abou-Arab and Roco, 1990; Roco, 1990).

2.4.2 Two-phase closure problem

In general, the averaged equations of the two-fluid model are very similar in form to the equations given in Section 1.3.3 irrespective of the averaging technique used; the basic differences were outlined in that section. The averaging process generates additional quantities (including averages of products) so that the number of unknowns is greater than the number of equations. The additional quantities must be modelled to close the system of equations, but typically it is not possible for the closure to apply to all flows. More importantly, Joseph and Lundgren (1990) noted that the closure models derived from one par-

ticular averaging approach (e.g. ensemble averaging) can be very different from those of another (e.g. volume averaging). In view of this, the development of constitutive relations must be treated with caution. This issue has also been pointed out in a few other studies (Hwang and Shen, 1993; van Wachem and Almstedt, 2003).

The development of constitutive models for multiphase flows continues to be a major research topic. This is due to the complex phenomena of fluid-fluid, fluid-particle, particle-particle, and particle-wall interactions. The physical properties and concentration of the solid particles are factors that strongly influence the interaction. The fluid-fluid interactions are modelled using single-phase flow approaches; the fluid-particle interactions are obtained from empirical correlations; and the particle-particle or particle-wall interactions are often modelled using constitutive equations derived from the kinetic theory of granular flows with or without modified plasticity models based on Coulomb friction. The pioneering work of Bagnold (1954) was crucial to understanding the particle-particle interaction phenomena in granular flows. The use of the kinetic theory of dense gases (Chapman and Cowling, 1970) with application to granular flows (Savage, 1983) to model these inter-particle interactions has received a lot of attention. Several studies based on the kinetic theory of granular flow have been applied to a wide range of particulate two-phase flows. However, only few studies have focused on a variety of liquid-solid flows (e.g. Abu-Zaid and Ahmadi, 1996; Greimann and Holly, 2001; Hsu et al., 2004; Ling et al., 2002).

2.4.2.1 Inter-phase momentum transfer

The inter-phase momentum transfer term typically has contributions from drag, lateral lift, virtual mass, and Basset forces. For the types of flow investigated in the present work, the lateral lift, virtual mass, and Basset forces are assumed negligible compared to the drag force and, therefore, only the momentum transfer due to drag is discussed below. In general, the drag force on a particle in a fluid-solid flow system is represented by the product of the inter-phase drag function β and the relative velocity.

Several correlations for β have been proposed in the literature. For flows with high solids concentrations, the correlations were obtained from pressure drop measurements in fixed, fluidized, or settling beds. Ergun (1952) performed pressure drop measurements in fixed liquid-solid beds at packed conditions. The extensive sedimentation experiments of Richardson and Zaki (1954) led to the correlation between settling velocity and voidage. The correlation has been extended in many forms to estimate β. Wen and Yu (1966) considered settling of solid particles in a liquid for a wide range of solids concentration. They correlated their data with those from other studies for solids concentration in the range $0.01 \leq C_{\mathrm{s}} \leq 0.63$.

In recent years, studies have been performed on the sensitivity of a number of drag correlations on predictions for gas-solids flows (e.g. Yasuna et al., 1995) and fluidized beds (e.g.7 van Wachem et al., 2001). Yasuna et al. (1995) investigated the inter-phase drag correlations of Ding and Gidaspow (1990), Syamlal (1990), Richardson and Zaki (1954), and Schiller and Naumann (1933) for gas-solid flows in a vertical pipe. Overall, it was concluded that the computed results were insensitive to the choice of the inter-phase drag correlation for the solids phase concentration range considered. van Wachem et al. (2001) investigated the effect of the inter-phase drag correlations of Gidaspow (1994), Syamlal et al. (1993), and Wen and Yu (1966) on flow predictions in freely bubbling, slugging and bubble injected fluidized beds. van Wachem et al. (2001) found that the inter-phase drag correlations of Gidaspow (1994) and Wen and Yu (1966) reproduced flow features observed in experiments better than the correlation of Syamlal et al. (1993). The performance of most of the current two-fluid models has been generally attributed to the accuracy of the inter-phase drag term used (Zhang and Reese, 2003a).

In dilute flows, the inter-phase drag function typically depends on the drag coefficient, C_{D}, for a single particle and is based on the number of particles per unit volume. A simple form is given by

$$\beta = \frac{3}{4} C_D \frac{c_{\mathrm{s}} \rho_{\mathrm{f}}}{d_{\mathrm{s}}} |U_{si} - U_{\mathrm{f}i}|, \tag{2.27}$$

where $d_{\rm s}$ is the diameter of the particle, C_D is the drag coefficient of a single particle, and $\rho_{\rm f}$ is the density of the fluid phase. The drag coefficient varies for different flow regimes and depends on the particle Reynolds number $Re_{\rm p}$. In the viscous and inertial regimes, the drag coefficient correlations commonly used are those of Schiller and Naumann (1933):

$$C_D = \begin{cases} 24/Re_{\rm p} & Re_{\rm p} \leq 0.1, \\ 24/Re_{\rm p}(1 + 0.15Re_{\rm p}^{0.687}) & 0.1 < Re_{\rm p} < 1000, \\ 0.44 & Re_{\rm p} \geq 1000, \end{cases} \tag{2.28}$$

where $Re_{\rm p} = \rho_{\rm f}|U_{\rm s} - U_{\rm f}|d_{\rm p}/\mu_{\rm s}$ is the Reynolds number. For many particulate flows with a wide range of solids concentration, the experimental studies mentioned above are usually employed to provide correlations for the inter-phase drag coefficient that account for the dense regions in the mixture. For dense flows, the so-called Ergun equation is used to obtain the inter-phase drag correlation in CFX-4.4 (Gidaspow, 1994);

$$\beta = 150\frac{c_{\rm s}^2\mu_{\rm f}}{(1-c_{\rm s})d_{\rm s}^2} + 1.75\frac{c_{\rm s}\rho_{\rm f}|U_{{\rm s}i} - U_{{\rm f}i}|}{d_{\rm s}} \quad . \tag{2.29}$$

For the Wen and Yu (1966) model, the inter-phase drag correlation is given by

$$\beta = \frac{3}{4}C_D\frac{c_{\rm s}c_{\rm f}\rho_{\rm f}}{d_{\rm s}}|U_{{\rm s}i} - U_{{\rm f}i}|\ c_{\rm f}^{\ -2.65} \tag{2.30}$$

In this case, the drag coefficient used is given by

$$C_D = \begin{cases} 24/c_{\rm f}Re\left[1 + 0.15(c_{\rm f}Re)^{0.687}\right] & c_{\rm f}Re < 1000 \\ 0.44 & c_{\rm f}Re \geq 1000. \end{cases} \tag{2.31}$$

The correlations of Garside and Al-Dibouni (1977) and Richardson and Zaki (1954) were used by Syamlal et al. (1993) to determine the terminal velocity in fluidized and settling beds expressed as a function of the solid volume fraction and the particle Reynolds number. The drag coefficient is readily determined from the terminal velocity. Thus, the inter-phase

drag correlation of Syamlal et al. (1993) is

$$\beta = \frac{3}{4} C_D \frac{c_\mathrm{s} c_\mathrm{f} \rho_\mathrm{f}}{v_\mathrm{r,s}^2 \, d_\mathrm{s}} |U_{\mathrm{s}i} - U_{\mathrm{f}i}|, \tag{2.32}$$

where the drag coefficient has the form derived by Dalla Valle (1961)

$$C_D = \left(0.63 + 4.8 \sqrt{\frac{v_\mathrm{r,s}}{Re}} \right)^2 \tag{2.33}$$

and $v_\mathrm{r,s}$ is the terminal velocity correlation of Garside and Al-Dibouni (1977) for the solid phase,

$$v_\mathrm{r,s} = 0.5 \left[a - 0.06 \; Re + \sqrt{(0.06Re)^2 + 0.12Re(2b - a) + a^2} \; \right]. \tag{2.34}$$

In equation (2.34), a and b are expressed as

$$a = c_\mathrm{f}^{4.14} \tag{2.35}$$

and

$$b = \begin{cases} 0.8 \; c_\mathrm{f}^{1.28} & c_\mathrm{s} \geq 0.15 \\ c_\mathrm{f}^{2.65} & c_\mathrm{s} < 0.15 \end{cases}. \tag{2.36}$$

2.4.2.2 Fluid-phase stress closures

Closure for the fluid-phase effective stress for turbulent flow is normally derived using methods available for single-phase flows. The viscous stress tensor is defined using the linear stress-strain relation. In the context of the $k - \varepsilon$ model, the turbulent or Reynolds stress tensor is calculated using the eddy-viscosity approximation based on the Boussinesq assumption. The determination of the eddy-viscosity requires a solution to the transport equations of the turbulence kinetic energy k and its dissipation rate ε. This approach has been widely adopted but also treated with caution (Bolio et al., 1995), since the constants appearing in the modelled equations of k and ε are the same as those used for single-phase flows.

Squires and Eaton (1994) investigated the values of two model constants in the transport equation of the dissipation rate of the turbulence kinetic energy by comparing the solutions from a gas-phase $k-\varepsilon$ model with DNS simulation data for homogeneous isotropic turbulence interacting with particles. The constants are C_{ε_2}, which appears in the source term for a single-phase flow and C_{ε_3} that appears as an additional source term that accounts for inter-phase turbulence interaction. They showed that these two constants depend on the Stokes number, i.e. the ratio of the turbulence time scale to the particle response time ($t_{\mathrm{T}}/t_{\mathrm{p}}$) and the loading, $X_{\mathrm{fs}} = c_{\mathrm{s}}\rho_{\mathrm{s}}/c_{\mathrm{f}}\rho_{\mathrm{f}}$. For the cases they investigated, the results showed that for $t_{\mathrm{T}}/t_{\mathrm{p}} = 0.14$ and $X_{\mathrm{fs}} = 1.0$, C_{ε_2} increased by a factor of 6 and C_{ε_3} by a factor of 4 compared to the single-phase values. The influence of particles was found to depend less on the loading for a higher Stokes number of $t_{\mathrm{T}}/t_{\mathrm{p}} = 1.5$. Bolio et al. (1995) performed a sensitivity test on the model constants c_1, c_2, c_μ, σ_k, and σ_ϵ, using a low-Reynolds number model and found the effect of the variations on their predictions to be insignificant when the values of the constants were varied by ± 0.1. In the study of Cao and Ahmadi (1995), the particle effect was accounted for by using a model constant that depends on the Stokes number and solids concentration in the eddy-viscosity relation.

2.4.2.3 Solids-phase stress closures

For the solids-phase, the effective stress tensor has been interpreted differently in the literature depending on whether the flow is dilute or dense. The treatment for the solids-phase viscous stress was discussed in Chapter 1. For dilute flows, Rizk and Elghobashi (1989) expressed the eddy-viscosity of the solids-phase in terms of that of the fluid-phase. Bolio et al. (1995) employed the kinetic theory of granular flow using the constitutive equations developed in the study of Lun et al. (1984) with a slight modification to account for the particle mean free path. In this case a transport equation for the so-called granular temperature was solved. The model of Bolio et al. (1995) was extended further by Hrenya and Sinclair (1997), who considered turbulence in the particle phase and employed a mixing length model for the solids-phase eddy-viscosity. Cao and Ahmadi (1995) modelled the solids-phase eddy-viscosity using a two-equation $k_{\mathrm{s}} - \varepsilon_{\mathrm{s}}$ model, where a transport equation for k_{s} was solved and ε_{s} was calculated using an algebraic equation. Interestingly, all of the

models used in these independent studies produced reasonable agreement with velocity and turbulence data from the dilute flow experiments of Tsuji et al. (1984).

Cao and Ahmadi (1995) extended their simulations to dense flows using data from the study of Miller and Gidaspow (1992) while Hrenya and Sinclair (1997) compared their results with the experimental data of Lee and Durst (1982). For dense flows, the effective stress tensor is modelled in terms of the granular pressure, collisional stress and kinetic or streaming stress (Gidaspow, 1994; Enwald et al., 1996; Peirano and Leckner, 1998). As well, when turbulent fluctuations in the solids-phase due to concentration fluctuations are assumed, additional terms appear in the momentum equation that must also be modelled. Presently, models based on the kinetic theory are developed using the following assumptions: mean spatial gradients of velocity and granular temperature are small, a low level of anisotropy exists, particles are nearly elastic and do not rotate, and the solids concentration gradient is assumed negligible. For liquid-solid flows, it is evident that these assumptions are not always met as the experimental data of Alajbegovic et al. (1994) demonstrates.

For horizontal flows that fall within the regimes shown in Figure 1.2, an elaborate model will be one that considers all three regimes, i.e. homogeneous, heterogeneous, and saltation flow regimes. This could be achieved by employing the concepts of slow and rapid granular flows.

Slow granular flows assume a quasi-static regime where the stress is determined using theories from soil mechanics. A number of models have been proposed since the derivation by Schaeffer (1987) and are typically based on the Coulomb yield friction criterion (cf. Jenike and Shield, 1959), which states that the principal shear stress is directly proportional to the principal normal stress, where the proportionality constant is the sine of the *internal friction angle* φ. Some of the proposed forms can be found in the works of Johnson and Jackson (1987); Johnson et al. (1990) and Syamlal et al. (1993). Rapid granular flow refers to the regime where random particle velocities exist. As in turbulence, the particle velocities can be decomposed into mean and fluctuating components. The en-

ergy associated with the fluctuating motions is represented by the granular temperature, T_{s}.

The study by Bagnold (1954) has been the motivation for the subsequent development of the kinetic theory of granular flow. Savage and Jeffrey (1981) and Jenkins and Savage (1983) applied the kinetic theory of dense gases to develop a more rigorous theory for rapid granular flows. An extensive literature on the subject exists, and detailed studies and reviews (Enwald et al., 1996; Peirano and Leckner, 1998; Simonin, 1996) as well as books (e.g. Gidaspow, 1994) have been published. Therefore, it is now a common practice to model solids-phase stresses in particulate two-phase flows using the kinetic theory of granular flow. The dry granular flow models of Gidaspow (1994) and Lun et al. (1984) with some minor modifications by other authors, as well as the extension of the work of Jenkins and Richman (1985) by Peirano and Leckner (1998) to account for interstitial fluid effects, can be considered state of the art models, at least for pneumatic transport and fluidization applications.

2.4.2.4 Coupling mechanisms

The coupling mechanisms in two-phase flows are related to the interaction between the primary phases (i.e. fluid) and the secondary phase (i.e. particles, droplets etc), and/or between the particles of the secondary phase and their effect on the fluid turbulence. For very dilute suspensions, say $c_{\mathrm{s}} \leq 10^{-6}$ or $l_{12}/d_{\mathrm{p}} \geq 100$, the particles have negligible effect on the turbulence of the fluid and their motion is governed by the turbulent motion of the fluid-phase. Here, l_{12} is the relative distance between two particles. In this regime, the dispersion of particles depends on the state of the fluid-phase turbulence but there is no feedback to the fluid-phase turbulence. This mechanism is termed 'one-way coupling'. A second regime, referred to as 'two-way coupling', is characterised by $10^{-6} < c_{\mathrm{s}} \leq 10^{-3}$ or $10 \leq l_{12}/d_{\mathrm{p}} < 100$, where the solids concentration is large enough so that the particles can either enhance or damp the turbulence. Gore and Crowe (1989) analysed several independent experimental data and observed that if $d_{\mathrm{p}}/l_{\mathrm{f}} > 0.1$ (l_{f} is the integral length scale), turbulence is enhanced and if $d_{\mathrm{p}}/l_{\mathrm{f}} < 0.1$, turbulence is attenuated. In addition to the two-

way coupling mechanism, a third regime arises if the relative distance between particles, l_{12} is small enough for particle-particle interactions to occur. The term 'four-way coupling' is often associated with this regime.

To determine the effect of particles on the fluid turbulence, Hetsroni (1989) suggested that particles enhance turbulence due to vortex shedding when the particle Reynolds number, $Re_{\mathrm{p}} > 400$. The particle Reynolds number is based on the particle diameter, the velocity of the particle relative to the fluid, and the fluid properties. Elghobashi (1994) proposed that the ratio of the particle response time scale t_{p} to the turbulence time scale t_{T} can be used to determine how the fluid turbulence is modified. This is illustrated in Figure 2.2. In Figure 2.2, particles at a concentration of $c_{\mathrm{s}} = 10^{-4}$ or less have negligible effect on the fluid turbulence irrespective of their time scale. Between $c_{\mathrm{s}} = 10^{-4}$ and $c_{\mathrm{s}} = 10^{-3}$, particles with a small response time decrease turbulence and those with large response time increase it. Beyond $c_{\mathrm{s}} = 10^{-3}$, the particle-particle interactions become dominant and independent of the particle time response time.

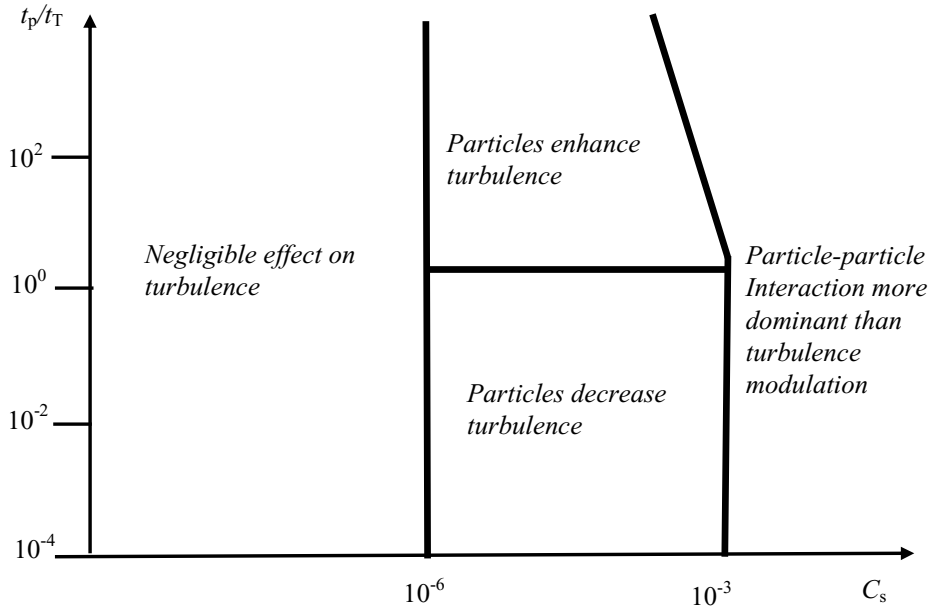

Figure 2.2: Particle effect on fluid turbulence.

2.5 Boundary Conditions

Like any other flow, accurate specification of boundary conditions for liquid-solid slurry flows is very important because it heavily influences the wall shear stress and the near-wall turbulence production. However, while the importance of the boundary conditions, especially for the solids-phase, have been emphasized in some studies, the free slip boundary condition or zero shear stress at the wall is commonly assumed. The pressure gradient required to overcome friction is an important design parameter for slurry pipelines. For single-phase flows and very dilute two-phase flows, specification of the wall boundary condition - from which the wall friction effects can be evaluated - is well established. Theoretically, the wall shear stress for dilute flows is estimated by considering the mixture as a single fluid as in the mixture model (e.g. Roco and Shook, 1983). The application of the two-fluid model allows consideration of phasic boundary conditions and their contributions to the total wall shear stress and hence the pipeline friction.

Both wall function and low-Reynolds number formulations for wall boundary conditions for the fluid phase are used by various authors. Rizk and Elghobashi (1989) showed using a low-Reynolds number model that the wall function formulation is questionable, even for dilute flows, since a significant deviation from single-phase flows can occur at relatively low solids concentration. Sinclair and co-workers (e.g. Bolio et al., 1995) and others, for example Cao and Ahmadi (1995, 2000), have used the low-Reynolds number models to simulate gas-solid flows and obtained good agreement with the experimental data of Tsuji et al. (1984). The use of a wall function for flows in which local agglomeration of particles occurs in the near-wall region was questioned by Rizk and Elghobashi (1989). However, the wall function formulation has also been used extensively for various two-phase flows. Louge et al. (1991) reported that for dilute flows, the presence of the particles does not greatly affect the applicability of the law of the wall. This will not be true for dense flows especially in the horizontal orientation where the flow can be significantly stratified leading to the formation of a stationary or moving bed. In the case where the particles settle, the particles will perturb the fluid-phase near-wall flow field. Such concerns have

been raised in recent years even for dilute flows (Benyahia et al., 2005; De Wilde et al., 2003). Using a two-phase boundary layer law-of-the-wall, Troshko and Hassan (2001) formulated a wall function to simulate bubbly flow in a vertical pipe. Hsu et al. (2004) used the wall function formulation in their sediment transport simulation and most recently, Benyahia et al. (2005) extended the wall function by accounting for particle drag at the wall and implemented it for dilute gas-particle flows.

For the solids-phase, a boundary condition which accounts for the physical interactions between the particles and the wall is required. For confined flows of particulate two-phase mixtures, the particle-wall interactions in the form of particle bouncing, sliding, and rolling all contribute to the difficulty in deriving a generic wall boundary condition (e.g. Sommerfeld, 1992). Often, a number of assumptions are made to simplify the problem: 1) coarse particles roll over the wall surface while fine particles stick to it, 2) the particles have a zero normal velocity at the wall, and 3) in the tangential flow direction at the wall the particle can experience a scenario between the free-slip and the no-slip condition. For Eulerian-Eulerian simulations of gas-solid flows, several studies (for example Bolio et al. (1995), Ding and Gidaspow (1990), Ding and Lyczkowski (1992), Hui et al. (1984), Johnson and Jackson (1987), and Tsuo and Gidaspow (1990)), have used different formulations for the solids-phase wall boundary condition. These approaches, often referred to as partial slip boundary conditions, imply a finite contribution of the particle wall shear stress to the total pressure gradient. The partial slip conditions are in contrast to the free-slip boundary condition for the solids-phase (i.e. zero particle wall shear stress) often applied in the two-fluid modelling of two-phase flows, particularly in commercial CFD packages.

2.6 Experimental Studies

Over the five decades since the experimental work of Bagnold (1954), the study of particulate flows has been the subject of many investigations. Experimental investigations of liquid-solid flows are relatively scarce compared to studies on gas-solid flows, although

several proprietary databases exist. Nonetheless, significant data of bulk flow quantities such as pressure drop have been accumulated over the years. Some of these studies include investigations by (Gillies et al., 1985; Gillies, 1993; Hanes and Inman, 1985; McKibben, 1992; Sumner et al., 1990; Sumner, 1992; Zisselmar and Molerus, 1986). In liquid-solid flows, these data include the pressure gradient, deposition velocity, and *in-situ* and delivered concentrations. Experimental studies of fluid-particle two-phase flows have mostly been limited to measurements of bulk parameters due to the inherent problems associated with local measurements in such mixtures.

To understand the physical mechanisms that control the solids concentration distribution in liquid-solid flows, detailed measurements are very important. Significant improvements have been made in the application of non-intrusive techniques to measure particulate two-phase flow quantities. The application of the Phase Doppler Particle Analyser (PDPA) and Laser Doppler Velocimetry (LDV) techniques to obtain local flow quantities including fluctuating quantities in particulate two-phase flows is becoming more common (Alajbegovic et al., 1994; Fessler and Eaton, 1999; Liljegren and Vlachos, 1983; Tsuji and Morikawa, 1982; Tsuji et al., 1984), although they are still limited to dilute flows. For liquid-solid slurry flows, the use of the conductivity probe together with the gamma ray densitometer for the measurement of local solids velocity and chord-averaged solids concentration, respectively, is a common practice. Extensive datasets on horizontal flows have been produced using these techniques for the past three decades (Brown et al., 1983; Gillies et al., 1984, 1985, 1999). The conductivity probe has also been extended to local concentration measurements (Gillies, 1993; Lucas et al., 2000; Nasr-El-Din et al., 1986, 1987; Sumner et al., 1990).

2.6.1 Vertical flow experiments

Vertical flows are often considered simpler than horizontal flows from an experimental viewpoint. However, due to their limited applications, fewer vertical flow experiments are reported in the literature. The experimental studies of Durand and Condolios (1952) and Newitt et al. (1955) began the series of work on vertical liquid-solid flows. The experi-

ments of Durand and co-workers were conducted in pipes with diameters ranging from 40 to 700 mm. The flows involved sand and gravel slurries with sizes in the range of 0.2 to 25 mm and the concentrations were between 5 - 60%. For experiments using a 150 mm vertical pipe with sand particles, they found that the frictional head loss was indistinguishable from that of the flow of pure water. In addition, the solids concentration profile was observed to be uniform for most of the pipe cross-section. Using different particle sizes between 0.1 mm and 3.8 mm, Newitt et al. (1955) studied the flow of liquid-solid mixtures in 25.4 mm and 54 mm vertical pipes. They also found that for solids concentration less than 20%, the frictional head loss was almost identical to that of single-phase water. A similar observation was made by Newitt et al. (1961) who used a 51 mm vertical pipe. Overall, they observed that for the coarse particles, the frictional head loss was similar to the observations of Durand and Condolios (1952). At lower solids mean concentrations, the effect on the fluid velocity profile was found to be negligible. In contrast, for higher solids mean concentration the maximum fluid velocity decreased with a corresponding increase in velocity near the wall of the pipe. The solids concentration was found to be higher in the central core of the pipe surrounded by an annulus of lower concentration.

In a collaborative work, McKibben (1992) and Sumner (1992) showed results that confirmed the observations by Newitt et al. (1961). For flows with larger particles particularly at high solids concentrations, the head loss observed was higher than for a single-phase flow of the carrier fluid (Shook and Bartosik, 1994). Shook and Bartosik (1994) noted the effect to be more significant as the particle size increases above 1.5 mm. Further studies by Ferré and Shook (1998) aimed at exploring this effect supported the observation that the wall friction in turbulent slurry flows in vertical pipes increases as the particle size increases. Alajbegovic et al. (1994) used a state-of-the-art Laser Doppler Velocimetry (LDV) system to measure both liquid and solids velocity, as well as solids concentration in a vertical pipe for dilute liquid-solid flows using ceramic and polystyrene particles. In addition to the mean field variables, they obtained phasic turbulence intensities in the axial and radial directions and phasic Reynolds shear stresses. The solids concentration measurements were calibrated against data measured with a gamma ray densitometer. They found that

the LDV can be used for two-phase liquid-solids flows to measure the liquid and solids velocity as well as the higher order statistics of both phase, The solids concentration was also obtained. The data were used to validated their numerical model.

2.6.2 Horizontal flow experiments

The investigations of Durand's and Newitt's group again were among some of the earliest detailed studies of horizontal slurry flows. The experimental work of Daniel (1965) is one of the first studies on coarse particle slurry flows focusing on velocity and concentration distributions. In his work, solids concentration distributions of liquid-solid flows in a 25 mm high by 102 mm wide rectangular channel were measured using a gamma ray densitometer. Different sized sand, nickel and lead particles were used. The solids concentration distributions obtained showed varied asymmetric characteristics that can be attributed to particle properties and solids concentration. In general, the solids concentration was large near the lower wall and decreased rapidly toward the upper wall. Mixture velocities were also obtained. The velocity showed asymmetric distributions, which depended on particle size and solids concentration. Besides slurry flows with fine particles (e.g. Gillies et al., 1984) and multi-component slurry flows (Gillies, 1993) for which extensive data has been acquired at the SRC, several coarse-particle data have also been collected (see Roco and Shook, 1983). These experiments have exhibited similar asymmetric features.

2.7 Summary

In this chapter, some of the predictive models as well as experimental techniques for particulate two-phase flows were reviewed. The methods for pressure drop prediction in slurry flows with coarse particles in both vertical and horizontal flows were discussed. Numerical prediction techniques using the two-fluid models were also presented. Flow characterization using various variables such as concentration, and length and time scales was reviewed. The limited availability of local experimental data necessary evaluating model predictions was noted.

Predictive approaches which use bulk parameters are desirable in the design process of slurry conveyance systems. However, they are limited in elucidating the microscopic description of the mechanisms associated with the transport process. In the present work, the experimental database is expanded by the provision of new sets of pressure drop results. In addition, the two-fluid model is used to model these flows. Only few applications of the two-fluid model for liquid-solids flows predictions, especially for high bulk concentrations, have been reported in the literature. The present study employs this model to predict the hydrotransport of coarse particles. The closure laws for the solids stress tensor are a particular focus of this study.

CHAPTER 3

MEASUREMENT OF PRESSURE DROP IN VERTICAL FLOWS

In this chapter, the experimental facility, instrumentation, and procedure used for measuring pressure drop in vertical flows are discussed. A circulating flow loop of circular cross-section built at the Saskatchewan Research Council (SRC) Pipe Flow Technology Centre is briefly described. The experimental results obtained for the flow of mixtures of water and glass beads at various bulk concentrations are discussed.

3.1 Experimental Apparatus and Instrumentation

The experimental facility used in this study consists of a 53.2 mm diameter, 9.5 m high vertical pipe flow loop which was constructed and installed at the SRC Pipe Flow Technology Centre. Figure 3.1 shows the layout of the flow loop. The flow loop was constructed using stainless steel for the upward (4) and downward (5) flow test sections and carbon steel for the remaining parts. The main components of the flow loop include a variable speed pump (13), a stand tank (11), and valves (2, 9, 14, and 15) to facilitate the operation of the system. The measurement instruments used are an electromagnetic flow meter (10), temperature sensor (12), and pressure transducers. Differential pressure transducers were used to measure pressure differences ΔP in the upward flow and downward flow test sections and a pressure gauge (7) was used for recording the overall pressure in the system.

A centrifugal slurry pump (Linatex 3×2 pump) with a 75 mm inlet and 50 mm discharge was used to circulate the mixture in the flow loop. The pump is powered by a 15 kW electric motor and a Reeves variable speed drive to control the pump speed and hence the flow rate. An electromagnetic flow meter (EMFM) - Foxboro Flowmeter (M-213326-

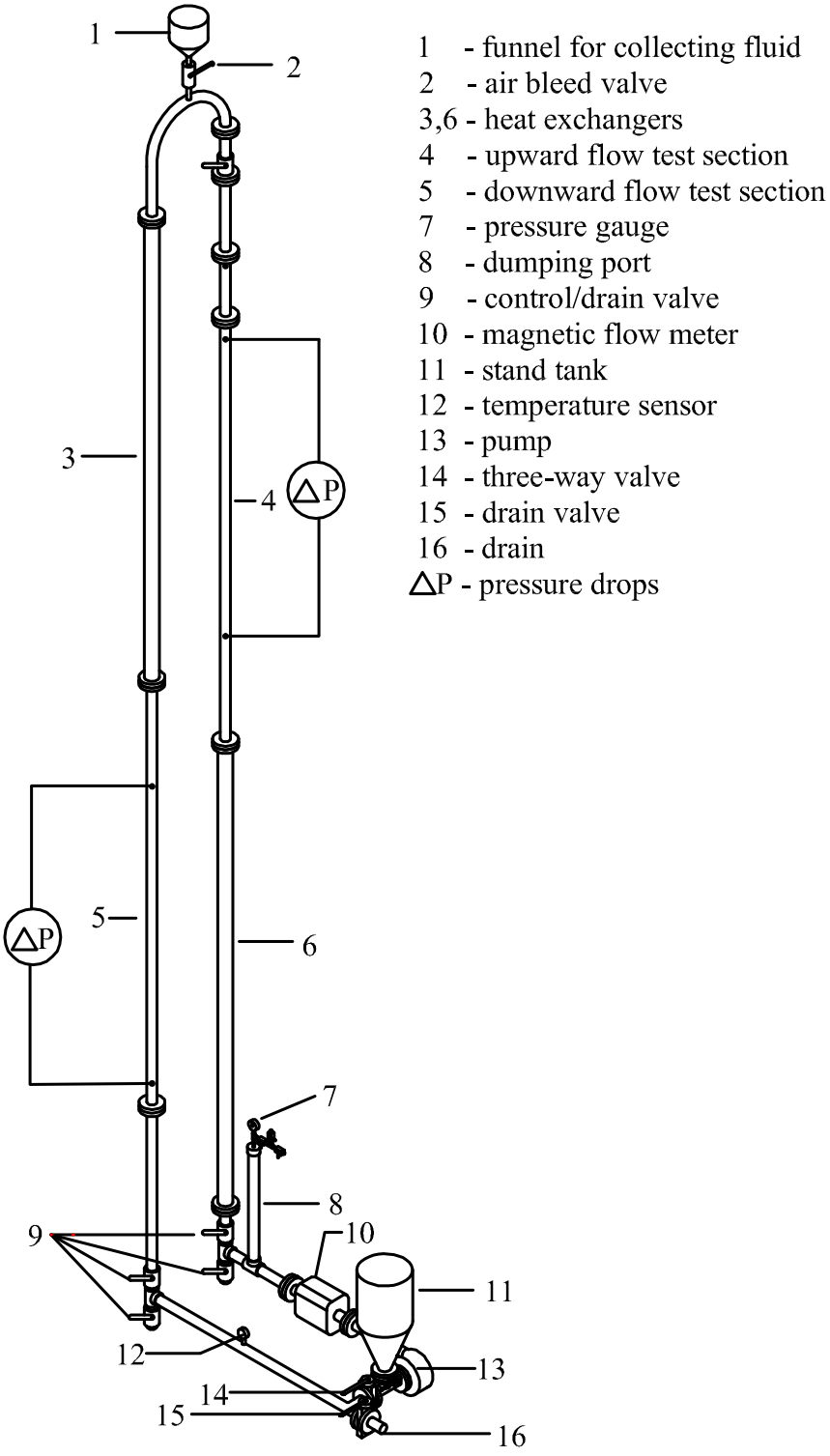

Figure 3.1: 53 mm vertical slurry flow loop

B) with a Foxboro Transmitter (E96S-IA) - was used to determine the flow rate in the flow loop. The flow meter was calibrated by collecting weighed samples over measured time intervals. An initial calibration was performed using water. Subsequent in-situ calibrations to verify the effect of solids concentration were performed. For this calibration, quantities of the water-sand mixture at different concentrations flowing through the electromagnetic flow meter were collected over a time interval and weighed. The data was compared with the case of single-phase water flow. The calibration results demonstrated that the output of the EMFM (i.e. voltage reading) was proportional to the total volume flow rate of the mixture. A detail description of this calibration procedure is provided in Appendix A.

Double pipe heat exchangers were installed on both the upward and downward sections of the loop to control the temperature of the mixture. The temperature was controlled by circulating warm or cold ethylene glycol-water mixtures through the annulus of the heat exchangers. For each condition considered, the temperature of the slurry was controlled within $\pm 3^{o}$ C. The pressure drops in the upward and downward sections of the flow loop were measured for steady flow conditions. Differential pressure transducers were used to determine the pressure difference between pressure taps located 2.134 m apart. For the present study, only the average pressure values were available as output for analysis. The test sections were preceded by long straight disturbance-free pipe section (about 4.0 m), which included the heat exchangers. Thus, in addition to their central function, the installation of the heat exchangers also facilitates fully-developed flow conditions prior to the measurement section.

The layout of the flow loop allows upward and/or downward flow measurements of local solids concentration and velocity profiles. Local measurements of both solids concentration and velocity using conductivity probe (the L-probe) for slurry flows were originally planned. However, during preliminary testing significant and inconsistent fluctuations in the conductivity measurements were observed due to changes in the chemistry of the mixture. As a result, it was decided that this aspect of the study should be deferred to future work. Here, a brief discussion of the solids velocity measurements is presented. The L-

probe followed previous designs by Brown et al. (1983) and Nasr-El-Din et al. (1986) at the University of Saskatchewan and SRC Pipe Flow Technology Centre. The probe, shown in Figure 3.2a, has a diameter of 3.2 mm. Compared to previous probes of this kind, the size of the probe used in this study was expected to produce fewer disturbances in the flow. The test section where the probe was installed is shown in Figure 3.2b. The probe consists of two pairs of sensor electrodes separated by 6.0 mm in the streamwise direction. Each pair of sensor electrodes is 2.0 mm apart. A field electrode is placed above each pair of sensor electrodes and the body of the probe acts as the electrical ground as shown in Figure 3.3. A similar probe was built into the wall of the test section.

The local solids concentration is determined from measurements of the electrical resistivity of the mixture and the carrier liquid. Since the voltage drop across a sensor electrode is directly proportional to the electrical resistance of the carrier fluid, the local solids concentration is determined by measuring the time-averaged mixture voltage drop E_{m} and the carrier fluid voltage drop E_{L}. Typically, for horizontal flow, the carrier fluid voltage drop is determined by stopping the flow and allowing the solids to settle. For vertical flow, to avoid the solids from settling and thereby plugging the flow loop, a small quantity of the mixture is bled and the voltage drop of the liquid in the collected mixture is measured and used as E_{L}. The solids concentration is calculated using the equation derived by Maxwell (cf. Sumner, 1992):

$$c_{\mathrm{s}} = \frac{2\left(E_{\mathrm{m}} - E_{\mathrm{L}}\right)}{\left(2E_{\mathrm{m}} + E_{\mathrm{L}}\right)}. \tag{3.1}$$

It is worth noting that the solids velocity measurements are not susceptible to the conductivity issues. The particle velocity is measured using the temporal fluctuations in the potential difference measured at the two pairs of sensor electrodes. Cross-correlation of these fluctuating signals results in a correlation peak corresponding to the time required for the particles to travel between the two pairs of sensor electrodes. The time-averaged velocity of the solids in the vicinity of the probe is determined by dividing the distance between the sensors by the time corresponding to the cross-correlation peak. These measurement techniques are detailed elsewhere (Gillies, 1993; Sumner, 1992). In the present study, the

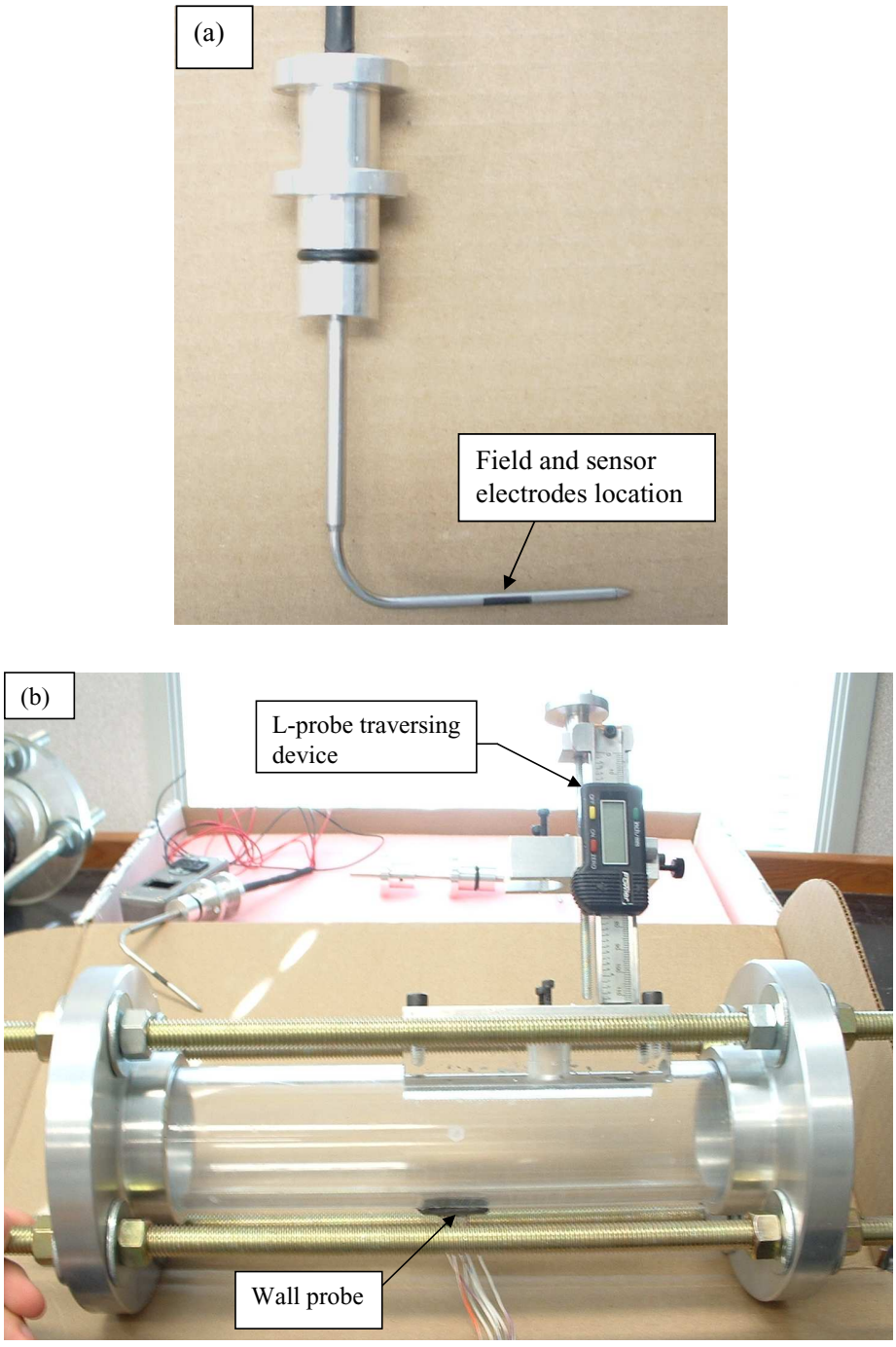

Figure 3.2: (a): Conductivity probe, and (b): test section.

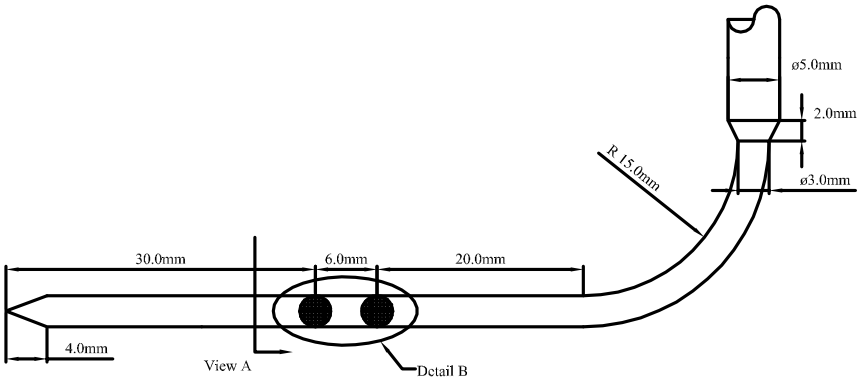

Conductivity Probe

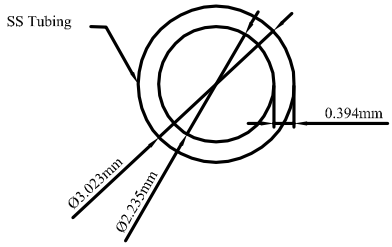

Cross Section of Tube

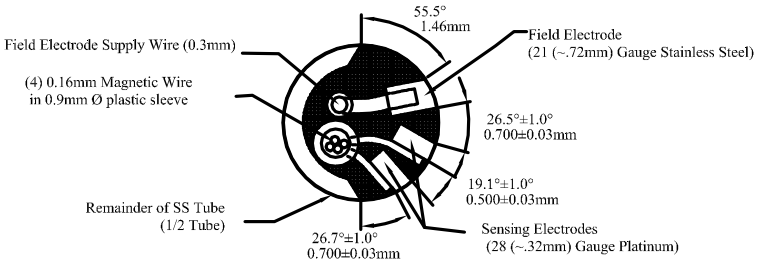

View A. Cross Section of Probe at Sensing Position 1

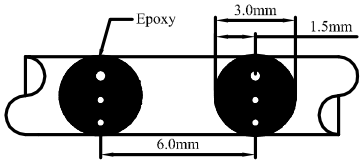

Detail B. Electrode Cluster Positions

Figure 3.3: Conductivity probe design.

cross-correlation algorithm used was developed in-house by Dr. Gillies at the SRC Pipe Flow Technology Centre.

As mentioned above, extensive measurement of local solids concentration and velocity was suspended after preliminary studies revealed inconsistent conductivity measurements. The problem associated with the conductivity probe only affected the concentration data and not the solids velocity data. Moreover, after running the solids in the flow loop for some time, the particles eroded the bend of the conductivity probe exposing and wearing off the wires leading to the electrodes. In addition, some of the 2.0 mm glass beads were broken after running the flow loop at 40% solids bulk concentration, which was the first test case for that particle size. The velocity data obtained with the conductivity probe are presented below.

3.2 Materials and Experimental Conditions

Two sizes of spherical glass beads (0.5 mm and 2.0) mm from Potters Industries Inc. were used in this study. The material density of the glass beads is 2500 kg m^{-3}. The density and viscosity of the water were determined from correlations using the temperature measured during the experiments. Measurements were made for mixture flows involving each particle diameter. For the smaller particles, six solids bulk concentrations from 0 to 45% were considered and for the larger ones, three solids bulk concentrations between 0 and 40% were investigated. The mean velocity ranged from approximately 1 to 5 $\mathrm{m\,s^{-1}}$ depending on the solids bulk concentration. Measurements were obtained for upward and downward flow directions.

3.3 Experimental Procedure

The experimental procedure involves the flow loop operation and data acquisition. The flow loop operation consists of the initial set-up of instrumentation, the start-up, solids addition, solids discharge, and the shut-down stages. For data acquisition, the pressure transducers were zeroed in both test sections prior to starting up the flow loop. During the

loop operation, pressure drop measurements were obtained for water and the water-solids mixture before and after the addition of the solids.

3.3.1 Flow loop operation and data acquisition

Hot water at approximately 50°C was first introduced into the flow loop through the drain (16) (see Figure 3.1) with all the valves, except those connected to the pressure taps and the air bleed valve (2), open. Hot water is used to speed the removal of excess air in the system. The stand tank valve (14) is closed when the stand tank is about three-quarters full. The air bleed valve is then opened and the filling of the flow loop is continued until water collects in the funnel (1) attached to the air bleed valve indicating flow loop overflow. The flow of water is stopped at this point, the drain and the air bleed valves are closed, and the stand tank valve (14) is opened. The hot water is further heated to 60°C by re-circulating hot glycol in the heat exchangers (3 and 6). At the same time the pump is powered and air bubbles trapped in the flow loop are removed through the stand tank. All the air in the system is assumed to be purged when air bubbles are no longer observed escaping from the stand tank. The water is slowly cooled to the desired operating temperature by re-circulating cold glycol in the double pipe heat exchangers. A flow rate is then set and pressure drop measurements are made when steady state is observed. The steady state condition is assumed when the change in the pressure drop is minimal for about five minutes. At this point, a number of pressure drops in the upward and downward sections are read and averaged within 60 seconds of reading. The pressure drop measurement is repeated for a number of flow rates at increments of about 0.5 $\mathrm{m\,s^{-1}}$ depending on the bulk concentration of the solids.

After the pure-water pressure drop measurements, a known mass of the glass beads is mixed with water and shaken to remove any air bubbles attached to the surfaces of the glass beads. This weighed quantity of solids is then added to the flow loop via the stand tank while the water is circulating. It should be noted that the solids bulk concentration of the glass beads is determined from the volume of the weighed quantity divided by the total volume of the flow loop. Complete mixing of the solids in the system is ensured

when the variation of the pressure drops in the flow loop becomes insignificant. After the pressure drops in the test sections stabilise, the pressure drop data for the two-phase mixture is acquired following the same approach discussed above for the pure water case. The solids concentration was increased by adding more solids and the flow rate-pressure drop measurements were repeated until the flow loop had to be shut down at the end of the work day.

To salvage the glass beads, the mixture was collected into a barrel and the solids were separated by wet sieving through a mesh. To avoid plugging the line by shutting down prior to removal of the solids, water was simultaneously fed through the stand tank while the mixture was being discharged via the drain into the barrel. This process was continued until the fluid discharging from the drain was free of solids. The drain valve was then closed and the supply of water terminated. The flow loop was then flushed and emptied. The glass beads were air dried over several days so that they could be reused. The drying was necessary in order to provide a better estimate of bulk concentration during loading of the solids into the flow loop.

3.4 Solids Velocity Profiles Measured with the L-Probe

As noted in Section 3.1, detailed concentration measurements with the L-probe were ultimately abandoned due to inconsistencies in the liquid conductivity. However, limited data for the solids velocity was acquired. The solids velocity profiles for the upward flow of 0.5 mm glass beads at bulk concentrations of 5% and 25% in water are shown in Figures 3.4 and 3.5, respectfully. Additional solids velocity profiles that were acquired for the 0.5 mm and 2.0 mm glass beads are plotted in Appendix B. In the figures, V is the bulk velocity (the mixture velocity measured with the electromagnetic flow meter) and U_{us} refers to the mean solids velocity calculated from the measured solids velocity profile. The general trend of the profiles resembles those obtained in the previous study of McKibben (1992). The data for the 2.0 mm glass beads was not realistic. As noted in Section 3.1, the conductivity probe was eroded by the particles, which rendered it unusable for the later experiments.

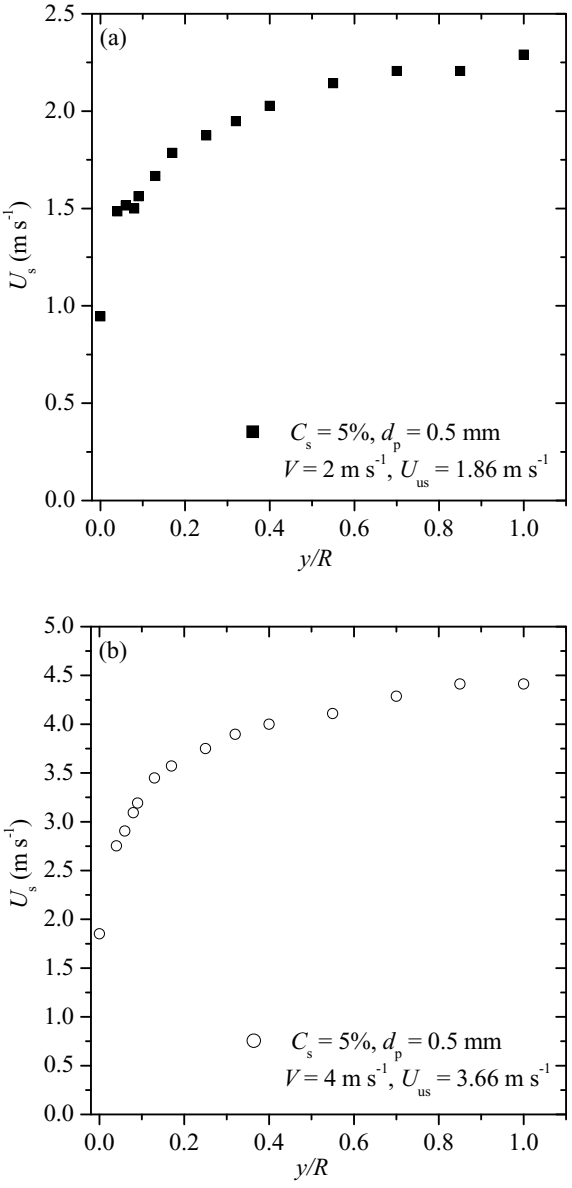

Figure 3.4: Solids velocity profiles for vertical upward flow of 0.5 mm glass beads at bulk solids concentration of 5% in water: (a) bulk velocity = 2 m s^{-1} and (b) bulk velocity = 4 m s^{-1}.

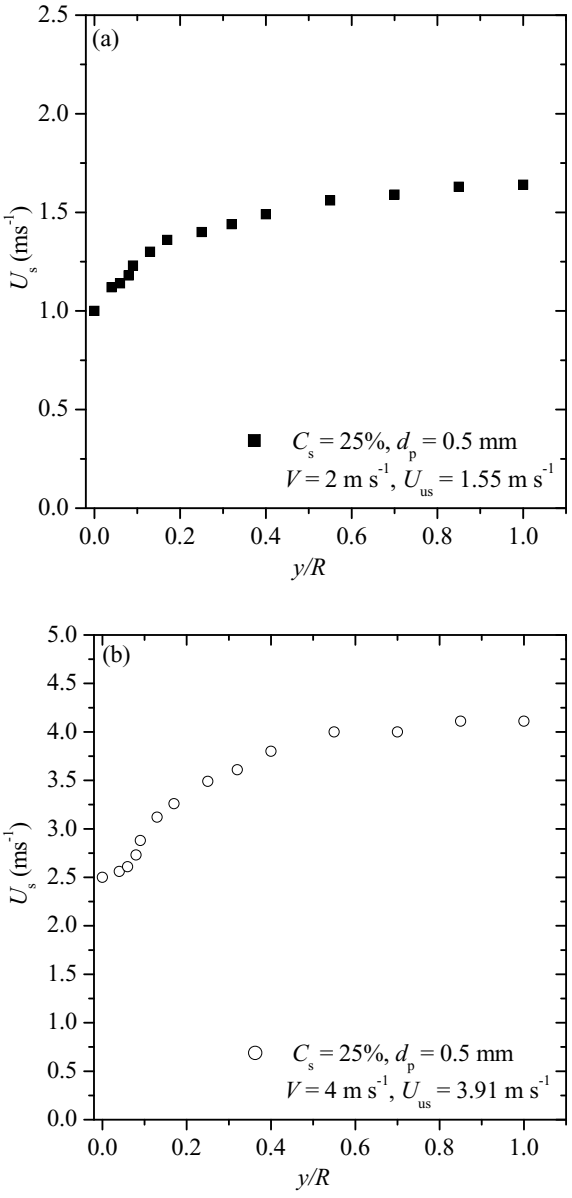

Figure 3.5: Solids velocity profiles for vertical upward flow of 0.5 mm glass beads at bulk solids concentration of 25% in water: (a) bulk velocity = 2 m s^{-1} and (b) bulk velocity = 4 m s^{-1}.

3.5 Analysis of Pressure Drop Measurements in the Flow Loop

Considering the definition of the mixture density (see equation (2.2)), the solids bulk concentration in the upward or downward ($C_{sx} = C_{su}$ or C_{sd}) flow directions can be calculated from

$$C_{sx} = \frac{\rho - \rho_f}{\rho_s - \rho_f}, \tag{3.2}$$

where $\rho = \rho_{mu}$ or ρ_{md}; the subscripts u and d denote upward flow and downward flow. The values of ρ_{mu} and ρ_{md} represent the densities in the upward and downward flow directions, respectively. Their values affect the magnitude of the pressure drop in the upward and downward flow sections and depend on the slip velocity in these sections. The slip velocity depends upon the volume flow rate of the mixture, solids properties, and solids loading.

From equation (2.1) and using Figure 3.6, the upward and downward flow pressure drops are

$$\frac{P_{u1} - P_{u3}}{L} = \rho_{mu} g + \frac{4\tau_{wu}}{D} \tag{3.3}$$

and

$$\frac{P_{d1} - P_{d3}}{L} = -\rho_{md} g + \frac{4\tau_{wd}}{D}, \tag{3.4}$$

In the pressure sensing lines, the hydrostatic pressure drop - of only the fluid - connecting the differential pressure transducers to the flow loop is

$$\frac{P_2 - P_3}{L} = \pm \rho_f g, + \text{ for upward flow and } - \text{for downward flow.} \tag{3.5}$$

Since the pressure sensing lines that connect the pressure transducers to the pipeline contain the carrier fluid, the measured pressure gradient calculated by subtracting equation (3.5) from (3.3) for the upward flow section (Ferré and Shook, 1998), and (3.4) for the downward flow section are

$$\left.\frac{\Delta P}{L}\right|_{upflow} = \frac{P_{u1} - P_{u2}}{L} = (\rho_{mu} - \rho_f)\, g + \frac{4\tau_{wu}}{D} \tag{3.6}$$

and

$$\left.\frac{\Delta P}{L}\right|_{downflow} = \frac{P_{d1} - P_{d2}}{L} = -(\rho_{md} - \rho_f)\, g + \frac{4\tau_{wd}}{D}. \tag{3.7}$$

It should be noted that the wall shear stresses τ_{wu} and τ_{wd} act in the opposite direction to the flow and are always considered positive. The equations also illustrate the two contributions to the pressure drop for fully-developed flow, friction, and gravity.

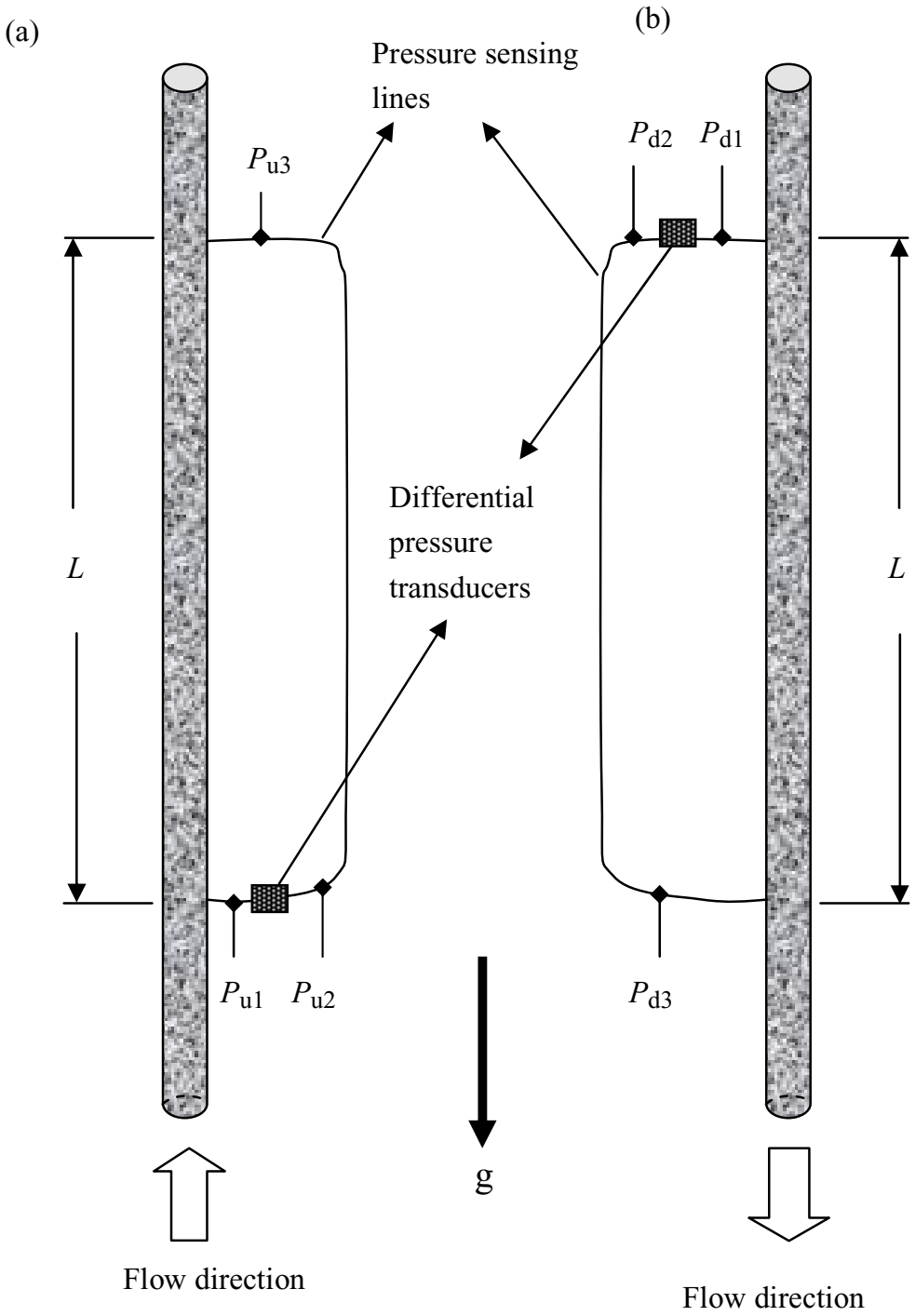

Figure 3.6: Schematic of pressure drop measurement sections and connecting tubing (a) upward test sections and (b) downward flow test sections.

From equations (3.3) and (3.4), the average pressure drop in the upward and downward sections of the flow loop can be expressed as

$$\begin{aligned}\left.\frac{\Delta P}{L}\right|_{\text{average}} &= 0.5\left(\left.\frac{\Delta P}{L}\right|_{\text{upflow}} + \left.\frac{\Delta P}{L}\right|_{\text{downflow}}\right) \\ &= 0.5\left(\left(\rho_{\text{mu}} - \rho_{\text{md}}\right) g + \frac{4}{D}\left(\tau_{\text{wu}} + \tau_{\text{wd}}\right)\right).\end{aligned} \tag{3.8}$$

In the scenario where the bulk solids concentrations in the upward and downward flow sections are different, the gravitational pressure drop would affect the relationship between the wall shear stresses in the flow test sections and the average pressure drop. Under such conditions, one would require knowledge of the respective solids bulk concentrations in the test sections to determine the wall shear stresses accurately. If the difference in mixture density is neglected, i.e. assuming negligible particle-fluid slip in the upward and downward flow directions, then the average pressure drop (equation (3.8)) becomes

$$\left.\frac{\Delta P}{L}\right|_{\text{average}} = 0.5\left(\left.\frac{\Delta P}{L}\right|_{\text{upflow}} + \left.\frac{\Delta P}{L}\right|_{\text{downflow}}\right) = \frac{4\tau_{\text{w}}}{D} \tag{3.9}$$

and the flow loop wall shear stress $\tau_{\text{w}} = 0.5(\tau_{\text{wu}} + \tau_{\text{wd}})$ can be determined. The wall shear stress values are discussed in Section 3.6.2.

Under zero velocity slip conditions, the mean solids concentration and hence, the mixture densities in the upward and downward flow sections will the same. The average mixture density in the upward and downward flow sections can be calculated by considering the difference between equations (3.3) and (3.4):

$$\rho_{\text{mu}} + \rho_{\text{md}} = 2\rho_{\text{f}} + \frac{1}{g}\left[\left(\left.\frac{\Delta P}{L}\right|_{\text{upflow}} - \left.\frac{\Delta P}{L}\right|_{\text{downflow}}\right) + \frac{4}{D}\left(\tau_{\text{wd}} - \tau_{\text{wu}}\right)\right]. \tag{3.10}$$

If one assumes that the wall shear stresses in the upward and downward flow sections are equal, the average mixture density in the flow loop can be obtained from

$$\rho_{\text{m}} = 0.5\left(\rho_{\text{mu}} + \rho_{\text{md}}\right) = \rho_{\text{f}} + \frac{0.5}{g}\left(\left.\frac{\Delta P}{L}\right|_{\text{upflow}} - \left.\frac{\Delta P}{L}\right|_{\text{downflow}}\right). \tag{3.11}$$

3.6 Pressure drops in upward and downward flow sections

Figure 3.7 shows the measured pressure drop for upward and downward flow measured as a function of the bulk velocity for the liquid-solid flow with the 0.5 mm glass beads. Figure 3.7a shows that the pressure drop in the upward flow direction, represented by equation (3.3), depends on both the mean velocity and the mean solids concentration. The data show the expected trend of increasing pressure drop as the bulk velocity increases due to increased shear at high velocity. Although the present study is different from previous work in terms of the particle properties and the range of bulk velocity considered, the dependence of the pressure drop on solids bulk concentration, observed in previous studies by Shook and co-workers (for example, Ferré and Shook (1998); Shook and Bartosik (1994)) and recently by Matousek (2002), is also evident. The work of Ferré and Shook (1998) involved the use of water or ethylene glycol as the carrier fluids and glass beads of diameter 1.8 mm and 4.6 mm as the particles in 40.27 mm diameter pipe. The range the the bulk velocities in the work of Ferré and Shook (1998) was from approximately 3.5 ms^{-1} to 7.5 ms^{-1}. Shook and Bartosik (1994) used sand, polystyrene, and PVC particles in water within the particle diameter range of 1.37 mm and 3.4 mm. Pipe diameters of 26 mm and 40 mm were used and the bulk velocity was between approximately 2 ms^{-1} and 7 ms^{-1}. In the study of Matousek (2002), flows with sand particles of 0.12 mm, 0.37 mm, and 1.85 mm, as well as mixtures of 0.37 mm +0.12 mm and 1.85 mm + 0.12 mm in water in a 150 mm diameter pipe were investigated. Three angles were considered; horizontal, vertical and -30^o. The range of the mean mixture velocity ranged between 2 ms^{-1} and 8 ms^{-1}.

From Figure 3.7a, it can be deduced that as the solids bulk concentration is increased, the pressure drop increased in part by an upward shift proportional to ρ_{mu}. Compared with the previous studies mentioned above, lower mixture velocities (less than 3.0 $\mathrm{m\,s}^{-1}$) were attained in the present work. The $C_{\mathrm{s}} = 45\%$ measurements were repeated and similar results were obtained as shown in Figures 3.7a and 3.7b. Figure 3.7b shows the pressure drop measured as a function of the bulk velocity for the flow with the 0.5 mm glass beads in the downward flow section of the flow loop. Recall that, the downward pressure drop can be

defined using equation (3.7) and the downward shift in its value is proportional to the value of ρ_{md}. Again, the expected relationship between the pressure drop and the bulk velocity is evident. The pressure drop in Figure 3.7b exhibits a downward shift as the solids bulk concentration is increased. Quantitatively, the pressure drop in the downward flow section is lower than the values in the upward flow section. This can be attributed to either the relative values of the mean solids-phase concentration in the downward and upward flow sections or the effect of concentration on the frictional pressure drop. The pressure drop data presented in Figures 3.7 and 3.8 consist of gravitational and frictional contributions. In addition, the frictional pressure drop is also partly determined by the value of the solids concentration at the wall.

Figure 3.8 shows the pressure drop data for flow with the 2.0 mm glass beads. Overall, the pressure drop for the 0.5 mm and the 2.0 mm glass beads in water show similar dependence on bulk velocity and solids bulk concentration.

The average concentration in the upward and downward sections of the flow loop can be calculated from the difference in the upward and downward pressure drops measurements (see equation (3.11)). This equation assumes that τ_{w} is the same for the upward and downward flows. The difference between the nominal solids bulk concentration C_{sn} (i.e. solids loaded into the flow loop) and that calculated from the upward and downward pressure drop measurements C_{sc} for the 5% and 40% concentrations and 0.5 mm and 2.0 mm glass beads are shown in Figure 3.9. The percentage difference lies within $\pm$20%. For both particle sizes, the percentage difference increased with velocity V for 5% concentration and decreased for 40% bulk concentration. A positive percentage difference indicates that the average solids-phase concentration in the upward and downward test section is higher than the nominal solids-phase concentration based on the amount of solids added to the liquid. Without the actual mean solids concentration data in the upward and/or downward test sections, it would be difficult to explain the reason for the positive percentage difference. A negative percentage difference could be explained by particles trapped in parts of the flow loop.

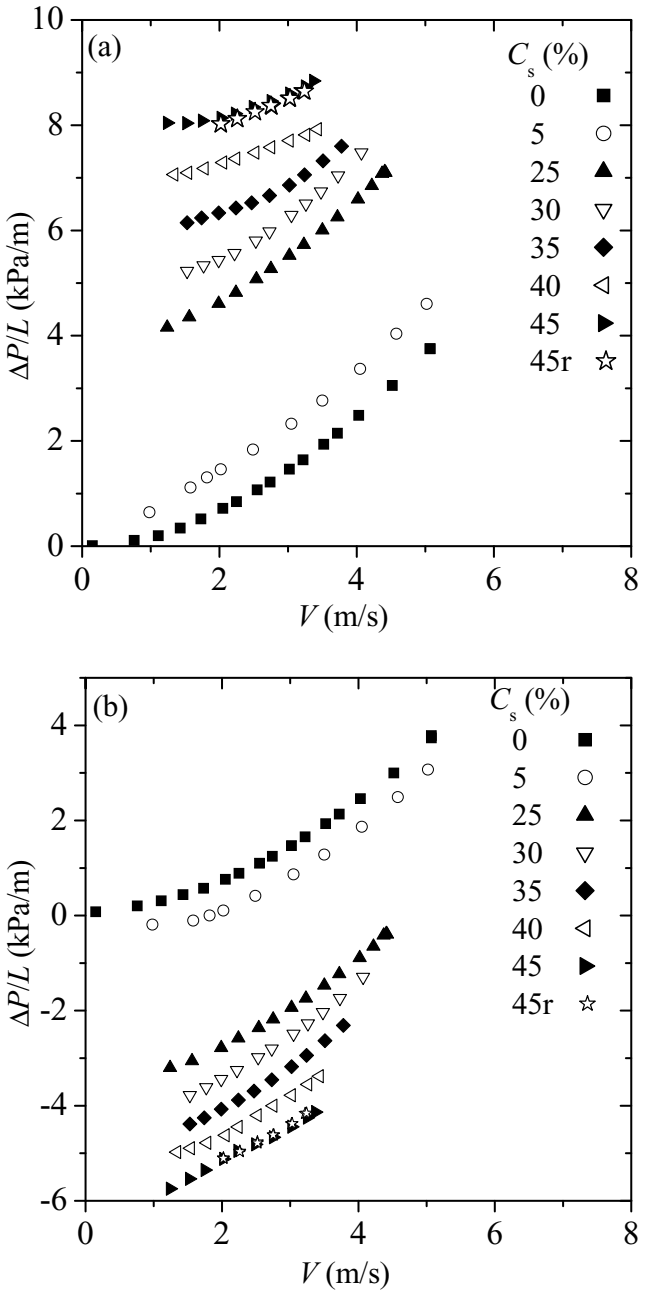

Figure 3.7: Measured pressure drop for flow of 0.5 mm glass beads-water mixture in the 53 mm diameter vertical pipe: (a) upward flow section and (b) downward flow section.

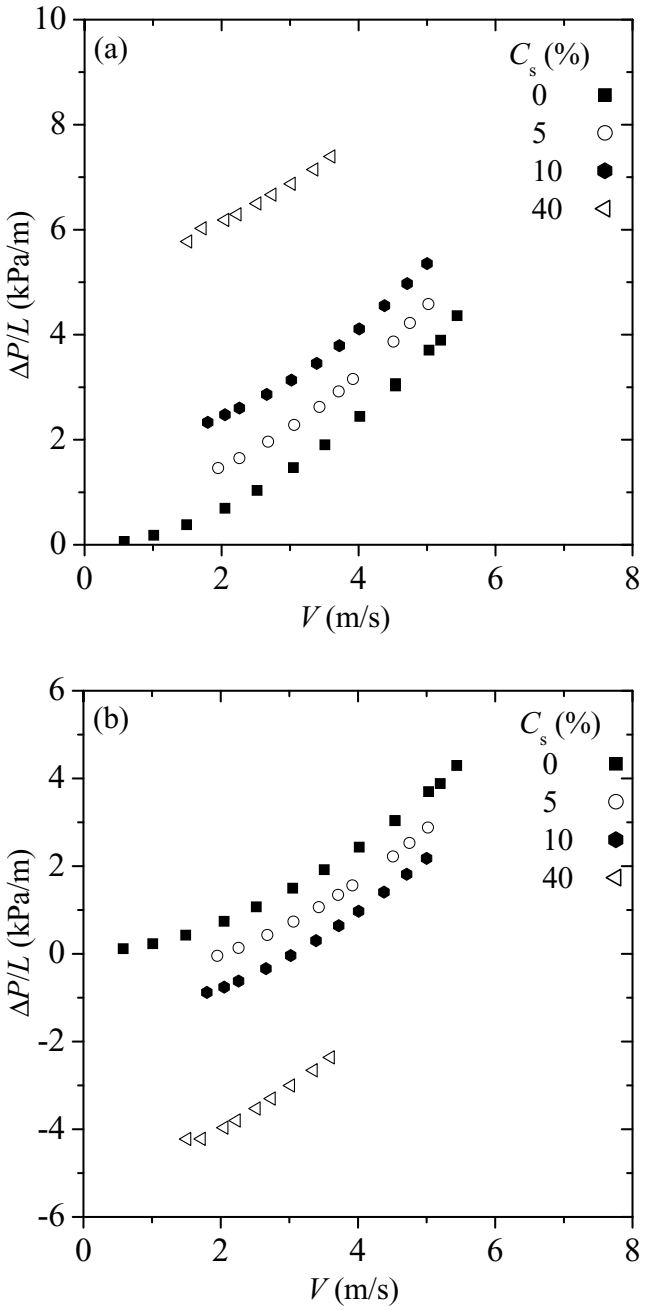

Figure 3.8: Measured pressure drops for flow of 2.0 mm glass beads-water mixture in the 53 mm diameter vertical pipe: (a) upward flow section and (b) downward flow section.

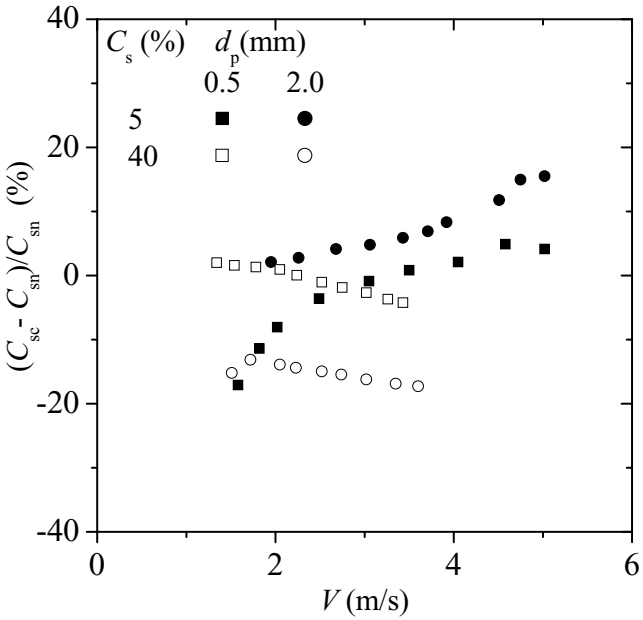

Figure 3.9: Percentage difference between solids bulk concentration values supplied to the flow and those estimated using equations (3.11) and (2.2), and the measured pressure drops.

3.6.1 Average pressure drop

Figure 3.10 shows the average of the upward and downward flow pressure drops (i.e. the average pressure drop given by equation (3.8)) versus the bulk velocity for the liquid-solid flow with the 0.5 mm and 2.0 mm glass beads. It should be noted that without direct measurements of the solids concentration in the upward and downward flow sections, it is difficult to estimate the effect of the net gravitational pressure drop (i.e. $(\rho_{\mathrm{mu}} - \rho_{\mathrm{md}})\, g$ in equation (3.8)) on the average pressure drop.

The data for the 0.5 mm and 2.0 mm glass beads at 0%, 5%, and 40% is compared using Figures 3.10a and 3.10b. In both figures, the pressure drops for the flows at 5% solids bulk concentration are identical to that for the flow with only water (i.e. 0% solids bulk concentration). On the other hand, the pressure drop for flow of the 0.5 mm glass beads at 40% solids bulk concentration deviates from that for the 2.0 mm at velocities less than 3 $\mathrm{m\,s^{-1}}$. For the flow of 0.5 mm glass beads (Figure 3.10a), the average pressure drop increases at high solids bulk concentration, particularly $C_{\mathrm{s}} > 35\%$, for similar bulk

velocities. For the 2.0 mm glass beads (Figure 3.10b), the data for the single-phase and liquid-solid flows at solids bulk concentration of 5% and 10% fall on the same curve. The average pressure drop for flow at solids bulk concentration of 40% is slightly higher than that for the single-phase flow for the range of bulk velocities reported.

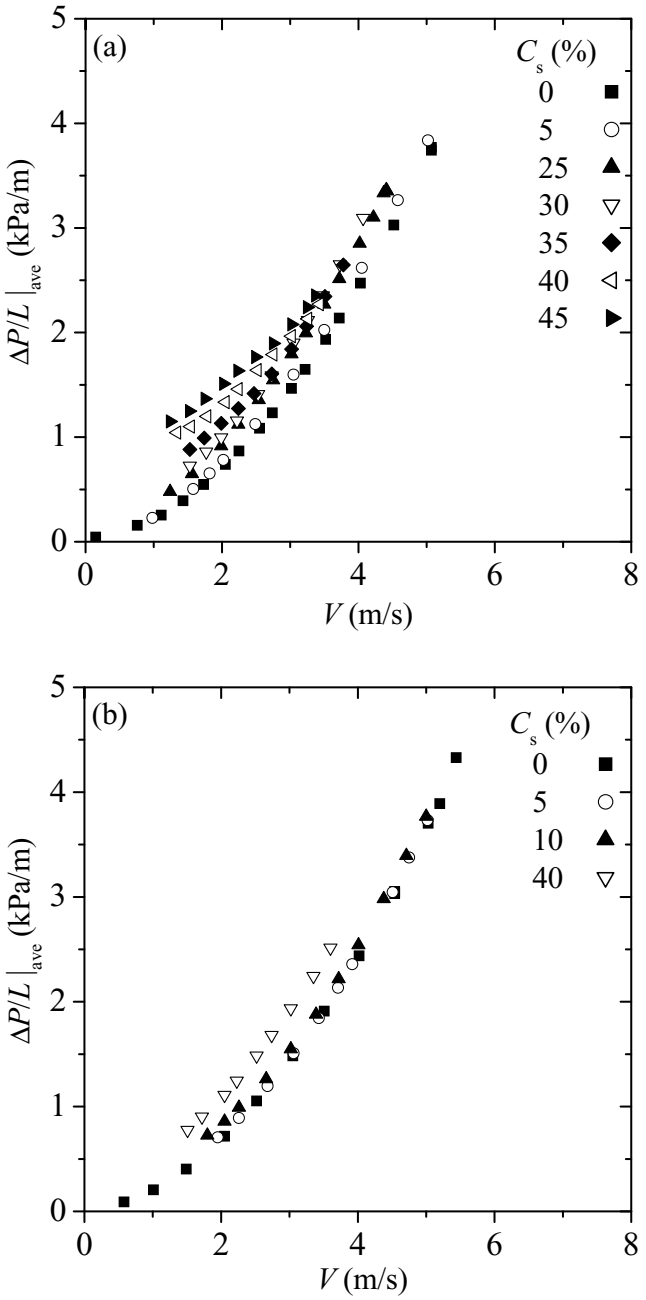

Figure 3.10: Average pressure drop in the flow loop for flow of glass beads-water mixture in the 53 mm diameter vertical pipe: (a) 0.5 mm glass beads, and (b) 2.0 mm glass beads.

3.6.2 Wall shear stresses

Figure 3.11a shows the wall shear stress τ_w plotted against the bulk velocity for 0.5 mm glass beads in the upward flow test section of the flow loop. The values of τ_w were calculated from the measured pressure drop using equation (3.3) and the overall solids bulk concentration in the flow loop. The use of the bulk solids concentration to determine the wall shear stress has been employed in previous studies (Ferré and Shook, 1998; Shook and Bartosik, 1994). As pointed out in Section 3.6.1 for the pressure drop, Figure 3.11 shows that the wall shear stress is essentially the same as for single-phase flow at the lowest solids concentration of 5%. At higher solids bulk concentrations, the wall shear stresses deviate from those measured for the single-phase flow as the bulk velocity decreases implying a dependence on concentration that becomes more distinct at lower mean velocities. This can further be explained using Figures 3.4 and 3.5. At high bulk velocity, lower slip velocity between the particles and the liquid. The mean solids concentration in the upward and downward flow sections is similar and, hence, equal to the solids bulk concentration in the flow loop. Therefore, the gravitational pressure drop is estimated well from using the bulk concentration loaded into the loop. This implies that the gravitational pressure drop estimated from the measurements is similar in both the upward and downward flow sections. Based on this, one can infer that the values of the wall shear stress at high bulk velocities in Figure 3.11 are not significantly dependent on concentration. At low bulk velocities, for example in Figure 3.11a, high slip velocity occurs due to the density difference between the particles and the liquid. The solids mean concentration in the upward flow direction will be expected to be higher due to the aforementioned slip velocity than the corresponding value in the downward flow section. For the upward flow case for example, the plotted wall shear stress in Figure 3.11a includes extra (i.e. undetermined) gravitational contribution to the pressure drop that is inherent in the shear stress.

In support of the above discussion, one can see from Figures 3.5a and 3.5b that the slip velocity in the upward flow section is qualitatively apparent. The solids mean velocity computed from the profiles in Figures 3.5a and 3.5b are 1.55 $\mathrm{m\,s^{-1}}$ and 3.91 $\mathrm{m\,s^{-1}}$. How-

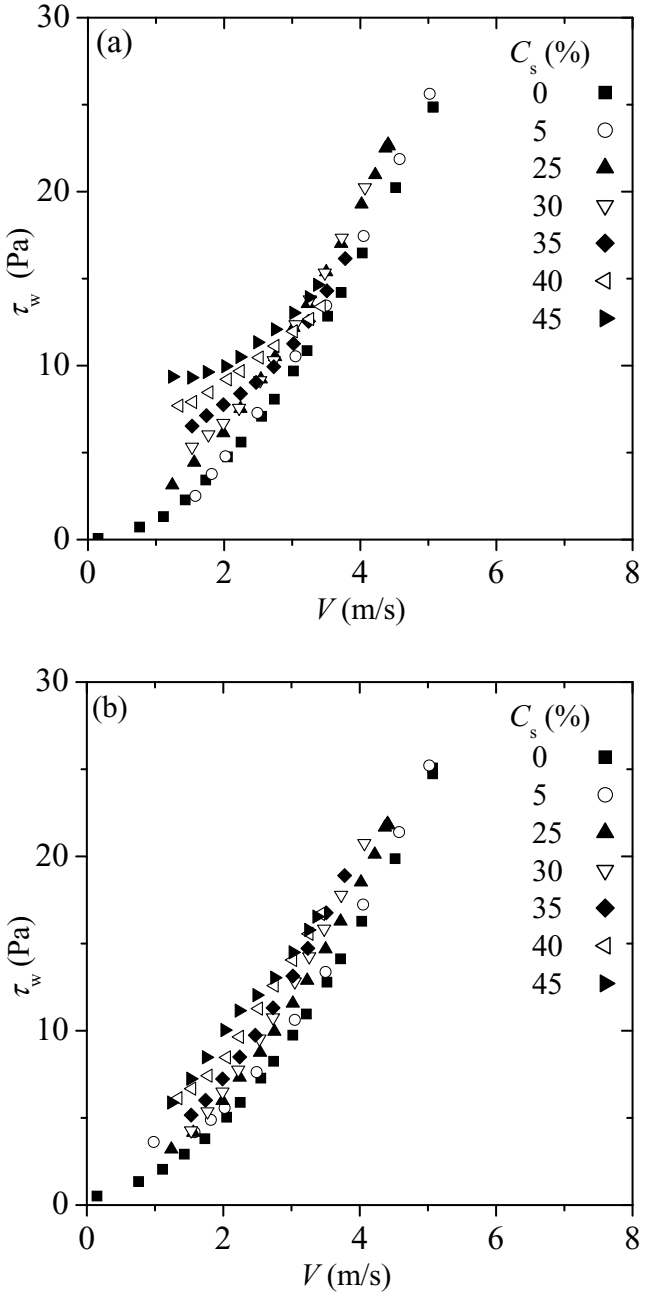

Figure 3.11: Wall shear stress for flow of 0.5 mm glass beads-water mixture in the 53 mm diameter vertical pipe: (a) upward flow section and (b) downward flow section.

ever, the absence of the phasic concentration data makes it difficult to quantify the exact magnitudes of the slip velocity in the flow sections. Such quantitative arguments will aid in calculating the extra pressure drop contribution hidden in the measured wall shear stress as a result of the slip velocity in the flow sections. Figure 3.11b shows the wall shear stress data for the 0.5 mm glass beads in the downward flow test section based on equation (3.4). The wall shear stress data obtained in the downward test section is similar to that of the upward test section except that the deviation extends to higher velocities. However, the deviation in the wall shear stress at higher solids bulk concentration is less pronounced than that measured in the upward flow test section at lower bulk velocities.

Figure 3.12a shows the wall shear stress for the 2.0 mm glass beads-water mixture flows for 0%, 5%, 10%, and 40% solids bulk concentrations. For the larger particles, the wall shear stresses for the mixture flows are more similar to that for single-phase flow. In Figure 3.12b, the downward flow wall shear stresses for the 2.0 mm particles are similar to those observed in the upward flow test section at $C_s = 5\%$ and 10%. At the highest concentration of C_s = 40%, the effect of concentration is reminiscent of that noted for the case of the smaller glass beads.

3.7 Summary

In this chapter, an experimental study of water slurries of glass beads is presented. Measurements for the pressure drop and estimates for the wall shear stress in the upward and downward test sections of a circulating flow loop are reported. The average pressure drop in the flow loop was also presented. The results obtained show that the pressure drops as well as the wall shear stresses increase with increasing velocity. The effect of particle size is mixed. The data from both test sections exhibited the generally expected trend. From the present work, and as noted in other studies (see for example, Ferré and Shook, 1998), the bulk concentration in the upward and downward flow sections is required to determine the wall shear stress. In conclusion, the measurements presented in the present study is incomplete in terms of measured parameters. This is consistent with previous studies and

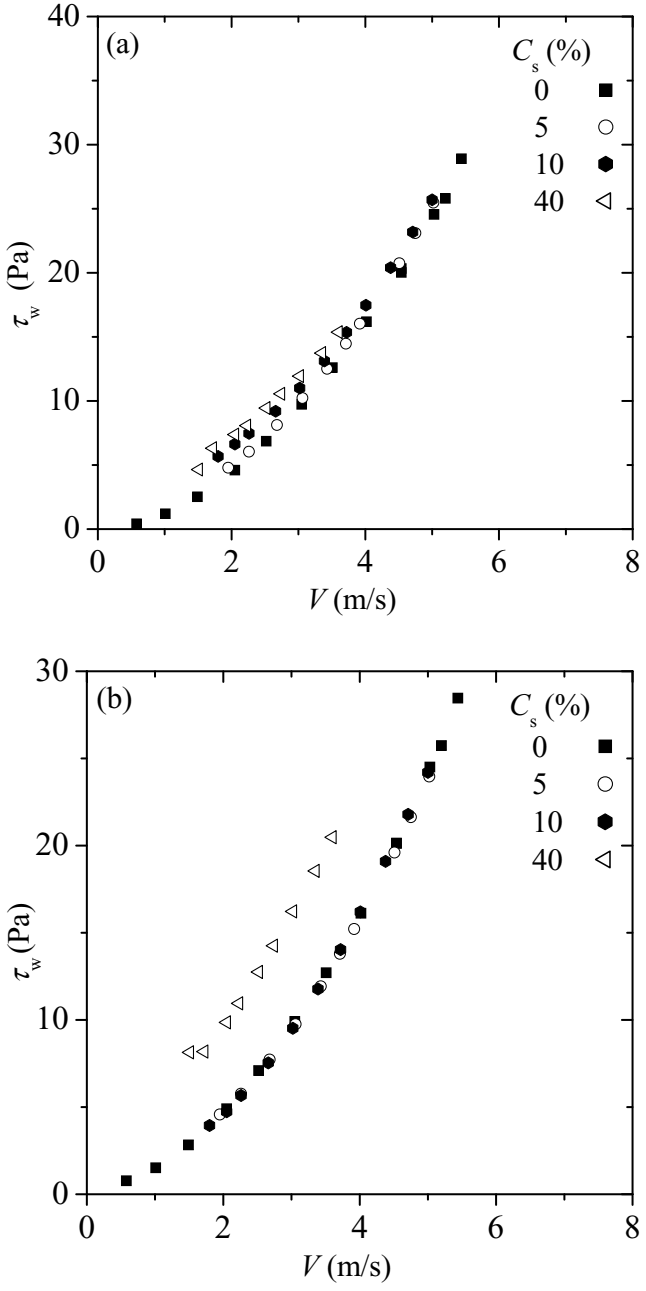

Figure 3.12: Wall shear stress for flow of 2.0 mm glass beads-water mixture in the 53 mm diameter vertical pipe: (a) upward flow section and (b) downward flow section.

further reveals lack of information for numerical simulations. Thus, for vertical flows of particulate slurry flows where significant slip velocity is expected, effort must be made to obtain velocity and concentration distributions of at least one phase.

CHAPTER 4

TWO-FLUID MODEL FORMULATION

4.1 Introduction

The governing equations for momentum and mass transport used in this study are presented in this chapter. A two-step averaging technique is used to derive the governing equations for the two-fluid model. The method involves both an ensemble averaging technique (Enwald et al., 1996) and a concentration-weighted averaging technique to account for concentration fluctuations. Details of the procedure are presented starting with the ensemble-averaged transport equations of mass and momentum. The concentration-weighted time-averaging process is then applied to the ensemble-averaged equations to obtain equations for the conservation of mass and momentum. Closure relations for the interaction terms common to each phase are discussed followed by those for the constitutive equations for the phasic stress tensors. Finally, a general overview of the phasic boundary conditions is presented.

4.2 Derivation of Governing Equations

4.2.1 Local instantaneous equations

The main governing equations for the two-fluid model are the mass and momentum transport equations. The local instantaneous conservation equation is derived for a general control volume $\mathcal{V}$, see Figure 4.1, through which a flow property ψ_α of the phase α in a two-phase mixture is transported (Enwald et al., 1996). For this control volume shared by the two phases, an interface of area $\mathcal{A}^{\text{int}}(t)$ and velocity u_i^{int} exists between the two phases; the subscript i is used here to indicate an arbitrary direction of the interface velocity. The

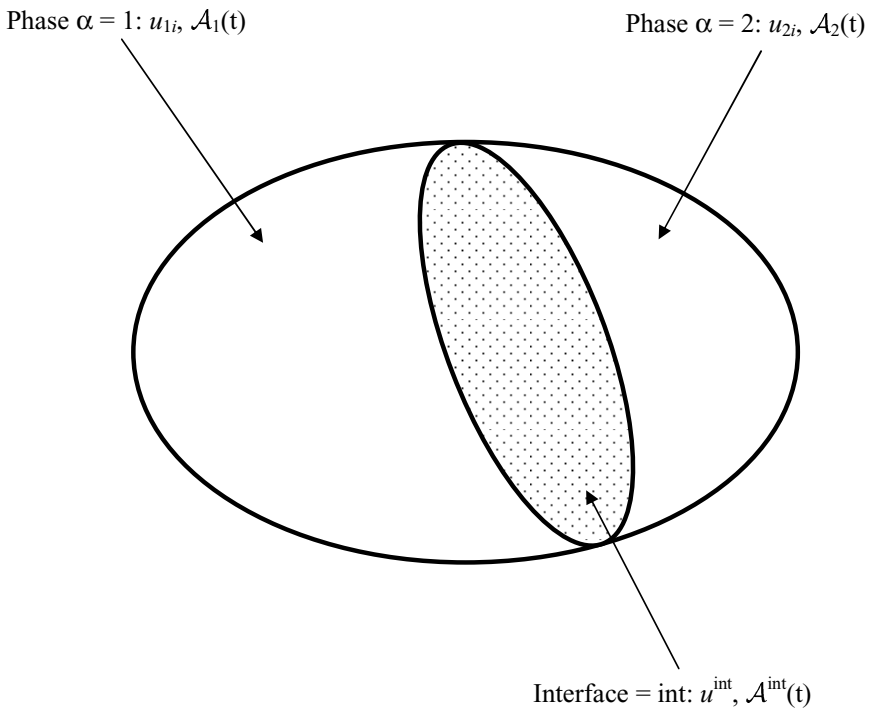

Figure 4.1: Fixed control volume with two phases with moving interface.

following integral balance can be written for a fixed coordinate system for the mixture:

$$\sum_{\alpha=1}^{2}\left(\frac{\mathrm{d}}{\mathrm{d}t}\int\limits_{\mathcal{V}_\alpha(t)}\rho_\alpha\psi_\alpha \mathrm{d}\mathcal{V}\right)=\int\limits_{\mathcal{A}^{\mathrm{int}}(t)}\Omega^{\mathrm{int}}\mathrm{d}\mathcal{A}+ \sum_{\alpha=1}^{2}\left(-\int\limits_{\mathcal{A}_\alpha(t)}\rho_\alpha\psi_\alpha(u_{\alpha i}n_i)\mathrm{d}\mathcal{A}+\int\limits_{\mathcal{V}_\alpha(t)}\rho_\alpha\Omega_\alpha \mathrm{d}\mathcal{V}-\int\limits_{\mathcal{A}_\alpha(t)}J_{\alpha i}n_i\mathrm{d}\mathcal{A}\right). \tag{4.1}$$

In equation (4.1), the term on the left-hand side is the time rate of change of ψ in the control volume $\mathcal{V}_\alpha(t)$, the portion of $\mathcal{V}$ occupied by α. On the right-hand side, the first term is the generation of ψ due to an interfacial source term Ω^{int}; the second term represents the convective flux of ψ across the surface of $\mathcal{V}_\alpha(t)$ at a velocity $u_{\alpha i}$; the third term is the production of ψ due to the source term Ω_α; and the fourth term represents the molecular flux $J_{\alpha i}$, where n_i is the outward-pointing normal to the interface of $\mathcal{V}_\alpha(t)$ occupied by phase α.

Using the Leibnitz theorem, the term in the parenthesis on left-hand side of equation (4.1) is transformed into the sum of a volume integral and a surface integral as

$$\frac{\mathrm{d}}{\mathrm{d}t}\int\limits_{\mathcal{V}_\alpha(t)}\rho_\alpha\psi_\alpha \mathrm{d}\mathcal{V} = \int\limits_{\mathcal{V}_\alpha(t)}\frac{\partial}{\partial t}\left(\rho_\alpha\psi_\alpha\right)\mathrm{d}\mathcal{V} + \int\limits_{\mathcal{A}^{\mathrm{int}}(t)}\left(\rho_\alpha\psi_\alpha u^{\mathrm{int}} n_i\right)\mathrm{d}\mathcal{A}. \tag{4.2}$$

Gauss theorem can be used to rewrite the second integration term on the right-hand side of equation (4.1) as the sum of a volume and a surface integral yielding

$$\int\limits_{\mathcal{A}_\alpha(t)}\rho_\alpha\psi_\alpha(u_{\alpha i}n_i)\mathrm{d}\mathcal{A} = \int\limits_{\mathcal{V}_\alpha(t)}\frac{\partial}{\partial x_i}\left(\rho_\alpha\psi_\alpha u_{\alpha i}\right)\mathrm{d}\mathcal{V} - \int\limits_{\mathcal{A}^{\mathrm{int}}(t)}\rho_\alpha\psi_\alpha(u_{\alpha i}n_i)\mathrm{d}\mathcal{A}. \tag{4.3}$$

Similarly, the last term on the right hand side of the same equation becomes

$$\int\limits_{\mathcal{A}_\alpha(t)}J_{\alpha i}n_i\mathrm{d}\mathcal{A} = \int\limits_{\mathcal{V}_\alpha(t)}\frac{\partial}{\partial x_i}\left(J_{\alpha i}n_i\right)\mathrm{d}\mathcal{V} - \int\limits_{\mathcal{A}^{\mathrm{int}}(t)}J_{\alpha i}n_i\mathrm{d}\mathcal{A}. \tag{4.4}$$

Using equations (4.2) through (4.4), equation (4.1) can be rewritten as a volume integral for the volume occupied by the two phases and a surface integral which expresses the jump conditions across the interface (see Enwald et al., 1996):

$$\begin{aligned}\sum_{\alpha=1}^{2}\int\limits_{\mathcal{V}_\alpha(t)}\left\{\frac{\partial}{\partial t}\left(\rho_\alpha\psi_\alpha\right)+\frac{\partial}{\partial x_i}\left(\rho_\alpha\psi_\alpha u_{\alpha i}+J_{\alpha i}\right)-\rho_\alpha\Omega_\alpha\right\}d\mathcal{V}-\\ \int\limits_{\mathcal{A}^{\mathrm{int}}(t)}\left\{\sum_{\alpha=1}^{2}\left(\rho_\alpha[u_{\alpha i}-u_i^{\mathrm{int}}]n_i\psi_\alpha+J_{\alpha i}n_i\right)+\Omega^{\mathrm{int}}\right\}d\mathcal{A}=0.\end{aligned} \tag{4.5}$$

In the present study, no mass transfer is considered. Therefore, the mass transfer per unit area of interface and time in equation (4.5) is neglected, i.e.

$$\left(\rho_\alpha[u_{\alpha i}-u_i^{\mathrm{int}}]n_i\right)=\dot{m}_\alpha^{\mathrm{int}}=0 \tag{4.6}$$

The generation of ψ_α due to an interfacial source term Ω^{int} is also not considered and therefore neglected. The integrand in each of the integrals in the remaining terms of equation

(4.5) must vanish since the equations are valid for all $\mathcal{V}_\alpha(t)$ and $\mathcal{A}_\alpha(t)$. Therefore, the local instantaneous conservation equation for a field variable ψ_α of a phase α can be written in general form as

$$\frac{\partial}{\partial t}(\rho_\alpha \psi_\alpha) + \frac{\partial}{\partial x_i}(\rho_\alpha \psi_\alpha u_{\alpha i} + J_{\alpha i}) - \rho_\alpha \Omega_\alpha = 0 \tag{4.7}$$

and the jump condition between the phases at the interface (see equation (4.5) in the flow is given by

$$\sum_{\alpha=1}^{2} J_{\alpha i} n_{\alpha i} = 0. \tag{4.8}$$

Equations (4.7) and (4.8) are used to obtain the transport equations for mass and momentum.

4.2.2 Ensemble averaging

Considering a point in space which is occupied by a two-phase mixture, only one phase will be present at any time. The properties of the ensemble average (see Appendix D) are reviewed in detail by Drew (1983) and include:

$$\begin{aligned}
&\langle f + g \rangle = \langle f \rangle + \langle g \rangle, \\
&\langle f \langle g \rangle \rangle = \langle f \rangle \langle g \rangle, \\
&\langle \text{constant} \rangle = \text{constant}, \\
&\left\langle \frac{\partial f}{\partial t} \right\rangle = \frac{\partial}{\partial t} \langle f \rangle, \\
&\left\langle \frac{\partial f}{\partial x_i} \right\rangle = \frac{\partial}{\partial x_i} \langle f \rangle,
\end{aligned} \tag{4.9}$$

where f and g are any scalar, vector or tensor variables. The averaging process uses weighted averages. The weighted average of a scalar, vector, or a tensor is given by

$$\langle \Psi \rangle^{\mathcal{W}} = \langle \mathcal{W} \psi \rangle / \langle \mathcal{W} \rangle, \tag{4.10}$$

where $\mathcal{W}$ is an arbitrary weighting factor. The flows considered in the present study are incompressible.

The presence of that phase is characterized by the phase indicator function, which is defined as

$$X_\alpha(\mathbf{r},t) = \begin{cases} 1, & \text{if } \mathbf{r} \textbf{ is in phase } \alpha \text{ at time } t \\ 0, & \text{otherwise} \end{cases}, \tag{4.11}$$

where X_α is a discontinuous function at the interface between the phases and its gradient is a delta-function that is non-zero only at the interface. The average of the phase indicator function is equivalent to the average occurrence of phase α:

$$c_\alpha = \langle X_\alpha \rangle, \tag{4.12}$$

where c_α is the concentration of a phase and the angular brackets $\langle\rangle$ denote an ensemble average. A fundamental property of X_α derived by (Drew, 1983; Drew and Passman, 1999) is

$$\frac{\mathrm{D}X_\alpha}{\mathrm{D}t} = \frac{\partial X_\alpha}{\partial t} + u_i^{\text{int}} \frac{\partial X_\alpha}{\partial x_i} = 0. \tag{4.13}$$

In the averaging process, the term Reynolds decomposition, which is specifically used in time-averaging process, is employed. Consider a general field variable ψ, we have

$$\psi = \langle \Psi \rangle^{\mathrm{W}} + \psi', \text{ with } \langle \psi' \rangle = 0 \tag{4.14}$$

where the first term on the right-hand side is a weighted mean value and the second term is the deviation from this mean value. The use of equation (4.14) in the averaging process results in terms containing correlations of the fluctuating components. These extra terms are analogous to the Reynolds stress terms for single-phase flows turbulence modelling (cf. Enwald et al., 1996).

4.2.3 Ensemble-averaged equations

The ensemble-averaged equations are derived by first multiplying the general instantaneous equation, i.e. equation (4.7), by the phase indicator function X_α and then performing the

averaging procedure. Thus, from equation (4.7) we have

$$\left\langle X_\alpha \frac{\partial}{\partial t}(\rho_\alpha \psi_\alpha) + X_\alpha \frac{\partial}{\partial x_i}(\rho_\alpha \psi_\alpha u_{\alpha i} + J_{\alpha i}) - X_\alpha \rho_\alpha \Omega_\alpha \right\rangle = 0. \tag{4.15}$$

Considering each term in equation (4.15) and employing the product rule for the differential terms, the following relations are obtained:

$$\left\langle X_\alpha \frac{\partial}{\partial t}(\rho_\alpha \psi_\alpha) \right\rangle = \left\langle \frac{\partial}{\partial t}(X_\alpha \rho_\alpha \psi_\alpha) \right\rangle - \left\langle (\rho_\alpha \psi_\alpha) \frac{\partial}{\partial t} X_\alpha \right\rangle, \tag{4.16}$$

$$\left\langle X_\alpha \frac{\partial}{\partial x_i}(\rho_\alpha \psi_\alpha u_{\alpha i}) \right\rangle = \left\langle \frac{\partial}{\partial x_i}(X_\alpha \rho_\alpha \psi_\alpha u_{\alpha i}) \right\rangle - \left\langle (\rho_\alpha \psi_\alpha u_{\alpha i}) \frac{\partial}{\partial x_i} X_\alpha \right\rangle \tag{4.17}$$

and

$$\left\langle X_\alpha \frac{\partial}{\partial x_i} J_{\alpha i} \right\rangle = \left\langle \frac{\partial}{\partial x_i}(X_\alpha J_{\alpha i}) \right\rangle - \left\langle J_{\alpha i} \frac{\partial}{\partial x_i} X_\alpha \right\rangle. \tag{4.18}$$

Substituting these relations into equation (4.15) and rearranging yields

$$\begin{aligned} \left\langle \frac{\partial}{\partial t}(X_\alpha \rho_\alpha \psi_\alpha) \right\rangle + \left\langle \frac{\partial}{\partial x_i}(X_\alpha \rho_\alpha \psi_\alpha u_{\alpha i}) \right\rangle + \left\langle \frac{\partial}{\partial x_i}(X_\alpha J_{\alpha i}) \right\rangle - \langle X_\alpha \rho_\alpha \Omega_\alpha \rangle \\ = \left\langle (\rho_\alpha \psi_\alpha) \frac{\partial}{\partial t} X_\alpha \right\rangle + \left\langle (\rho_\alpha \psi_\alpha u_{\alpha i}) \frac{\partial}{\partial x_i} X_\alpha \right\rangle + \left\langle J_{\alpha i} \frac{\partial}{\partial x_i} X_\alpha \right\rangle. \end{aligned} \tag{4.19}$$

Multiplying equation (4.13) by $\rho_\alpha \psi_\alpha$ and averaging the result yields

$$\left\langle \rho_\alpha \psi_\alpha \frac{\partial}{\partial t} X_\alpha \right\rangle + \left\langle \rho_\alpha \psi_\alpha u_i^{\text{int}} \frac{\partial}{\partial x_i} X_\alpha \right\rangle = 0, \tag{4.20}$$

which when subtracted from the right hand side of equation (4.19) simplifies to

$$\begin{aligned} \left\langle \frac{\partial}{\partial t}(X_\alpha \rho_\alpha \psi_\alpha) \right\rangle + \left\langle \frac{\partial}{\partial x_i}(X_\alpha \rho_\alpha \psi_\alpha u_{\alpha i}) \right\rangle + \left\langle \frac{\partial}{\partial x_i}(X_\alpha J_{\alpha i}) \right\rangle \\ - \langle X_\alpha \rho_\alpha \Omega_\alpha \rangle = \left\langle \rho_\alpha \psi_\alpha (u_{\alpha i} - u_i^{\text{int}}) \frac{\partial}{\partial x_i} X_\alpha \right\rangle + \left\langle J_{\alpha i} \frac{\partial}{\partial x_i} X_\alpha \right\rangle. \end{aligned} \tag{4.21}$$

With no mass transfer between the phases, the averaged conservation equation becomes

$$\left\langle \frac{\partial}{\partial t}(X_\alpha \rho_\alpha \psi_\alpha) \right\rangle + \left\langle \frac{\partial}{\partial x_i}(X_\alpha \rho_\alpha \psi_\alpha u_{\alpha i}) \right\rangle + \left\langle \frac{\partial}{\partial x_i}(X_\alpha J_{\alpha i}) \right\rangle - \langle X_\alpha \rho_\alpha \Omega_\alpha \rangle = \left\langle J_{\alpha i} \frac{\partial}{\partial x_i} X_\alpha \right\rangle . \tag{4.22}$$

Averaged continuity equation

From equation (4.14), let $\psi = 1$ and $J_{\alpha i} = \Omega = 0$ and substitute into equation (4.22). After utilizing equation (4.9), the mass balance for incompressible flow becomes

$$\underbrace{\frac{\partial}{\partial t}(\rho_\alpha \langle X_\alpha \rangle)}_{\text{C1}} + \underbrace{\frac{\partial}{\partial x_i}\left(\rho_\alpha \langle X_\alpha \left(U_{\alpha i} + u'_{\alpha i}\right) \rangle\right)}_{\text{C2}} = 0. \tag{4.23}$$

The transient term (term C1) becomes

$$\text{Term C1} \equiv \frac{\partial}{\partial t}(\rho_\alpha \langle X_\alpha \rangle) = \frac{\partial}{\partial t}(c_\alpha \rho_\alpha). \tag{4.24}$$

Term C2 can be expanded as follows:

$$\text{Term C2} \equiv \frac{\partial}{\partial x_i}\left(\rho_\alpha \langle X_\alpha U_{\alpha i} \rangle + \rho_\alpha \langle X_\alpha u'_{\alpha i} \rangle\right). \tag{4.25}$$

Applying the averaging properties to each term,

$$\langle U_{\alpha i} \rangle = \frac{\langle X_\alpha U_{\alpha i} \rangle}{\langle X_\alpha \rangle} \equiv \frac{\langle X_\alpha U_{\alpha i} \rangle}{c_\alpha} \tag{4.26}$$

and

$$\langle u'_{\alpha i} \rangle = \frac{\langle X_\alpha u'_{\alpha i} \rangle}{\langle X_\alpha \rangle} \equiv \frac{\langle X_\alpha u'_{\alpha i} \rangle}{c_\alpha} = 0, \tag{4.27}$$

and then substituting back into (4.25) yields

$$\text{Term C2} \equiv \frac{\partial}{\partial x_i}\left[c_\alpha \rho_\alpha \left(U_{\alpha i} + \langle u'_{\alpha i} \rangle\right)\right] = \frac{\partial}{\partial x_i}\left(c_\alpha \rho_\alpha U_{\alpha i}\right). \tag{4.28}$$

From equations (4.24) and (4.28), the ensemble-averaged continuity equation is written as

$$\frac{\partial}{\partial t}(c_\alpha \rho_\alpha) + \frac{\partial}{\partial x_i}\left(c_\alpha \rho_\alpha U_{\alpha i}\right) = 0. \tag{4.29}$$

Note that the angle brackets $\langle\rangle$ in the averaged equation (i.e. equation (4.29)) are dropped for convenience. This also the case for the momentum equation below.

Averaged momentum equation

Setting $\psi = U_{\alpha i}$, $J_{\alpha i} = p_\alpha - \mathcal{T}_{\alpha ij}$, and $\Omega = g_i$, where p_α is the pressure within a phase, $\mathcal{T}_{\alpha ij}$ is the stress due to viscous effects, and g_i is the acceleration due to gravity, in equation (4.22) leads to

$$\begin{aligned}\underbrace{\frac{\partial}{\partial t}\left[\rho_\alpha \left\langle X_\alpha \left(U_{\alpha i} + u'_{\alpha i}\right)\right\rangle\right]}_{\text{M1}} + \underbrace{\frac{\partial}{\partial x_j}\left[\rho_\alpha \left\langle X_\alpha \left(U_{\alpha i} + u'_{\alpha i}\right)\left(U_{\alpha j} + u'_{\alpha j}\right)\right\rangle\right]}_{\text{M2}} = \\ \underbrace{-\frac{\partial}{\partial x_i}\left(\left\langle X_\alpha (p_\alpha - \mathcal{T}_{\alpha ij})\right\rangle\right)}_{\text{M3}} \underbrace{-\rho_\alpha \left\langle X_\alpha g_i\right\rangle}_{\text{M4}} \underbrace{-\left\langle (p_\alpha \delta_{ij} - \mathcal{T}_{\alpha ij})\frac{\partial}{\partial x_i} X_\alpha \right\rangle}_{\text{M5}}.\end{aligned} \tag{4.30}$$

In equation (4.30), the quantity in the square brackets of term M1 is identical to the corresponding term C2 in the continuity equation. Following equations (4.25) through (4.28), we have

$$\text{Term M1} \equiv \frac{\partial}{\partial t}\left[\rho_\alpha \left\langle X_\alpha \left(U_{\alpha i} + u'_{\alpha i}\right)\right\rangle\right] = \frac{\partial}{\partial t}\left(c_\alpha \rho_\alpha U_{\alpha i}\right). \tag{4.31}$$

The convection term is represented by term M2. Expanding and transforming this term using the Reynolds-type decomposition results in

$$\begin{aligned}\text{Term M2} &\equiv \frac{\partial}{\partial x_j}\left[\rho_\alpha \left\langle X_\alpha \left(U_{\alpha i} + u'_{\alpha i}\right)\left(U_{\alpha j} + u'_{\alpha j}\right)\right\rangle\right] \\ &= \frac{\partial}{\partial x_j}\left[\rho_\alpha \left(\left\langle X_\alpha U_{\alpha i} U_{\alpha j}\right\rangle + \left\langle X_\alpha U_{\alpha i} u'_{\alpha j}\right\rangle + \left\langle X_\alpha U_{\alpha j} u'_{\alpha i}\right\rangle + \left\langle X_\alpha u'_{\alpha i} u'_{\alpha j}\right\rangle\right)\right]\end{aligned} \tag{4.32}$$

The first term in equation (4.32) is phase averaged, whereas the second and third terms vanish. The fourth term is a stress tensor term denoted by τ_{ij}^{pif}, which is phase averaged as

$$\tau_{ij}^{\text{pif}} = -\frac{\rho_\alpha \langle X_\alpha u'_{\alpha\, i} u'_{\alpha j} \rangle}{\langle X_\alpha \rangle} = -\frac{\rho_\alpha \langle X_\alpha u'_{\alpha\, i} u'_{\alpha j} \rangle}{c_\alpha}. \tag{4.33}$$

Substituting into equation (4.32), the final form for term M2 is obtained:

$$\text{Term M2} \equiv \frac{\partial}{\partial x_j}\left(c_\alpha \rho_\alpha U_{\alpha\, i} U_{\alpha j}\right) - \frac{\partial}{\partial x_j}(c_\alpha \tau_{ij}^{\text{pif}}). \tag{4.34}$$

The stress term, M3, is obtained using equation (4.10) and by decomposing into mean and fluctuating parts (i.e. $p_\alpha = p_\alpha + p'_{\alpha\, i}$ and $\mathcal{T}_{\alpha\, ij} = \tau_{\alpha\, ij} + \tau'_{\alpha\, ij}$), we have

$$\begin{aligned} \text{Term M3} &\equiv \frac{\partial}{\partial x_i}\left(\langle X_\alpha (p_\alpha - \mathcal{T}_{\alpha\, ij})\rangle\right) \\ &= \frac{\partial}{\partial x_i}\left(\left\langle X_\alpha \left[(p_\alpha + p'_{\alpha\, i}) - (\tau_{\alpha\, ij} + \tau'_{\alpha\, ij})\right]\right\rangle\right). \end{aligned} \tag{4.35}$$

Equation (4.35) simplifies after expanding the terms and averaging to

$$\text{Term M3} \equiv \frac{\partial}{\partial x_i}\left[c_\alpha (p_\alpha - \tau_{\alpha\, ij})\right]. \tag{4.36}$$

The gravity term, M4, is similarly averaged to yield

$$\text{Term M4} \equiv \rho_\alpha \langle X_\alpha g_i \rangle = c_\alpha \rho_\alpha g_i. \tag{4.37}$$

The last term on the right hand side of equation (4.30), term M5, is the momentum source due to interaction between phases. The ensemble average of term M5 is expressed as

$$\text{Term M5} \equiv \langle M_{\alpha\, i} \rangle = \left\langle (p_\alpha \delta_{ij} - \mathcal{T}_{\alpha\, ij}) \frac{\partial}{\partial x_i} X_\alpha \right\rangle. \tag{4.38}$$

The averaged pressure and stress tensor P_α^{int} and $\tau_{\alpha\, ij}^{\text{int}}$, respectively, at the fluid-solids interface are introduced to separate the mean field effects from the local effects in the interface momentum source term. Expressing the interfacial pressure in terms of its mean and fluc-

tuating components, we have

$$p_\alpha = P_\alpha^{\text{int}} + p_\alpha^{\text{int}\prime}; \tag{4.39}$$

a similar expression for the interfacial stress is

$$\mathcal{T}_{\alpha\, ij} = \tau_{\alpha\, ij}^{\text{int}} + \tau_{\alpha\, ij}^{\text{int}\prime}. \tag{4.40}$$

Introducing equations (4.39) and (4.40) into equation (4.38) and applying the averaging rules results in the following:

$$\begin{aligned}
\text{Term M5} &\equiv \left\langle p_\alpha \delta_{ij} \frac{\partial}{\partial x_i} X_\alpha \right\rangle - \left\langle \mathcal{T}_{\alpha\, ij} \frac{\partial}{\partial x_i} X_\alpha \right\rangle \\
&= P_\alpha^{\text{int}} \delta_{ij} \left\langle \frac{\partial}{\partial x_i} X_\alpha \right\rangle - \tau_{\alpha\, ij}^{\text{int}} \left\langle \frac{\partial}{\partial x_i} X_\alpha \right\rangle + \left\langle (p'_\alpha \delta_{ij} - \tau'_{\alpha\, ij}) \frac{\partial}{\partial x_i} X_\alpha \right\rangle \\
&= P_\alpha^{\text{int}} \delta_{ij} \frac{\partial c_\alpha}{\partial x_i} - \tau_{\alpha\, ij}^{\text{int}} \frac{\partial c_\alpha}{\partial x_i} + \left\langle (p'_\alpha \delta_{ij} - \tau'_{\alpha\, ij}) \frac{\partial}{\partial x_i} X_\alpha \right\rangle \\
&= \frac{\partial}{\partial x_i} \left(c_\alpha P_\alpha^{\text{int}} \delta_{ij} \right) - c_\alpha \frac{\partial}{\partial x_i} P_\alpha^{\text{int}} \delta_{ij} - \tau_{\alpha\, ij}^{\text{int}} \frac{\partial c_\alpha}{\partial x_i} + M'_{\alpha\, i},
\end{aligned} \tag{4.41}$$

where $M'_{\alpha\, i}$ is the averaged momentum transfer between the phases, after the mean pressure and stress terms have been subtracted:

$$M'_{\alpha\, i} = \left\langle (p'_\alpha \delta_{ij} - \tau'_{\alpha\, ij}) \frac{\partial}{\partial x_i} X_\alpha \right\rangle. \tag{4.42}$$

The term $M'_{\alpha\, i}$ represents local surface forces, which are due to interfacial-averaged pressure and shear stress deviations.

Substituting equations (4.31), (4.34), (4.36), (4.37), and (4.41) into equation (4.30) and rearranging yields the ensemble-averaged momentum equation for a phase α given by equation (4.43)

$$\begin{aligned}
\frac{\partial}{\partial t}(c_\alpha \rho_\alpha U_{\alpha\, i}) + \frac{\partial}{\partial x_j}\left(c_\alpha \rho_\alpha U_{\alpha\, i} U_{\alpha j}\right) &= -c_\alpha \frac{\partial}{\partial x_i} P_\alpha^{\text{int}} + \frac{\partial}{\partial x_j}\left[c_\alpha \left(\mathcal{T}_{\alpha ij} + \tau_{\alpha\, ij}^{\text{pif}}\right)\right] \\
&\quad - \frac{\partial}{\partial x_j}\left[c_\alpha \left(P_\alpha - P_\alpha^{\text{int}}\right) \delta_{ij}\right] - \tau_{\alpha\, ij}^{\text{int}} \frac{\partial c_\alpha}{\partial x_i} + c_\alpha \rho_\alpha g_i + M'_{\alpha\, i}.
\end{aligned} \tag{4.43}$$

This form of the momentum equation is valid for both the liquid and solids phase after making some important assumptions; also the closures for each phase are physically different for some of the terms. Equations (4.29) and (4.43) are frequently used as the governing equations for multiphase flows. Equations in this form have been presented in several studies with applications to fluidization (e.g. Enwald et al., 1996; Peirano and Leckner, 1998) and sediment transport (e.g. Drew, 1975; Greimann and Holly, 2001).

In equation (4.43), P_{α}^{int} and $\tau_{\alpha\, ij}^{\text{int}}$ are the averaged interfacial pressure and stress tensor, respectively introduced to separate the mean field effects from the local effects in the interface momentum source term. In the traditional ensemble averaging procedure, $\tau_{\alpha\, ij}^{\text{pif}}$ is often considered a Reynolds stress due to turbulence in a phase as a result of the decomposition used during the averaging process (see for example Enwald et al., 1996). As such, it is used to represent the correlations of velocity fluctuations in regions smaller than several particle diameters. In the present study, $\tau_{\alpha\, ij}^{\text{pif}}$ is physically interpreted differently by relating it to stresses resulting from small-scale interaction (Hsu et al., 2003) between the fluid and solids phases (e.g. $\text{pif} \equiv$ phase-induced fluctuation). To this end, $\tau_{\alpha\, ij}^{\text{pif}}$ is regarded as a small-scale Reynolds stress, which is identified with particle-induced turbulence for the fluid phase or turbulence in a dilute region for the solids phase. Further discussion of $\tau_{\alpha\, ij}^{\text{pif}}$ is provided in Section 4.4.3.

4.3 Double-Averaged Equations

To physically account for momentum transport due to turbulent fluctuations on the scale of mean flow variations, a second averaging process is applied to the ensemble-averaged equations derived in the preceding section. This is achieved by time averaging equations (4.29) and (4.43). The double averaging procedure has also been recommended to remove discontinuity in first derivatives of field variables resulting from single averaging procedures (e.g., see Ren et al. (1994)). Except for the additional closure requirements, the double-averaged transport equations are essentially unchanged in form. For constant material properties of both phases, the concentration-weighted averaging technique is similar to the so-called

Favré-averaging process (Burns et al., 2004; Hsu et al., 2003). To begin, the concentration field is decomposed into a mean and fluctuating part:

$$c_\alpha = \overline{c}_\alpha + c''_\alpha, \tag{4.44}$$

where c_α, $\overline{c}_\alpha$, and c''_α are the ensemble-averaged, time-averaged, and fluctuating concentrations, respectively; the single prime is associated with large-scale fluctuations. The following definition

$$\overline{c_\alpha U_{\alpha\, i}} = \frac{1}{T}\int_{t-T/2}^{t+T/2} c_\alpha U_{\alpha\, i}\mathrm{d}(\tau) \tag{4.45}$$

is used so that the phasic concentration-weighted mean velocity is

$$\widetilde{U}_{\alpha\, i} = \frac{\overline{c_\alpha U_{\alpha\, i}}}{\overline{c}_\alpha}. \tag{4.46}$$

With the above relations, the time-average quantities and the concentration-average of the field variable $\Psi_{\alpha\, i}$ can be related using the expressions

$$\overline{c_\alpha \Psi_{\alpha\, i}} = \overline{(\overline{c}_\alpha + c''_\alpha)(\overline{\Psi}_{\alpha\, i} + \psi''_{\alpha\, i})} \Rightarrow \widetilde{\Psi}_{\alpha\, i} = \overline{\Psi}_{\alpha\, i} + \frac{\overline{c''_\alpha \psi''_{\alpha\, i}}}{\overline{c}_\alpha} \tag{4.47}$$

so that the time-average and concentration-weighted average variables are related by

$$\widetilde{\Psi}_\alpha = \overline{\Psi}_\alpha + \overline{\widehat{\psi}}_{\alpha\, i}, \qquad \text{where} \qquad \overline{\widehat{\psi}}_{\alpha\, i} = \frac{\overline{c''_\alpha \psi''_{\alpha\, i}}}{\overline{c}_\alpha}. \tag{4.48}$$

The quantity $\overline{c''_\alpha \psi''_{\alpha\, i}}$ represents the transport of phasic concentration by velocity fluctuations so that the physical effect of $\overline{\widehat{\psi}}_{\alpha\, i}$ is turbulent dispersion and thus, is modelled as a diffusion process with an appropriate dispersion coefficient. Equation (4.47) provides the correspondence between the time-averaged and concentration-weighted average variables provided that $\overline{c''_\alpha \psi''_{\alpha\, i}}$ can also be measured.

4.3.1 Continuity equation

The concentration-weighted time averaging is performed on the ensemble-averaged equations to account for the large-scale fluctuations in the flow. For constant density, the left

hand side of the continuity equations (4.29) becomes

$$\begin{aligned}\overline{\frac{\partial}{\partial t}(c_\alpha \rho_\alpha)} + \overline{\frac{\partial}{\partial x_i}(c_\alpha \rho_\alpha U_{\alpha i})} =& \frac{\partial}{\partial t}\left[\rho_\alpha \overline{(\overline{c}_\alpha + c''_\alpha)}\right] + \\ & \frac{\partial}{\partial x_i}\left[\rho_\alpha \overline{(\overline{c}_\alpha + c''_\alpha)\left(\overline{U}_{\alpha i} + u''_{\alpha i}\right)}\right] \\ =& \frac{\partial}{\partial t}(\overline{c}_\alpha \rho_\alpha) + \frac{\partial}{\partial x_i}\left[\rho_\alpha \left(\overline{c_\alpha U_{\alpha i}} + \overline{c''_\alpha u''_{\alpha i}}\right)\right].\end{aligned} \tag{4.49}$$

Using the concentration-weighted process, equation (4.47), the continuity equation reduces to

$$\frac{\partial}{\partial t}(\overline{c}_\alpha \rho_\alpha) + \frac{\partial}{\partial x_i}\left(\rho_\alpha \overline{c}_\alpha \widetilde{U}_{\alpha i}\right) = 0. \tag{4.50}$$

with the additional constraint

$$\sum_{\alpha=1}^{2} \overline{c}_\alpha = 1 \tag{4.51}$$

for mass conservation. Equation (4.50) is similar in form to the ensemble-averaged continuity equation.

4.3.2 Momentum equation

Applying the concentration-weighted averaging to the momentum equation (4.43) and simplifying terms yields

$$\begin{aligned}\frac{\partial}{\partial t}\left(\rho_\alpha \overline{c}_\alpha \widetilde{U}_{\alpha i}\right) + \frac{\partial}{\partial x_j}\left(\rho_\alpha \overline{c}_\alpha \widetilde{U}_{\alpha i}\widetilde{U}_{\alpha j}\right) =& -\overline{c}_\alpha \frac{\partial}{\partial x_i}\overline{P}_\alpha^{\text{int}} + \overline{c''_\alpha \frac{\partial}{\partial x_i} P_\alpha^{\text{int}'}} \\ & + \frac{\partial}{\partial x_j}\overline{\left[\overline{c}_\alpha\left(\tau_{\alpha ij} + \tau_{\alpha ij}^{\text{pif}}\right)\right]} - \frac{\partial}{\partial x_j}\left(\rho_\alpha \overline{\overline{c}_\alpha u''_{\alpha i} u''_{\alpha j}}\right) \\ & + \rho_\alpha \overline{c}_\alpha g_i - \frac{\partial}{\partial x_j}\overline{[\overline{c}_\alpha (P_\alpha - P_\alpha^{\text{int}})]}\delta_{ij} - \overline{\tau_{\alpha ij}^{\text{int}} \frac{\partial \overline{c}_\alpha}{\partial x_i}} + \overline{M'_{\alpha i}}.\end{aligned} \tag{4.52}$$

On the left-hand side of equation (4.52), the first and second terms represent the local time rate of change and the rate of convection, respectively, of linear momentum of phase α per unit volume. On the right-hand side, the first term is the contribution of the phasic pressure to the force acting on phase α per unit volume, whereas the second term is the contribution of the corresponding time-averaged interfacial pressure; $P_\alpha^{\text{int}'} \equiv P_\alpha^{\text{int}} - \overline{P}_\alpha^{\text{int}}$ is assumed

to be an interfacial pressure fluctuation. The third term is comprised of the phasic viscous (laminar) and small-scale Reynolds (or phase-induced turbulent) stress, the fourth term denotes the phasic large-scale Reynolds stress, and the fifth term is the gravitational body force term. All of these stresses contribute to the forces acting on phase α per unit volume. The sixth term accounts for the difference between the interfacial pressure and the phasic pressure, and the seventh term is the interfacial averaged viscous stress contribution of phase α. The last term on the right-hand side of equation (4.52) is the so-called averaged interfacial momentum exchange or the inter-phase momentum transfer. The inter-phase momentum transfer term accounts for the inter-phase drag, lateral lift force, virtual mass force, Basset force, and the wall force. Equations (4.50) and (4.52) are used to represent the double-averaged phasic continuity and momentum equations.

4.4 Closure Equations

As in the case for single-phase momentum equation for turbulent flows, the closure problem arises when averaged transport equations for two-phase flows are derived. More terms require constitutive equations or closures compared to single-phase flows. Some of the terms on the right-hand side of equation (4.52) require constitutive relations that need to be interpreted in the context of the contribution to each phase. Prior to discussing the closure models, the physical mechanisms influencing the different regimes or regions in liquid-solid slurry flows are considered.

4.4.1 Physical mechanisms in slurry flows

The physical mechanisms discussed here pertain to the use of scaling, intuition, and phenomenological concepts to describe the stresses that contribute to the momentum transport of liquid-solids mixtures. The regimes considered cover essentially the entire dilute-to-dense spectrum.

For dilute flows or in the dilute regions of a flow, the distances between particles are large and particle-particle interaction effects are minimized. The particles in dilute regions

can be entrained by the flowing fluid and are easily suspended by the fluid turbulence. At the same time, particularly for large particles that are not easily perturbed by the fluid turbulence, the inertia of the particle determines the level of concentration. On the basis of time scales, the inertia effects are determined by the value of β or the Stokes number, St. In this regime, the suspension mechanism is dominated by the fluid turbulence.

At moderate to high solids concentrations, the average inter-particle distance is small. Consequently, the solids-phase stresses are generated via particle-particle interactions in the presence of the interstitial fluid, or due to the enduring contact experienced by the particles. In the former case, the concept of macro-viscous flow first considered by Bagnold (1954) comes to mind. The effect of the interstitial fluid on the dynamics of the solids phase makes the analysis of the stresses more complex. While current understanding of the interstitial fluid effect is far from complete, the classical study of Bagnold (1954) led him to introduce the dimensionless Bagnold number expressed by equation (2.8).

At very high solids concentration of heavy particles, flow scenarios with moving or stationary beds are likely to be encountered. In this case, the fluid turbulence is small, if not completely absent, in the moving or stationary bed regions. The main mechanism for suspension and momentum transport is the gradient of the solids phase stresses. In the context of liquid-solid flows, the moving bed regime is analogous to the intermediate flow regime, whereas the stationary bed regime can be thought of as either a quasi-static (often assumed) or static flow regime. For the quasi-static flow regime, the frictional forces between the particles are predominant. The phasic velocities are finite and the concentration gradient in the bed region would not necessarily be zero in the quasi-static regime. An immobile bed formation is typically a static flow regime and for this regime, the velocity of the particles in the bed region is zero and the solids concentration is at maximum packing. Stationary bed formation is undesirable in the hydrotransport of slurries and accurate models for the quasi-static or static regime is important to determining efficient operating conditions. In spite of it being the most common flow regime, little is know about the intermediate flow regime due to the difficulty in constructing theoretical models (Savage, 1998). As a result,

the intermediate regime is treated by combining the effects of the rapid granular and quasi-static flow regimes. For practical coarse-particle slurry flows, all the above regimes often occur simultaneously. Thus, any modelling of the flow must consider these regimes in their entirety. An important limitation of this modelling effort is the treatment of the boundaries between regimes.

4.4.2 Closures common to both phases

4.4.2.1 Momentum transfer term

The interfacial momentum force on the solids equals the opposite of the interfacial momentum force on the fluids. For the momentum transfer term $\overline{M'_{\alpha\, i}}$, we begin from $M'_{\alpha\, i}$ (equation (4.42)). It is assumed that linear combinations of physical forces such as drag, lift, added mass, Basset forces, etc can be used to obtain the closure for $M'_{\alpha\, i}$. In this study, only the drag force contribution is considered for simplicity. Therefore, the inter-phase drag term is expressed (Greimann et al., 1999) as

$$M'_{\alpha i} = M'_{\alpha i_{\mathrm{Drag}}} = \left\langle \frac{X_\alpha \rho_{\mathrm{s}}}{t_{\mathrm{p}}} \left(u_{\mathrm{f}i} - u_i^{int} \right) \right\rangle, \tag{4.53}$$

where t_{p} is the particle relaxation time. Applying the ensemble averaging process to equation (4.53) and retaining second order correlations involving X_α, while neglecting higher order ones yields

$$M'_{\alpha i_{\mathrm{Drag}}} = \frac{c_{\mathrm{s}} \rho_{\mathrm{s}}}{t_{\mathrm{p}}} \left[\left(U_{\mathrm{f}i} - U_{\mathrm{s}\,i} \right) + \frac{1}{c_{\mathrm{s}}} \left\langle X_\alpha u'_{\mathrm{f}i} \right\rangle \right]. \tag{4.54}$$

The quantity $\left\langle X_\alpha u'_{\mathrm{f}i} \right\rangle / c_{\mathrm{s}}$ represents a diffusive flux and is referred to as the drift velocity. It accounts for the dispersion effect due to the particle transport by the fluid turbulence. Following the theoretical analysis of discrete particles suspended in homogeneous turbulence performed by Deutsch and Simonin (1991), the diffusive flux can be modelled as (Greimann and Holly, 2001)

$$\frac{1}{c_{\mathrm{s}}} \left\langle X_\alpha u'_{\mathrm{f}i} \right\rangle = -D_{\mathrm{fs}\,ij} \left(\frac{1}{c_{\mathrm{s}}} \frac{\partial c_{\mathrm{s}}}{\partial x_i} - \frac{1}{c_{\mathrm{f}}} \frac{\partial c_{\mathrm{f}}}{\partial x_i} \right), \tag{4.55}$$

where $D_{\mathrm{fs}\,ij}$ is a particle diffusion or dispersion tensor. From equations (4.54) and (4.55), we have

$$M'_{\alpha i_{\mathrm{Drag}}} = \frac{c_{\mathrm{s}}\rho_{\mathrm{s}}}{t_{\mathrm{p}}}\left[(U_{\mathrm{f}i} - U_{\mathrm{s}\,i}) - D_{\mathrm{fs}\,ij}\left(\frac{1}{c_{\mathrm{s}}}\frac{\partial c_{\mathrm{s}}}{\partial x_i} - \frac{1}{c_{\mathrm{f}}}\frac{\partial c_{\mathrm{f}}}{\partial x_i}\right)\right]. \tag{4.56}$$

Equation (4.56) is modelled after the concentration-weighted time average:

$$\overline{M'}_{\alpha\, i_{\mathrm{Drag}}} = \frac{\overline{c}_{\mathrm{s}}\rho_{\mathrm{s}}}{t_{\mathrm{p}}}\left(\widetilde{U}_{\mathrm{f}i} - \widetilde{U}_{\mathrm{s}\,i}\right) - \frac{\overline{c}_{\mathrm{s}}\rho_{\mathrm{s}}}{t_{\mathrm{p}}}\overline{c''_{\mathrm{s}}u''_{\mathrm{f}i}} - \frac{\overline{c}_{\mathrm{s}}\rho_{\mathrm{s}}}{t_{\mathrm{p}}}D_{\mathrm{fs}\,ij}\left(\frac{1}{\overline{c}_{\mathrm{s}}}\frac{\partial \overline{c}_{\mathrm{s}}}{\partial x_i} - \frac{1}{\overline{c}_{\mathrm{f}}}\frac{\partial \overline{c}_{\mathrm{f}}}{\partial x_i}\right). \tag{4.57}$$

The particle relaxation time can be express as a function of the inter-phase drag function β:

$$t_{\mathrm{p}} = \frac{c_{\mathrm{s}}\rho_{\mathrm{s}}}{\beta}. \tag{4.58}$$

The inter-phase drag function is modelled with using empirical correlations. The correlation proposed by Richardson and Zaki (1954) for β is usually used (Roco, 1990; Hsu et al., 2004) for liquid-solid slurry flows or sediment transport simulations. For particulate flows with a wide range of solids concentration distributions, especially in fluidized bed simulations, those of Wen and Yu (1966) and Gidaspow (1994) are often preferred. For the flows investigated in this work, the local solids concentration varies over a wide range. In the present study, the inter-phase drag function β is calculated from equations (2.29) and (2.30).

The second term in equation (4.57) includes the correlation between the solids phase concentration fluctuation and the fluid phase velocity fluctuation, which is modelled by a gradient transport term:

$$\overline{c''_{\mathrm{s}}u''_{\mathrm{f}i}} = -\nu_{\mathrm{ft}}\frac{\partial \overline{c}_{\mathrm{s}}}{\partial x_i}, \tag{4.59}$$

where ν_{ft} is the fluid phase turbulent viscosity, the closure of which is discussed in Section 4.4.4.1.

Presently, the particle diffusion tensor $D_{\mathrm{fs}\,ij}$ is not very well understood. For non-

isotropic cases, $D_{\mathrm{fs}\,ij}$ can be generalized as

$$D_{\mathrm{fs}\,ij} = t_{\mathrm{fs}}\,\overline{u''_{\mathrm{f}i}u''_{\mathrm{s}\,i}}, \tag{4.60}$$

where $k_{\mathrm{fs}} = \overline{u''_{\mathrm{f}i}u''_{\mathrm{s}\,i}}$ is the covariance correlation between the turbulent velocity fluctuations of the two-phases. This quantity presented via its modelled transport equation is further discussed in Chapter 5. In equation (4.60), t_{fs} is the interaction time between particle motion and liquid phase fluctuations if a relative motion exists between the two phases, and is given by

$$t_{\mathrm{fs}} = C_\mu \frac{3k_{\mathrm{f}}}{2\varepsilon_{\mathrm{f}}}\left(1 + C_\beta \frac{3|U_{\mathrm{s}i} - U_{\mathrm{f}i}|^2}{2k_{\mathrm{f}}}\right)^{-1/2}. \tag{4.61}$$

The coefficient C_β is expressed as

$$C_\beta = 1.85 - 1.35\cos^2\theta \tag{4.62}$$

where θ is the angle between the mean particle and the mean relative velocities (Csanady, 1963). Squires and Eaton (1991) explained the particle diffusion process using two concepts: the crossing trajectory and inertia effects. The crossing-trajectory effect is attributed to the fact that the particles 'fall' out of the fluid phase turbulent eddies. This causes them to more quickly lose correlation with the surrounding fluid. The crossing trajectory effect is quantified by the fluid-particle interaction time (see Chapter 5). The inertia effect is due to the inability of the particles to track exactly the fluid motion. The above effects were used by Greimann and Holly (2001). Enwald et al. (1996) calculated $D_{\mathrm{fs}\,ij}$ using

$$D_{\mathrm{fs}\,ij} = \frac{1}{3}t_{\mathrm{fs}}k_{\mathrm{fs}}. \tag{4.63}$$

4.4.2.2 Pressure and interfacial stress terms

For liquid-solids flows, the pressure at the liquid-solid interface can be assume to be equal to that of the liquid-phase. Therefore, a simple constitutive relation would be

$$\overline{P}_\alpha^{\mathrm{int}}\Big|_{\alpha=\mathrm{f\ or\ s}} = \overline{P}_{\mathrm{f}}. \tag{4.64}$$

In this case, the first term on the right hand side of equation (4.52) becomes

$$-\overline{c}_\alpha \frac{\partial}{\partial x_i}\overline{P}_\alpha^{\,\mathrm{int}}\bigg|_{\alpha=\mathrm{f\ or\ s}} = -\overline{c}_\alpha \frac{\partial}{\partial x_i}\overline{P}_\mathrm{f}. \tag{4.65}$$

Following Roco (1990) and Roco and Shook (1985), the correlation between c''_α and $P_\alpha^{\mathrm{int}'}$, that is the second term on the right hand side of equation (4.52), is neglected.

4.4.3 Solids-phase stress closures

The third, fourth, fifth, and sixth terms, i.e. $\overline{c_\mathrm{s}(\tau_{\mathrm{s}\,ij}+\tau_{\mathrm{s}\,ij}^{\mathrm{pif}})}$, $\rho_\mathrm{s}\overline{c_\mathrm{s}u''_{\mathrm{s}i}u''_{\mathrm{s}j}}$, $\overline{c_\mathrm{s}\left(P_\mathrm{s}-P^{\,\mathrm{int}}\right)}$, on the right hand side of equation (4.52) require constitutive relations. In the present study, different types of closures for the solids-phase stress are investigated in the context of kinetic theory of granular flow. Several methods based on the kinetic theory of dense gases originally postulated by Chapman and Cowling (1970) have been used to derive constitutive equations for the solids-phase stresses. The works of Campbell (1990), Jenkins and Richman (1985), Lun et al. (1984), Peirano and Leckner (1998), and Simonin (1996) are just a few examples. This modelling approach leads to closure relations that account for the solids stresses in rapid granular flows. The modelling efforts followed here consider flow mechanisms over the dilute-dense spectrum of solids concentration while taking into account interstitial fluid and frictional effects.

There are a number of models for the solids-phase stresses contributing to kinetic and collisional effects; the difference between them is mainly in the expressions for the transport coefficients. The models of Gidaspow (1994) and Lun et al. (1984) using the kinetic theory approach covers a wide range of solids concentration. These models were developed for dry granular flows. The models proposed by Peirano and Leckner (1998) are extensions of those of Jenkins and Richman (1985) to include interstitial fluid effects, and are essentially limited to dilute flows.

The stresses due to particle-particle interaction are modelled in a way analogous to the constitutive relation for the molecular stress in a single-phase Newtonian fluid. The

transport coefficients are, in this case, determined from the kinetic theory of granular flow. Thus, written in the conventional form, we have

$$\overline{c_{\mathrm{s}}\tau_{\mathrm{s}\,ij}} = 2\mu_{\mathrm{s}}S_{\mathrm{s}\,ij} + \left[\left(\xi_{\mathrm{s}} - \frac{2}{3}\mu_{\mathrm{s}}\right)S_{\mathrm{s}jj} - P_{\mathrm{s}}\right]\delta_{ij}, \tag{4.66}$$

where $S_{\mathrm{s}\,ij}$ is the strain-rate tensor defined by $2S_{\mathrm{s}\,ij} = (U_{\mathrm{s}\,i,j} + U_{\mathrm{s}j,i})$; the transport coefficients μ_{s} and ξ_{s} are the solids-phase dynamic and bulk viscosities, respectively; and P_{s} is the so-called solids-phase (particle) pressure. The closure equations for μ_{s}, ξ_{s}, and P_{s} used in the present study are provided in Chapter 5.

For dispersed two-phase flows, the average interfacial stress term is often considered insignificant (Ishii and Mishima, 1984), thus the 7th term in equation (4.52) is

$$\overline{\tau_{ij}^{\mathrm{int}}\frac{\partial \overline{c}_{\alpha}}{\partial x_i}} \approx 0. \tag{4.67}$$

In dense particulate flows, additional stresses exist due to friction between particles. These extra stresses are largely based on the critical state theory of soil mechanics (Jackson, 1983; Roco, 1990; Roco and Shook, 1983). It is assumed that the material of the solids-phase is non-cohesive but possesses rheological characteristics similar to that in the plastic regime (Schaeffer, 1987; Tardos et al., 2003). Such characteristics are generally modelled as

$$\tau_{\mathrm{s}\,ij}^{\mathrm{f}} = P_{\mathrm{s}}^{\mathrm{f}}\delta_{ij} + \mathfrak{F}(P_{\mathrm{s}}^{\mathrm{f}}, c_{\mathrm{s}})\frac{\hat{S}_{\mathrm{s}\,ij}}{\sqrt{\hat{S}_{\mathrm{s}\,ij} : \hat{S}_{\mathrm{s}\,ij}}}, \tag{4.68}$$

where $P_{\mathrm{s}}^{\mathrm{f}}$ is the averaged normal frictional stress or pressure; $\hat{S}_{\mathrm{s}\,ij} = S_{\mathrm{s}\,ij} - S_{\mathrm{s}\,mm}\delta_{ij}/3$ is the deviatoric part of the strain rate tensor (Srivastava and Sundaresan, 2003); and $\mathfrak{F}(P_{\mathrm{s}}^{\mathrm{f}}, c_{\mathrm{s}})$ is a function to be specified. Different functional forms of $P_{\mathrm{s}}^{\mathrm{f}}$ and $\mathfrak{F}(P_{\mathrm{s}}^{\mathrm{f}}, c_{\mathrm{s}})$ have been considered in recent studies (Makkawi and Ocone, 2006; Srivastava and Sundaresan, 2003; Tardos et al., 2003). The stress induced by the fluid flow on the solids-phase (i.e. pit = phase-induced turbulence) is neglected:

$$\overline{c_{\mathrm{s}}\tau_{\mathrm{s}\,ij}^{\mathrm{pif}}} \doteq 0. \tag{4.69}$$

The eddy-viscosity assumption is used to model the solids-phase turbulent stresses, i.e.

$$\rho_{\mathrm{s}}\overline{c_{\mathrm{s}}u''_{\mathrm{s}i}u''_{\mathrm{s}j}} = 2\mu_{\mathrm{st}}S_{\mathrm{s}\,ij} - \frac{2}{3}\rho_{\mathrm{s}}c_{\mathrm{s}}k_{\mathrm{s}}\delta_{ij}. \tag{4.70}$$

Different models for the eddy viscosity for the solids-phase are used in the present study as discussed in Chapters 5 and 6.

In the quasi-static rate-independent flow regime, inter-particle stresses arise because of the friction experienced by particles in enduring contact. Under conditions of high solids concentration, particles interact with multiple neighbours. The normal and the tangential forces due to friction effects are the main contributions to the solids-phase stresses and hence, momentum transport. In many studies where the kinetic-frictional closure is considered, the modelling process assumes the frictional contribution as an additional stress in an *ad hoc* manner. For particulate flows where inter-particle contact is inevitable, as in the case of flow with a moving or stationary bed, the pressure difference can be used to account for extra pressure due to contact. Following Drew (1983), we have

$$P_{\mathrm{s}} = (P^{\,\mathrm{int}} + P_{\mathrm{s}}^{\mathrm{f}}) \tag{4.71}$$

where $P_{\mathrm{s}}^{\mathrm{f}}$ is intuitively assumed to be an extra normal stress due to enduring contact. The stress term $\overline{c_{\mathrm{s}}\,(P_{\mathrm{s}} - P^{\,\mathrm{int}})}$ is, therefore, simplified as

$$\overline{c_{\mathrm{s}}\,(P_{\mathrm{s}} - P^{\,\mathrm{int}})} = P_{\mathrm{s}}^{\mathrm{f}}. \tag{4.72}$$

As noted by Drew (1983), several modellers have used $P_{\mathrm{s}}^{\mathrm{f}} = P_{\mathrm{s}}^{\mathrm{f}}(c_{\mathrm{s}})$ to model the pressure difference.

4.4.4 Liquid phase stress closures

For the fluid phase, the effective stress consists of the third and fourth terms in equation (4.52). Often, the second part of the third term, τ_{ij}^{pif} is modelled using one of the following approaches:

1. As the Reynolds stress (see Enwald et al., 1996) in which case the fourth term in equation (4.52) does not appear. This approach is usually applied when only the ensemble-averaging procedure is used,

2. decomposed into particle-induced and shear-induced stress components (for example, Alajbegovic et al., 1999; Burns et al., 2004), or

3. As the averaged small-scale Reynolds stress generated due to the interaction between the fluid and the particles or by fluctuations in the particles (Hsu et al., 2004; Hwang and Shen, 1993). This basis is often unique to the double-averaging technique and the concept of large-scale fluctuation, where concentration fluctuations are also introduced (see also Zeng et al., 2005).

Even though this study investigates different two-fluid models, the discussion to follow in section 4.4.4.1 is tailored towards the third approach.

4.4.4.1 Effective fluid-phase stress tensor

Applying equation (4.52) to the fluid phase, the third term contains the viscous and a Reynolds-like stress, which is identified as the stress resulting from the small-scale or particle induced fluctuations. The viscous shear stress of the fluid (liquid phase) is calculated using the linear stress-strain rate relationship:

$$\overline{c_{\mathrm{f}}\tau_{\mathrm{f}ij}} = c_{\mathrm{f}}\rho_{\mathrm{f}}\mu_{\mathrm{f}}\left(\frac{\partial U_{\mathrm{f}i}}{\partial x_j} + \frac{\partial U_{\mathrm{f}j}}{\partial x_i}\right). \tag{4.73}$$

In dilute flows, the phase-induced turbulence is assumed due to the slip between the fluid and the particles. The effect of the slip can be characterised by the particle diameter as the length scale and the relative velocity as the velocity scale (Gore and Crowe, 1989). In addition, the solids concentration in the dilute regions is low and the effect on the mean flow is expected to be negligible. For dense flows, where particle-particle interactions are still dominant, particle-induced turbulence may be included in the fluid phase closure as discussed by Hwang and Shen (1993).

The fluid-phase turbulent stress is modelled using the eddy viscosity model:

$$\rho_{\mathrm{f}}\overline{c_{\mathrm{f}}u''_{\mathrm{f}i}u''_{\mathrm{f}j}} = c_{\mathrm{f}}\left[\mu_{\mathrm{ft}}\left(\frac{\partial U_{\mathrm{f}i}}{\partial x_j}+\frac{\partial U_{\mathrm{f}j}}{\partial x_i}\right)-\frac{2}{3}\rho_{\mathrm{f}}k_{\mathrm{f}}\delta_{ij}\right], \tag{4.74}$$

where the eddy viscosity of the fluid phase μ_{ft} is calculated using the two-equation $k_{\mathrm{f}}-\varepsilon_{\mathrm{f}}$ turbulence model

$$\mu_{\mathrm{ft}} = C_\mu\rho_{\mathrm{f}}\frac{k_{\mathrm{f}}^2}{\varepsilon_{\mathrm{f}}}. \tag{4.75}$$

In equation (4.75), C_μ is a model constant (see Table 4.1); k_{f} is the fluid phase turbulence kinetic energy; and ε_{f} is the dissipation rate of k_{f}. For the fluid phase, the sixth term in equation (4.52) vanishes.

4.4.4.2 Fluid-phase two-equation turbulence model

In this work, the transport equations for k_{f} and ε_{f} are solved to compute μ_{ft}. By definition, the fluid-phase turbulence kinetic energy is

$$k_{\mathrm{f}} = \frac{1}{2\overline{c}_{\mathrm{f}}}\overline{c_{\mathrm{f}}u''_{\mathrm{f}}u''_{\mathrm{f}}}. \tag{4.76}$$

The transport equation for k_{f} is derived by subtracting the governing equation of the mean kinetic energy of the instantaneous fluid phase velocity from that of the kinetic energy of the concentration-weighted mean velocity. Dropping the $\tilde{}$ symbol and using some of the closure equations in the preceding sections, we have Hsu et al. (2004)

$$\begin{aligned}\frac{\partial}{\partial t}\left(c_{\mathrm{f}}\rho_{\mathrm{f}}k_{\mathrm{f}}\right)+\frac{\partial}{\partial x_j}\left(c_{\mathrm{f}}\rho_{\mathrm{f}}U_{\mathrm{f}j}k_{\mathrm{f}}\right) &= \mathfrak{T}_{\mathrm{f}ij}\frac{\partial U_{\mathrm{f}i}}{\partial x_j}\\ &+\frac{\partial}{\partial x_j}\left[\overline{\tau_{\mathrm{f}ij}c_{\mathrm{f}}u''_{\mathrm{f}i}}-\rho_{\mathrm{f}}\overline{\frac{1}{2}c_{\mathrm{f}}u''_{\mathrm{f}i}u''_{\mathrm{f}i}u''_{\mathrm{f}i}}-\overline{c_{\mathrm{f}}u''_{\mathrm{f}i}P''_{\mathrm{f}}}\right]\\ &+\overline{P''_{\mathrm{f}}\frac{\partial c_{\mathrm{f}}u''_{\mathrm{f}i}}{\partial x_i}}-\overline{c_{\mathrm{f}}\tau_{\mathrm{f}ij}\frac{\partial u''_{\mathrm{f}i}}{\partial x_i}}\\ &-\frac{c_{\mathrm{s}}\rho_{\mathrm{s}}}{t_{\mathrm{p}}}\overline{c''_{\mathrm{s}}u''_{\mathrm{f}i}}(U_{\mathrm{f}i}-U_{\mathrm{s}i})-c_{\mathrm{f}}\rho_{\mathrm{f}}\frac{c_{\mathrm{s}}\rho_{\mathrm{s}}}{t_{\mathrm{p}}}\overline{c_{\mathrm{s}}u''_{\mathrm{f}i}(u''_{\mathrm{f}i}-u''_{\mathrm{s}i})}\end{aligned} \tag{4.77}$$

Following single-phase flow arguments (Wilcox, 2002), equation (4.77) is transformed to the standard convection-diffusion form. On the right-hand side, the first term is the produc-

tion term, where $\mathfrak{T}_{\mathrm{f}\,ij} = \overline{c_\mathrm{f}\tau_{\mathrm{f}ij}} + \rho_\mathrm{f}\overline{c_\mathrm{f}u''_{\mathrm{f}i}u''_{\mathrm{f}j}}$ is the effective stress. The second term is treated as the diffusion term:

$$\frac{\partial}{\partial x_j}\left[\overline{\tau_{\mathrm{f}ij}c_\mathrm{f}u''_{\mathrm{f}i}} - \rho_\mathrm{f}\overline{\frac{1}{2}c_\mathrm{f}u''_{\mathrm{f}i}u''_{\mathrm{f}i}u''_{\mathrm{f}i}} - \overline{c_\mathrm{f}u''_{\mathrm{f}i}P''_\mathrm{f}}\right] = \frac{\partial}{\partial x_j}\left[c_\mathrm{f}\left(\mu_\mathrm{f} + \frac{\mu_\mathrm{ft}}{\sigma_k}\right)\frac{\partial k_\mathrm{f}}{\partial x_j}\right], \tag{4.78}$$

where σ_k is the Prandtl number of the k_f equation. Following Roco and Shook (1983), the third term is ignored. The fourth term is the dissipation rate of the fluid phase turbulence kinetic energy k_f, which is given by

$$\varepsilon_\mathrm{f} = \frac{1}{\overline{c}_\mathrm{f}\rho_\mathrm{f}}\overline{c_\mathrm{f}\tau_{\mathrm{f}ij}\frac{\partial u''_{\mathrm{f}i}}{\partial x_i}}. \tag{4.79}$$

The correlations in the last term in equation (4.77) is modelled as

$$\Pi_{k_\mathrm{f}} = \frac{c_\mathrm{s}\rho_\mathrm{s}}{t_\mathrm{p}}\left(-2c_\mathrm{f}k_\mathrm{f} + k_\mathrm{fs} + (U_{\mathrm{f}i} - U_{\mathrm{s}i})U_{\mathrm{d}i}\right). \tag{4.80}$$

where $U_{\mathrm{d}i}$ is the drift velocity defined as

$$U_{\mathrm{d}i} = t_\mathrm{fs}\frac{k_\mathrm{fs}}{3}\left(\frac{1}{c_\mathrm{f}}\frac{\partial c_\mathrm{f}}{\partial x_i} - \frac{1}{c_\mathrm{s}}\frac{\partial c_\mathrm{s}}{\partial x_i}\right). \tag{4.81}$$

Thus, the modelled transport equation for k_f is given by

$$\begin{aligned}\frac{\partial}{\partial t}\left(c_\mathrm{f}\rho_\mathrm{f}k_\mathrm{f}\right) + \frac{\partial}{\partial x_j}\left(c_\mathrm{f}\rho_\mathrm{f}U_{\mathrm{f}j}k_\mathrm{f}\right) = {}& \frac{\partial}{\partial x_j}\left[c_\mathrm{f}\left(\mu_\mathrm{f} + \frac{\mu_\mathrm{ft}}{\sigma_k}\right)\frac{\partial k_\mathrm{f}}{\partial x_j}\right] \\ & + \frac{c_\mathrm{s}\rho_\mathrm{s}}{t_\mathrm{p}\rho_\mathrm{f}}\mu_\mathrm{ft}\frac{\partial c_\mathrm{f}}{\partial x_j}(U_{i\mathrm{f}} - U_{i\mathrm{s}}) + \mathfrak{T}_{\mathrm{f}\,ij}\frac{\partial U_{\mathrm{f}i}}{\partial x_j} \\ & - \rho_\mathrm{f}c_\mathrm{f}\varepsilon_\mathrm{f} + c_\mathrm{f}\rho_\mathrm{f}\Pi_{k_\mathrm{f}}\end{aligned} \tag{4.82}$$

Following a similar approach, the transport equation for ε_f can be obtained as follows:

$$\begin{aligned}\frac{\partial}{\partial t}\left(c_\mathrm{f}\rho_\mathrm{f}\varepsilon_\mathrm{f}\right) + \frac{\partial}{\partial x_j}\left(c_\mathrm{f}\rho_\mathrm{f}U_{\mathrm{f}j}\varepsilon_\mathrm{f}\right) = {}& \frac{\partial}{\partial x_j}\left[c_\mathrm{f}\left(\mu_\mathrm{f} + \frac{\mu_\mathrm{ft}}{\sigma_\varepsilon}\right)\frac{\partial \varepsilon_\mathrm{f}}{\partial x_j}\right] + C_{\varepsilon 1}\frac{\varepsilon_\mathrm{f}}{k_\mathrm{f}}\mathfrak{T}_{\mathrm{f}\,ij}\frac{\partial U_{\mathrm{f}i}}{\partial x_j} \\ & - C_{\varepsilon 2}\frac{\varepsilon_\mathrm{f}}{k_\mathrm{f}}c_\mathrm{f}\rho_\mathrm{f}\varepsilon_\mathrm{f} + C_{\varepsilon 3}\frac{\varepsilon_\mathrm{f}}{k_\mathrm{f}}\frac{c_\mathrm{s}\rho_\mathrm{s}}{t_\mathrm{p}\rho_\mathrm{f}}\mu_\mathrm{ft}\frac{\partial c_\mathrm{f}}{\partial x_j}(U_{i\mathrm{f}} - U_{i\mathrm{s}}) \\ & - C_{\varepsilon 3}\frac{\varepsilon_\mathrm{f}}{k_\mathrm{f}}c_\mathrm{f}\rho_\mathrm{f}\Pi_{k_\mathrm{f}}\end{aligned} \tag{4.83}$$

Equations (4.82) and (4.83) are the generic forms used to calculate k_{f} and ε_{f} in the present study. The specific closure terms and relations used for the flows calculated in this work for vertical and horizontal flows are discussed in Sections 5.1 and 6.2, respectively.

With the exception of $C_{\varepsilon 3}$, the numerical coefficients of the fluid-phase $k-\varepsilon$ turbulence model provided in Table 4.1 are those calibrated for single-phase flows. Appropriate values for the constants, including that for $C_{\varepsilon 3}$, for the case of two-phase flows are still the subject of debate (Bolio et al., 1995; Rizk and Elghobashi, 1989; Simonin, 1996; Squires and Eaton, 1994) and the focus of recent investigations (Zhang and Reese, 2001, 2003b).

Table 4.1: Model constants in the fluid-phase $k-\varepsilon$ turbulence model.

C_μ	$C_{\varepsilon 1}$	$C_{\varepsilon 2}$	$C_{\varepsilon 3}$	σ_k	σ_ε
0.09	1.44	1.92	1.2	1.0	1.3

4.5 Boundary Conditions

Boundary conditions have to be imposed at the inlets, outlets and bounding walls of the flow domain. The inlet and outlet boundary conditions are discussed in Chapter 5. The total wall shear stress is a very useful parameter in two-phase flow system design. Thus, in systems where head losses are considered important, the correct formulation of the wall boundary condition, particularly in the two-fluid formulation, is crucial. To this end, discussion and formulation of phasic wall boundary conditions is presented in the following sections. The wall function formulation is adopted for the fluid phase, while some of the existing formulations for the solids-phase are presented.

4.5.1 Fluid-phase wall boundary conditions

In turbulent flows, the wall-function formulation typically uses a logarithmic relation for the near-wall velocity in inner coordinates ($y^+_{\mathrm{fn}} \cong 30 - 200$):

$$U^+ = \frac{U_{\mathrm{fn}}}{u_\tau} = \frac{1}{\kappa}\ln(\mathrm{E}y^+_{\mathrm{fn}}), \tag{4.84}$$

where

$$y^+_{\mathrm{fn}} = \rho u_\tau y_{\mathrm{fn}}/\mu \quad \text{and} \quad u_\tau = \sqrt{\tau_{\mathrm{fw}}/\rho}. \tag{4.85}$$

The subscript fn refers to the first node from the wall; u_τ is the friction velocity; U_{fn} is the velocity parallel to the wall at a distance of y_{fn} from the wall; y^+_{fn} is the dimensionless distance from the wall; and E = 9.793 is the log-layer constant. The values of k_{fn} and $\varepsilon_{\mathrm{fn}}$ at the first node are,

$$k_{\mathrm{fn}} = \frac{u_\tau^2}{\sqrt{C_\mu}} \quad \text{and} \quad \varepsilon_{\mathrm{fn}} = \frac{u_\tau^3}{\kappa y_{\mathrm{fn}}} = \frac{{C_\mu}^{3/4} k_{\mathrm{fn}}^{3/2}}{\kappa y_{\mathrm{fn}}}. \tag{4.86}$$

This formulation does not consider the effect of the solids-phase on the fluid at the wall. The effect of the solids-phase can be accounted for through the inter-phase drag term to reflect the effect of turbulence interaction between the phases (Benyahia et al., 2005).

4.5.2 Solids-phase wall boundary conditions

Several approaches are used for the solids-phase wall boundary condition in the literature. Considering particle-wall interactions of neutrally buoyant wax spheres, Bagnold (1954) proposed dispersive stress relations for the 'macro-viscous' and 'grain-inertia' regimes, respectively, and developed a solids-phase wall shear stress, which can be recast in Newtonian form using equation (2.7). As noted in Chapter 2, Shook and Bartosik (1994), calculated the solids-phase velocity gradient at the wall using a stress-strain relation. They assumed that the velocity gradient of the solids at the wall is equal to that of the liquid. The solids mean concentration C_{s} was used to calculate the linear concentration λ_{L}. Considering the grain-inertia regime, they modified equation (2.7) to the form given by equation (2.10). Shook and Bartosik (1994) and Bartosik (1996) adopted these approximations be-

cause local solids velocity and concentration measurements were not obtained during their study. For the present work, the solids-phase velocity gradient is explicitly calculated to determine the solids-phase wall shear stress.

Eldighidy et al. (1977) proposed a slip condition for the solids-phase wall boundary condition in the form

$$U_s\big|_{\mathrm{w}} = -\lambda_{\mathrm{slip}} \left(\frac{\partial U_s}{\partial y} \right) \Bigg|_{\mathrm{w}}, \tag{4.87}$$

where, $U_s\big|_{\mathrm{w}}$ is the particle velocity at the wall, y is the wall-normal direction, and the coefficient λ_{slip} is known as the slip parameter. Different approaches were used to estimate λ_{slip} for the two-fluid application by Ding and Gidaspow (1990) and Ding and Lyczkowski (1992). In the study by Ding and Gidaspow (1990), λ_{slip} was assumed to be the mean distance between particles and estimated it from

$$c_{\mathrm{s}} \frac{4\pi}{3} \left(\frac{\lambda_{\mathrm{slip}}}{2} \right)^3 = \frac{\pi}{6} {d_{\mathrm{p}}}^3 \tag{4.88}$$

to obtain

$$\lambda_{\mathrm{slip}} = \frac{d_{\mathrm{p}}}{c_{\mathrm{s}}^{1/3}} \tag{4.89}$$

The estimated expression for λ_{slip} in the study of Ding and Lyczkowski (1992) was obtained more rigorously via the kinetic theory approach. Ding and Lyczkowski (1992) defined λ_{slip} in the same way as Ding and Gidaspow (1990) and obtained an expression for λ_{slip} in the form

$$\lambda_{\mathrm{slip}} = \frac{\sqrt{3\pi}}{24} \frac{d_{\mathrm{p}}}{c_{\mathrm{s}} g_0}. \tag{4.90}$$

The radial distribution function g_0 is given by

$$g_0 = \left(1 - \frac{c_{\mathrm{s}}}{C_{\mathrm{max}}} \right)^{-2.5 C_{\mathrm{max}}}. \tag{4.91}$$

In equation (4.91), $C_{\mathrm{max}} = 0.63$ is the maximum volume fraction. The slip parameter developed by Ding and Lyczkowski (1992) was used by Ding et al. (1993) to simulate laminar flow of a liquid-solid mixture using a multi-fluid model.

The preceding discussions on the treatment of the solids-phase wall boundary condition provide a simplistic approach to its formulation and numerical implementation. However, as noted above, the mechanisms involved in the particle-wall interaction are physically more complex. The heuristic approach proposed by Hui et al. (1984) was used by Johnson and Jackson (1987) and Johnson et al. (1990) to account for particle-wall friction. More rigorous derivations of the solids-phase boundary conditions, which are expected to be physically amendable to particle-wall mechanism, have been attempted in several studies (Benyahia et al., 2005; Jenkins and Louge, 1997; Jenkins and Richman, 1986; Louge, 1994; Richman, 1988). Johnson and Jackson (1987) formulated the following boundary conditions for granular materials in a plane shear flow:

$$n \cdot \mathfrak{T}_{\mathrm{s}} \frac{U_{\mathrm{s}}}{|U_{\mathrm{s}}|} + \frac{\sqrt{3}\phi\pi c_{\mathrm{s}}\rho_{\mathrm{s}}g_{\mathrm{o}}|U_{\mathrm{s}}|T_{\mathrm{s}}^{1/2}}{6C_{\max}} + \tau_{sn}^{\mathrm{f}}\tan\varphi = 0; \tag{4.92}$$

for the solids-phase velocity and

$$\Gamma_{T_{\mathrm{s}}} \frac{\partial T_{\mathrm{s}}}{\partial r}\bigg|_{\mathrm{w}} = \frac{\sqrt{3}\pi c_{\mathrm{s}}\rho_{\mathrm{s}}g_{\mathrm{o}}T_{\mathrm{s}}^{1/2}}{6C_{\max}} \left[\phi|U_{\mathrm{s}}|^2 - \frac{3T_{\mathrm{s}}}{2}(1-e_{\mathrm{w}}^2)\right] \tag{4.93}$$

for the granular temperature, where e_{w} is the restitution coefficient at the wall and $0 \leq \phi \leq 1$ is known as the specularity coefficient; $\Gamma_{T_{\mathrm{s}}}$ is the coefficient of the granular temperature equation. When the frictional term in equation (4.92) is neglected, $\phi = 0$ leads to the free-slip (or smooth wall) boundary condition and a value of $\phi = 1$ defines a rough wall condition (cf. Benyahia et al., 2005). The specularity coefficient is characteristic of the fraction of diffuse particle-wall collisions.

4.6 Summary

The transport equations for particulate two-phase flows have been presented in this chapter. A general overview of the closure relations for the terms that require constitutive equations were also discussed. The specific transport equations, closure models, and modelled transport equations for auxiliary quantities used for simulations in this work are discussed in detail in Chapter 5, where vertical flow simulations are reported, and in 6, the horizontal

pipe flow calculations are performed. Due to the limitations of the user, the simulations were limited to the models that were simple to implement.

CHAPTER 5

VERTICAL FLOW SIMULATIONS

In this chapter, the model predictions of local flow distributions and frictional head losses for liquid-solid vertical flows made using the commercial CFD software ANSYS CFX-4.4 are presented. As noted in the preceding chapter, specific constitutive relations for the solids-phase stress and associated auxiliary transport equations are investigated. Specifically, three types of closures for the solids-phase stress are considered. Prediction of solids-phase velocity and concentration profiles are compared with measured data for high solids bulk concentration flows. For the frictional head loss, the effects of various solids-phase wall boundary condition models are investigated for liquid-solid vertical flows.

5.1 Two-Fluid Model Equations

For isothermal two-phase flows where both phases are considered turbulent with no inter-phase mass transfer, equations (1.1) to (1.5), which are simplified forms of equations (4.50) and (4.52) are used to describe the mass and momentum transport in each phase. For all the simulations, the fluid-phase effective stress is calculated using the $k_{\mathrm{f}} - \varepsilon_{\mathrm{f}}$ model (equations (4.77) and (4.83)) with the wall function formulation. The treatment of the effective stress for the solids-phase for the different models investigated is discussed in Section 5.1.1. Different models are available for the solids-phase stress closure in the literature. The three common two-fluid models, often referred to as $k_{\mathrm{f}} - \varepsilon_{\mathrm{f}} - k_{\mathrm{s}} - \varepsilon_{\mathrm{s}}$, $k_{\mathrm{f}} - \varepsilon_{\mathrm{f}} - k_{\mathrm{s}} - \varepsilon_{\mathrm{s}} - T_{\mathrm{s}}$, and $k_{\mathrm{f}} - \varepsilon_{\mathrm{f}} - k_{\mathrm{s}} - k_{\mathrm{fs}}$, are investigated in the present study; k_{fs} is the fluid-solids covariance (cf. Peirano and Leckner, 1998).

5.1.1 The $k_{\mathrm{f}} - \varepsilon_{\mathrm{f}} - k_{\mathrm{s}} - \varepsilon_{\mathrm{s}}$ model

The $k_{\mathrm{f}} - \varepsilon_{\mathrm{f}} - k_{\mathrm{s}} - \varepsilon_{\mathrm{s}}$ model considered in this study is the baseline model for two-phase turbulent flows in the CFX-4.4 code. The essential assumption in this case is that the turbulence model for the fluid can be adopted for the solids-phase. It should be noted that, for this model, the last term in equations (4.82) and (4.83) does not appear and hence, is not considered. The effective solids-phase stress tensor in this case is modelled in terms of collision and kinetic (or 'turbulent') contributions, i.e.,

$$\mathfrak{T}_{\mathrm{s}\,ij} = P_{\mathrm{s}}\delta_{ij} + \tau_{\mathrm{s}\,ij} + \tau_{\mathrm{st}\,ij}. \tag{5.1}$$

The solids-phase stress due to collision is expressed in terms of a normal component P_{s} and a shear component $\tau_{\mathrm{s}\,ij}$. The normal component of the collisional stress is given in the form of a simple solids pressure model (Bouillard et al., 1989)

$$\frac{\partial P_{\mathrm{s}}}{\partial x_i} = G_{\mathrm{o}}\left[\exp\left(-C_{\mathrm{M}}\{c_{\mathrm{s}} - C_{\max}\}\right)\right]\frac{\partial c_{\mathrm{s}}}{\partial x_i}, \tag{5.2}$$

where G_{o} is known as the reference elastic modulus; C_{M} is the compaction modulus; and $C_{\max}$ is the maximum packing concentration of the particles. The effect of equation (5.2) is to prevent the calculated solids concentration from exceeding the maximum packing in dense regions for a given nominal particle size. Following Bouillard et al. (1989), values of $G_{\mathrm{o}} = 1$ Pa and $C_{\mathrm{M}} = 600$ were used in equation (5.2).

The collisional shear stress $\tau_{\mathrm{s}\,ij}$ is expressed in the same way as for the fluid-phase molecular shear stress. However, unlike the fluid-phase for which the laminar viscosity is constant, the solids-phase viscosity depends strongly on the transport mechanisms affecting the solids-phase. In the literature, the solids viscosity is typically modelled in one of three ways: constant solids viscosity (Sun and Gidaspow, 1999; Gómez and Milioli, 2001), empirical or semi-empirical correlations (Enwald et al., 1996), or from the kinetic theory (Chapman and Cowling, 1970). While kinetic theory leads to a specific constitutive relation for the solids viscosity (see below), the use of negligible solids viscosity is also

quite common. For the present study, the collisional shear stress $\tau_{\mathrm{s}\,ij}$ is expressed in the same way as for the liquid-phase, where the dynamic viscosity was set to a very small value of 10^{-8} Pa·s following the aforementioned studies.

The solids-phase turbulent stress $\tau_{\mathrm{st}\,ij}$ is modelled using a $k-\varepsilon$ type two-equation model similar to that of the fluid-phase. The default model constants of the $k-\varepsilon$ turbulence model in ANSYS CFX-4.4, given in Table 4.1, were retained in the simulations.

5.1.2 The $k_{\mathrm{f}}-\varepsilon_{\mathrm{f}}-k_{\mathrm{s}}-\varepsilon_{\mathrm{s}}-T_{\mathrm{s}}$ model

For the $k_{\mathrm{f}}-\varepsilon_{\mathrm{f}}-k_{\mathrm{s}}-\varepsilon_{\mathrm{s}}-T_{\mathrm{s}}$ model, the solids-phase is assumed to experience small- (T_{s} equation) and large-scale (k_{s} equation) fluctuations. For this model, the $k_{\mathrm{f}}-\varepsilon_{\mathrm{f}}-k_{\mathrm{s}}-\varepsilon_{\mathrm{s}}$ part is solved using the approach described in the preceding section. Since the small-scale solids-phase fluctuations are attributed to collisions at the particle scale, the effects are accounted for via the kinetic theory of granular flow. Thus, the solids-phase stress due to particle-particle collision is modelled using equation (4.66). In terms of the kinetic theory of granular flows (e.g. Lun et al., 1984), the relations for the solids-phase dynamic and bulk viscosities and pressure depend, among other parameters, on the granular temperature T_{s}, which must be computed.

Using the constitutive relations of Lun et al. (1984), the solids-phase dynamic viscosity is written as

$$\mu_{\mathrm{s}} = \mu_{\mathrm{s\,dil}}\left(g_1 + g_2\right), \tag{5.3}$$

where $\mu_{\mathrm{s\,dil}}$ is calculated from

$$\mu_{\mathrm{s\,dil}} = \frac{5\pi^{1/2}}{96} d_{\mathrm{p}} \rho_{\mathrm{s}} T_{\mathrm{s}}^{1/2}; \tag{5.4}$$

and g_1 and g_2 are given by

$$g_1 = \frac{1}{\eta\left(2-\eta\right) g_0}\left[1 + \frac{8}{5}\eta\left(3\eta - 2\right) c_{\mathrm{s}} g_0\right] \tag{5.5}$$

and

$$g_2 = \frac{8c_\mathrm{s}}{5\left(2-\eta\right)}\left[1+\frac{8}{5}\eta\left(3\eta-2\right)c_\mathrm{s}g_0\right]+\frac{768}{25\pi}\eta c_\mathrm{s}^2 g_0, \tag{5.6}$$

where

$$\eta = \frac{1}{2}(1+e). \tag{5.7}$$

The bulk viscosity is

$$\xi_\mathrm{s} = \frac{8}{3}c_\mathrm{s}\rho_\mathrm{s}d_\mathrm{p}g_0\eta\left(\frac{T_\mathrm{s}}{\pi}\right)^{1/2} \tag{5.8}$$

and the solids-phase pressure is given by

$$P_\mathrm{s} = c_\mathrm{s}\rho_\mathrm{s}T_\mathrm{s}\left[1+4c_\mathrm{s}g_0\eta\right]. \tag{5.9}$$

The modelled form of the transport equation for T_s obtained from the granular flow kinetic theory (Bolio et al., 1995; Lun et al., 1984) is

$$\frac{\partial}{\partial x_j}\left(c_\mathrm{s}\rho_\mathrm{s}U_{\mathrm{s}j}T_\mathrm{s}\right) = \frac{\partial}{\partial x_j}\left(\Gamma_{T_\mathrm{s}}\frac{\partial T_\mathrm{s}}{\partial x_j}\right) - 2\mathfrak{T}_{\mathrm{s}\,ij}\frac{\partial U_{si}}{\partial x_j} - \frac{2c_\mathrm{s}\rho_\mathrm{s}}{t_\mathrm{fs}}\left(3T_\mathrm{s}-\overline{u'_{\mathrm{f}k}u'_{\mathrm{s}k}}\right)+\gamma. \tag{5.10}$$

In equation (5.10), the diffusion coefficient Γ_{T_s} is given by

$$\Gamma_{T_\mathrm{s}} = \frac{25\pi^{1/2}}{128}d_\mathrm{p}\rho_\mathrm{s}T_\mathrm{s}^{1/2}\left(g_3+g_4\right), \tag{5.11}$$

where

$$g_3 = \frac{8}{\eta\left(41-33\eta\right)g_0}\left[1+\frac{12}{5}\eta^2\left(4\eta-3\right)c_\mathrm{s}g_0\right]; \tag{5.12}$$

and

$$g_4 = \frac{96}{5\left(41-33\eta\right)g_0}\left[1+\frac{12}{5}\eta^2\left(4\eta-3\right)c_\mathrm{s}g_0+\frac{16}{15\pi}\eta\left(41-33\eta\right)c_\mathrm{s}g_0\right]. \tag{5.13}$$

For the simulations results presented in this work, models for $\overline{u'_{\mathrm{f}k}u'_{\mathrm{s}k}}$ was not implemented. The dissipation of the solids kinetic energy via collision in equation (5.10) γ is expressed as

$$\gamma = \frac{12\left(1-e^2\right)g_0}{d_\mathrm{s}\sqrt{\pi}}c_\mathrm{s}\rho_\mathrm{s}T_\mathrm{s}. \tag{5.14}$$

The treatment of the additional transport equations are the same for the $k_{\mathrm{f}} - \varepsilon_{\mathrm{f}} - k_{\mathrm{s}} - \varepsilon_{\mathrm{s}}$ model.

5.1.3 The $k_{\mathrm{f}} - \varepsilon_{\mathrm{f}} - k_{\mathrm{s}} - k_{\mathrm{fs}}$ model

For this model, the fluid-phase transport equations for the $k_{\mathrm{f}} - \varepsilon_{\mathrm{f}}$ model as given by equations (4.82) and (4.83) are solved. For the solids-phase, a two-equation type model represented here as the $k_{\mathrm{s}} - k_{\mathrm{fs}}$ model is soled to compute the constitutive relation for the stress tensor. The model investigated here is that proposed by Peirano and Leckner (1998). The solids-phase stress tensor for this case is similar to that given by equation (5.1) but the effective solids-phase viscosity is treated as a sum of collisional and kinetic contributions. It should be noted that in some studies, the kinetic part of the solids-phase viscosity is referred to as either streaming (e.g, van Wachem et al., 2001) or turbulent (e.g, Peirano and Leckner, 1998) viscosity. Thus, we have

$$\mu_{\mathrm{s}} = \mu_{\mathrm{sc}} + \mu_{\mathrm{st}}, \tag{5.15}$$

where the expressions for the collisional and turbulent viscosity are

$$\mu_{\mathrm{sc}} = \frac{8}{5} c_{\mathrm{s}} \rho_{\mathrm{s}} g_0 \eta \left(\mu_{\mathrm{st}} + d_{\mathrm{s}} \sqrt{\frac{2k_{\mathrm{s}}}{3\pi}} \right), \tag{5.16}$$

and

$$\mu_{\mathrm{st}} = \frac{2}{3} \rho_{\mathrm{s}} \left[\frac{t_{\mathrm{fs}}}{t_p} k_{\mathrm{fs}} + \left(1 + c_{\mathrm{s}} g_0 \mathfrak{A}\right) k_{\mathrm{s}} \right] \left[\frac{2}{t_p} + \frac{\mathfrak{B}}{t_c} \right]^{-1}. \tag{5.17}$$

The parameters $\mathfrak{A}$ and $\mathfrak{B}$ are given by

$$\mathfrak{A} = \frac{2}{5}\left(1+e\right)\left(3e-1\right) \quad \text{and} \quad \mathfrak{B} = \frac{1}{5}\left(1+e\right)\left(3-e\right). \tag{5.18}$$

and t_{fs} is defined by equation (4.61). The quantity t_{c} is the inter-particle collision time defined as

$$t_{\mathrm{c}} = \frac{\pi^{1/2}}{24 c_{\mathrm{s}} g_{\mathrm{o}}} d_{\mathrm{p}} \left(\frac{3}{2k_{\mathrm{s}}} \right)^{1/2}. \tag{5.19}$$

Note that in the above formulation, the isotropic relation between the granular temperature and the solids-phase turbulence kinetic energy introduced in Chapter 4 is assumed. The

bulk viscosity and the solids pressure are given by equations (5.8) and (5.9), respectively.

Clearly, the solids-phase stress depends on the turbulence kinetic energy k_s of the solids-phase and k_fs. Therefore, transport equations for k_s and k_fs are required. The modelled equation for k_s is

$$\frac{\partial}{\partial x_j}\left(c_\mathrm{s}\rho_\mathrm{s}U_{\mathrm{s}j}k_\mathrm{s}\right) = \frac{\partial}{\partial x_j}\left[c_\mathrm{s}\left(\mathfrak{K}_\mathrm{sc}+\mathfrak{K}_\mathrm{st}\right)\frac{\partial k_\mathrm{s}}{\partial x_j}\right] - \mathfrak{T}_{\mathrm{s}\,ij}\frac{\partial U_{\mathrm{s}i}}{\partial x_j} - \frac{2c_\mathrm{s}\rho_\mathrm{s}}{t_\mathrm{fs}}\left(2k_\mathrm{s}-k_\mathrm{fs}\right) - c_\mathrm{s}\rho_\mathrm{s}\frac{1-e^2}{3t_\mathrm{c}}k_\mathrm{s}, \tag{5.20}$$

where $\mathfrak{K}_\mathrm{sc}$ and $\mathfrak{K}_\mathrm{st}$ are the collisional and kinetic diffusivities, respectively. The collisional diffusivity is given by

$$\mathfrak{K}_\mathrm{sc} = c_\mathrm{s}g_0(1+e)\left(\frac{6}{5}\mathfrak{K}_\mathrm{st}+\frac{4}{3}d_\mathrm{p}\sqrt{\frac{2k_\mathrm{s}}{3\pi}}\right) \tag{5.21}$$

and the kinetic diffusivity is defined by

$$\mathfrak{K}_\mathrm{st} = \left[\frac{3}{5}\frac{t_\mathrm{fs}}{t_p}k_\mathrm{fs}+\frac{2}{3}\left(1+c_\mathrm{s}g_0\mathfrak{C}\right)k_\mathrm{s}\right]\left[\frac{9}{5t_p}+\frac{\mathfrak{D}}{t_c}\right]^{-1}, \tag{5.22}$$

where $\mathfrak{C} = 3(1+e)^2(2e-1)/5$ and $\mathfrak{D} = (1+e)(49-33e)/100$. The closed form of the transport equation for k_fs (Enwald et al., 1996) is

$$\frac{\partial}{\partial x_j}\left(c_\mathrm{s}\rho_\mathrm{s}U_{\mathrm{s}j}k_\mathrm{fs}\right) = \frac{\partial}{\partial x_j}\left(c_\mathrm{s}\frac{\mu_{k_\mathrm{fs}}}{\sigma_{k_\mathrm{fs}}}\frac{\partial k_\mathrm{fs}}{\partial x_j}\right) - c_\mathrm{s}\rho_\mathrm{s}\overline{u''_{\mathrm{f}i}u'_{\mathrm{s}j}}\frac{\partial U_{\mathrm{s}i}}{\partial x_j} - c_\mathrm{s}\rho_\mathrm{s}\overline{u''_{\mathrm{f}j}u'_{\mathrm{s}i}}\frac{\partial U_{\mathrm{f}i}}{\partial x_j} - \frac{c_\mathrm{s}\rho_\mathrm{s}}{t_\mathrm{p}}\left[\left(1+S_{c\rho}\right)k_\mathrm{fs}-2k_\mathrm{f}-2S_{c\rho}k_\mathrm{s}\right] - c_\mathrm{s}\rho_\mathrm{s}\frac{k_\mathrm{fs}}{t_\mathrm{fs}}. \tag{5.23}$$

In equation (5.23), $\mu_{k_\mathrm{fs}} = \rho_\mathrm{s}k_\mathrm{fs}t_\mathrm{fs}/3$ is known as the fluid-solids turbulent viscosity; $S_{c\rho} = c_\mathrm{s}\rho_\mathrm{s}/c_\mathrm{f}\rho_\mathrm{f}$ is referred to here as the phasic-weighted density ratio; and $\overline{u''_{\mathrm{f}j}u'_{\mathrm{s}i}}$ is the fluid-solids velocity correlation tensor modelled using the eddy viscosity assumption:

$$-\rho_\mathrm{s}\overline{u''_{\mathrm{f}i}u'_{\mathrm{s}j}} = \mu_{k_\mathrm{fs}}\left(S_{\mathrm{fs}ij}-\frac{1}{3}S_{\mathrm{fs}ij}\delta_{ij}\right) - \frac{1}{3}k_\mathrm{fs}\delta_{ij}. \tag{5.24}$$

In the correlation $\overline{u''_{\mathrm{f}i}u'_{\mathrm{s}j}}$, $u''_{\mathrm{f}i}$ is defined as the fluctuating velocity of the liquid phase seen by the particles (Peirano and Leckner, 1998). Recall also that $u'_{\mathrm{s}j}$ is the solids-phase velocity fluctuation. The fluid-solids strain rate tensor is defined by

$$S_{\mathrm{fs}ij} = \frac{\partial U_{\mathrm{f}i}}{\partial x_j} + \frac{\partial U_{\mathrm{s}j}}{\partial x_i}. \tag{5.25}$$

5.1.4 Boundary Conditions

Uniform profiles were used at the inlet for the solids-phase velocity and concentration. The level of these quantities was set to the mean values reported in the experimental study of Sumner et al. (1990). Details of the data of Sumner et al. (1990) are summarized in Section 5.1.5.1. There were no measurements for the liquid-phase velocity so its value was set by assuming no slip between the phases at the inlet. The inlet concentration for the liquid was specified using the constraint in equation (1.3). Fully developed flow is assumed at the outlet of the pipe. The flow was treated as axi-symmetric and a symmetric boundary condition was specified at the axis of the pipe. For the $k_{\mathrm{f}} - \varepsilon_{\mathrm{f}} - k_{\mathrm{s}} - \varepsilon_{\mathrm{s}}$ model, a no-slip boundary condition using the wall function formulation presented in Section 4.5.1 was imposed at the wall for the liquid-phase, while a free slip condition was specified for the solids-phase. For simulations using the $k_{\mathrm{f}} - \varepsilon_{\mathrm{f}} - k_{\mathrm{s}} - \varepsilon_{\mathrm{s}} - T_{\mathrm{s}}$ and $k_{\mathrm{f}} - \varepsilon_{\mathrm{f}} - k_{\mathrm{s}} - k_{\mathrm{fs}}$ models, the wall function formulation was also applied for the liquid-phase and equations (4.92) and (4.93) were implemented for the solids-phase velocity and granular temperature, respectively.

5.1.5 Numerical Simulations

Steady-state simulations for upward flow of water-sand particle mixtures in a 0.04 m diameter vertical pipe were performed using a two dimensional grid in CFX-4.4. A pipe length of 4.0 m was considered. After a series of preliminary simulations, a grid system consisting of 50 $\times$ 40 control volumes distributed uniformly in the axial direction and non-uniformly in the radial direction was found to be sufficient to obtain a grid-independent solution (see Section 5.1.6.1). In addition to the boundary conditions, equations (2.29) and (2.31) and the models discussed in sections 5.1.2 and 5.1.3 were implemented via user-Fortran rou-

tines. While implementation of user-routines in CFX-4.4 is sometimes straightforward, the case of physical model testing requires a detailed knowledge of how the code works. For example, in some cases, the user-routines have to be bounded to avoid divergence. Often the user, not the developer, is essentially working with a *black box*. A sample command file is provided in Appendix E. The simulation was considered converged when the normalized residuals were reduced to a value of 10^{-4}. Typical CPU time for the calculations on a PC at 2.66 GHz was about 3.3×10^3 s for the $k_\mathrm{f} - \varepsilon_\mathrm{f} - k_\mathrm{s} - \varepsilon_\mathrm{s}$ model simulations, 3.2×10^4 s for those with the $k_\mathrm{f} - \varepsilon_\mathrm{f} - k_\mathrm{s} - \varepsilon_\mathrm{s} - T_\mathrm{s}$ model, and 3.04×10^4 s for those with the $k_\mathrm{f} - \varepsilon_\mathrm{f} - k_\mathrm{s} - k_\mathrm{fs}$ model.

5.1.5.1 Experimental data used for comparison

The numerical simulations were performed and completed prior to performing the experimental work presented in Chapter 3. Therefore, the numerical results discussed herein were compared with previous experimental results. Sumner et al. (1990), measured solids-phase concentration and velocity distributions in turbulent upward flow of slurries in vertical pipes using an L-shaped conductivity probe. A similar probe built into the wall was used to obtain the concentration and solids-phase velocity at the wall. The experiments were conducted in two vertical loops with pipes of diameters $D = 0.025$ m and 0.04 m using two types of particles, plastic and sand. Two sizes of plastic particles were used and four sizes were considered for the sand. The mean concentration ranged between 10% and 50% by volume. Axial velocities in the range of 3-7 m/s and 2-4 m/s were attained in the 0.025 m and 0.04 m pipes, respectively. For these measurements, Sumner (1992) reported an error of 1.5%, which increased with increasing particle diameter, when the mean of the solids-phase velocity distribution was compared with the bulk velocity measured by the magnetic flow meter. The error in particle concentration was found to be $\pm 2.5\%$ for particle diameters smaller than the sensor electrode spacing. The distance between the pair of sensor electrodes was 10 mm and the measurement domain of each pair was reported to be about 1 mm. For particles larger than the electrode spacing, $\pm 5\%$ precision was reported.

The experimental conditions chosen for the present simulations are shown in Table 5.1.

Table 5.1: Properties of liquid and solids-phase, flow conditions and CFX-4.4 model parameters/constants.

Description	Symbol	Value
Constituent properties		
fluid density	ρ_{f}	998 kgm^{-3}
fluid viscosity	μ_{f}	10^{-3} Pa·s
solids density	ρ_{s}	2650 kgm^{-3}
solids viscosity	μ_{s}	10^{-8}, 0.25 Pa·s and model
particle diameter	d_{p}	0.47, 1.7 mm
Inlet conditions		
mean velocity of fluid	U_{f}	$2.6 \sim 2.8$ ms^{-1}
volume fraction of fluid	$(1 - C_{\mathrm{s}})$	$0.722 < (1 - C_{\mathrm{s}}) < 0.915$
turbulence intensity	TI	0.1
turbulence kinetic energy of fluid	k_{f}	$3(U_{\mathrm{f}}TI)^2/2$
dissipation rate of fluid	ε_{f}	$0.09^{3/4}k_{\mathrm{f}}^{3/2}/(0.007d_{\mathrm{p}})$
mean velocity of solids	U_{s}	$2.6 \sim 2.8$ ms^{-1}
volume fraction of solids	C_{s}	$0.085 < C_{\mathrm{s}} < 0.278$
turbulence kinetic energy of solids	k_{s}	$3(U_{\mathrm{s}}TI)^2/2$
dissipation rate of solids	ε_{s}	$0.09^{3/4}k_{\mathrm{s}}^{3/2}/(0.007d_{\mathrm{p}})$
granular temperature	T_{s}	$3k_{\mathrm{s}}/2$

Also shown in Table 5.1 are values of the constant solids viscosity investigated for the case of the $k_f - \varepsilon_f - k_s - \varepsilon_s$ model. The value of C_s is the bulk concentration of the solids-phase reported in the experimental studies. The simulation matrix shown in Table 5.2 identifies the specific experimental data chosen for the simulations. In the present study, attention is focus on modelling issues, hence only a few select test cases are considered. A detailed parametric investigation of constant solids viscosity using baseline models in CFX-4.4 can be found in Krampa-Morlu et al. (2004). The use of the constant solids viscosity produced mixed results. Extension of the best model to a wider range of flow conditions is deferred to future studies.

Table 5.2: Simulation matrix

Run	Particle diameter d_p (μm)	Solids bulk conc. C_s (%)	Solids mean velocity U_{sav} (m/s)
1	470	8.7	2.6
2	470	27.8	2.6
3	1700	8.5	2.8
4	1700	17.7	2.8

5.1.6 Simulation Results and Discussion

5.1.6.1 Single-phase flow

Preliminary simulations of single-phase flow for a range of Reynolds numbers between $Re_D \approx 4.0 \times 10^4$ and 2.0×10^5 based on the mean velocity and pipe diameter were performed to test implementation of the code and verify the numerical grid. The predicted velocity U, at the end of the pipe, plotted against distance from the wall normalized by the pipe radius R is shown in Figure 5.1a. Using grids of 20, 40, and 60 control volumes (CV) non-uniformly distributed in the wall-normal direction, one can see that the results are similar, particularly for 40 CV and 60 CV. However, compared to the 1/7-power law velocity profile, the calculated velocities are higher in the middle part of the half pipe.

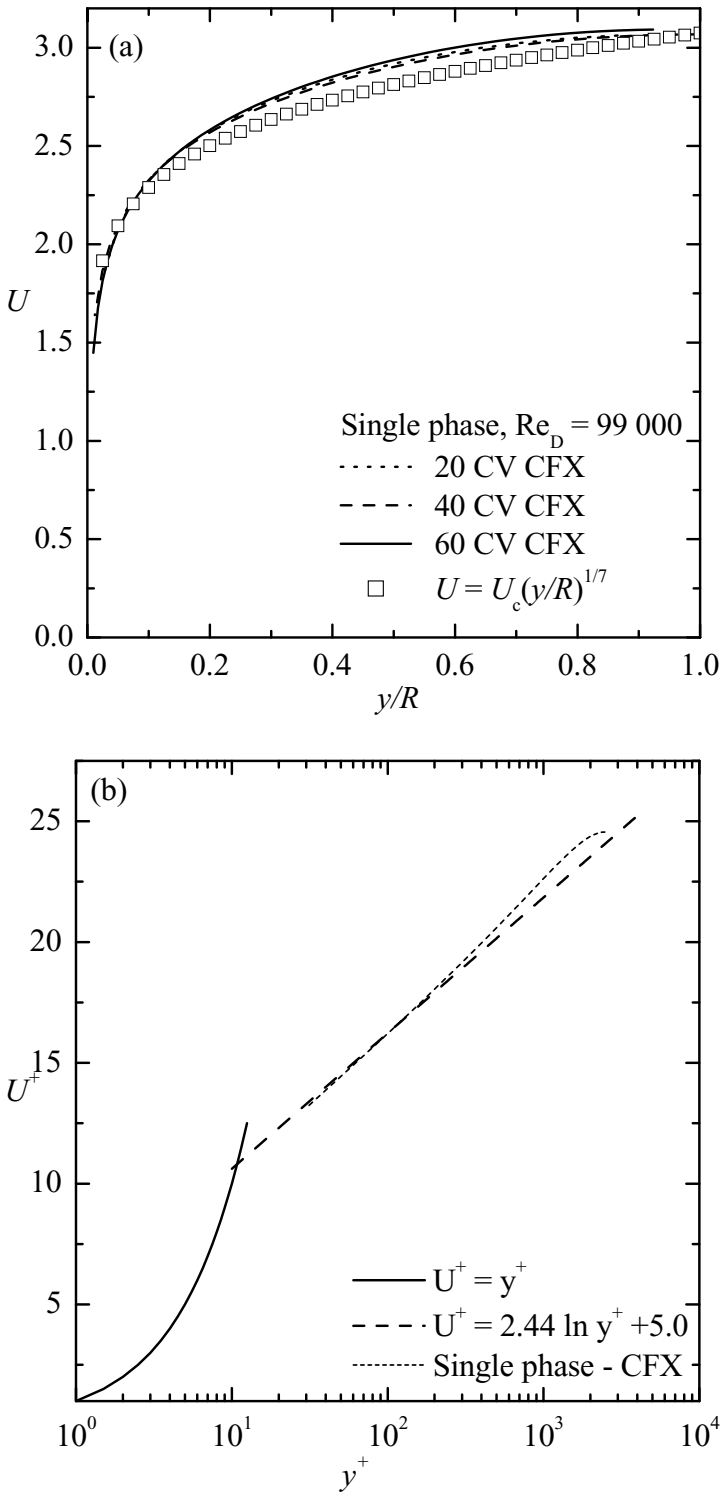

Figure 5.1: Velocity predictions in outer and inner coordinates for single-phase pipe flow: (a) Outer coordinates and (b) Inner coordinates.

The velocity profile in inner coordinates matched the log-law as expected in Figure 5.1b using the 40 CV grid. The first grid point in Figure 5.1b is located at $y^+(= yu_\tau/\nu) \approx 30$. For smooth wall conditions, the predicted friction factors were within approximately 3% of those given by the Churchill (1977) equation and are in good agreement with Prandtl's equation as shown in Figure 5.2. This indicates that the grid is appropriate for the range of Reynolds numbers considered.

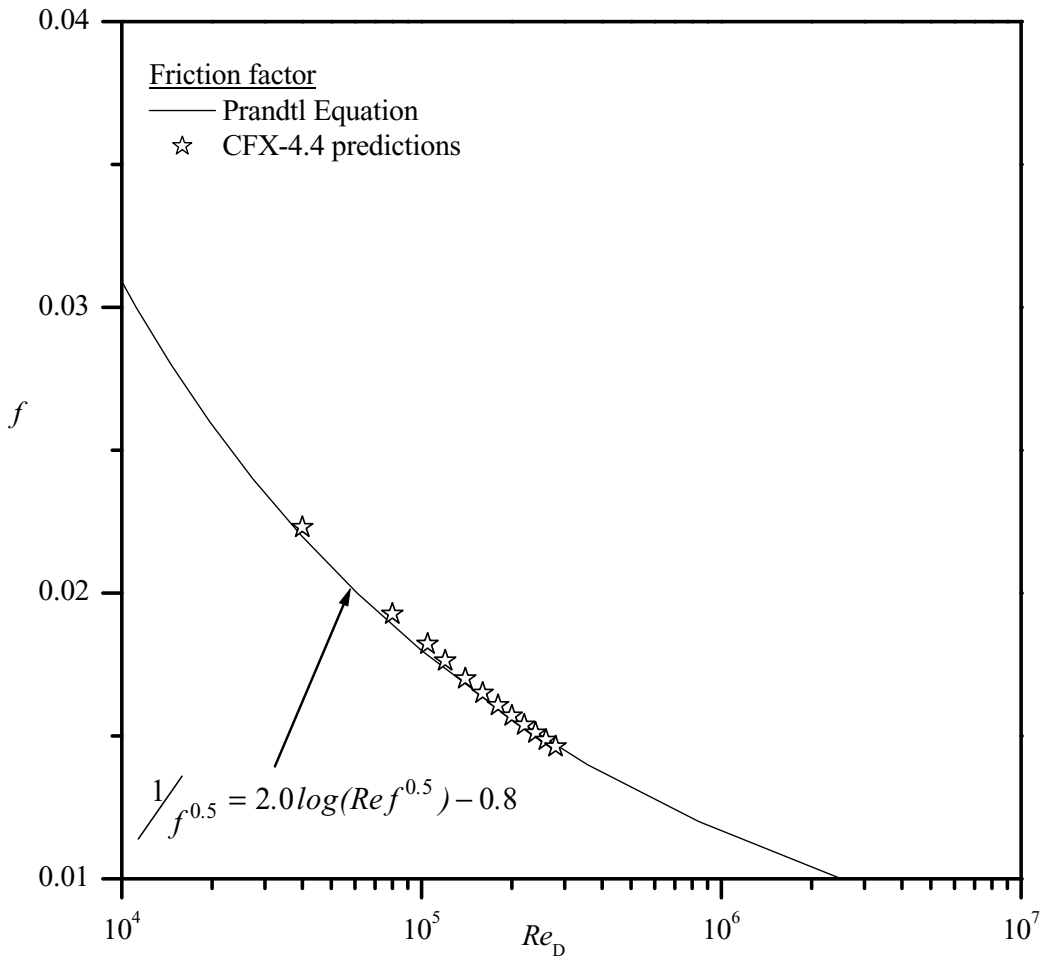

Figure 5.2: Friction factor prediction for water in upward vertical smooth pipe flow. Comparison between correlation, experimental data, and predictions

5.1.6.2 Solids-phase velocity and concentration distributions

In this section, the predicted results for the solids-phase velocity and solids concentration are discussed for the models presented above. For the case of the $k_{\mathrm{f}} - \varepsilon_{\mathrm{f}} - k_{\mathrm{s}} - \varepsilon_{\mathrm{s}}$ model, the two values of constant solids viscosity in Table 5.1 were investigated for the flows with the 470 μm particles.

Flow with 470 μm diameter particles

Figure 5.3 shows the numerical results for the 470 μm particles at a mean concentration of approximately 8.7%, which corresponds to **Run 1** in Table 5.2. Overall, the predicted solids-phase velocity profiles shown in Figure 5.3a compare well to the experimental data. As shown in Figure 5.3b, the solids-phase velocity predicted with the lower solids viscosity trends toward the measured data point near the wall, whereas the velocity calculated with the higher solids viscosity remains higher near the wall of the pipe. Similar effects of the solids viscosity were observed for the other conditions in Table 5.2. The solids-phase velocity was slightly under-predicted for the case of the $k_{\mathrm{f}} - \varepsilon_{\mathrm{f}} - k_{\mathrm{s}} - \varepsilon_{\mathrm{s}}$ model with $\mu_{\mathrm{s}} = 0.25$ Pa·s in the core region. The solids-phase velocity predictions by the $k_{\mathrm{f}} - \varepsilon_{\mathrm{f}} - k_{\mathrm{s}} - \varepsilon_{\mathrm{s}} - T_{\mathrm{s}}$ and the $k_{\mathrm{f}} - \varepsilon_{\mathrm{f}} - k_{\mathrm{s}} - k_{\mathrm{fs}}$ models lie between those predicted by the $k_{\mathrm{f}} - \varepsilon_{\mathrm{f}} - k_{\mathrm{s}} - \varepsilon_{\mathrm{s}}$ model using two values of the solids-phase viscosity in the core of the pipe. Both of these models also produced a higher value of the solids velocity close to the wall. The solids-phase velocity results shown in Figure 5.3 indicate the importance of the closure for the solids stress tensor. There is a clear, and small distinction between the predictions using a constant particle viscosity and those for which the kinetic theory of granular flow was employed. This is also observed in the other flow conditions presented below.

Figure 5.4 compares the predictions and the experimental data for the concentration distribution for **Run 1**. Overall, Figure 5.4a shows that the concentration profiles compare fairly well with the experimental data for $y/R \geq 0.2$. The concentration prediction close to the wall is re-plotted in Figure 5.4b. Except for the $k_{\mathrm{f}} - \varepsilon_{\mathrm{f}} - k_{\mathrm{s}} - \varepsilon_{\mathrm{s}}$ model using $\mu_{\mathrm{s}} = 10^{-8}$ Pa·s, the predicted profiles exhibit an overshoot near the wall and then become

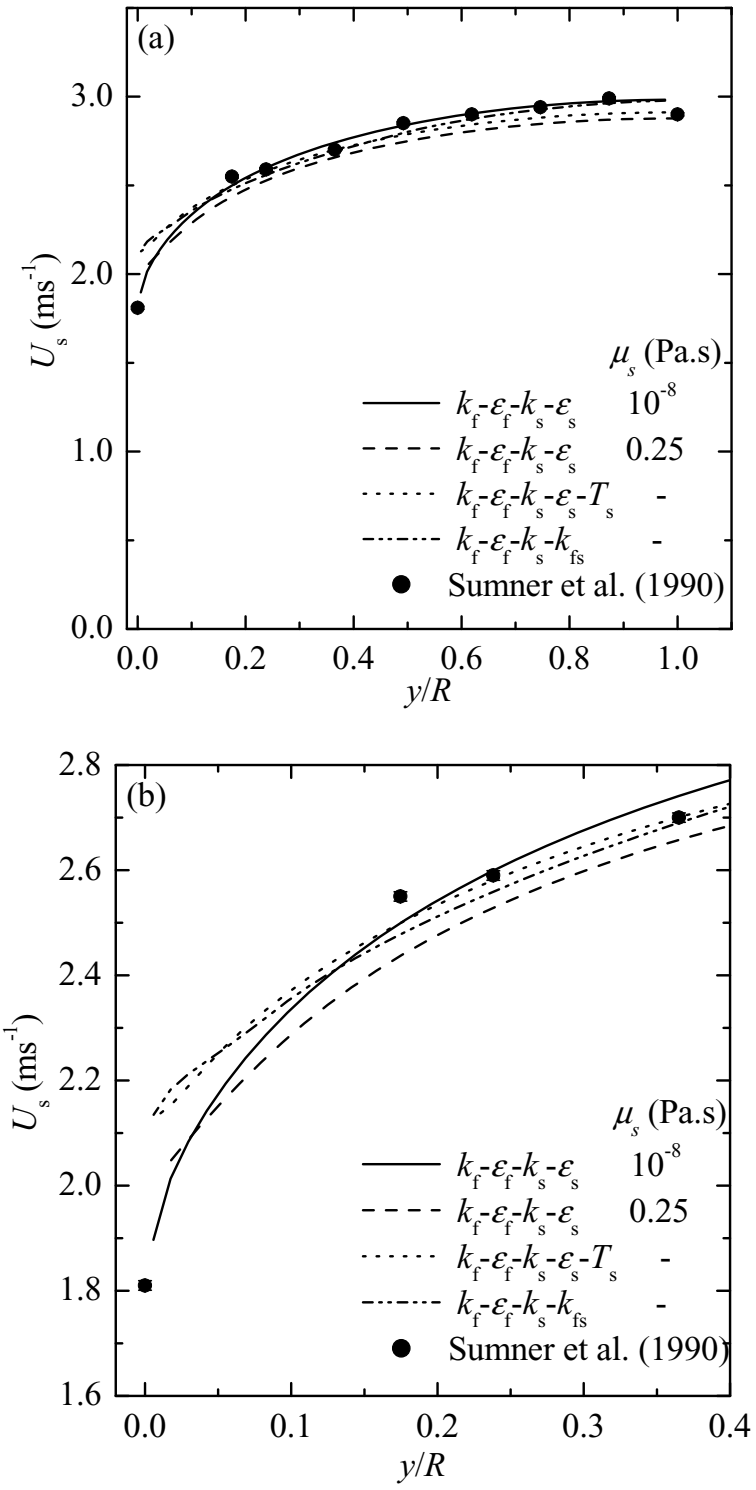

Figure 5.3: Comparison of predicted and measured particle velocities for $d_{\mathrm{p}} = 470$ μm particles at $C_{\mathrm{s}} = 8.7\%$ (**Run 1**): (a) cross-section profile, and (b) near-wall solids-phase velocity distribution.

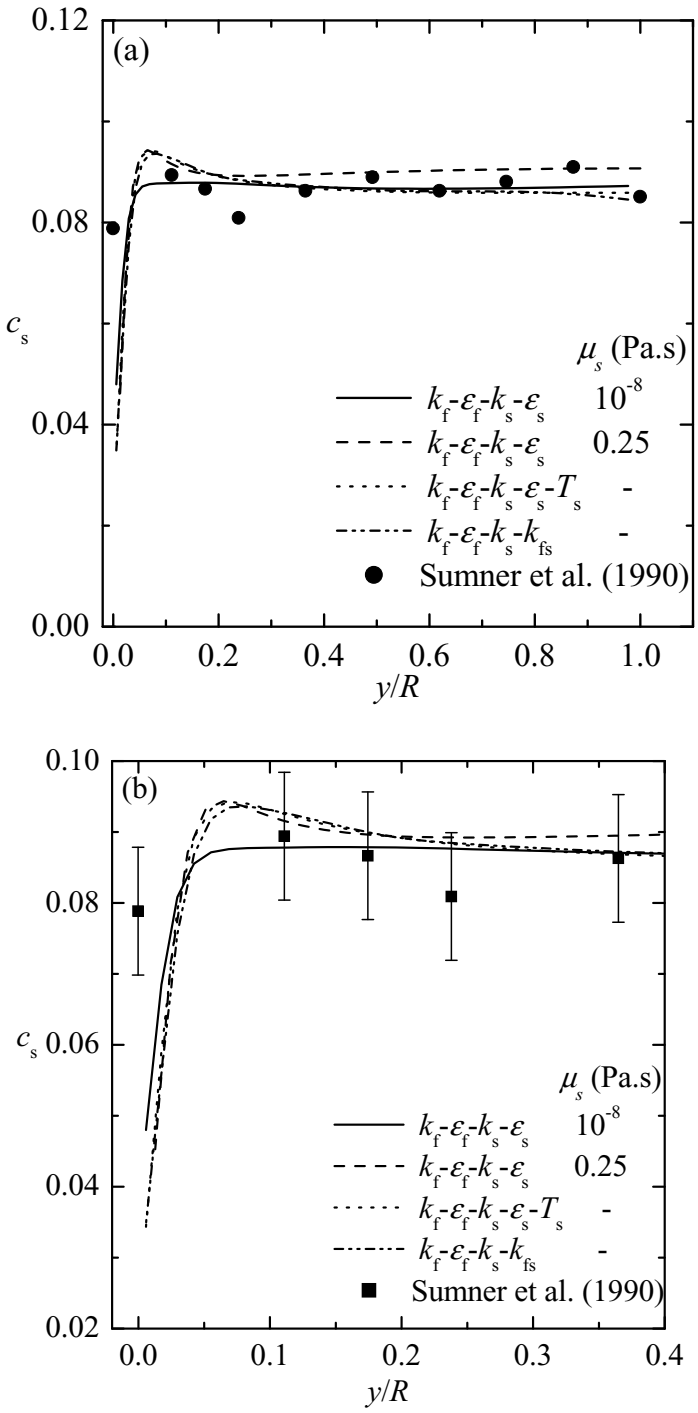

Figure 5.4: Comparison of predicted and measured solids-phase concentration for $d_{\mathrm{p}} = 470$ μm particles at $C_{\mathrm{s}} = 8.7\%$ (**Run 1**): (a) cross-section profile and (b) near-wall solids-phase concentration distribution.

relatively flat over most of the pipe cross-section. The $k_f - \varepsilon_f - k_s - \varepsilon_s$ model with $\mu_s = 10^{-8}$ Pa·s predicted a higher particle concentration very close to the wall than the other models. However, the concentration predicted at the wall by all models is much less than that measured at the wall.

The predicted results for **Run 2** (i.e. particles with $d_p = 470$ μm and $C_s = 27.8\%$) are compared to the experimental data in Figure 5.5. The shapes of the velocity profiles shown in Figure 5.5a are similar to those in Figure 5.3a. The profile obtained using the $k_f - \varepsilon_f - k_s - \varepsilon_s$ model with $\mu_s = 10^{-8}$ Pa·s nearly matches the experimental data across the entire pipe cross-section. The solids-phase velocity was slightly under-predicted by the $k_f - \varepsilon_f - k_s - \varepsilon_s$ model with $\mu_s = 0.25$ Pa·s and the $k_f - \varepsilon_f - k_s - \varepsilon_s - T_s$ model in the core region; both of these models actually produced identical velocities for $y/R \geq 0.2$. At the wall, the velocity predicted by the models, with the exception of the $k_f - \varepsilon_f - k_s - \varepsilon_s$ model with $\mu_s = 10^{-8}$ Pa·s, was clearly higher than the experimental data.

The concentration profiles for **Run 2** are given in Figure 5.5b. For the predicted profiles, the trends are similar to those observed in Figure 5.4a except that the overshoots close to the wall are more pronounced. In general, the predicted profiles are almost uniform for most of the pipe cross-section, whereas the experimental data, apart from the near-wall region, exhibited a steady, albeit slight, decrease in concentration moving from the wall to the pipe centreline.

Flow with 1700 μm diameter particles

The numerical results for the 1700 μm particles for **Run 3** (i.e. particles with $d_p = 1700$ μm and $C_s = 8.5\%$) are shown in Figure 5.6. For this case, only predictions by the $k_f - \varepsilon_f - k_s - \varepsilon_s$ model with $\mu_s = 10^{-8}$ Pa·s, $k_f - \varepsilon_f - k_s - \varepsilon_s - T_s$, and the $k_f - \varepsilon_f - k_s - k_{fs}$ models are discussed. For the larger particles, both the predicted and experimental velocity profiles are flatter. However, the predicted velocity profiles exhibit distinctly more curvature than the experimental profile, with the largest deviation towards the centreline of the pipe. It is interesting to note that the present observation is opposite to that made

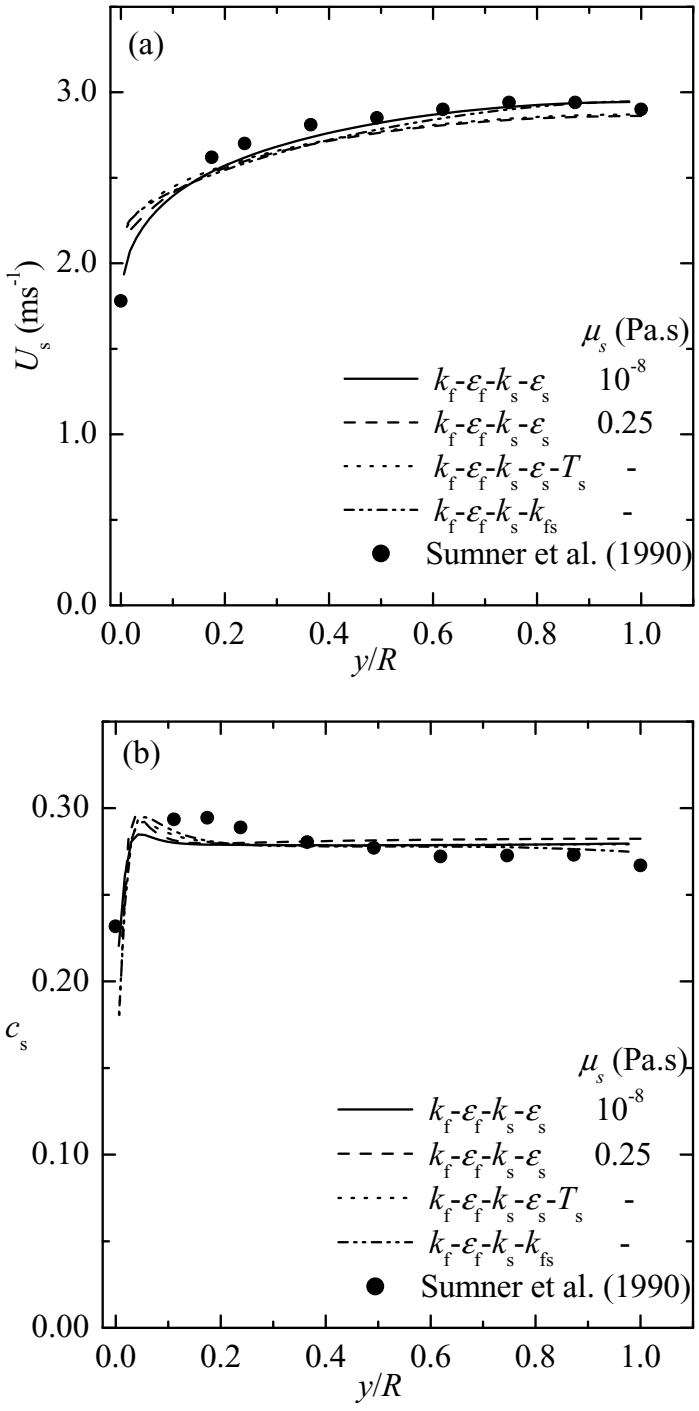

Figure 5.5: Comparison of predicted and measured results for $d_{\mathrm{p}} = 470$ μm particles at $C_{\mathrm{s}} = 27.8\%$ (**Run 2**): (a) solids-phase velocity and (b) particle concentration.

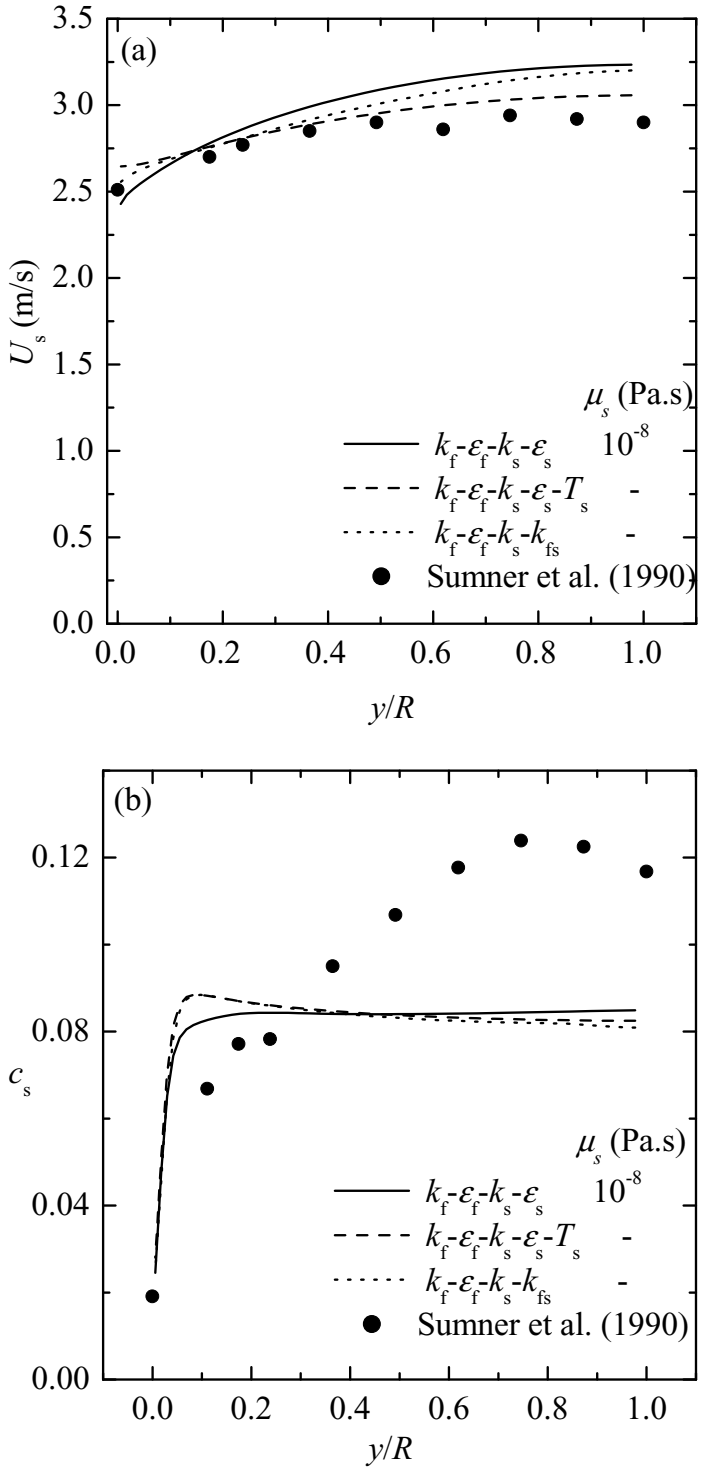

Figure 5.6: Comparison of predicted and measured results for $d_{\mathrm{p}} = 1700$ μm particles at $C_{\mathrm{s}} = 8.5\%$ (**Run 3**): (a) solids-phase velocity and (b) particle concentration.

by Krampa-Morlu et al. (2004) when default software settings were chosen. Close to the wall, the predicted velocity almost matches the measured velocity for the $k_{\mathrm{f}} - \varepsilon_{\mathrm{f}} - k_{\mathrm{s}} - k_{\mathrm{fs}}$ model. The solids-phase velocity in the region close the wall is slightly under-predicted by the $k_{\mathrm{f}} - \varepsilon_{\mathrm{f}} - k_{\mathrm{s}} - \varepsilon_{\mathrm{s}}$ model and the $k_{\mathrm{f}} - \varepsilon_{\mathrm{f}} - k_{\mathrm{s}} - \varepsilon_{\mathrm{s}} - T_{\mathrm{s}}$ model produced a higher value. Away from the wall and for $y/R \geq 0.2$, the $k_{\mathrm{f}} - \varepsilon_{\mathrm{f}} - k_{\mathrm{s}} - \varepsilon_{\mathrm{s}} - T_{\mathrm{s}}$ produced less deviation compared to the other two models.

In Figure 5.6b, the predicted particle concentration profiles are significantly different than the measured profile. The discrepancy between the measured and predicted concentrations is most pronounced in the core region of the pipe. The predicted profiles are flat in the core region, and also show a sharper transition to the wall value than the experimental profile. The overshoot in the predicted profiles near the wall is less pronounced compared to those observed for the smaller particles in Figure 5.4.

The results for **Run 4** (i.e. particles with $d_{\mathrm{p}} = 1700$ μm and $C_{\mathrm{s}} = 17.7\%$) are shown in Figure 5.7. For the larger particles, the profiles are flat for the liquid-solid flow at 17.7% solids bulk concentration as discussed for Figure 5.6a. Except for the $k_{\mathrm{f}} - \varepsilon_{\mathrm{f}} - k_{\mathrm{s}} - \varepsilon_{\mathrm{s}} - T_{\mathrm{s}}$ and $k_{\mathrm{f}} - \varepsilon_{\mathrm{f}} - k_{\mathrm{s}} - \varepsilon_{\mathrm{s}} - k_{\mathrm{fs}}$ models, which performed well in the region $y/R \leq 0.2$, the predicted solids-phase velocity profiles did not closely follow the experimental data. In Figure 5.7b, the predictions for the concentration profiles are similar to those in Figure 5.6b for a mean concentration of 8.5%. Again, there is a significant discrepancy between the predictions and experimental result. The strong variation in concentration across the pipe observed for the larger particles is simply not captured by the predicted profiles.

5.1.6.3 Turbulence kinetic energy and viscosity distributions

The predictions for the velocity and concentration profiles depend on the closure models used. In the present study, only closure models for the solids-phase stress tensor are investigated. Since experimental data is limited to the mean flow fields of solids velocity and concentration (those for the turbulence field are not available for the slurry flows), only the model predictions of the turbulence kinetic energy and the eddy viscosity are presented.

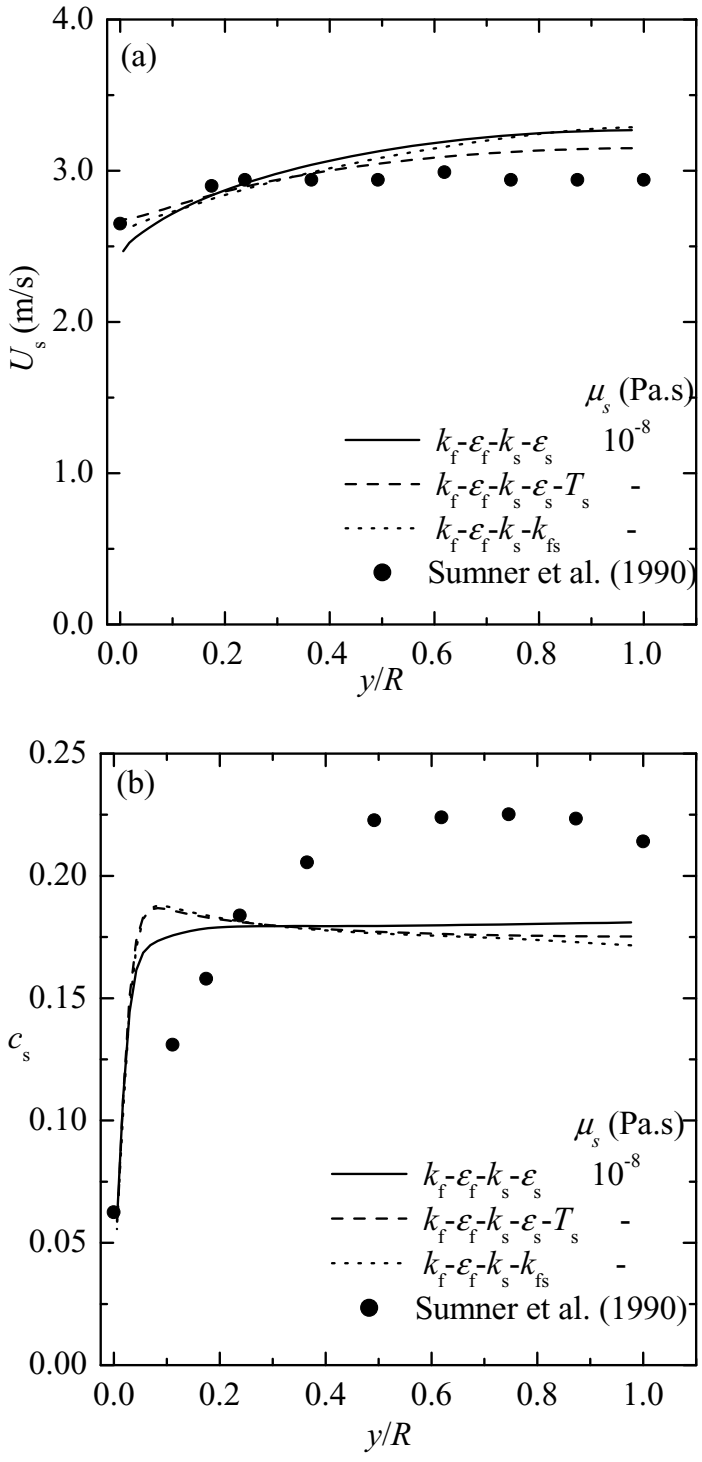

Figure 5.7: Comparison of predicted and measured results for $d_{\mathrm{p}} = 1700$ μm particles at $C_{\mathrm{s}} = 17.7\%$ (**Run 4**): (a) solids-phase velocity and (b) particle concentration.

The predicted results for the turbulence kinetic energy and eddy viscosity are shown in Figures 5.8 through 5.10.

Flow with 470 μm diameter particles

Figure 5.8 shows the predicted radial distributions of the turbulence kinetic energy for single-phase water flow (k), and for the water-sand flow (k_{f}), as well as the solids-phase turbulence kinetic energy (k_{s}) for **Run 1**. Figures 5.8a, 5.8b, and 5.8c show the predictions for the $k_{\mathrm{f}} - \varepsilon_{\mathrm{f}} - k_{\mathrm{s}} - \varepsilon_{\mathrm{s}}$, $k_{\mathrm{f}} - \varepsilon_{\mathrm{f}} - k_{\mathrm{s}} - \varepsilon_{\mathrm{s}} - T_{\mathrm{s}}$, and $k_{\mathrm{f}} - \varepsilon_{\mathrm{f}} - k_{\mathrm{s}} - k_{\mathrm{fs}}$ models, respectively. The k profile for the single-phase flow attains a peak value very near the wall, and then drops gradually toward the axis of the pipe which is prototypical of turbulence in a wall-bounded flow. In Figure 5.8a, the k_{f} profile calculated using the $k_{\mathrm{f}} - \varepsilon_{\mathrm{f}} - k_{\mathrm{s}} - \varepsilon_{\mathrm{s}}$ model is similar to the single-phase profile, except that it drops more sharply near the wall. The value of k_{f} for the slurry is generally lower than k for the single-phase flow, indicating the attenuation of turbulence in the liquid. For the solids-phase, k_s shows a relatively smooth profile which increases from almost zero at the wall to a peak value located at $y/R \approx 0.1$, away from the wall. In Figure 5.8b, the calculated k_{f} profile by the $k_{\mathrm{f}} - \varepsilon_{\mathrm{f}} - k_{\mathrm{s}} - \varepsilon_{\mathrm{s}} - T_{\mathrm{s}}$ model is much lower compared to Figure 5.8a. The solids-phase turbulence kinetic energy in this case exhibits a more gentle slope close to the wall and peaks at a higher value (about 30% higher than in Figure 5.8a). The peak value is also further away from the wall when compared with the k_{s} profile in Figure 5.8a.

Towards the centre of the pipe, the value of k_{s} is significantly higher relative to that predicted by the $k_{\mathrm{f}} - \varepsilon_{\mathrm{f}} - k_{\mathrm{s}} - \varepsilon_{\mathrm{s}}$ model. Note that, in the present study, no turbulence modulation model was introduced in the $k_{\mathrm{f}} - \varepsilon_{\mathrm{f}} - k_{\mathrm{s}} - \varepsilon_{\mathrm{s}}$ and $k_{\mathrm{f}} - \varepsilon_{\mathrm{f}} - k_{\mathrm{s}} - \varepsilon_{\mathrm{s}} - T_{\mathrm{s}}$ models and, therefore, no additional source or sink terms are present in the phasic turbulent transport equations. Calculations with the $k_{\mathrm{f}} - \varepsilon_{\mathrm{f}} - k_{\mathrm{s}} - \varepsilon_{\mathrm{s}}$ model use a constant solids-phase laminar viscosity, whereas in the case of the $k_{\mathrm{f}} - \varepsilon_{\mathrm{f}} - k_{\mathrm{s}} - \varepsilon_{\mathrm{s}} - T_{\mathrm{s}}$ model, the solids-phase laminar viscosity is modelled from the kinetic theory of granular flows with the constitutive equations given by equations (5.3) to (5.6).

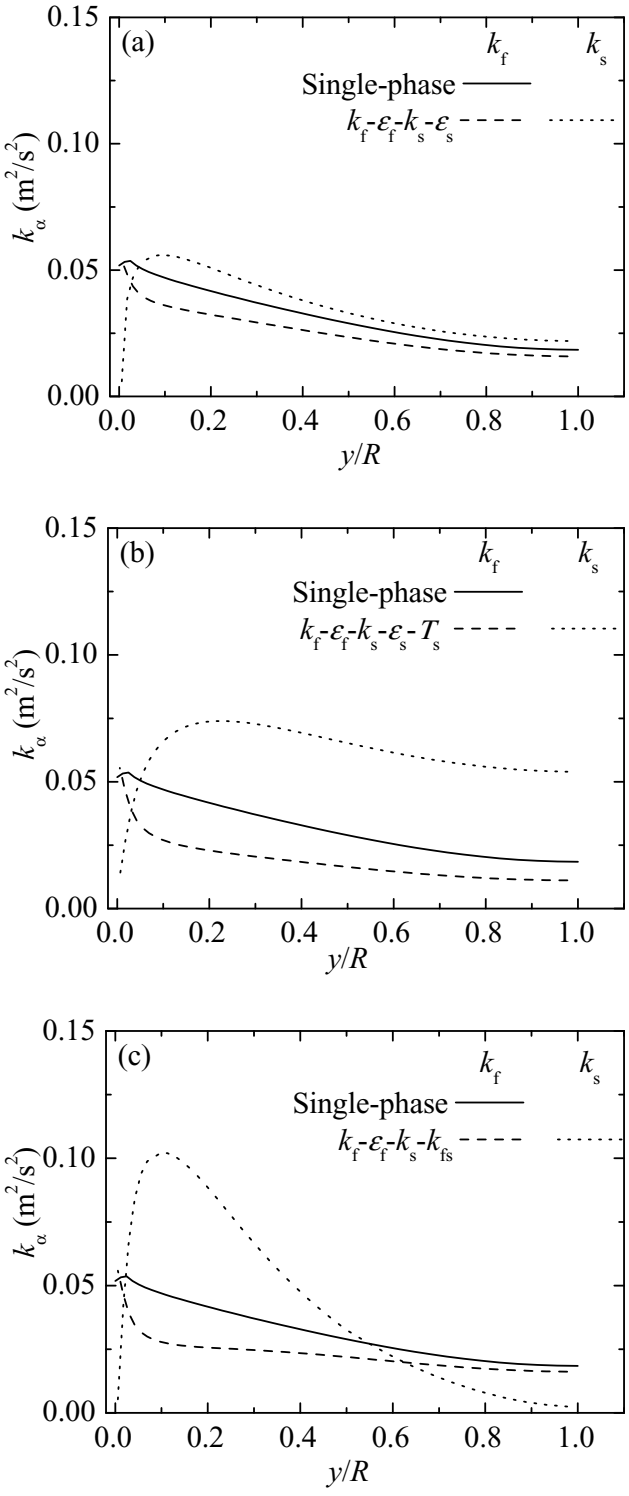

Figure 5.8: Predictions of turbulence kinetic energy for $d_p = 470$ μm particles at $C_s = 8.7\%$ (**Run 1**): (a) $k_f - \varepsilon_f - k_s - \varepsilon_s$ model, (b) $k_f - \varepsilon_f - k_s - \varepsilon_s - T_s$ model, and (c) $k_f - \varepsilon_f - k_s - k_{fs}$ model.

The comparative study of the order of magnitude of constant solids viscosity in liquid-solid flow simulations by Krampa-Morlu et al. (2004) indicated that local variation of the solids viscosity is required for improved prediction of concentration and velocity distributions. The k_f profile predicted by the $k_f - \varepsilon_f - k_s - k_{fs}$ model, which provides this feature, is shown in Figure 5.8c. The shape of both profiles is similar to those shown in Figures 5.8a and 5.8b; the magnitude is discussed below using Figure 5.9a.

To more clearly compare the k_f and k_s values predicted by the three models, the results are plotted again in Figures 5.9a and 5.9b. The single-phase results for k_f are also included in Figure 5.9a. Figure 5.9a shows that the liquid-phase turbulence as characterised by the magnitude of k_f is attenuated. The extent of attenuation is greatest over the entire pipe cross-section in the case of the $k_f - \varepsilon_f - k_s - \varepsilon_s - T_s$ model. The k_f profile predicted by the $k_f - \varepsilon_f - k_s - k_{fs}$ model lies between those predicted by the $k_f - \varepsilon_f - k_s - \varepsilon_s$ and $k_f - \varepsilon_f - k_s - \varepsilon_s - T_s$ models in the region $0.1 \leq y/R \geq 0.6$. Outside this region, the k_f value predicted by the $k_f - \varepsilon_f - k_s - k_{fs}$ model is identical to that predicted by the $k_f - \varepsilon_f - k_s - \varepsilon_s - T_s$ model for $y/R < 0.1$ and to that of the $k_f - \varepsilon_f - k_s - \varepsilon_s$ model for $y/R > 0.6$. The predictions of k_s are shown in Figure 5.9b. While the shape of the profiles is generally similar, the magnitudes for the three models are very different. Close to the wall of the pipe, the peak value of k_s for the $k_f - \varepsilon_f - k_s - k_{fs}$ model is about twice as high as for the baseline $k_f - \varepsilon_f - k_s - \varepsilon_s$ model. The peak of k_s for the $k_f - \varepsilon_f - k_s - \varepsilon_s - T_s$ model lies between the peak value of the other two models. In the region closer to the centre of the pipe, the k_s value for the $k_f - \varepsilon_f - k_s - k_{fs}$ model decreases more rapidly, giving the lowest prediction at the centre.

Figure 5.10 shows the corresponding distribution of the liquid-phase eddy viscosity predicted for single-phase flow (ν_t) and liquid-solid flow (ν_{ft}), as well as the distribution of the solids-phase eddy viscosity (ν_{st}) for **Run 1**. The liquid-phase eddy viscosity is almost the same as for the single-phase flow, which indicates that the effective viscosity of the liquid-phase is almost unaffected by the presence of the solids at a 8.7% mean concentration. For two phase flow, the behaviour of ν_{st} is similar to that of ν_{ft} for the two models

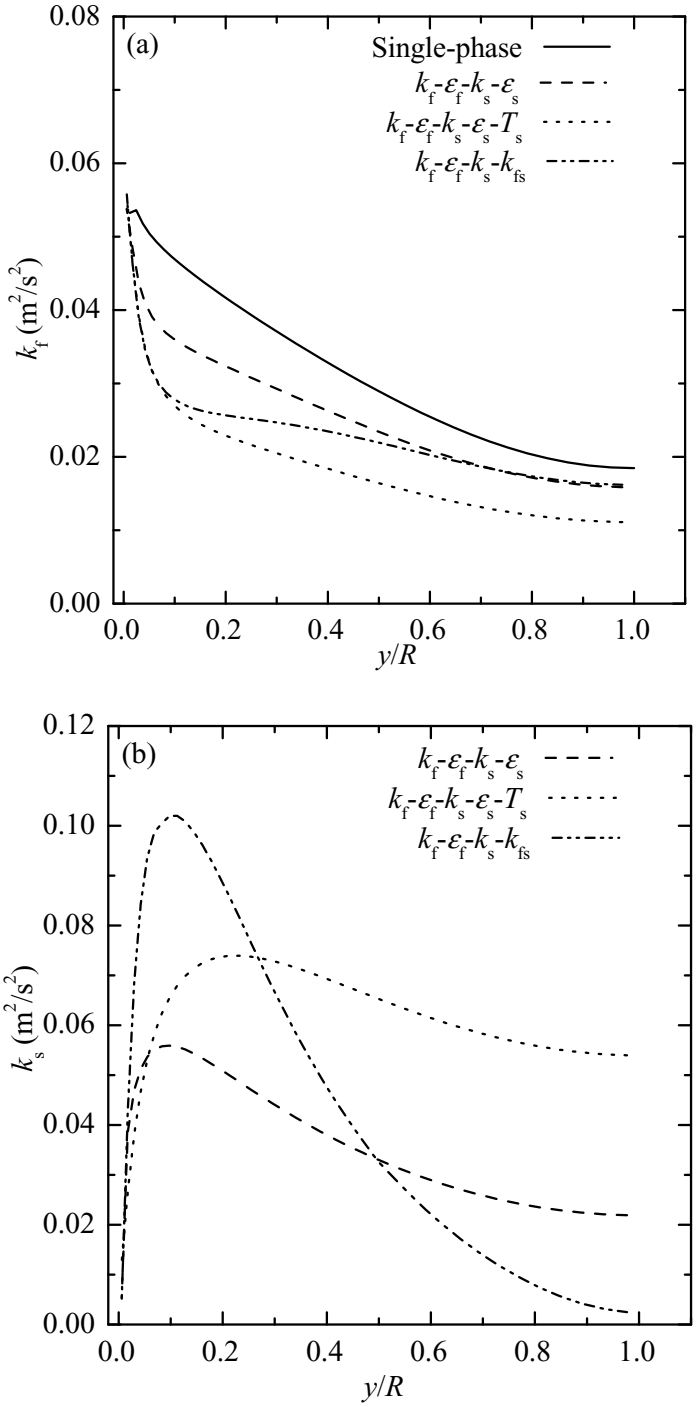

Figure 5.9: Predictions of phasic turbulence kinetic energy for $d_p = 470$ μm particles at $C_s = 8.7\%$ (**Run 1**): (a) liquid-phase turbulence kinetic energy, and (b) solids-phase turbulence kinetic energy.

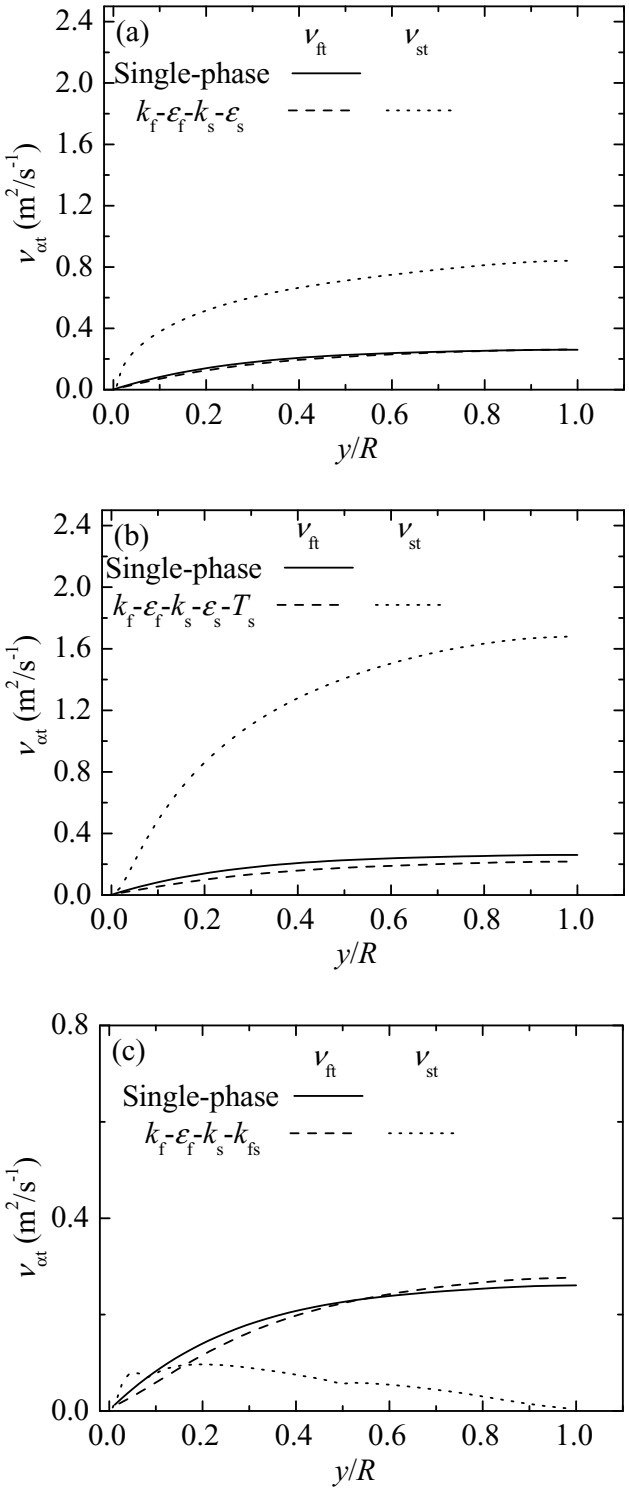

Figure 5.10: Predictions of eddy viscosity for $d_{\mathrm{p}} = 470$ μm particles at $C_{\mathrm{s}} = 8.7\%$ (**Run 1**): (a) $k_{\mathrm{f}} - \varepsilon_{\mathrm{f}} - k_{\mathrm{s}} - \varepsilon_{\mathrm{s}}$ model, (b) $k_{\mathrm{f}} - \varepsilon_{\mathrm{f}} - k_{\mathrm{s}} - \varepsilon_{\mathrm{s}} - T_{\mathrm{s}}$ model, and (c) $k_{\mathrm{f}} - \varepsilon_{\mathrm{f}} - k_{\mathrm{s}} - k_{\mathrm{fs}}$ model.

shown in Figures 5.10a and 5.10b, but the value of ν_{st} is significantly higher for most of the pipe cross-section. For the $k_{\mathrm{f}} - \varepsilon_{\mathrm{f}} - k_{\mathrm{s}} - \varepsilon_{\mathrm{s}}$ model (Figure 5.10a), the effective viscosity of the solids-phase is dominated by the solids-phase turbulence and the effect of the laminar solids kinematic viscosity ($10^{-8}/\rho_{\mathrm{s}}$ $\mathrm{m^2 s^{-1}}$) is insignificant in the core region of the pipe. The observation in the case of the $k_{\mathrm{f}} - \varepsilon_{\mathrm{f}} - k_{\mathrm{s}} - \varepsilon_{\mathrm{s}} - T_{\mathrm{s}}$ model (Figure 5.10b) is similar, although the *laminar* viscosity of the solids-phase, i.e. equation (5.3), is derived from the kinetic theory of *dry* granular flows. The solids-phase laminar viscosity was found to be very small, $O(10^{-4})$, compared with the values of ν_{st} reported in Figure 5.10b. In Figure 5.10c, while the liquid-phase *eddy* viscosity, ν_{ft}, calculated using the $k_{\mathrm{f}} - \varepsilon_{\mathrm{f}} - k_{\mathrm{s}} - k_{\mathrm{fs}}$ model is similar to those shown in Figures 5.10a and 5.10b, the prediction for ν_{st} is very different. This peculiar behaviour of the model warrants further investigation.

In Figure 5.11, the turbulence results for a solids mean concentration of 27.8% are shown for each model. From Figures 5.11a and 5.11b, where the results from the $k_{\mathrm{f}} - \varepsilon_{\mathrm{f}} - k_{\mathrm{s}} - \varepsilon_{\mathrm{s}}$ and $k_{\mathrm{f}} - \varepsilon_{\mathrm{f}} - k_{\mathrm{s}} - \varepsilon_{\mathrm{s}} - T_{\mathrm{s}}$ models are presented, the value of k_f decreases sharply moving away from the wall for the two-phase flow compared to that for the lower concentration. As well, the k_{f} profile exhibits a local minimum just outside the near-wall region. A local minimum of k_{f} close to the wall is also present in the profile shown in Figure 5.11c (for the $k_{\mathrm{f}} - \varepsilon_{\mathrm{f}} - k_{\mathrm{s}} - k_{\mathrm{fs}}$ model). However, towards the pipe centreline, the behaviour of the fluid turbulence differs for the three models. In particular, the liquid-phase turbulence kinetic energy in Figure 5.11c is higher in the core region of the pipe. An obvious explanation, which requires further investigation, comes from the modelling of the turbulence transport equations in the $k_{\mathrm{f}} - \varepsilon_{\mathrm{f}} - k_{\mathrm{s}} - k_{\mathrm{fs}}$ model. In this case, a turbulence modulation model, in accordance with the formulation of Simonin (1996), was introduced. In a related study of gas-solids flow, Krampa-Morlu et al. (2006) predicted a trend similar to that exhibited in Figure 5.11c when a simplified model (Zhang and Reese, 2003b) for the turbulence modulation term was implemented. For the solids-phase turbulence kinetic energy k_{s}, the trend in Figure 5.11 is similar to that in Figure 5.8, however, as expected the level of k_{s} is significantly lower across the entire pipe cross-section, indicating that k_{s} decreases as the solids concentration is increased. Increased solids concentration reduces

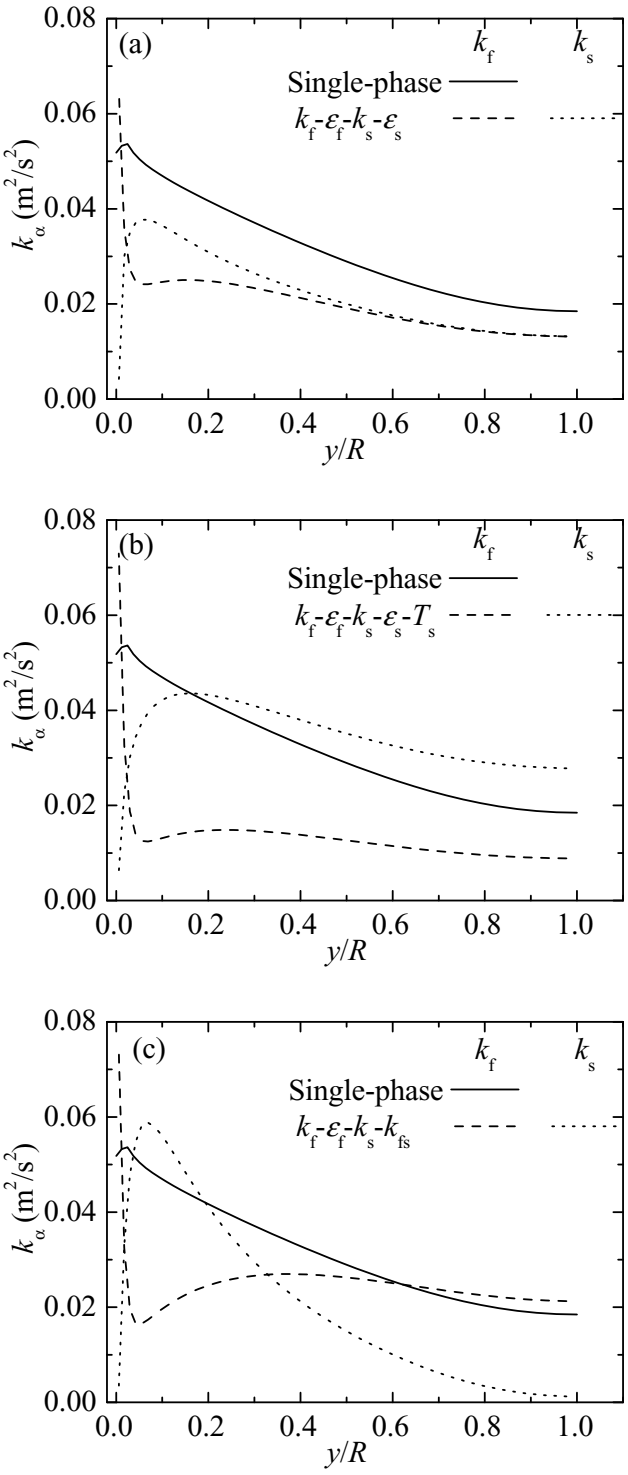

Figure 5.11: Predictions of turbulence kinetic energy for $d_\mathrm{p} = 470$ μm particles at $C_\mathrm{s} = 27.8\%$ (**Run 2**): (a) $k_\mathrm{f} - \varepsilon_\mathrm{f} - k_\mathrm{s} - \varepsilon_\mathrm{s}$ model, (b) $k_\mathrm{f} - \varepsilon_\mathrm{f} - k_\mathrm{s} - \varepsilon_\mathrm{s} - T_\mathrm{s}$ model, and (c) $k_\mathrm{f} - \varepsilon_\mathrm{f} - k_\mathrm{s} - k_\mathrm{fs}$ model.

the inter-particle distance and thus, the length scale of the interacting particles is reduced resulting in lower k_s values.

Figures 5.12a and 5.12b compare the k_f and k_s profiles predicted by the three models. Except for the $k_f - \varepsilon_f - k_s - k_{fs}$ model prediction near the centre of the pipe where enhancement of turbulence is observed, the value of k_f is lower than that for single-phase flow (Figure 5.12a). At a mean concentration of 27.8%, the extent of turbulence attenuation is greater than observed for flows with a solids mean concentration of 8.7%. As well, unlike the case for $C_s = 8.7\%$ k_s is similar for all three models near the pipe wall. Recall that in Figure 5.9a, the $k_f - \varepsilon_f - k_s - \varepsilon_s$ and $k_f - \varepsilon_f - k_s - k_{fs}$ models produced very similar liquid-phase turbulence kinetic energy towards the centre of the pipe. The predictions of k_s for $C_s = 27.8\%$ shown in Figure 5.12b are similar in shape to those shown in Figure 5.9b but the levels are generally higher for the lower solids bulk concentration.

Figure 5.13 shows the liquid-phase eddy viscosity predictions for a flow with a solids mean concentration of 27.8% (**Run 2**). Figure 5.13a shows the predictions using the $k_f - \varepsilon_f - k_s - \varepsilon_s$ model, Figure 5.13b shows those for the $k_f - \varepsilon_f - k_s - \varepsilon_s - T_s$ model, and the phasic eddy viscosities obtained using the $k_f - \varepsilon_f - k_s - k_{fs}$ model are shown in Figure 5.13c. As noted for the case of the 8.7% solids mean concentration, the liquid-phase eddy viscosity is almost the same as for the single-phase flow in Figures 5.13a and Figure 5.13b but the magnitude is slightly lower in this case. In Figure 5.13c, the liquid-phase eddy viscosity for the liquid-solid flow is higher than for the single-phase flow in the core region of the pipe. Overall, the trend of the calculated values of ν_{ft} and ν_t are similar to those observed in Figure 5.10, i.e. the profile of ν_{ft} is almost identical to that of ν_t. The ν_{st} profile for **Run 2** is lower than in **Run 1** (Figure 5.10), which is consistent with the reduction in the turbulence kinetic energy due to the increased solids concentration. Although the turbulence predicted by the models are significantly different, this has little effect on the calculated mean transport. One notable effect is the lower solids velocity produced by the high solids-phase eddy viscosity predicted by the $k_f - \varepsilon_f - k_s - \varepsilon_s - T_s$ model compared to the other models, especially for flows with larger particles.

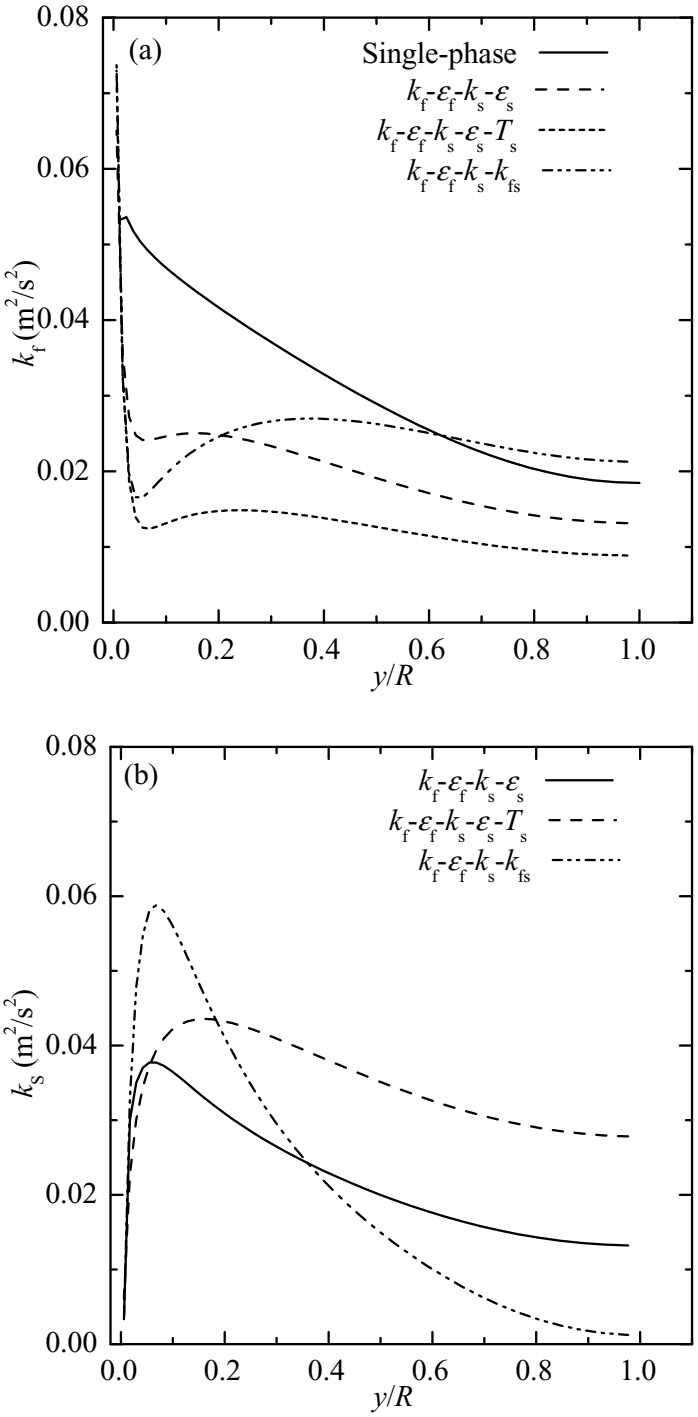

Figure 5.12: Predictions of phasic turbulence kinetic energy for $d_p = 470$ μm particles at $C_s = 27.8\%$ (**Run 2**): (a) liquid-phase turbulence kinetic energy, and (b) solids-phase turbulence kinetic energy.

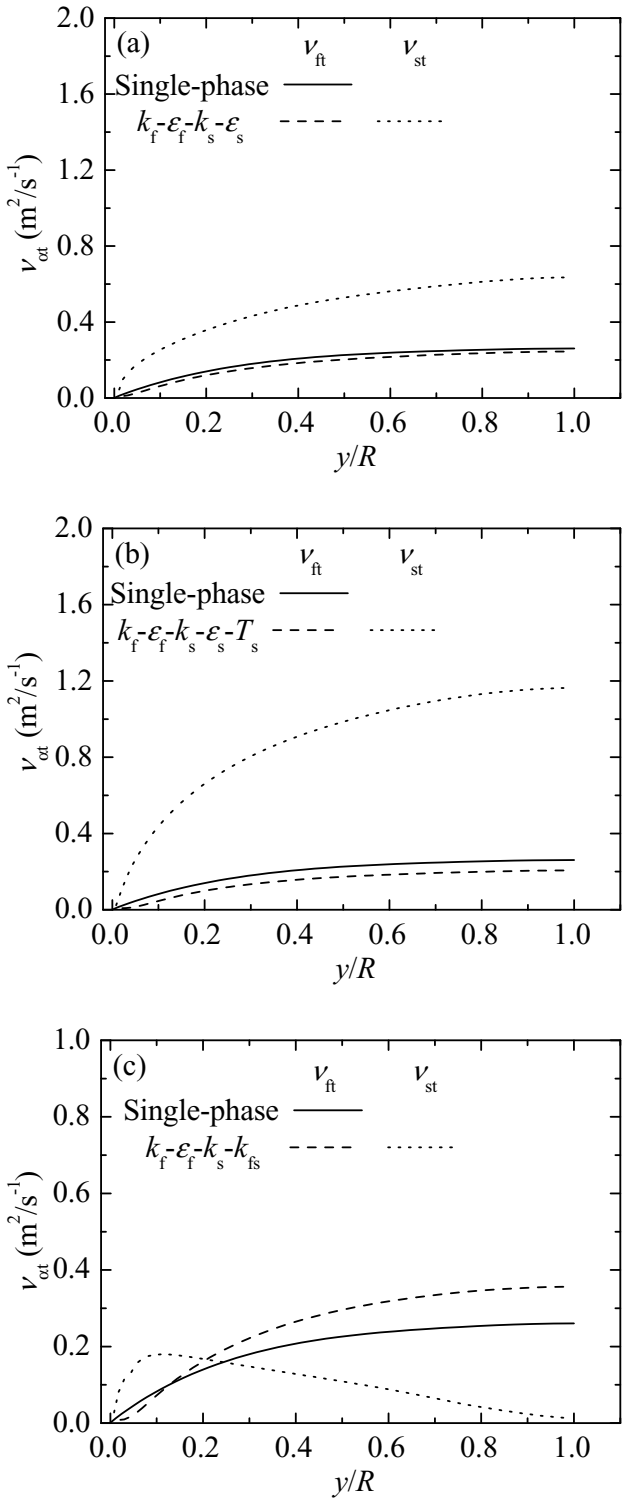

Figure 5.13: Predictions of eddy viscosity for $d_{\mathrm{p}} = 470$ μm particles at $C_{\mathrm{s}} = 27.8\%$ (**Run 2**): (a) $k_{\mathrm{f}} - \varepsilon_{\mathrm{f}} - k_{\mathrm{s}} - \varepsilon_{\mathrm{s}}$ model, (b) $k_{\mathrm{f}} - \varepsilon_{\mathrm{f}} - k_{\mathrm{s}} - \varepsilon_{\mathrm{s}} - T_{\mathrm{s}}$ model, and (c) $k_{\mathrm{f}} - \varepsilon_{\mathrm{f}} - k_{\mathrm{s}} - k_{\mathrm{fs}}$ model.

Flow with 1700 μm diameter particles

Figures 5.14 and 5.15 show the turbulence kinetic energy results for **Run 3**. In Figure 5.14, the phasic turbulence kinetic energies are presented for each model. The near-wall decrease in k_{f} is more gradual, and the value of k_{s} is noticeably higher in the core region of the pipe compared to the results for the smaller particles (see Figure 5.8 for comparison). The peak value of k_{s} is lower and shifted to the right ($y/R \approx 0.2$) compared to the case of the smaller particles (Figure 5.8), except for the case of the $k_{\mathrm{f}} - \varepsilon_{\mathrm{f}} - k_{\mathrm{s}} - \varepsilon_{\mathrm{s}} - T_{\mathrm{s}}$ model, where the peak vanishes and k_{s} becomes almost constant for $y/R \geq 0.4$ (Figure 5.14b). In Figure 5.15a, the k_{f} calculated from each model is compared. It can be seen that the $k_{\mathrm{f}} - \varepsilon_{\mathrm{f}} - k_{\mathrm{s}} - \varepsilon_{\mathrm{s}}$ model predicted the highest value of the liquid-phase turbulence kinetic energy, which is still lower than for single-phase flow, and the $k_{\mathrm{f}} - \varepsilon_{\mathrm{f}} - k_{\mathrm{s}} - \varepsilon_{\mathrm{s}} - T_{\mathrm{s}}$ model predicted the lowest value of k_{f}. The behaviour of the k_{s} predictions shown in Figure 5.15b is similar to those obtained for the smaller particles (Figure 5.9b), except for the magnitude of the predictions, which is higher for the larger particles. Besides the slight difference in magnitude, the turbulence kinetic energy results at a solids mean concentration of 17.8% **Run 4 (not shown** are similar to those of **Run 3**. Unlike the case of the smaller particles, an increase in the solids concentration does not significantly change the turbulence kinetic energy values.

Figures 5.16 and 5.17 show the eddy viscosity results for **Run 3** and **Run 4**, respectively. These results indicate a slightly lower value of ν_{ft} and a much higher value of ν_{st} compared to ν_{t} for single-phase flow. For the $k_{\mathrm{f}} - \varepsilon_{\mathrm{f}} - k_{\mathrm{s}} - \varepsilon_{\mathrm{s}}$ and $k_{\mathrm{f}} - \varepsilon_{\mathrm{f}} - k_{\mathrm{s}} - \varepsilon_{\mathrm{s}} - T_{\mathrm{s}}$ models, the value of ν_{st} is about four times larger than the corresponding ν_{ft} value in the core region of the pipe as shown in Figures 5.16a and 5.16b for the 8.5% solids mean concentration. A similar observation is made for Figures 5.17a and 5.17b for 17.7% solids mean concentration. The ν_{st} profile calculated with the $k_{\mathrm{f}} - \varepsilon_{\mathrm{f}} - k_{\mathrm{s}} - k_{\mathrm{fs}}$ model is similar to that obtained for the smaller particles at both solids mean concentrations. Note that, in general, the level of the solids-phase eddy viscosity for the larger particles (Figures 5.16 and Figure 5.17) is enhanced over that for the smaller particles (Figures 5.10 and 5.13) at

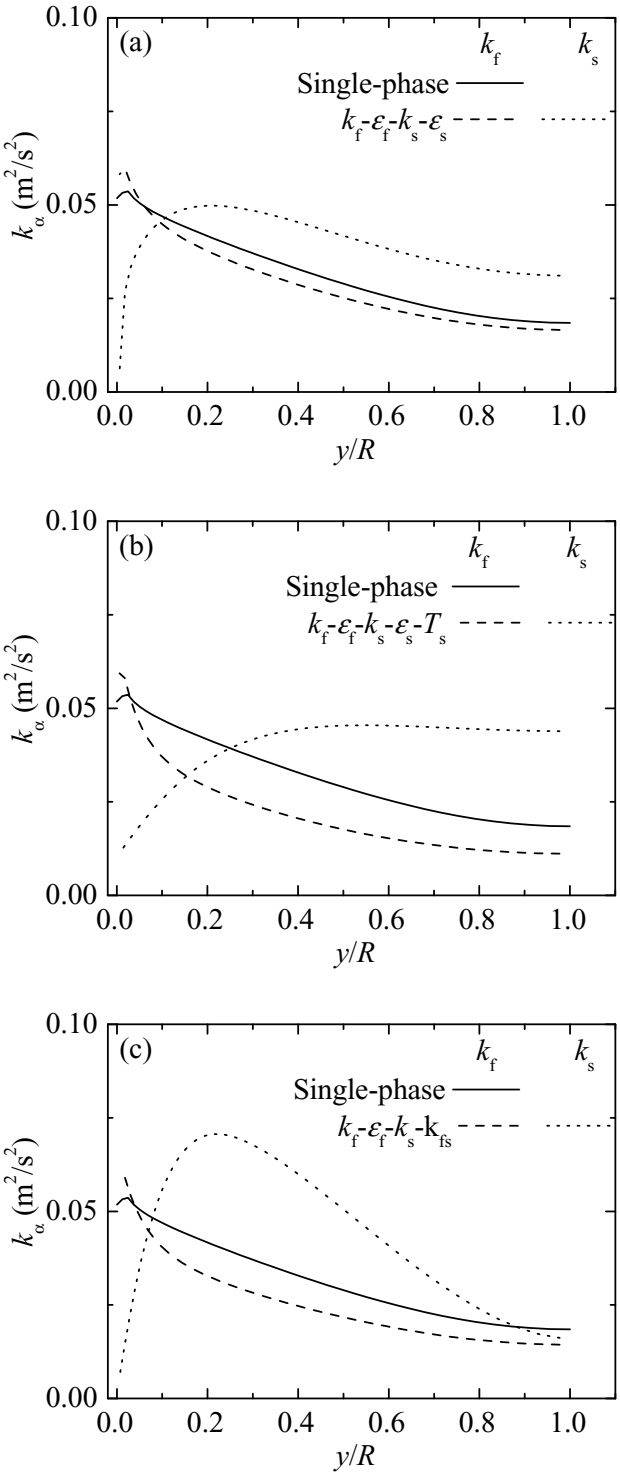

Figure 5.14: Predictions of turbulence kinetic energy for $d_\mathrm{p} = 1700$ μm particles at $C_\mathrm{s} = 8.5\%$ (**Run 3**): (a) $k_\mathrm{f} - \varepsilon_\mathrm{f} - k_\mathrm{s} - \varepsilon_\mathrm{s}$ model, (b) $k_\mathrm{f} - \varepsilon_\mathrm{f} - k_\mathrm{s} - \varepsilon_\mathrm{s} - T_\mathrm{s}$ model, and (c) $k_\mathrm{f} - \varepsilon_\mathrm{f} - k_\mathrm{s} - k_\mathrm{fs}$ model.

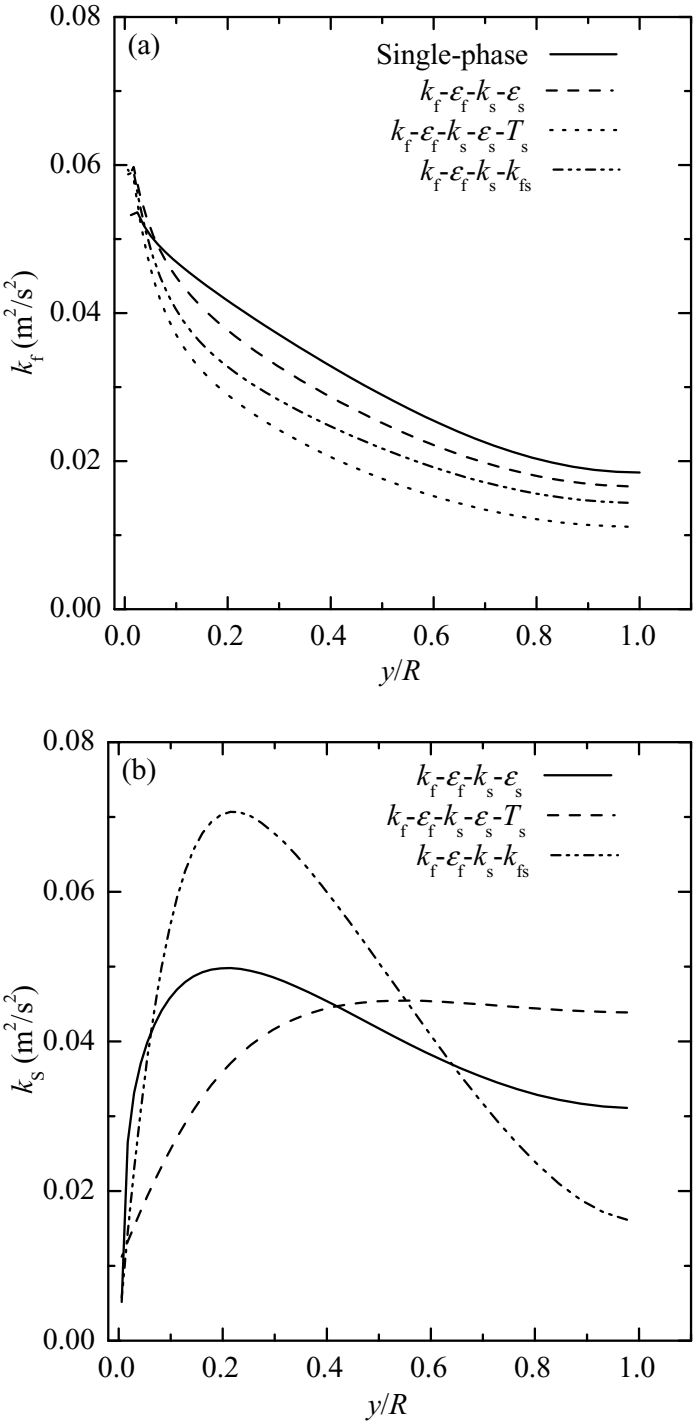

Figure 5.15: Predictions of phasic turbulence kinetic energy for $d_p = 1700$ μm particles at $C_s = 8.5\%$ (**Run 3**): (a) liquid-phase turbulence kinetic energy, and (b) solids-phase turbulence kinetic energy.

both mean concentration values.

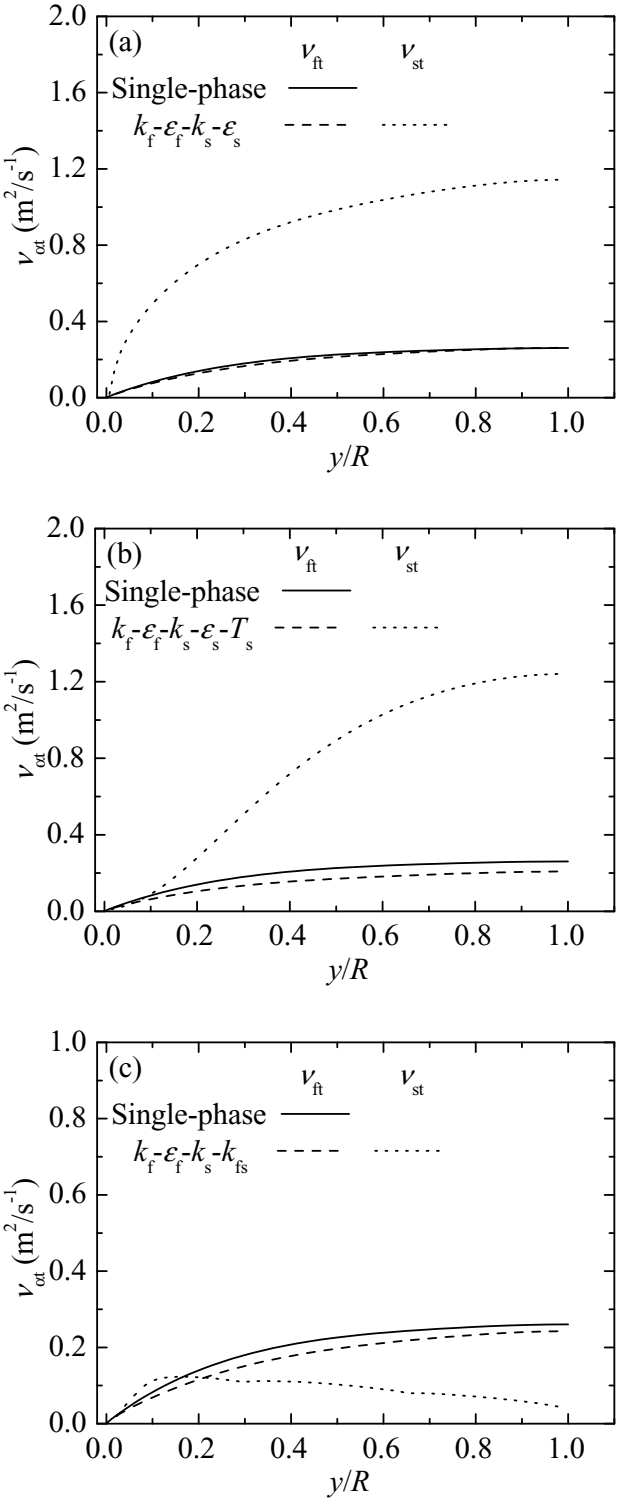

Figure 5.16: Predictions of eddy viscosity for $d_p = 1700$ μm particles at $C_s = 8.5\%$ (**Run 3**): (a) $k_f - \varepsilon_f - k_s - \varepsilon_s$ model, (b) $k_f - \varepsilon_f - k_s - \varepsilon_s - T_s$ model, and (c) $k_f - \varepsilon_f - k_s - k_{fs}$ model.

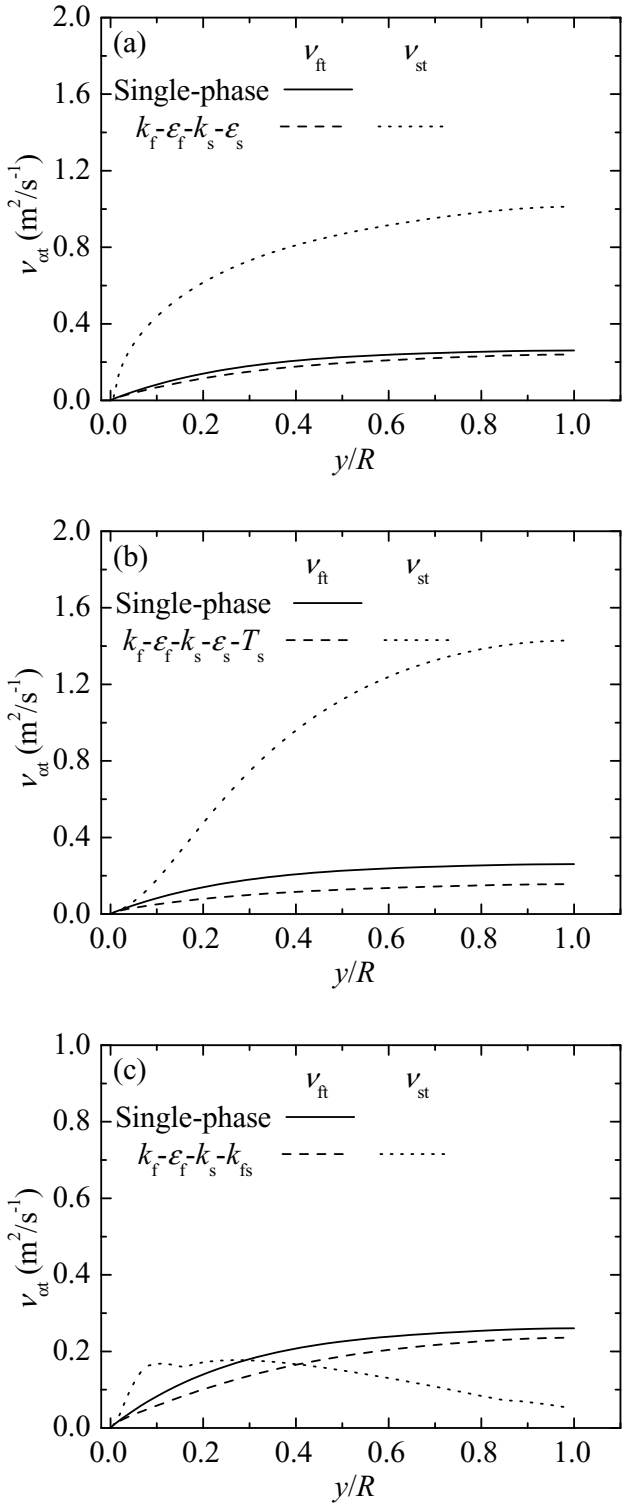

Figure 5.17: Predictions of eddy viscosity for $d_{\mathrm{p}} = 1700\ \mu$m particles at $C_{\mathrm{s}} = 17.7\%$ (**Run 4**): (a) $k_{\mathrm{f}} - \varepsilon_{\mathrm{f}} - k_{\mathrm{s}} - \varepsilon_{\mathrm{s}}$ model, (b) $k_{\mathrm{f}} - \varepsilon_{\mathrm{f}} - k_{\mathrm{s}} - \varepsilon_{\mathrm{s}} - T_{\mathrm{s}}$ model, and (c) $k_{\mathrm{f}} - \varepsilon_{\mathrm{f}} - k_{\mathrm{s}} - k_{\mathrm{fs}}$ model.

5.2 Effect of Solids Wall Boundary Conditions on Pressure Drop Predictions

In this section, the effect of different solids-phase wall boundary conditions is evaluated for liquid-solid flows in a vertical pipe. The wall boundary conditions of Ding and Gidaspow (1990) given by equation (4.87); Ding and Lyczkowski (1992) given by equation (4.87); and Bartosik (1996) i.e., equation (2.10), as well as the no-slip and free-slip conditions were investigated. Predictions of frictional head losses for turbulent flow of coarse particle slurries at high solids concentrations in a vertical pipe were obtained from numerical computations. The computations were performed with the two-fluid model using the commercial CFD code ANSYS CFX-4.4, in which the solids-phase wall boundary conditions were implemented via user-Fortran routines. The predicted frictional head losses were compared to the experimental data of Shook and Bartosik (1994).

5.2.1 Solids-phase boundary conditions

Apart from the solids-phase boundary condition at the wall, the other boundary conditions were specified as discussed in Section 5.1.4. Partial-slip can occur at the wall due to the complex particle-wall interactions as discussed in Section 4.5.2. To investigate these particle-wall interactions, and particularly evaluate the effect of the particle wall boundary condition on the total frictional head loss (i.e. equation (2.5)), the wall boundary condition for the solids-phase is specified using the following relations:

1. no-slip condition - (NS);
2. free-slip condition - (FS);
3. partial-slip velocity: equation (4.87) with the slip parameter given by equation (4.89) - (DG90) (Ding and Gidaspow, 1990);
4. partial-slip velocity: equation (4.87) with the slip parameter given by equation (4.90) - (DL92) (Ding and Lyczkowski, 1992); and
5. modified wall dispersive shear stress: equation (2.10) - (B96) (Bartosik, 1996).

The last three cases were implemented in ANSYS CFX-4.4 using user-Fortran routines. The phasic wall shear-stresses, which were obtained as output from the software were then

used to calculate the frictional head losses. The total frictional losses were determined from equations (2.4) and (2.5):

$$i_{\mathrm{m}} = \frac{-4(\tau_{\mathrm{fw}} + \tau_{\mathrm{sw}})}{\rho_{\mathrm{f}} g D}. \tag{5.26}$$

5.2.2 Experimental cases considered and numerical set-up

Simulations of water-PVC plastic mixture flows in a pipe were performed using ANSYS CFX-4.4. The numerical predictions for frictional head losses in fully-developed steady upward vertical pipe flows of the mixture are compared with the experimental data reported by Shook and Bartosik (1994). In the study of Shook and Bartosik (1994), two separate re-circulating plastic pipelines of internal diameters 26 mm and 40 mm were used. Particles of different sizes and densities were investigated; the solids concentrations (by volume) ranged between 10% to 45%. Recall that in the experimental work of Shook and Bartosik (1994), the liquid-phase wall stress was determined by estimating the liquid-phase friction factor f_{L} for the pipe using the Reynolds number ($Re = DV\rho_{\mathrm{L}}/\mu_{\mathrm{L}}$) and the pipe roughness (k). The velocity gradient for the solids-phase was assumed to be equal to that of the liquid-phase so that the solids wall shear stress could be calculated from the ratio of the estimated liquid-phase wall shear stress to the liquid-velocity. The solids-phase velocity gradient was then applied in equation (2.7). The total frictional head loss was then calculated from equation (5.26). For the present work, the frictional head losses predicted for flows with solids mean concentrations between 10% and 40% of 3.4 mm PVC plastic particles are compared with the measured data. The density of the particles used is 1400 $\mathrm{kg\ m^{-3}}$ (i.e. the density ratio is $\rho_{\mathrm{s}}/\rho_{\mathrm{l}} \approx 1.4$). A pipe length of 4.0 m was considered and the flow was treated as axi-symmetric. The numerical simulations were performed using the same approach discussed in Section 5.1.5 and a simulation was considered converged when the normalized residuals were reduced to a value of 10^{-8}. Typical calculations - depending on the mean velocity and solids mean concentration - took between 5.7×10^3 s and 2.7×10^4 s of CPU time on the 2.66 GHz PC mentioned in Section 5.1.5.

5.2.3 Model predictions for 10% solids mean concentration

Figure 5.18 shows the predicted frictional head loss plotted against the mean mixture velocity for different wall boundary conditions for the solids-phase at a solids mean concentration of 10%. The predictions are compared with experimental data from the study of Shook and Bartosik (1994). The computed frictional head loss of single-phase water flow, which matches the measured data, is also shown in the figure. Overall, the numerical results show the expected trend of increasing frictional head loss as the mean mixture velocity increases.

Figure 5.18 shows that the calculated frictional head losses produced by the DL92 slip boundary condition and the B96 wall shear-stress formulation are very similar. The frictional head loss produced by the DG90 partial-slip condition under-predicts the data for the liquid-solid flow and instead matches the single-phase flow data. This is due to the negligible solids wall shear-stress values computed compared to those of the liquid-phase (See Table 5.3).

Compared to the measured data, the total or mixture frictional head losses predicted for the 10% solids mean concentration using the NS, FS, and the DG90 formulations are much lower. The prediction by the DG90 partial-slip condition lies between the predictions made using the NS and FS boundary conditions. The frictional head losses predicted with the DL92 partial-slip condition and the B96 wall shear-stress formulation are higher than those predicted using the NS and FS conditions for the range of mean mixture velocities investigated. Overall, they produce more promising results in this case. The prediction by the DL92 partial-slip condition is lower than the measured data for $U_{\mathrm{m}} \sim 5.0$ ms^{-1} but matches the data reasonably well beyond that velocity. A similar trend is observed for the B96 wall shear-stress formulation.

The above observations suggest that the free-slip boundary condition for the solids-phase is inappropriate and the no-slip condition is also not applicable. The NS and the FS

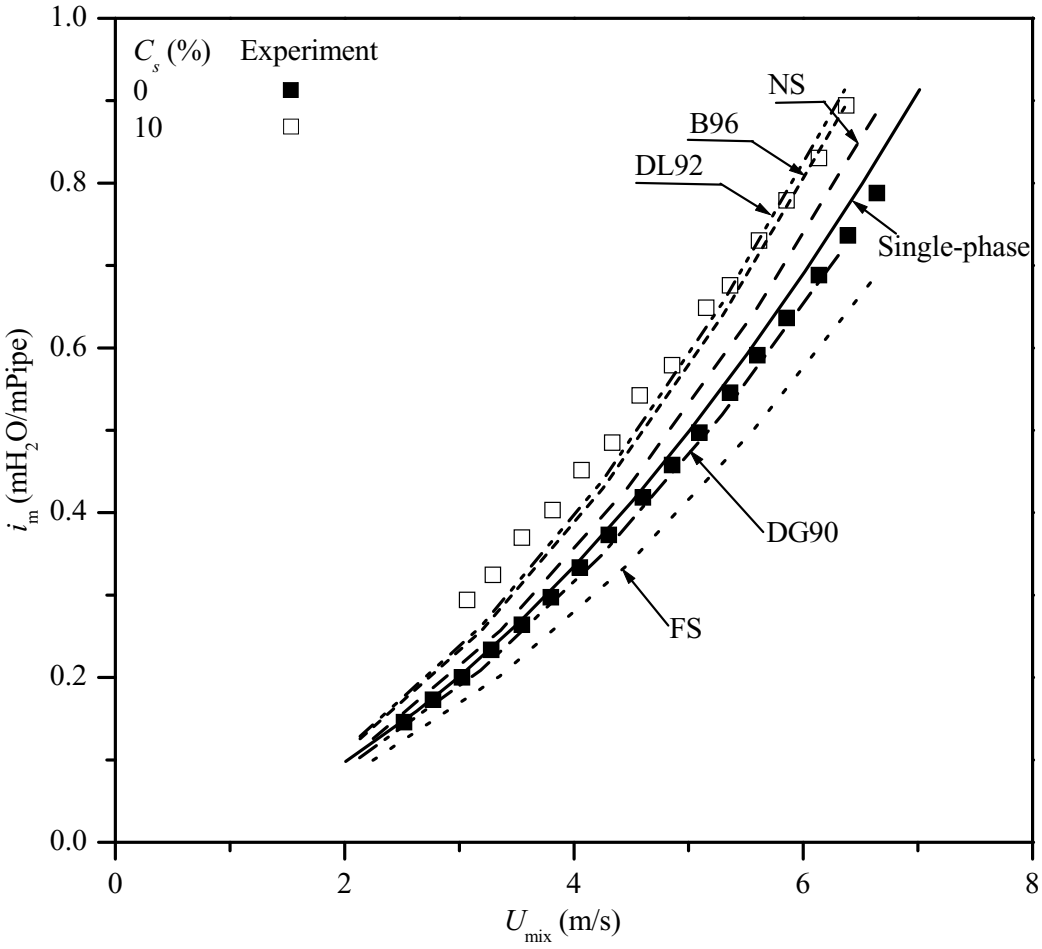

Figure 5.18: Predicted and measured frictional head losses for the upward vertical flow of 3.4 mm PVC particles in water; $C_s = 10\%$. Experimental measurements published by Shook and Bartosik (1994).

wall boundary conditions are considered to physically define the two limits of the wall conditions. In this context, the DG90 partial-slip condition falls between these limits, whereas the B96, DL92, and the experimental data do not. The results presented shows that the present models fail in predicting the pressure drop for the flows of interest in the study.

Table 5.3 shows predictions for the phasic wall quantities at various mean mixture velocities for the flows with mean concentration of 10%. The values of the liquid-phase wall shear-stress are similar for all the formulations presented in the table. The magnitudes of the solids-phase wall shear-stress are similar for the NS, DL92 and B96 conditions and both are significantly higher than that calculated by the DG90 condition. The solids concentration computed at the first node from the wall are similar for the wall boundary conditions shown in Table 5.3. The computed solids-phase concentration at the wall increases with increase in the mean mixture velocity. From Table 5.3, it is interesting to note that the differences between the slip parameters λ_{slip} used in the boundary conditions for the DG90 and the DL92 models are marginal. Therefore, the large difference in the corresponding values of the solids wall shear-stress ($-\tau_{\text{sw}}$) for the DG90 and DL92 slip conditions must be related to the solids velocity gradient at the wall. Analysis of the slip parameters (i.e. equations 4.89 and 4.90) indicates that the solids concentration at the wall for these equations does not contribute to an increase in the overall frictional head loss observed in the experiments.

5.2.4 Effect of solids mean concentration

In this section, only predictions with the DL92 partial-slip condition and the B96 wall shear-stress formulation are discussed, since they produced reasonable results for the 10% concentration case. Figure 5.19a shows the predicted frictional head loss for 10% and 20% solids mean concentrations compared with the measured data. Predictions made using either wall boundary conditions produced lower frictional head losses, particularly at lower mean mixture velocities, than observed for the experimental data. Typically, the frictional head loss produced using the DL92 partial slip condition was about 2% higher than that produced with the B96 wall shear-stress formulation. The frictional head loss

Table 5.3: Computed wall quantities for flow at 10% mean concentration

	C_s	c_{sw}	U_m (m/s)	u_{sw} (m/s)	$-\tau_{fw}$ (Pa)	$-\tau_{sw}$ (Pa)	λ_{slip}
FS	0.107	0.018	2.25	1.66	9.77	-	-
	0.103	0.028	3.36	2.52	19.81	-	-
	0.102	0.035	4.46	3.37	32.96	-	-
	0.101	0.040	5.56	4.22	49.06	-	-
	0.101	0.043	6.67	5.08	67.96	-	-
NS	0.107	0.023	2.25	1.57	9.76	2.56	-
	0.104	0.035	3.36	2.35	19.79	5.40	-
	0.102	0.045	4.47	3.13	32.92	9.20	-
	0.102	0.052	5.57	3.91	48.99	13.95	-
	0.101	0.057	6.68	4.69	67.90	19.36	-
DG90	0.106	0.022	2.13	1.71	10.05	0.02	0.012
	0.103	0.035	3.19	2.60	20.46	0.03	0.010
	0.102	0.046	4.24	3.48	34.13	0.03	0.010
	0.101	0.054	5.29	4.34	50.90	0.04	0.009
	0.101	0.059	6.35	5.21	70.62	0.05	0.009
DL92	0.106	0.023	2.13	1.57	10.02	2.58	0.019
	0.104	0.036	3.19	2.36	20.35	5.43	0.012
	0.102	0.046	4.25	3.14	33.87	9.24	0.009
	0.102	0.054	5.31	3.92	50.44	14.00	0.008
	0.101	0.060	6.36	4.70	69.93	19.68	0.007
B96	0.106	0.023	2.13	1.57	9.76	2.56	-
	0.104	0.035	3.19	2.35	19.79	5.40	-
	0.102	0.045	4.25	3.13	32.92	9.20	-
	0.102	0.052	5.31	3.91	48.99	13.95	-
	0.101	0.057	6.36	4.69	67.90	19.63	-

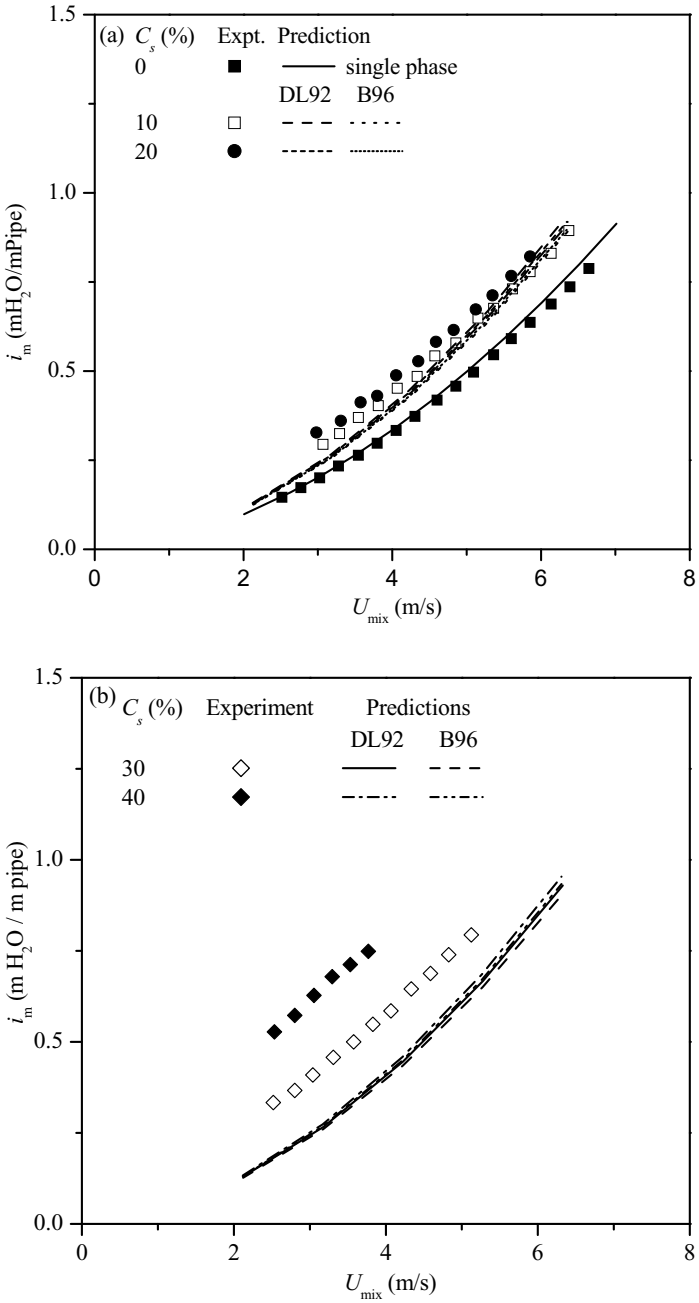

Figure 5.19: Predicted and measured frictional head losses for the upward vertical flow of 3.4 mm PVC particles in water for (a) $C_s = 10\%$ and 20% and (b) $C_s = 30\%$ and 40%. Experimental measurements published by Shook and Bartosik (1994).

predictions using the DL92 partial-slip boundary condition and the B96 wall shear-stress formulation at a solids mean concentration of 20% were very similar to the predictions for the case of 10% solids mean concentration. The predictions indicate that the DL92 partial-slip condition and B96 wall shear-stress formulation exhibit almost no effect of solids mean concentration for the range of velocities and concentrations considered in the study. These formulations, which include the effect of concentration via the radial distribution function (Ding and Lyczkowski, 1992) or the linear concentration (Bartosik, 1996), do not reproduce the effect of concentration. The frictional head loss predictions compared with the experimental data for 30% and 40% solids mean concentration are shown in Figure 5.19b. Both models significantly under-predict the measured data and fail to demonstrate significant variations with C_s.

In Figure 5.20, the effect of mean concentration on the total frictional head loss predictions are presented using the DG92 slip condition. It is observed from the figure that the total frictional head loss computed from equation (5.26), increases with solids concentration. The behaviour is verified in Table 5.4 using the predicted wall quantities obtained with the slip boundary conditions of Ding and Lyczkowski (1992). It can be seen from the table that, irrespective of the solids mean concentration, both the liquid and the solids wall shear-stresses are similar at lower mean mixture velocities as evidenced in the preceding figures. As the solids mean mixture velocity increases, both the liquid and the solids wall shear-stresses increase non-linearly. As well, the calculated wall solids concentration increases as the mean mixture velocity increased. The resulting slip parameter reduces leading to lower values of the solids wall shear stress than the liquid-phase values. On the other hand, as concentration increase, the solids-phase wall shear stress increase whereas the liquid-phase wall shear stress decrease. Sumner et al. (1990) observed that at higher velocities and concentration, the wall region is depleted of solids.

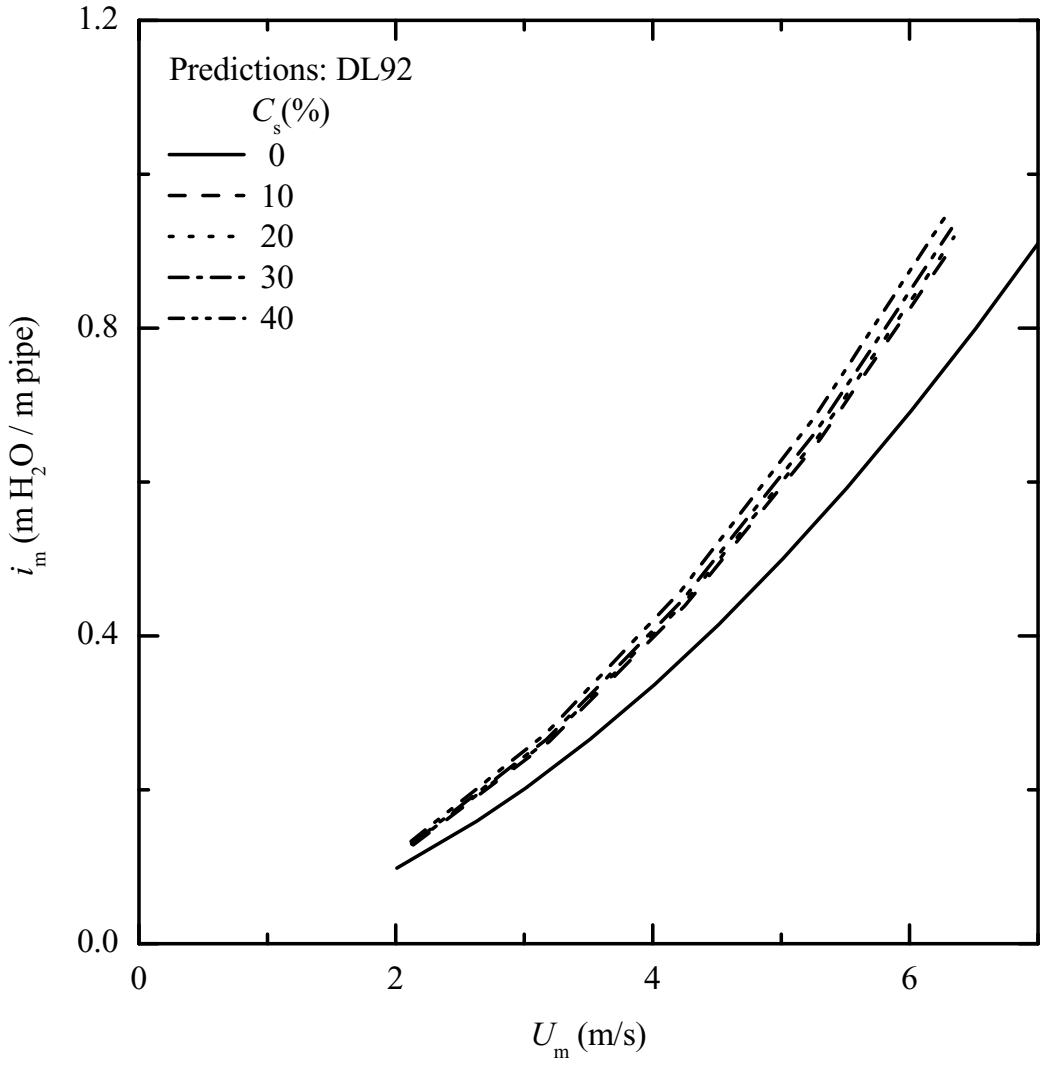

Figure 5.20: Effect of solids mean concentration on frictional head loss predictions for upward vertical flow of 3.4 mm PVC particles in water using the wall boundary condition model of (Ding and Lyczkowski, 1992).

Table 5.4: Computed solids wall boundary condition quantities of (Ding and Lyczkowski, 1992) model.

	C_s	c_{sw}	U_m (m/s)	u_{sw} (m/s)	$-\tau_{fw}$ (Pa)	$-\tau_{sw}$ (Pa)	λ_{slip}
	0.106	0.023	2.13	1.57	10.02	2.58	0.0187
	0.104	0.036	3.19	2.36	20.35	5.43	0.0118
10	0.102	0.046	4.25	3.14	33.87	9.24	0.0091
	0.102	0.054	5.31	3.92	50.44	14.00	0.0078
	0.101	0.060	6.36	4.70	69.93	19.68	0.0070
	0.206	0.057	2.13	1.58	10.02	2.63	0.0073
	0.203	0.075	3.19	2.37	20.34	5.56	0.0055
20	0.202	0.089	4.24	3.16	33.87	9.47	0.0046
	0.202	0.100	5.29	3.95	50.46	14.32	0.0041
	0.202	0.108	6.35	4.73	70.01	20.12	0.0037
	0.307	0.131	2.12	1.52	10.27	2.45	0.0030
	0.304	0.160	3.18	2.29	20.88	5.23	0.0024
30	0.303	0.176	4.23	3.06	34.76	8.97	0.0022
	0.303	0.187	5.28	3.83	51.75	13.68	0.0020
	0.302	0.194	6.33	4.55	72.26	18.94	0.0019
	0.407	0.219	2.12	1.44	10.81	2.25	0.0017
	0.405	0.250	3.17	2.18	21.99	4.84	0.0014
40	0.403	0.269	4.22	2.93	36.62	8.35	0.0013
	0.403	0.281	5.27	3.68	54.52	12.77	0.0013
	0.403	0.289	6.31	4.43	75.54	18.08	0.0012

5.3 Summary

Simulations of sand slurries in vertical pipes have been performed and presented in this chapter. The performance of three different models for the solids-phase effective stress in turbulent fluid-particle flows has been investigated. The $k_{\mathrm{f}} - \varepsilon_{\mathrm{f}} - k_{\mathrm{s}} - \varepsilon_{\mathrm{s}}$, $k_{\mathrm{f}} - \varepsilon_{\mathrm{f}} - k_{\mathrm{s}} - \varepsilon_{\mathrm{s}}$, and $k_{\mathrm{f}} - \varepsilon_{\mathrm{f}} - k_{\mathrm{s}} - \varepsilon_{\mathrm{s}}$ models have been used to simulate coarse particle liquid-solid flows in vertical pipes. The numerical results show that the models predict reasonably well the solids-phase mean flow characteristics, i.e., the solids phase velocity and concentration distribution for smaller particles at lower than 10% solids mean concentration. The results at higher solids mean concentration were not reproduced by the models. For the particular case of the concentration distribution, additional modelling effort must be considered for accurate prediction of non-uniform concentration distribution. The computed phasic turbulence kinetic energy and eddy viscosity qualitatively were different for the models investigated. Presently, experimental results are not available to validate such computations. The effect of boundary conditions on the frictional loss prediction was also investigated. Again, the models investigated fail to reproduce the frictional losses observed in experiments at high solids mean concentration. In general, it is obvious that the present physically-based models developed for dilute particulate flows are not suitable for dense flows.

CHAPTER 6

HORIZONTAL FLOW SIMULATIONS

6.1 Introduction

In this chapter, a more current version of CFX (ANSYS CFX-10) is employed to compute horizontal flows again in an attempt to investigate its application to coarse-particle liquid-solid slurry flows. It is worth noting that CFX-10 was chosen for the horizontal flow simulations due to its release at the initial stages of the problem set-up and the fact that further development of CFX-4.4 was not supported. The physical models implemented in ANSYS CFX-10 for dense multiphase flows are investigated. The effect of solids bulk concentration, particle diameter, and pipe diameter on computed solids-phase velocity and concentration are examined. The predicted profiles are also compared with measured data.

6.2 Mathematical Model

A general set of governing equations for mass and momentum conservation in particulate turbulent flows using the two-fluid model were given in equations (1.1) to (1.5). The constitutive relation for the solids stress used in CFX-10 is given by equation (4.66), which is recast in the form

$$\mathcal{T}_{\mathrm{s}\,ij} = -P_{\mathrm{s}}\delta_{ij} + 2\mu_{\mathrm{s}}\left(S_{\mathrm{s}\,ij} - \frac{1}{3}S_{\mathrm{s}jj}\delta_{ij}\right) + \xi_{\mathrm{s}}S_{\mathrm{s}jj}\delta_{ij}. \tag{6.1}$$

In the context of kinetic theory, the solids pressure is given by equation (5.9), where the radial distribution function g_0 is calculated using equation (4.91). In CFX-10, to prevent the value of g_0 calculated from equation (5.9) from becoming infinity as $c_{\mathrm{s}} \longrightarrow C_{\max}$, it

calculated using

$$g_0 = C_0 + C_1 \left(c_s - C_{crit}\right) + C_2 \left(c_s - C_{crit}\right)^2 + C_3 \left(c_s - C_{crit}\right)^3, \qquad c_s \geq C_{crit} \tag{6.2}$$

where $C_{crit} = C_{max} - 0.001$ and $C_0 = 1079$, $C_1 = 1.08 \times 10^6$, $C_2 = 1.08 \times 10^9$, and $C_3 = 1.08 \times 10^{12}$. Similar to the discussion in Chapter 5, the solids shear viscosity is divided into kinetic and collisional contributions. In ANSYS CFX-10, the kinetic solids viscosity is modelled following Gidaspow (1994) and Lun and Savage (1986). Following the model of Lun and Savage (1986) in the present study, we have

$$\mu_s = \frac{5\pi^{1/2}}{96} d_p \rho_s \left(\frac{1}{\eta g_0} + \frac{8c_s}{5}\right) \left[\frac{1 + \frac{8}{5}\eta\left(3\eta - 2\right) c_s g_0}{2 - \eta}\right] T_s^{1/2}, \tag{6.3}$$

which is essentially the same as equations (5.4) to (5.6) without the last term in equation (5.6). The collisional viscosity is not implemented in ANSYS CFX-10 and also omitted in this work. For completeness of the granular flow models in the documentation of the software, collisional viscosity is given by

$$\mu_s = \frac{4}{5} c_s^2 d_p \rho_s g_0 \left(1 + \eta\right) \frac{T_s}{\pi}^{1/2}. \tag{6.4}$$

The bulk viscosity is modelled by equation (5.8). In CFX-10, the values of the granular temperature can be calculated using one of three approaches: specifying a constant value, a zero-equation model (ZEM), or an algebraic equilibrium model (AEM). In addition, one can choose not to select models for the granular temperature altogether. In this study, the case where not granular temperature is calculated (hereafter referred to as NTM), the ZEM, and the AEM models were investigated.

6.2.1 Zero-equation model for T_{s}

The zero-equation model was derived by Ding and Gidaspow (1990). Considering a simple shear single-phase flow, the granular temperature given by equation (5.10) was reduced to

$$\mathfrak{T}_{xy}\frac{\partial U_x}{\partial y} - \gamma = 0. \tag{6.5}$$

Substituting the constitutive equations (6.1) and (5.14) into equation (6.5) and simplifying yields

$$T_{\mathrm{s}} = \frac{d_{\mathrm{s}}^2}{5(3-a)}\frac{1}{(1-e)}\left(\frac{\partial U_x}{\partial y}\right)^2, \tag{6.6}$$

where a can be either 0 or 1. In CFX-10, a is set to 0, and equation (6.6) is implemented as

$$T_{\mathrm{s}} = \frac{d_{\mathrm{s}}^2}{15(1-e)}S_{sij}^2. \tag{6.7}$$

6.2.2 The algebraic equilibrium model for T_{s}

The algebraic equilibrium model is based on the local equilibrium assumption applied to the modelled transport equation of the granular temperature (e.g. equation (5.10)). In its application, the advection and diffusion parts of equation (5.10) are neglected so that the production is equal to the dissipation:

$$\text{Production} = \text{Dissipation} \Longrightarrow \mathfrak{T}_{\mathrm{s}\,ij}\frac{\partial U_{si}}{\partial x_j} = \gamma \tag{6.8}$$

It is worth noting that the interaction source term in equation (5.10), which can be positive or negative depending on the flow physics (see for example Krampa-Morlu et al., 2006), is not implemented in CFX-10. The production term is calculated from the product of equation (6.1) and the solids-phase velocity gradient. Therefore, the left hand side of equation (6.8) is expanded as

$$\mathfrak{T}_{\mathrm{s}\,ij}\frac{\partial U_{si}}{\partial x_j} = \underbrace{-P_{\mathrm{s}}\frac{\partial U_{si}}{\partial x_j}\delta_{ij}}_{-P_{\mathrm{s}}\mathfrak{D}} + \underbrace{\mu_{\mathrm{s}}\left(\frac{\partial U_{si}}{\partial x_j}+\frac{\partial U_{sj}}{\partial x_i}\right)\frac{\partial U_{si}}{\partial x_j}}_{\mu_{\mathrm{s}}\mathfrak{S}^2} + \underbrace{\left(\xi_{\mathrm{s}}-\frac{2}{3}\mu_{\mathrm{s}}\right)\left(\frac{\partial U_{sk}}{\partial x_k}\delta_{ij}\right)^2}_{\lambda_{\mathrm{s}}\mathfrak{D}^2}, \tag{6.9}$$

The dissipation term is also modelled differently from equation (5.14) as

$$\gamma = 3\left(1-e^2\right)c_{\mathrm{s}}^2\rho_{\mathrm{s}}g_0T_{\mathrm{s}}\left[\frac{4}{d_{\mathrm{s}}}\left(\sqrt{\frac{T_{\mathrm{s}}}{\pi}}-\frac{\partial U_{sk}}{\partial x_k}\delta_{ij}\right)\right]. \tag{6.10}$$

Since the solids pressure, shear, and bulk viscosities depend on T_{s}, one can write

$$\begin{aligned} P_{\mathrm{s}} &\propto T_{\mathrm{s}} \\ \mu_{\mathrm{s}} &\propto T_{\mathrm{s}}^{1/2} \\ \xi_{\mathrm{s}} &\propto T_{\mathrm{s}}^{1/2} \end{aligned} \tag{6.11}$$

or

$$\begin{aligned} &P_{\mathrm{s}} = P_{\mathrm{s}}^{(0)}T_{\mathrm{s}} \\ &\mu_{\mathrm{s}} = \mu_{\mathrm{s}}^{(0)}T_{\mathrm{s}}^{1/2} \ \text{ and } \ \xi_{\mathrm{s}} = \xi_{\mathrm{s}}^{(0)}T_{\mathrm{s}}^{1/2} \ \Rightarrow \ \lambda_{\mathrm{s}} = \lambda_{\mathrm{s}}^{(0)}T_{\mathrm{s}}^{1/2}. \end{aligned} \tag{6.12}$$

In equation (6.12), quantities with the superscript $^{(0)}$ denote proportionality constants. It should be noted that the treatment of these proportionality constants are not outlined in the documentation of the software. Recall the definition of λ_{s} from equation (6.9).

Substituting equation (6.12) into equations (6.10) and (6.9), and using equation (6.8) yields a quadratic expression in the form

$$A_{\mathrm{D}}T_{\mathrm{s}} + \left(B_{\mathrm{P}} - B_{\mathrm{D}}\right)T_{\mathrm{s}}^{\frac{1}{2}} - A_{\mathrm{P}} = 0. \tag{6.13}$$

In equation (6.13), the subscript P and D denote production and dissipation coefficients, respectively. For the production coefficients,

$$A_{\mathrm{P}} = \lambda_{\mathrm{s}}^{(0)}\mathfrak{D}^2 + \mu_{\mathrm{s}}^{(0)}\mathfrak{S}^2 \tag{6.14}$$

and

$$B_{\mathrm{P}} = P_{\mathrm{s}}^{(0)}\mathfrak{D}; \tag{6.15}$$

where

$$\lambda_s = \lambda_s^{(0)} T_s^{\frac{1}{2}} = \left(\xi_s^{(0)} - \frac{2}{3} \mu_s^{(0)} \right) T_s^{\frac{1}{2}} \geq 0 \quad \text{and} \quad P_s = P_s^{(0)} T_s \tag{6.16}$$

are deduced from their functional relationship with the granular temperature. Similarly for the case of the dissipation, we have in conjunction with equation (6.10),

$$A_D = \frac{4}{d_s \pi} E_D \quad \text{and} \quad B_D = E_D \mathfrak{D}; \tag{6.17}$$

where

$$E_D = 3 \left(1 - e^2\right) c_s^2 \rho_s g_0 \geq 0. \tag{6.18}$$

From equations (6.17) and (6.18), equation (6.13) has a unique solution of the form

$$T_s^{\frac{1}{2}} = \frac{B_D - B_P + \sqrt{\left(B_D - B_P\right)^2 + 4 A_D A_P}}{2 A_D}, \tag{6.19}$$

which is always positive. In regions of low solids concentration, un-physical and very large values of T_s are calculated with this model. This problem is overcome by setting, as a reasonable estimate, an upper limit for T_s using the square of the mean velocity scale; the particular velocity scale used was not indicated in the software documentation.

6.2.3 Consideration for solids-phase turbulence

The solids-phase turbulence model in CFX-10 is an extension of the single-phase turbulence model. For phasic considerations, the models available are phase-dependent models comprised of algebraic (with options for zero-equation, user-defined eddy viscosity, or dispersed-phase zero-equation), two-equation, and Reynolds stress models. The two-equation and Reynolds stress models are recommended for use with the continuous phase. The developers of the multiphase models in CFX-10 limit the turbulence models for the dispersed phase to zero-equation and dispersed phase zero-equation models. In the present study, the dispersed-phase zero-equation model, which is the default model, is employed and calculated from

$$\mu_{st} = \frac{\rho_s}{\rho_f} \frac{\mu_{ft}}{\sigma}. \tag{6.20}$$

The value of the parameter σ depends on the relative magnitudes of the particle relaxation time and the turbulence dissipation time scale. By default it is set to $\sigma = 1$.

6.3 Summary of Experimental Data used for Comparison

The experiments simulated in the present study were taken from Gillies (1993). In the work of Gillies (1993), four pipe flow loops with nominal diameters of 53.2, 158.3, 263, and 495 mm were considered. A wide range of narrow and broad size distributions of sand were tested. Coal-in-water flow experiments were also performed in the 263 mm diameter pipe flow loop. The narrow size distribution sand particles consisted of mean diameters from $d_{\mathrm{p}} = 0.18$ mm to 2.4 mm, while the broad size distribution of sand had d_{p} from 0.29 mm to 0.38mm and coal particle diameters varied from 0.8 to 1.1 mm. In the study of Gillies (1993), a large database of pressure drop versus mixture velocity as well as local distributions of solids-phase velocity and concentration were provided using specialized equipment designed for particle-in-water slurry flows. The solids-phase velocities were measured along the arcs at $r/R = 0.4$ and 0.8 (see Figure 6.1) with a conductivity probe.

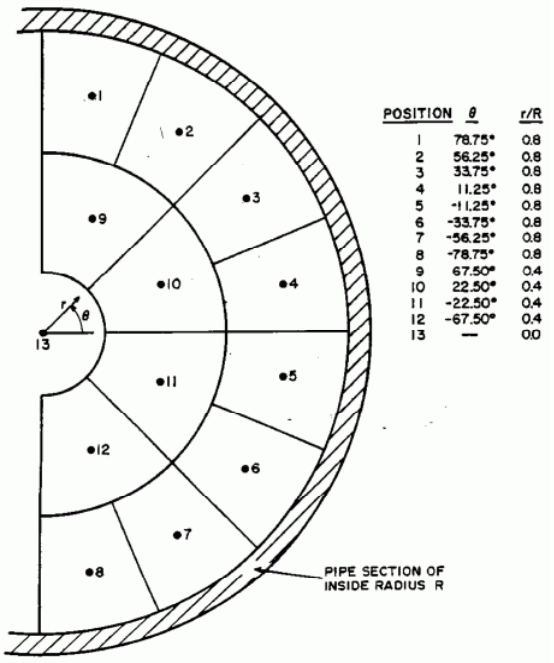

Figure 6.1: Sampling positions for particle velocity measurements. *Reproduced with permission from Pipeline Flow of Coarse Particle Slurries*, R. Gillies, Copyright (1993), University of Saskatchewan.

6.4 Simulation Matrix and Numerical Method

6.4.1 Simulation matrix

Two sets of the narrow size distribution sand particles with nominal diameters of $d_{\mathrm{p50}} = 0.18$ mm and 0.55 mm, and density $\rho_{\mathrm{s}} = 2650\mathrm{kgm}^3$ were considered. Preliminary investigation with larger sand particles, specifically $d_{\mathrm{p}} = 2.4$ mm lead to instabilities and divergence of the solver and, therefore was deferred to future work. Flows with solids bulk concentrations of 15 and 30% by volume in three different pipe flow loops of diameters, $D_{\mathrm{p}} = 53.2$, 158.3, and 263 mm were simulated. The experimental conditions used for the simulations are shown in Table 6.1. An overview of the specific flow conditions considered in this study are shown in Table 6.2. For the simulations reported here, the predictions by the

Table 6.1: Properties of liquid and solids-phase, flow conditions and CFX-10 model parameters and constants.

Description	Symbol	Value *Constituent properties*
fluid density	ρ_{f}	$\sim$ 998 kgm^{-3}
fluid viscosity	μ_{f}	10^{-3} Pa·s
solids density	ρ_{s}	2650 kgm^{-3}
solids viscosity	μ_{s}	10^{-8} and from models used
particle diameter	d_{p}	0.18, 0.55 mm
Inlet conditions		
mean velocity of fluid	U_{f}	3.05 $\sim$ 4.20 ms^{-1}
volume fraction of fluid	$(1 - C_{\mathrm{s}})$	0.85, 0.70
turbulence intensity	TI	0.1
turbulence kinetic energy of fluid	k_{f}	software default selected
dissipation rate of fluid	ε_{f}	software default selected
mean velocity of solids	U_{s}	3.05 $\sim$ 4.20 ms^{-1}
volume fraction of solids	C_{s}	0.15, 0.30
turbulence kinetic energy of solids	k_{s}	software default selected
dissipation rate of solids	ε_{s}	software default selected
granular temperature	T_{s}	software default selected

solids-phase stress models are compared with experimental results from Gillies (1993) as noted above while at the same time, some variation in the test conditions was also sought. Thus, only the input parameters of Runs 1 through 8, 15, and 16 in Table 6.2 match the experiments.

Table 6.2: Experimental and other flow conditions used in simulations

Run #	$d_p(\mu m)$	C_s (%)	U_{mixin} (m/s)	U_{sin} (m/s)	D (mm)	T_s model
1	180	15	3.05	2.94	53.2	-
2	180	15	3.05	2.94	53.2	Zero
3	180	15	3.05	2.94	53.2	AEM
4	180	30	3.05	2.72	53.2	AEM
5	550	15	3.05	2.78	53.2	AEM
6	550	30	3.05	2.68	53.2	-
7	550	30	3.05	2.68	53.2	Zero
8	550	30	3.05	2.68	53.2	AEM
9	180	15	3.05	2.94	158.3	AEM
10	180	30	3.05	2.72	158.3	AEM
11	550	15	3.05	2.78	158.3	AEM
12	550	30	3.05	2.68	158.3	AEM
13	180	15	3.05	2.94	263.0	AEM
14	180	30	3.05	2.72	263.0	AEM
15	550	15	4.21	4.09	263.0	AEM
16	550	30	4.17	4.00	263.0	AEM

6.4.2 Simulation approach

Initially, geometries were created in ANSYS Workbench (version 10), and a series of grid compositions using the Cad2Mesh suite from ANSYS CFX-10, were tested using unstructured mesh as well as a mesh system consisting of unstructured mesh with structured mesh near the wall of the pipe (hybrid mesh). In addition, structured meshes generated using CFX- Build from CFX-4 were also tested in CFX-10. After extensive preliminary evaluations of the grid systems, the hybrid mesh was found to produce the most realistic results.

For the three pipe diameters investigated, a pipe length of L = 2.0 m was used. An example of cross-sectional meshes for the hybrid grid at z = 0.25L, 0.5L, 0.75L, and L is

shown in Figure 6.2a. Initially, a major challenge in the present simulations was obtaining realistic results. This was not easily attainable with default parameters. The application of a 'black box' like CFX requires careful extensive parameter tuning. The use of the grid adaptation option with default setting of the adaptation parameters seemed to produced better qualitative results. The aim of the grid adaptation was to better resolve the characteristic asymmetric form of the field variables. It is acknowledged that a parametric study of the available grid adaptation parameter settings and variables to adapt would be worthwhile. However, this would be costly given the computational time for each simulation. A set of meshes resulting from the adaptation process as the flow becomes fully developed is shown in Figure 6.2b. The simulation was considered converged when the normalized residuals were reduced to a value $< 10^{-6}$ and not reducing, although all the simulations were slightly unstable around the converged value. A typical total CPU time for the calculations on a PC at 2.66 GHz with 1 GB of RAM ranges between approximately 3.3×10^3 and 1.7×10^5 seconds.

6.4.3 Boundary conditions

The inlet and outlet boundary conditions were specified in the same fashion as mentioned in the preceding chapter; for the wall boundary condition, the no-slip condition was set for both the liquid-phase and the solids-phase. It should be noted that in the two-fluid model context, the wall boundary condition for the solids-phase, particularly in horizontal flows such as the kind investigated in this study, is complex. The discussion in the preceding chapter on this topic for vertical flows with high solids bulk concentrations also indicate that existing models are inadequate. Moreover, the current version of CFX-10 does not provide an easily accessible option for setting the solids wall boundary condition. Hence, the present choice of a no-slip condition for the solids-phase is made to at least account for regions of the pipe where the no-slip condition for the solids-phase may be satisfied. It is assumed that in the near-stationary or moving-bed region, both phases would move at the same rate and, therefore, the liquid conditions can be applied to the solids. This is somewhat similar to the no-slip condition often imposed for the mixture model in the works of Roco and Shook (e.g. Roco, 1990). It should also be noted that the above argument is not

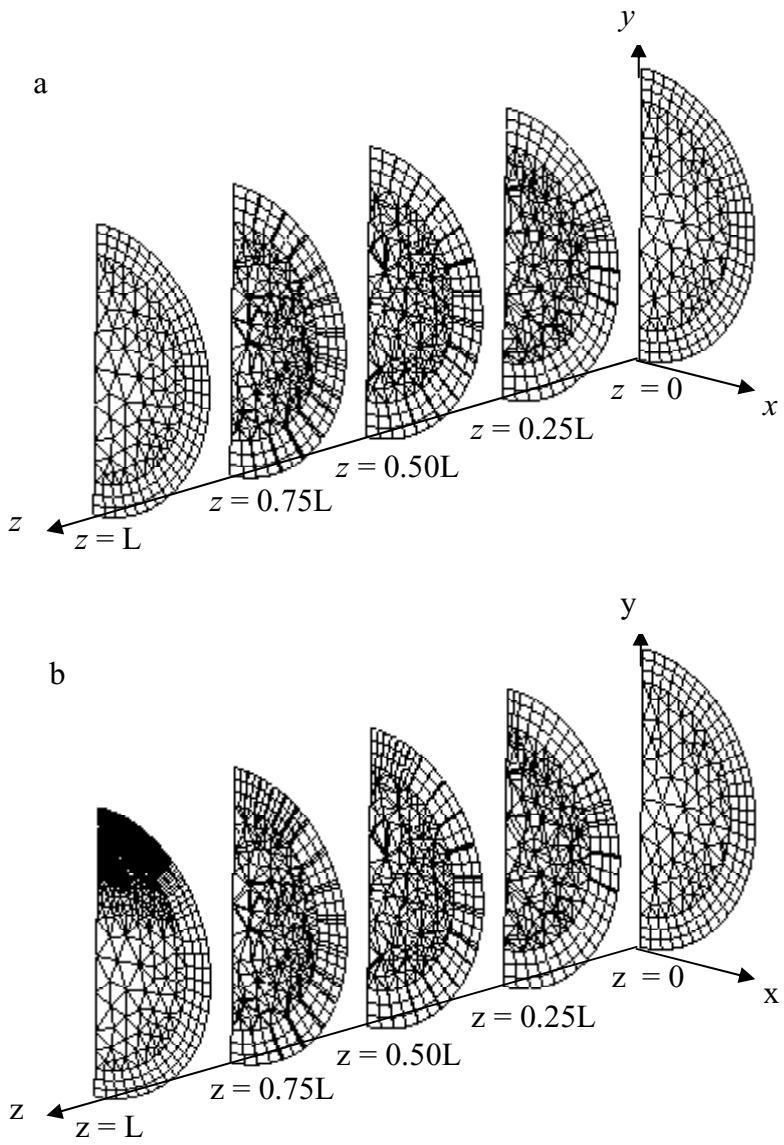

Figure 6.2: Cross-sectional grid distributions before and after simulation. (a) Original mesh generated prior to simulation; (b) Mesh due to adaptation after simulation.

completely true since at higher velocities, repulsive forces, in addition to particle-particle interactions, could cause the particles to move away from the wall creating a depleted solids region close to the wall. This phenomena has been observed by Daniel (1965) and linked to the so-called off-the-wall-lift model in the recent theoretical work of Wilson et al. (2000).

6.5 Discussion of Results

6.5.1 Preliminary simulations: Solids stress model comparison

Initial studies were conducted to investigate the solids-phase stress for two particle sizes at two solids bulk concentrations. The simulations correspond to Runs 1 to 3, and 6 to 8 in Table 6.2. Three cases in terms of the models for the granular temperature were considered: the NTM, ZEM, and the AEM models. The simulation results at $z = \mathrm{L}$ are used for the discussion in the sections below.

6.5.1.1 Flow with medium particles

Contour plots for the solids-phase velocity and concentration are shown in Figure 6.3 for the 180 μm sand particles with solids bulk concentration of 15% in water in the 53.2 mm pipe (Runs 1 through 3). In Figure 6.3, the expected characteristics of negatively buoyant particles in liquid flows can be seen. All three plots show that the location of the maximum solids-phase velocity, presented on the left hand side, is located above the centre of the pipe. The solids concentration contours are shown on the right hand side of Figure 6.3. The concentration contours produced by all the models appear similar, especially for Runs 1 and 3, and the distributions are non-symmetric as in the case of the solids-phase velocity distribution. The phasic velocity and concentration distributions plotted along the centre-line in the vertical plane of the pipe are shown in Figures 6.4a through 6.4c. It is interesting to note that the velocity and concentration predictions are identical and collapse onto one curve for all three cases. That is the NTM, ZEM, and the AEM models produce similar phasic velocity and concentration distributions. In Figure 6.4a, the liquid-phase velocity increases from the bottom wall of the pipe, attains a maximum value at about $0.75D$ from the bottom wall and then decreases to a finite value at the top wall. The trend is similar for the

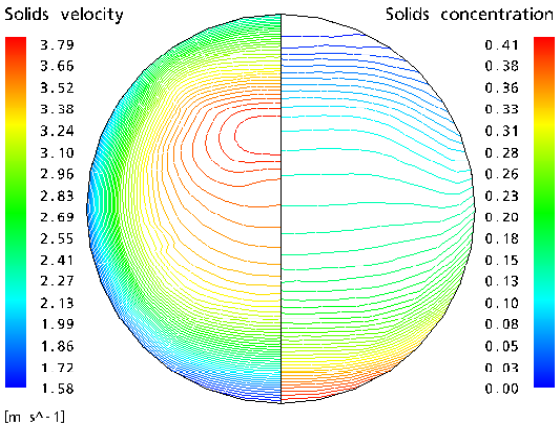

(a) Run 1: No model for T_s

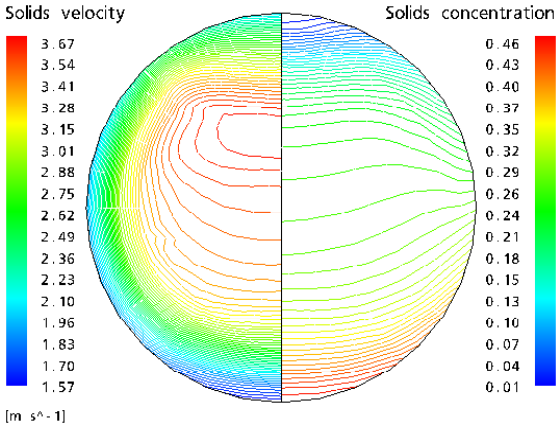

(b) Run 2: Zero-equation model

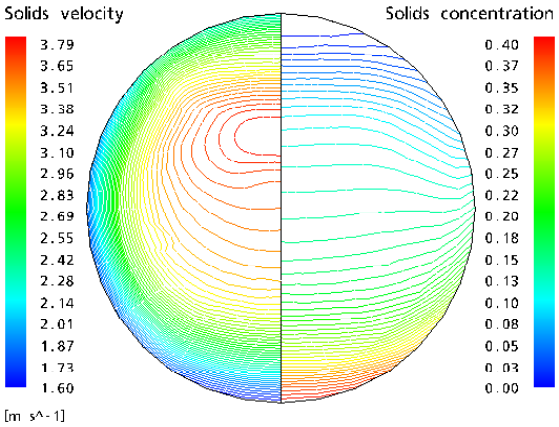

(c) Run 3: Algebraic equilibrium model

Figure 6.3: Contour plots of solids-phase velocity and concentration for 0.18 mm sand-in-water flow in 53.2 mm pipe with $C_s = 15\%$: comparison of solids stress models.

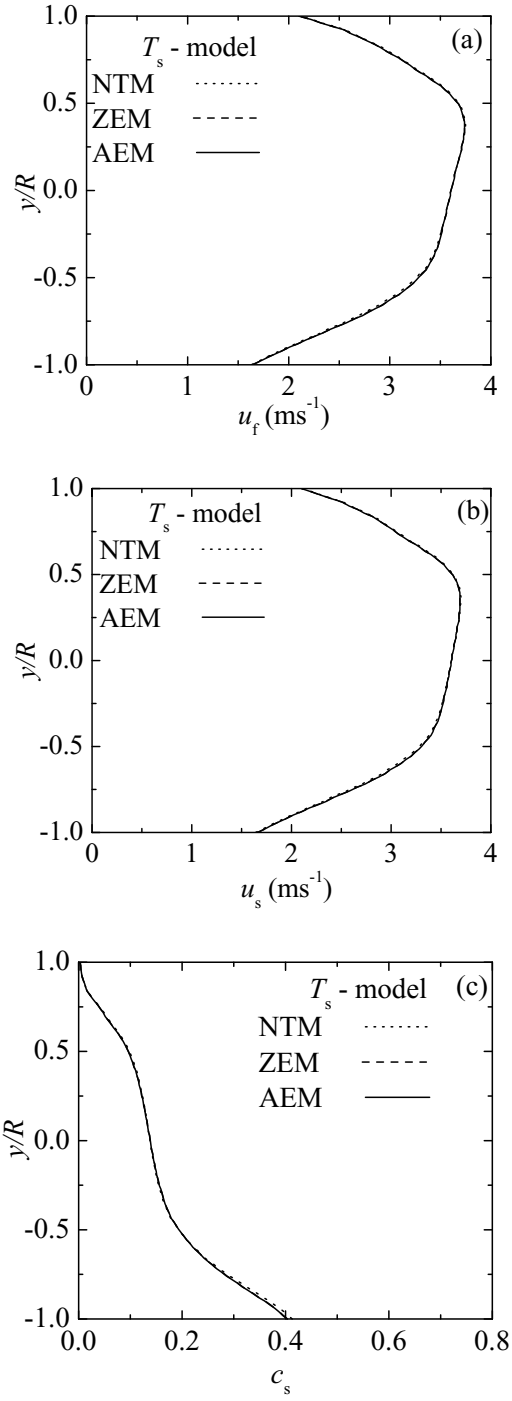

Figure 6.4: Comparison between model predictions of phasic velocity and concentration distributions for 0.18 mm sand-in-water flow in 53.2 mm pipe at $C_s = 15\%$. (a) Liquid velocity, (b) solids-phase velocity, and (c) Solids concentration.

solids-phase, for which the velocity (Figure 6.4b) increases as the concentration decreases (Figure 6.4c) from the bottom wall of the pipe toward the top, but then decreases near the top wall.

6.5.1.2 Flow with coarse particles

The model predictions were also obtained in the 53.2 mm pipe for larger particles at a higher solids bulk concentration of 30% (see Run 6 through 8 in Table 6.2). The solids-phase velocity predicted using the zero-equation and the algebraic equilibrium models for the granular temperature are again very similar. Figure 6.5 shows the predictions of the solids-phase velocity and concentration contours for the AEM case. Similar observations of asymmetric feature can also be made for the solids concentration contours on the right hand side of Figure 6.5 as for the case of the medium particles. For the larger particles at higher solids bulk concentration, the solids concentration is lower near the top of the pipe. In Figure 6.6, the local distribution of phasic velocity and concentration are presented for Run 6 through 8. The results produced by the case of the NTM model are different from those using the ZEM and AEM models, particularly in the lower part of the pipe. As it can be seen from Figures 6.6a and 6.6b, the values of the velocity predicted with the NTM model for both the liquid and solids-phase are about 0.5 m s^{-1} lower than those calculated with the ZEM and AEM models. For the solids concentration, the NTM model predicted a higher value, which exceeds the maximum packing of 0.63%, than that predicted by the granular theory models. However, the type of granular temperature model did not influence the results.

From the viewpoint of the flow physics, it can be seen that the additional stress due to the solids-phase is important for medium and coarse particles in liquid-solid flows. In addition, the wall boundary conditions cannot be neglected as was noted for vertical flows in Chapter 5 when dense flows are considered. Even though wall boundary conditions were not specifically investigated, their effect cannot be ignored. For the negatively buoyant particles of interest in the present work, higher solids concentration at the bottom wall

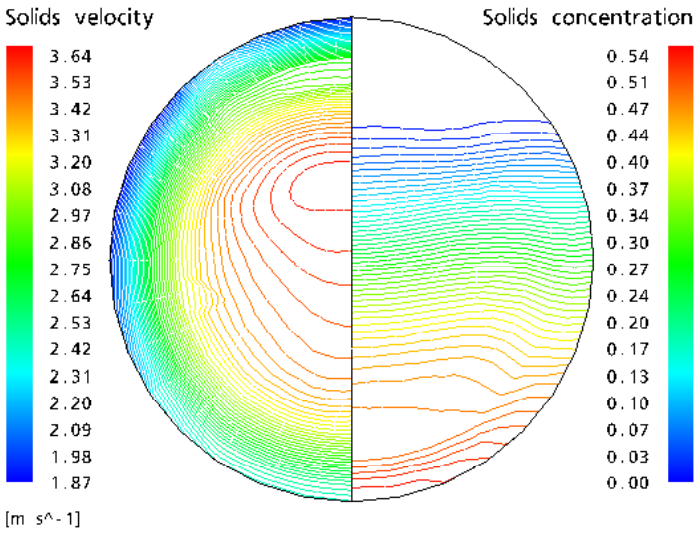

Figure 6.5: Contour plots of solids-phase velocity and concentration for 0.55 mm sand-in-water flow in 53.2 mm pipe with $C_s = 30\%$ using the AEM model (Run 8).

and lower at the top wall is inevitable. The solids concentration distribution are dependent on the volume flow rate, which also controls the interaction between the solids and the wall. The contour plots have shown qualitatively that the solids concentration at the wall influences the velocity prediction along the wall of the pipe.

6.5.2 Comparison between predictions and experimental data

In this section, solids-phase velocity and concentration distributions are compared with measured data. The experimental data was taken from the study of Gillies (1993). The calculations with the AEM model for T_s are used for the comparison. The AEM was chosen for two reasons. First, the NTM model does not consider closure for the solids-phase stress. For larger particles at high solids bulk concentration, the NTM model appears to over-predict the solids concentration at the bottom wall of the pipe. Secondly, the ZEM model was derived on the assumption that the flow is a simple shear single-phase flow with a uniform granular temperature. Hence, the solids concentration has to be zero to derive the ZEM model. Thus, while the AEM does not count for convection and diffusion in the transport of the fluctuating energy of the solids-phase, it is less *ad hoc* compared to the NTM and the ZEM models.

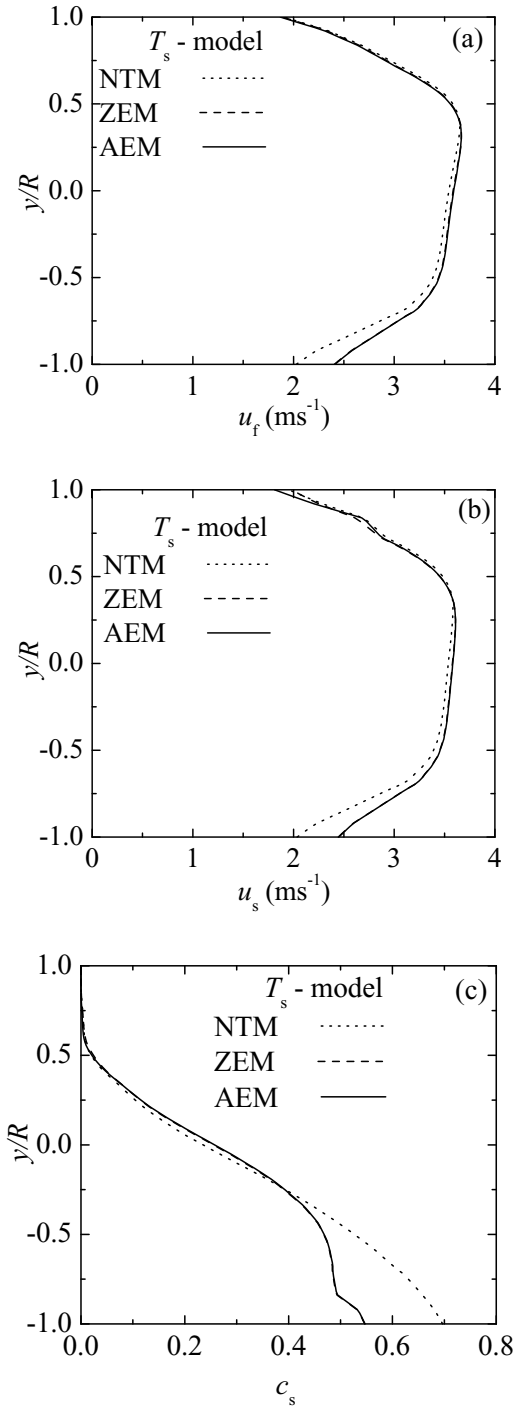

Figure 6.6: Comparison between model predictions of phasic velocity and concentration distributions for 0.55 mm sand-in-water flow in 53.2 mm pipe at $C_s = 30\%$. (a) Liquid velocity, (b) solids-phase velocity, and (c) Solids concentration.

Figure 6.7a shows the predicted and measured solids-phase velocity for 0.18 mm particles at a concentration of 15%. The locations plotted correspond to points 1 through 8 in Figure 6.1 ($r/R = 0.8$). Here the results are plotted against normalized vertical distance (y/R) from the bottom wall. That is the (y/R) points corresponds to the projection of the (r/R) points on the vertical centreline. It should, therefore, be noted that the velocity profiles actually represent values not far from the wall of the pipe. The predicted velocity is higher than the corresponding measured values.

The solids concentration is shown in Figure 6.7b where both the experimental and the predicted profiles are chord-averaged. It is worth noting that for the experimental data, the locations of the chord-average concentration profiles do not correspond to those for the velocity data. For this vertical distribution, the prediction matches the measured data in the core region of the pipe, but not near the wall. The solids concentration is, especially, over-predicted at the lower wall. This is consist for other conditions simulated. While the wall boundary condition for the solids concentration is usually specified by setting the normal gradient to zero,

$$\frac{\partial c_s}{\partial n} = 0, \tag{6.21}$$

the form of its implementation in CFX-10 is unknown to the user. An incorrect wall boundary condition for the solids-phase velocity would consequently lead to inaccurate concentration at the wall. The physical importance and implications of wall boundary conditions for these kinds of flows have been noted in the preceding chapters. In the region away from the top and bottom walls, the concentration prediction matched the measured data. Similar observations can be made for the 0.18 mm particles at solids bulk concentration of 30% (Figures 6.8a and b), and the 0.55 mm particles at solids bulk concentrations of 15% and 30% (Figures 6.8c to f), respectively. It is, therefore, noted that whereas the contour plot predictions are qualitatively reasonable, the point values do not match the measured data. A critical observation and conclusion is that the present models in CFX-10 cannot satisfactorily predict dense flow of large particles in liquids. In slurry flow, a paramount objective is to move the mixture without settling the particles. Therefore, from modelling viewpoint,

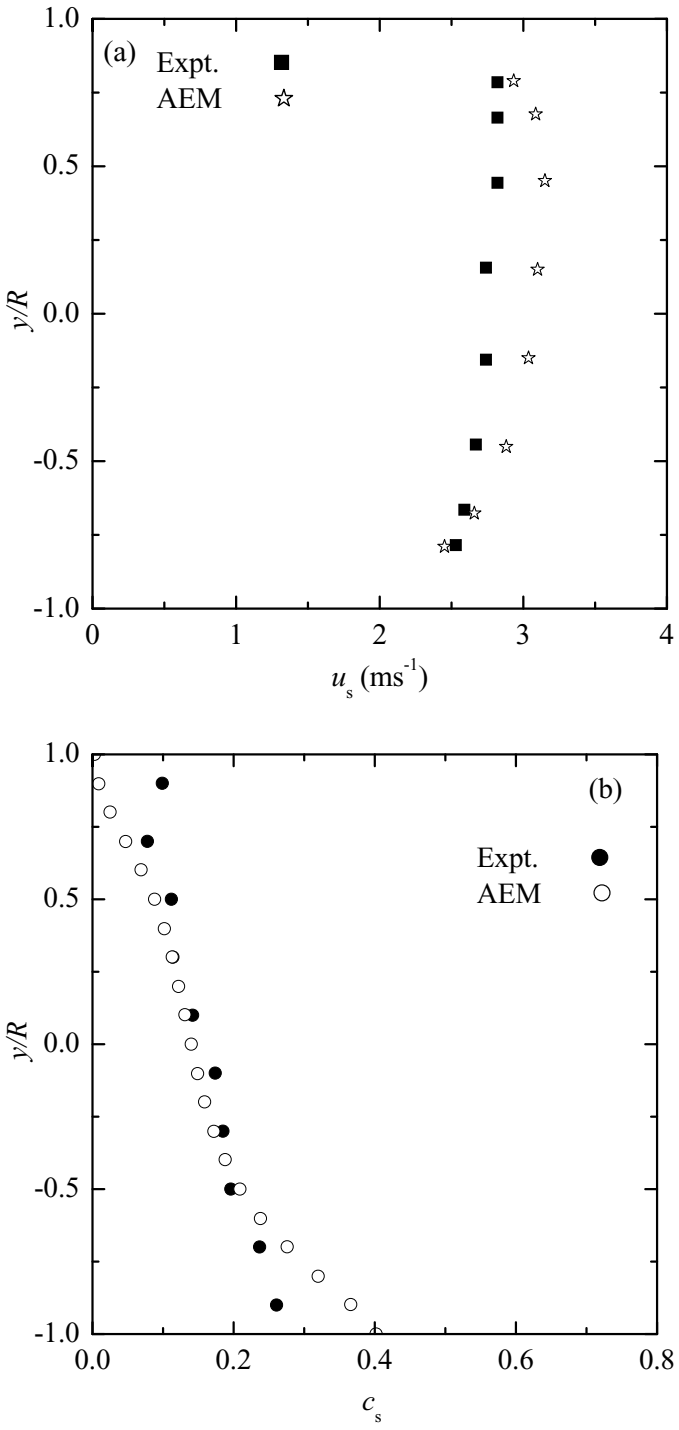

Figure 6.7: Comparison between model predictions and experimental data for 0.18 mm sand-in-water flow in a 53.2 mm horizontal pipe at $C_s = 15\%$; (a) solids-phase velocity profile along $r/R = 0.8$ plotted against projected vertical distance along the centreline, and (b) chord-averaged solids concentration distributions. Experimental data was taken from Gillies (1993).

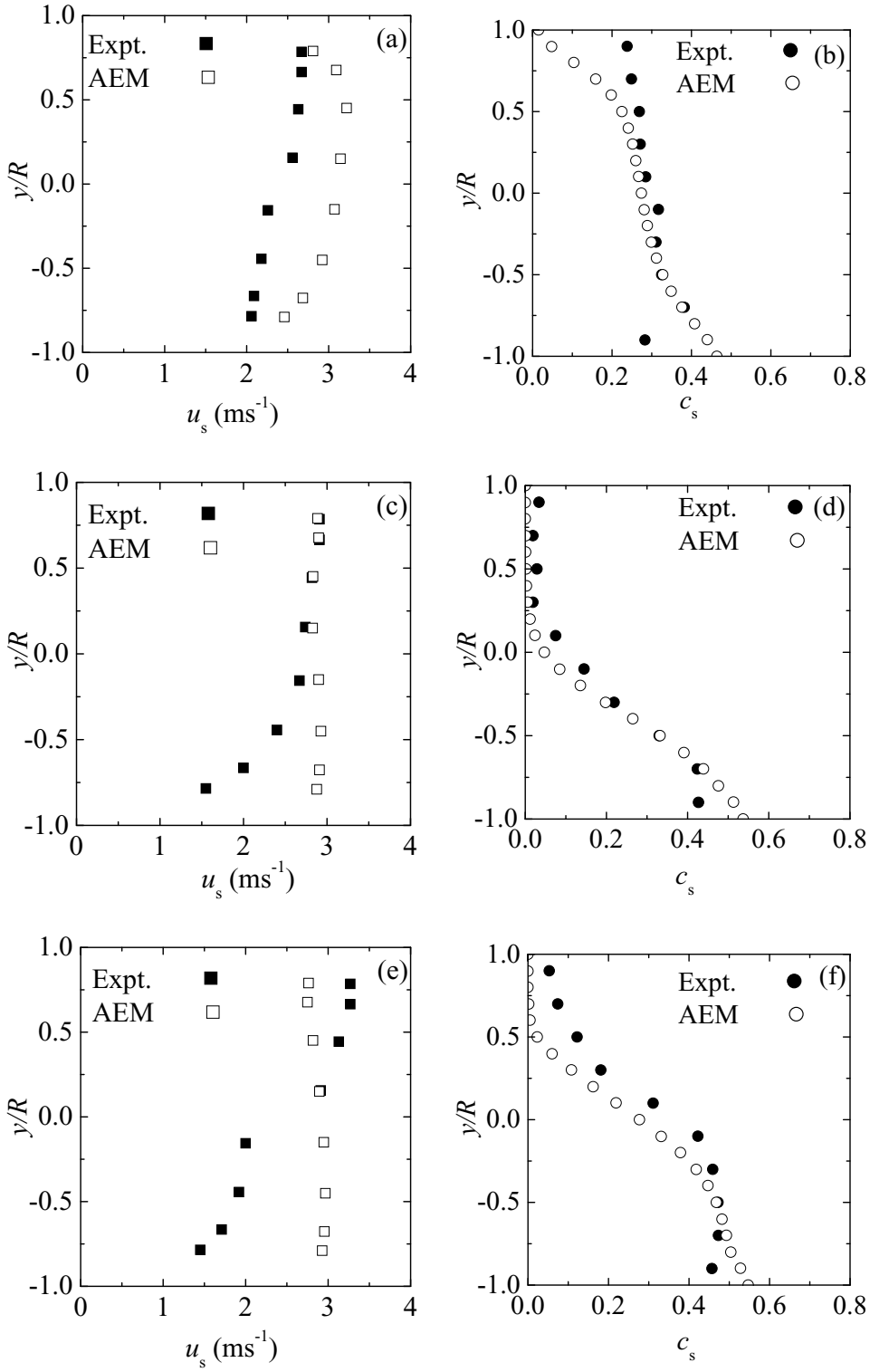

Figure 6.8: Comparison between experimental and predicted phasic velocity and concentration distributions of sand-in-water flow in 53.2 mm pipe: (a)-(b) 0.18 mm particles at $C_s = 30\%$; (c)-(d) 0.55 mm particles at $C_s = 15\%$; and (e)-(f) 0.55 mm particles at $C_s = 30\%$. Experimental data was taken from Gillies (1993).

the flow dynamics in the wall region is of particular interest. The predictions presented in this study indicate that the models investigated fail to reproduce velocity and concentration behaviour in the bottom wall regions of the pipe.

6.5.3 Discussion of concentration, particle size, and pipe diameter effects

In this section, discussion of the model predictions using the algebraic equilibrium model for the granular temperature is presented. The effects of solids bulk concentration, particle diameter, and pipe diameter are discussed. It is worth noting that the results obtained for Runs 13 through to 16 are not discussed in this section. The solids-phase velocity and concentration contours are shown in Figures F.1 and F.2 in Appendix F. The velocity predictions were somewhat similar to other calculations but the concentration distributions calculated were different. For these simulations, the solids concentration distributions along the centreline did not exhibit the expected features.

6.5.3.1 Solids concentration effect in the 53.2 mm pipe

The effects of solids bulk concentration on the flow of 0.18 mm and 0.55 mm particles in the 53.2 mm diameter pipe are discussed in this section. The contours of solids-phase velocity and concentration calculated for the 0.18 mm sand particles using the AEM model at solids bulk concentrations of 15% and 30% (i.e. Runs 3 and 4) are shown in Figure 6.9. Both plots show the expected asymmetric feature of the velocity and concentration distributions for the solids-phase. The solids-phase velocity and concentration profiles along the vertical through the centre of the pipe are shown in Figure 6.10. Figure 6.10 presents the (a) the solids-phase velocity and (b) the solids concentration profiles for the 0.18 mm sand particles for Runs 3 and 4. The vertical location is normalized by the radius of the pipe. In Figure 6.10a, the solids-phase velocity profiles have almost the same shape indicating no effect of solids bulk concentration on the 0.18 mm sand slurry flows at 15% and 30% solids bulk concentration. Figure 6.10a shows that in the lower 25% region of the pipe, the effect of concentration on the velocity is negligible and a constant shear layer depicted by the almost linear curve can be seen. In the same region the solids concentrations, shown in Figure 6.10b, decreases as the distance from the bottom wall increases but the solids

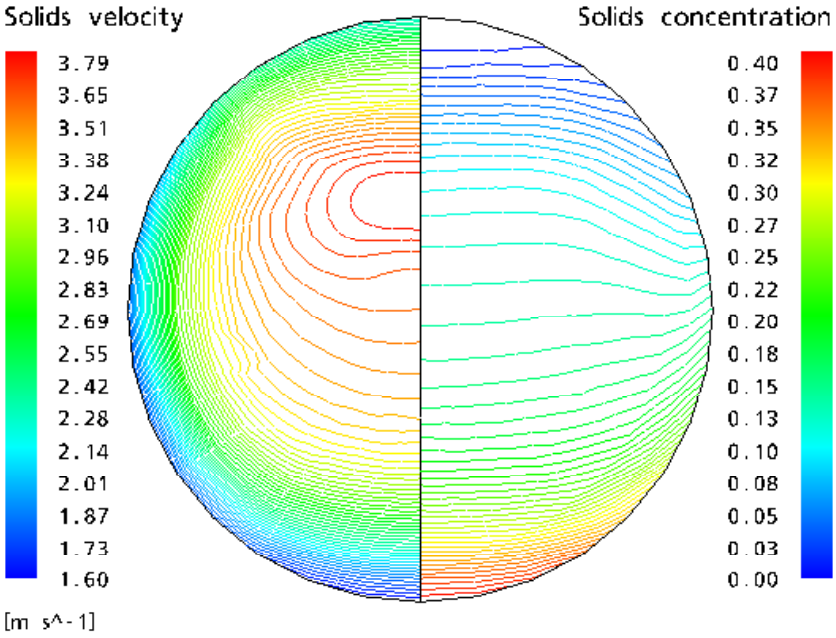

(a) solids-phase velocity and concentration at $C_s = 15\%$

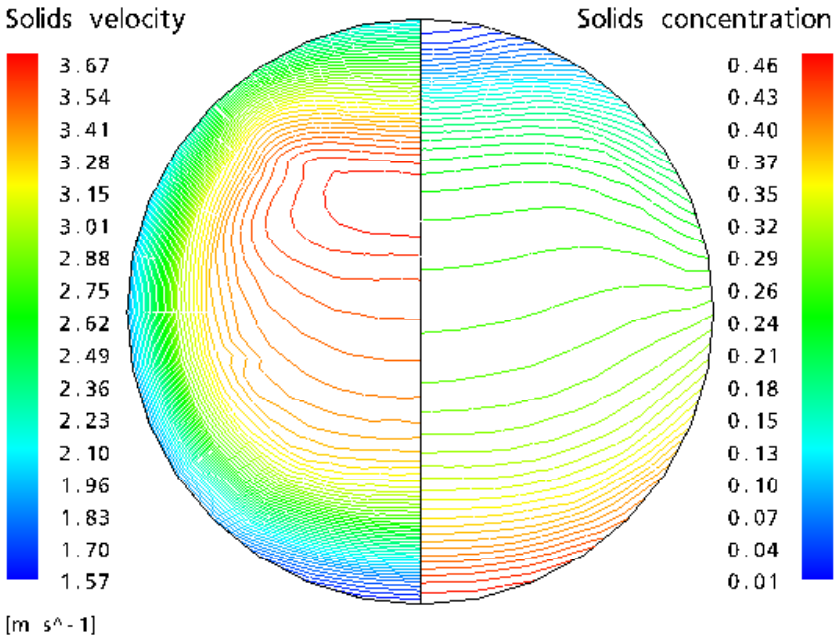

(b) solids-phase velocity and concentration at $C_s = 30\%$

Figure 6.9: Contour plots of solids-phase velocity and concentration for 0.18 mm sand-in-water flow in 53.2 mm pipe.

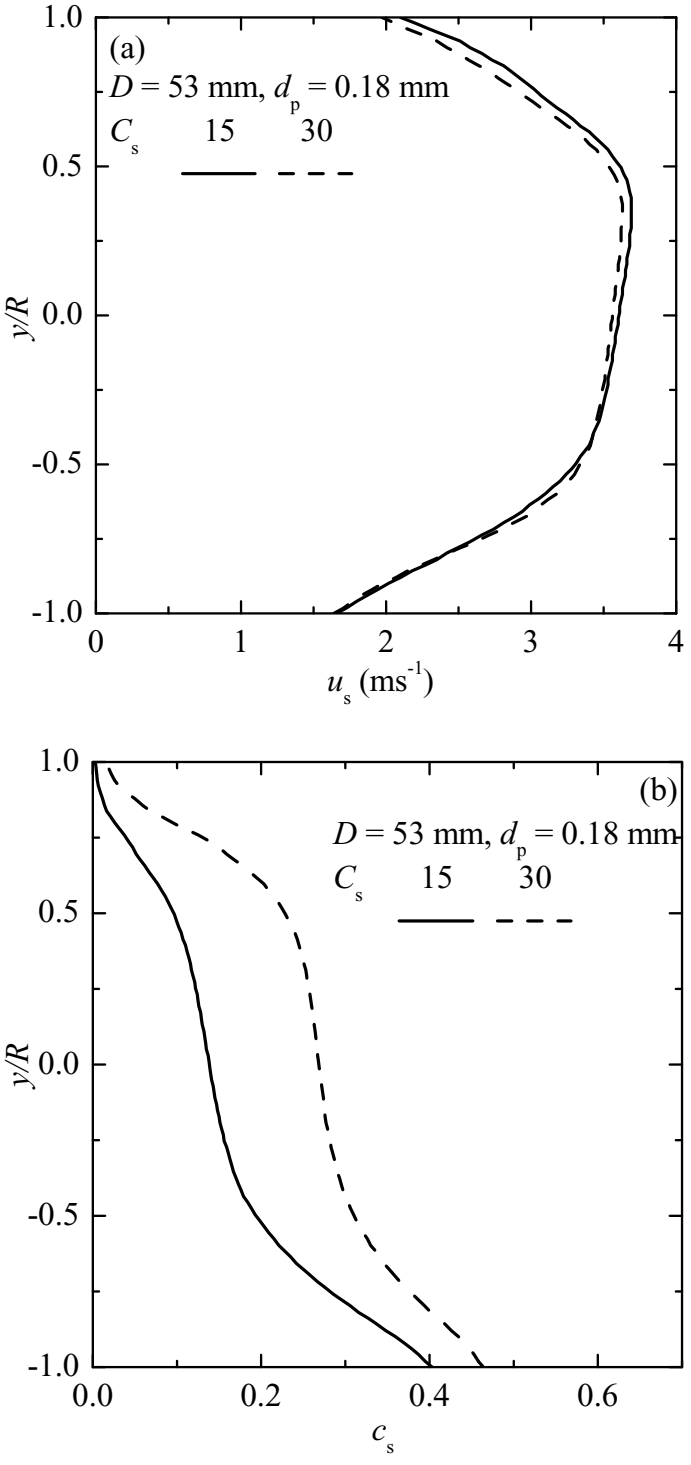

Figure 6.10: solids bulk concentration effect on solids-phase velocity and concentration distributions in 53.2 mm pipe for flow with 0.18 mm particles. (a) solids-phase velocity , and (b) concentration of 0.18 mm sand-in-water mixture in 53.2 mm pipe at $C_s = 15\%$ and 30%.

concentration for the 15% mean value is much lower than that for the 30% mean value. Physically, the values of the solids concentration is expected to be the same in that region. In the core region, $-0.5 < y/R < 0.5$, another constant and much lower shear is apparent and the solids-phase velocity at solids bulk concentration of 15% is only slightly larger than that of 30%. In the same region, the difference between the solids concentration profiles also increases. The solids-phase velocity peaks around $y/R \approx 0.5$ (generally observed for the conditions simulated) and beyond that decreases to a minimum at the upper wall. Correspondingly, the solids concentration decreases to a minimum at the upper wall, where the value for the 30% solids bulk concentration is still higher than that for the 15% case.

For the larger particles ($d_{\mathrm{p}} = 0.55$ mm for Runs 5 and 6), shown in Figure 6.11, the respective magnitudes of both the velocity and concentration for the two solids bulk concentrations show that variations exist, particularly, in the solids concentration field. The solids-phase velocity and concentration profiles for Runs 5 and 6 are presented in Figures 6.12a and 6.12b, respectively. It can be seen that the solids-phase velocity profiles at solid mean concentrations of 15% and 30% are almost identical. The solids concentrations near the lower and upper walls are also similar, whereas in the core region, the solids concentration values are consistently different.

6.5.3.2 Solids concentration effect in the 158.3 mm pipe

Figure 6.13a shows contour plots for the solids-phase velocity and concentration for flow in a 158.3 mm pipe using the 0.18 mm sand particles at solids bulk concentration of 15% (i.e. Run 9). Recall that the inlet velocity and concentration fields for this run are the same as those of Run 3 (see Table 6.2) to enable investigation of any pipe diameter effect. For this pipe diameter, Gillies (1993) reported no flow information for the particles with a narrow size distribution. Figure 6.13b presents contours for the flow at 30% mean concentration. The solids concentration effect on the solids-phase velocity in Figures 6.13a and 6.13b is not significant. The solids-phase velocity profiles along the centreline presented in 6.14a show similar behaviour. On the right-hand side of the contour plots, the solids concentration is constant in the core region of the pipe (this is more clearly shown using

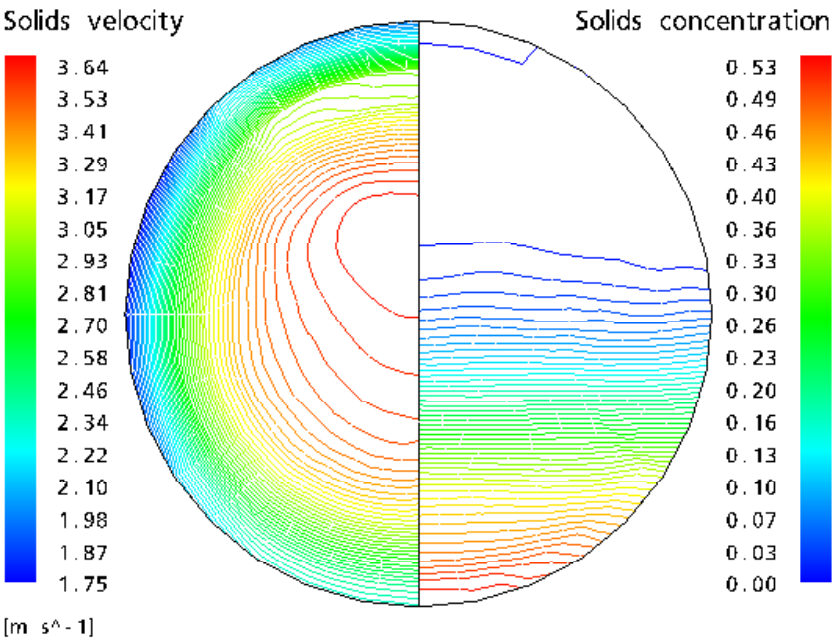

(a) solids-phase velocity and concentration at $C_s = 15\%$

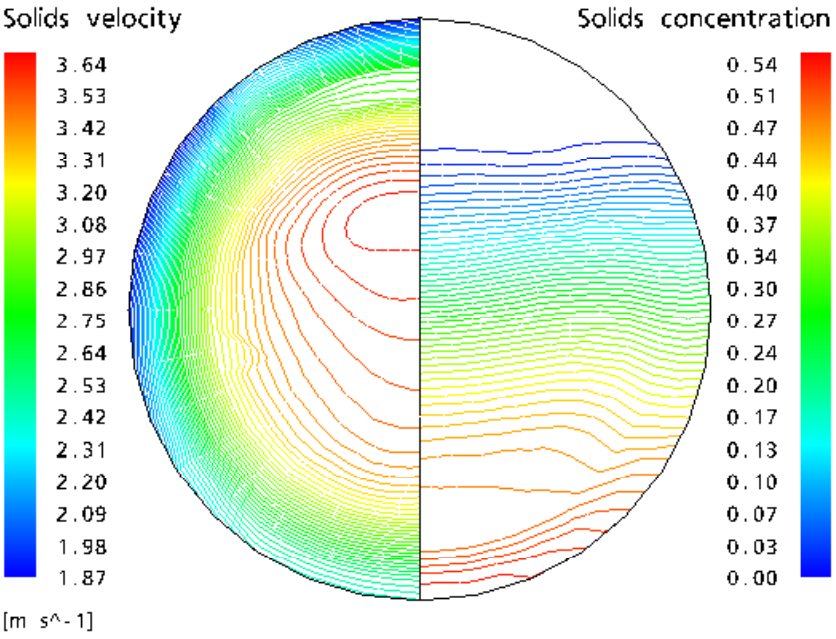

(b) solids-phase velocity and concentration at $C_s = 30\%$

Figure 6.11: Contour plots of solids-phase velocity and concentration for 0.55 mm sand-in-water flow in 53.2 mm pipe.

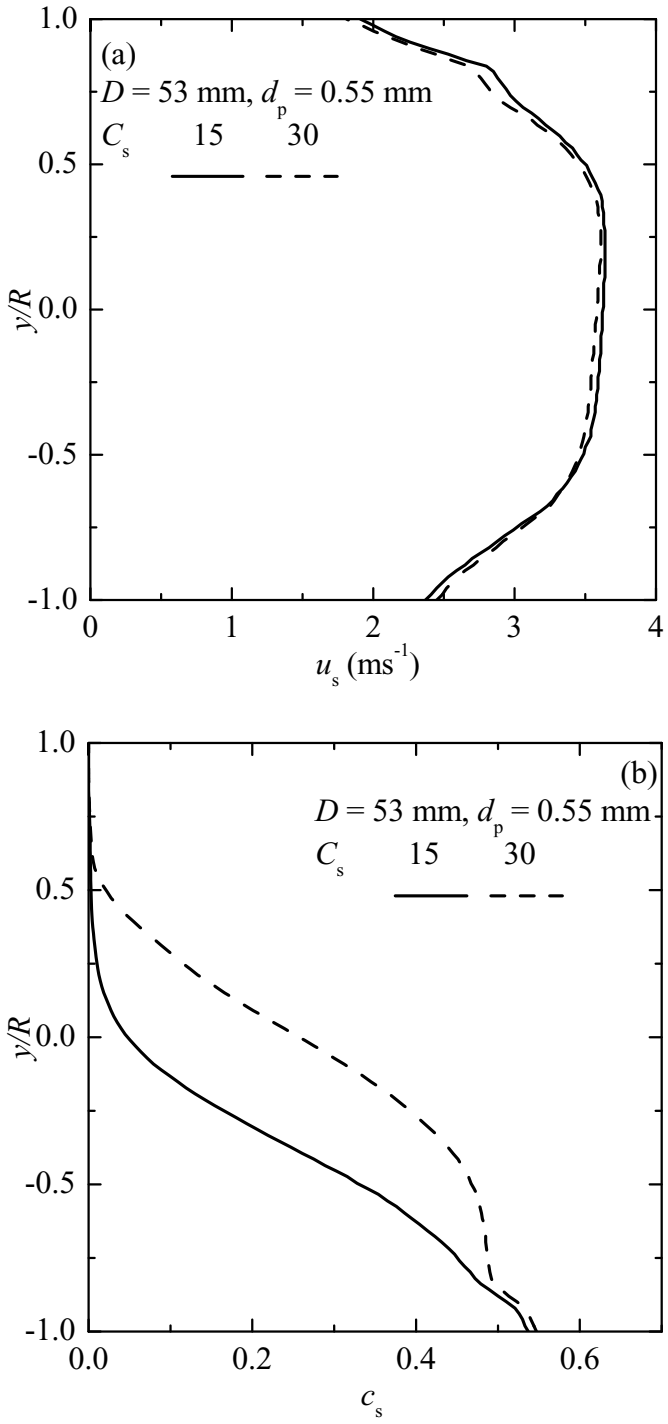

Figure 6.12: Solids bulk concentration effect on solids-phase velocity and concentration distributions in 53.2 mm pipe for flow with 0.55 mm particles. (a) solids-phase velocity, (b) concentration of 0.55 mm sand-in-water mixture in 53.2 mm pipe at C_s = 15% and 30%.

the centreline profile in Figure 6.14b).

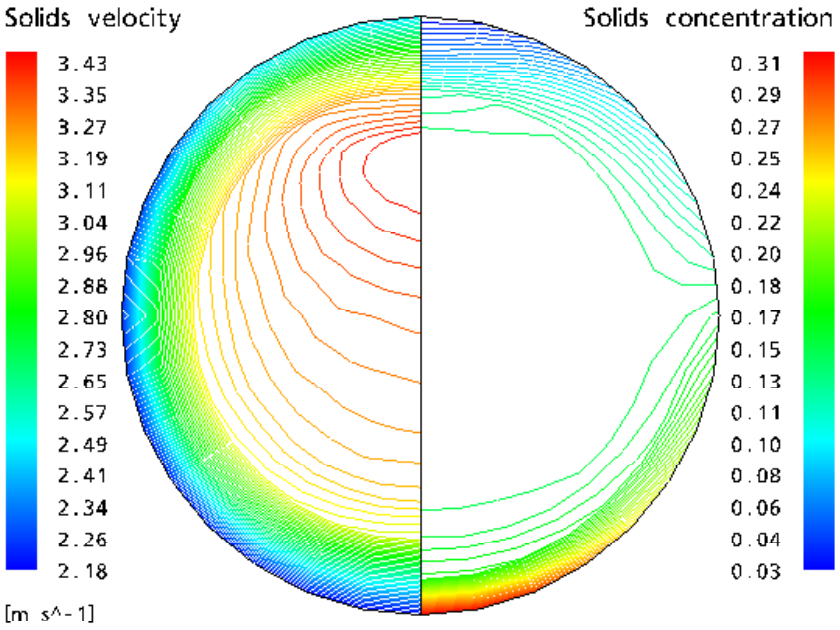

(a) solids-phase velocity and concentration at $C_s = 15\%$

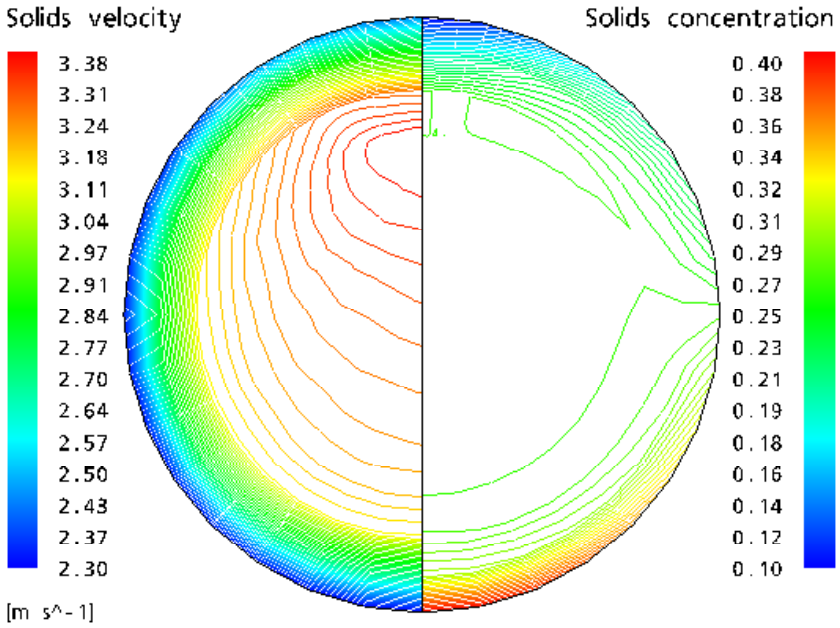

(b) solids-phase velocity and concentration at $C_s = 30\%$

Figure 6.13: Contour plots of solids-phase velocity and concentration for 0.18 mm sand-in-water flow in 158.3 mm pipe.

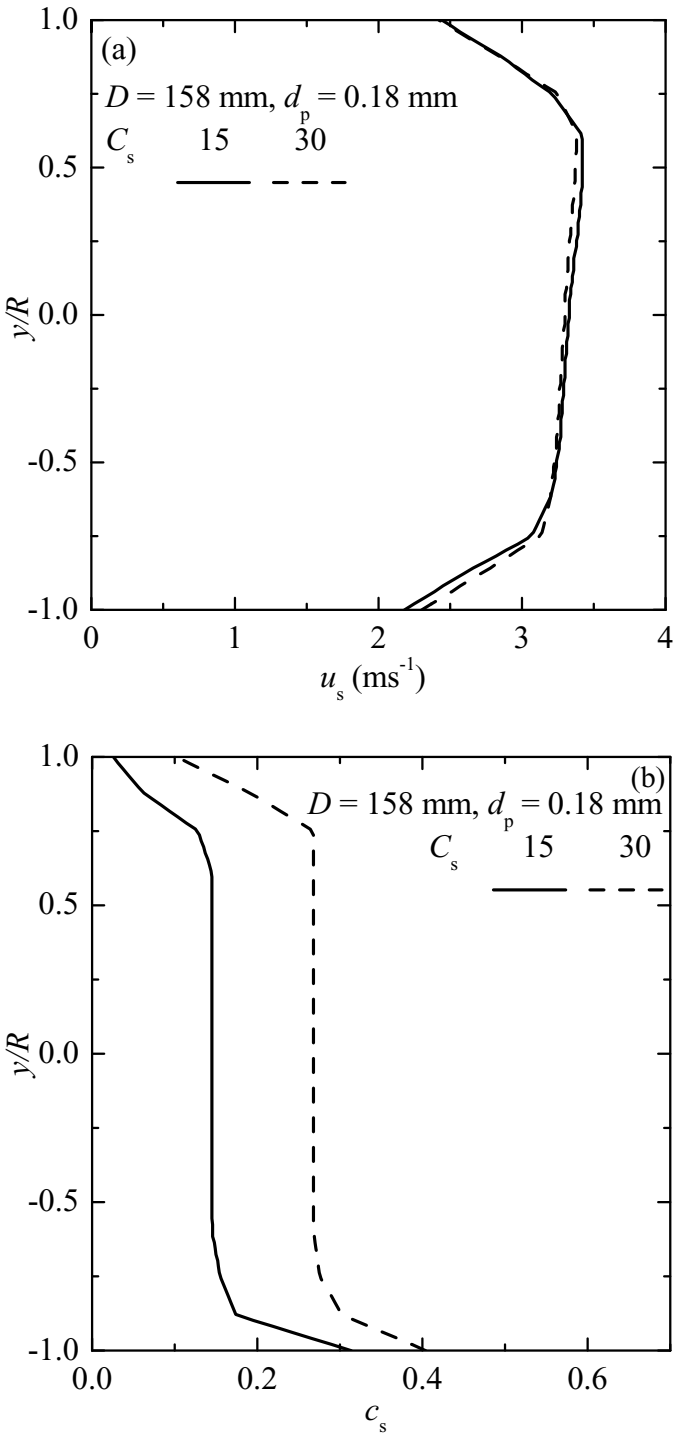

Figure 6.14: solids bulk concentration effect on solids-phase velocity and concentration distributions in 158.3 mm pipe for flow with 0.18 mm particles. (a) solids-phase velocity , (b) concentration of 0.18 mm sand-in-water mixture in 158.3 mm pipe at $C_s = 15\%$ and 30%.

The results for the larger particles (0.55 mm) are shown in Figure 6.15 in which the contour plots for the solids-phase velocity and the concentration are presented. As discussed above for flow in the smaller pipe in Section 6.5.3.1, the data shows that the magnitudes of the velocity and concentration for the two solids bulk concentrations are similar. In Figure 6.16a, the vertical profiles of the solids-phase velocity are similar, whereas the solids concentration in Figure 6.16b exhibits a trend that is similar to that observed for Run 3. However, the solids concentration at the wall is much higher and identical ($\approx$ 60%) for both solids bulk concentrations.

6.5.3.3 Particle diameter effect

Figures 6.17a and 6.17b show the solids-phase velocity and concentration profiles, respectively, for flows with 0.18 mm and 0.55 mm sand particles at a solids bulk concentration of 15% for flow in the 53.2 mm diameter flow loop. In Figure 6.17a, the flow with the 0.55 mm particles produced a higher solids-phase velocity than that for the 0.18 mm particles in the lower half of the pipe. However, the solids-phase velocity is slightly higher in the upper half of the pipe for the 0.18 mm particles. A similar trend can be seen for the solids concentration in Figure 6.17b. The solids concentration at the wall is higher for the 0.55 mm particles indicating a strong particle diameter effect. In the wall region, smaller particles can be trapped within the liquid-phase sublayer where the local turbulence is damped. For larger particles, their sizes can be larger than the characteristic size of the sublayer and the local turbulent hydrodynamic force can dislodge them from the sublayer resulting in acceleration. The effect of particle diameter on the solids-phase velocity at a solids bulk concentration of 30% is shown in Figure 6.18a and on the solids concentration in Figure 6.18b. The behaviour is almost identical to those noted for the case of the 15% solids bulk concentration. Moreover, the solids concentration is higher in lower region of the pipe. The effect of particle diameter in the larger pipe was similar to that described above. The main difference was that both the velocity and solids concentration fields are uniform in the core region of the pipe.

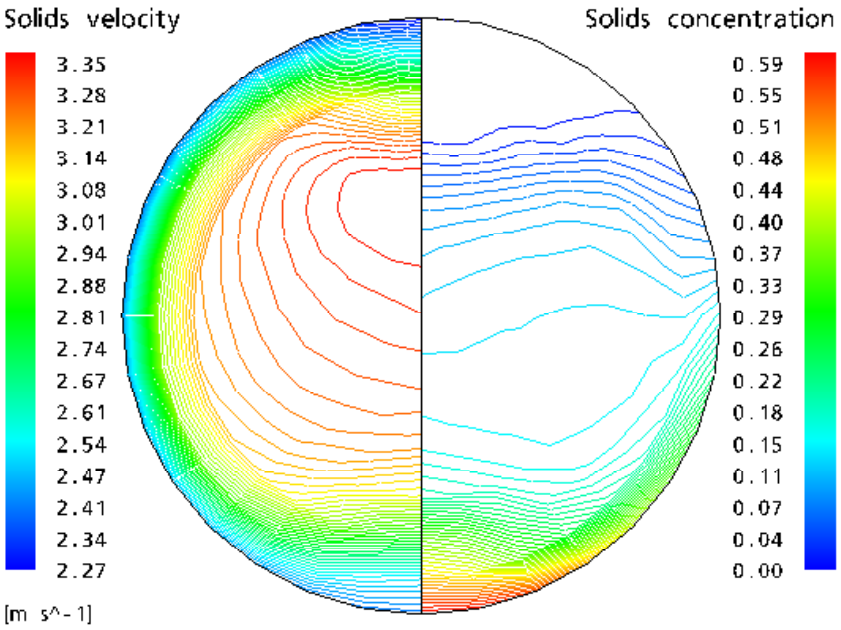

(a) solids-phase velocity and concentration at $C_s = 15\%$

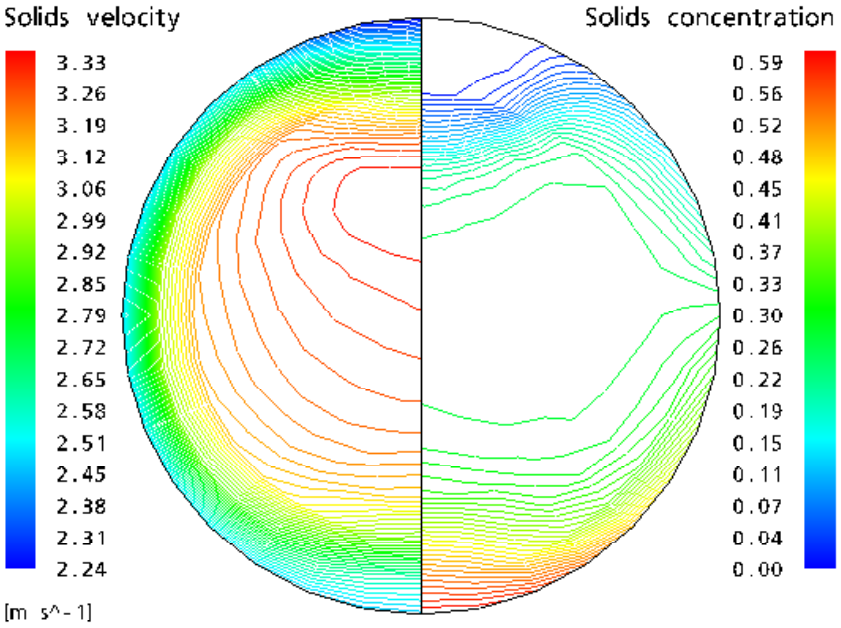

(b) solids-phase velocity and concentration at $C_s = 30\%$

Figure 6.15: Contour plots of solids-phase velocity and concentration for 0.55 mm sand-in-water flow in 158.3 mm pipe.

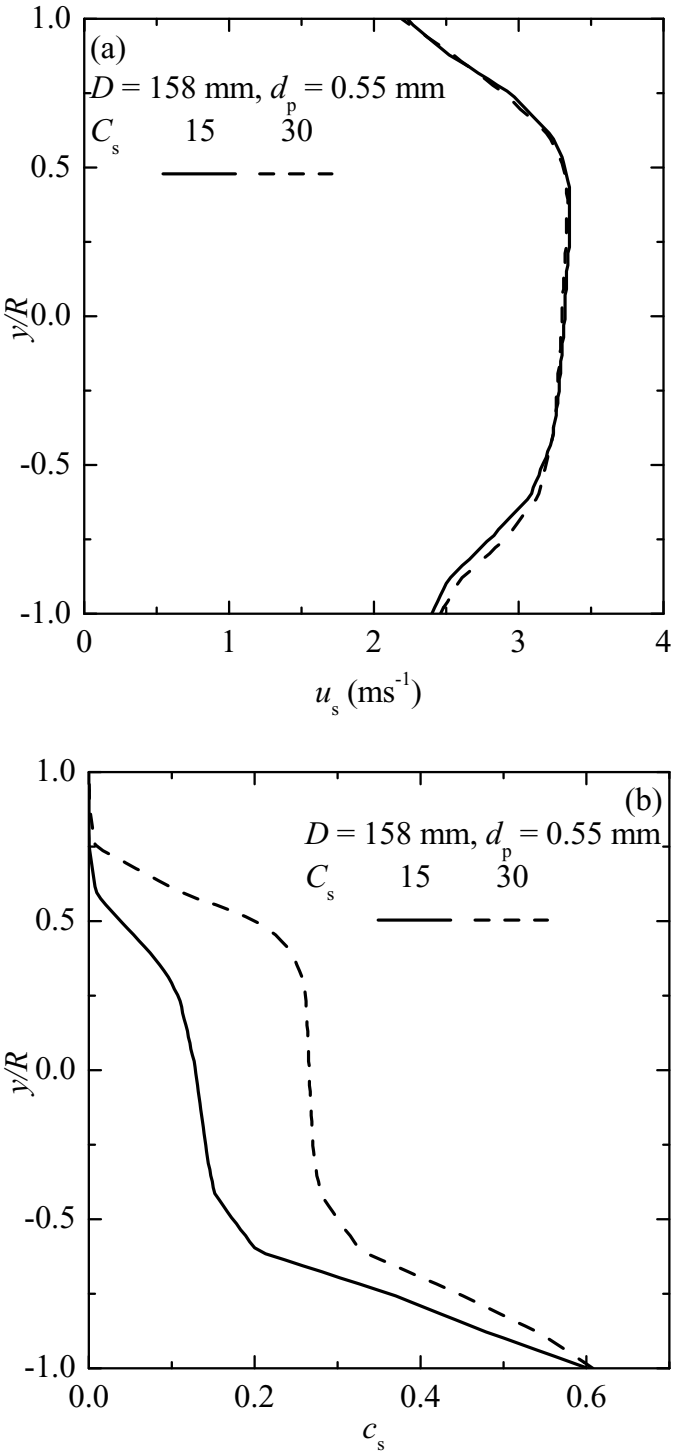

Figure 6.16: solids bulk concentration effect on solids-phase velocity and concentration distributions in 158.3 mm pipe for flow with 0.55 mm particles

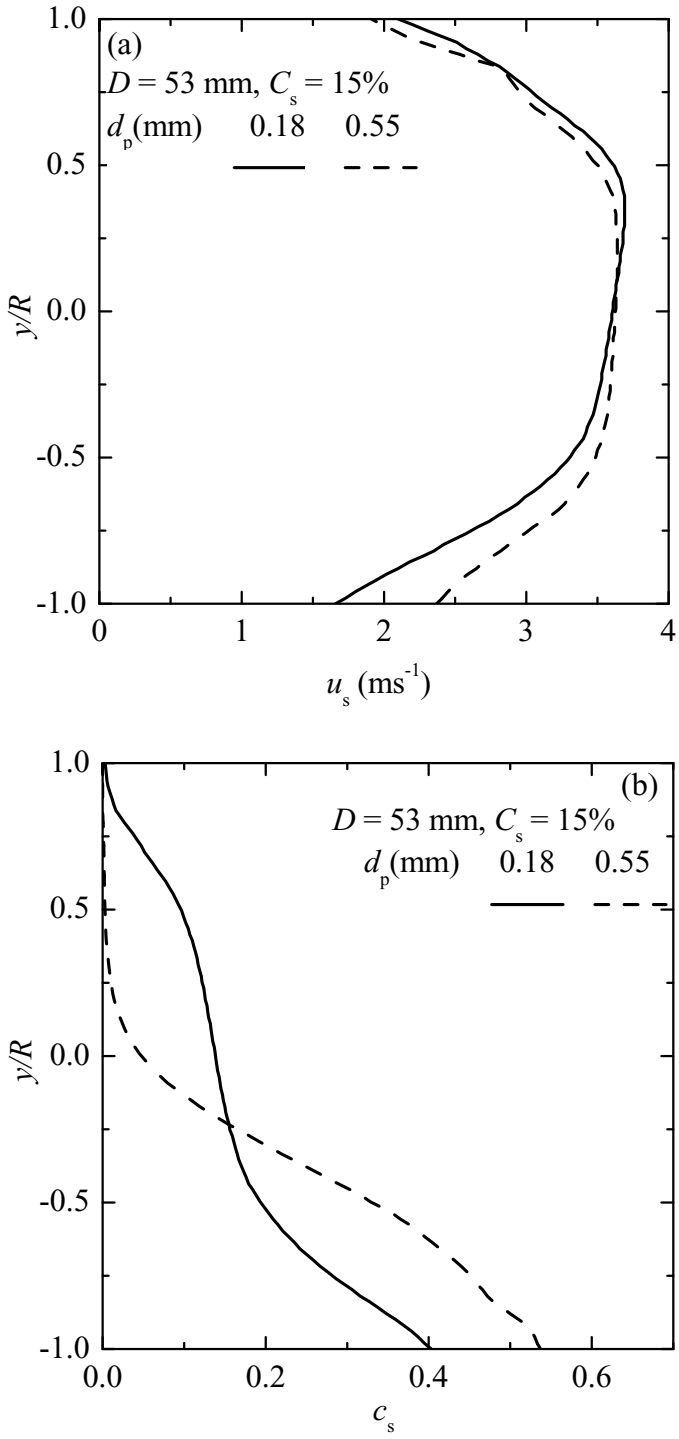

Figure 6.17: Particle diameter effect on solids-phase velocity and concentration distributions at $C_s = 15\%$ in 53.2 mm diameter pipe. (a) solids-phase velocity for $C_s = 15\%$, and (b) Solids concentration for $C_s = 15\%$.

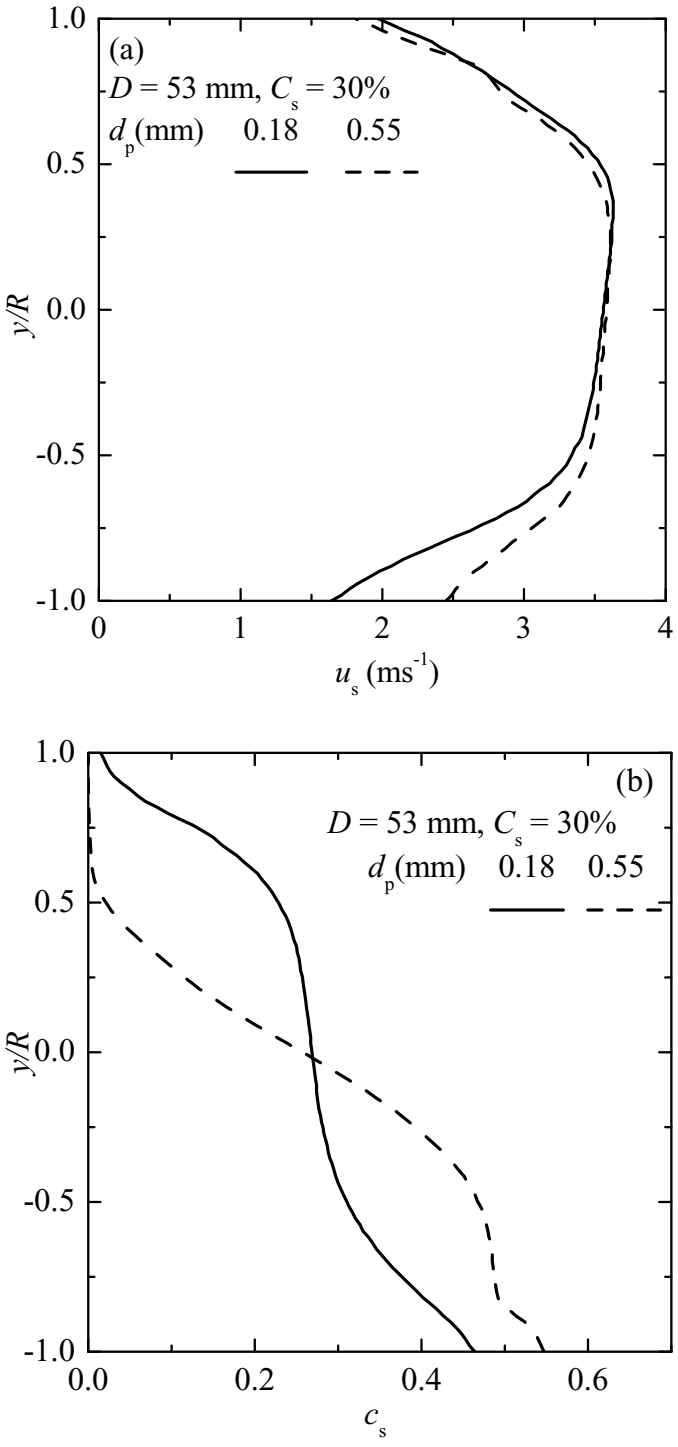

Figure 6.18: Particle diameter effect on solids-phase velocity and concentration distributions at $C_s = 30\%$ in 53.2 mm diameter pipe. (a) solids-phase velocity for $C_s = 30\%$, and (b) Solids concentration for $C_s = 30\%$.

6.5.3.4 Pipe diameter effect

The pipe diameter effect can be inferred from the concentration and particle size effects discussed the in the preceding sections. The results for the coarse particles (0.55 mm sand particles) are selected for discussion in this section. The results for the flows in the 53.2 mm and 158.3 mm pipe are compared. It should be noted that the bulk velocities in both pipe are the same (see Table 6.2) at 3.05 ms^{-1}. Therefore, the volume flow rates in both pipes are not the same and so is their characteristic Reynolds numbers. Overall, the solids-phase velocity and concentration distributions in the larger pipe become more uniform especially in the core region of the pipe suggesting a different flow behaviour.

In Figure 6.19 the influence of pipe diameter on the predicted solids-phase velocity profiles (6.19a) and those for the solids concentration (6.19b) for the coarse particle (0.55 mm sand particles) flows at solids bulk concentration of 15% are presented. The characteristic Reynolds number based on the bulk velocity, the diameter of the pipe and the liquid properties is approximately 161000 for the flow in the 53.2 mm pipe and 480000 for the flow in the 158.3 mm pipe. In Figure 6.19a, the solids-phase velocity in both pipes are similar at the wall. In the core region, the solids-phase velocity in the 53.2 mm diameter pipe is higher than that predicted using the larger 158.3 mm pipe. The solids concentration at the bottom wall is higher for flow in the larger pipe, whereas at upper wall the expected minimum values are obtained. However, the solids are more concentrated in the region around the lower 25% of the pipe in the 53.2 mm diameter pipe compared to that in the 158.3 mm diameter pipe. Beyond that region, the opposite can be noticed. At 30% solids bulk concentration, the trends for the solids-phase velocity in Figure 6.19a and the solids concentration in Figure 6.19b are similar to those described above for the 15% concentration flow. A particular difference lies in the physics of the concentration effect.

6.6 Summary

The physical models in ANSYS CFX-10 for the calculation of horizontal liquid-solid flows were investigated in this chapter. As a primary objective, the physical models for the solids-

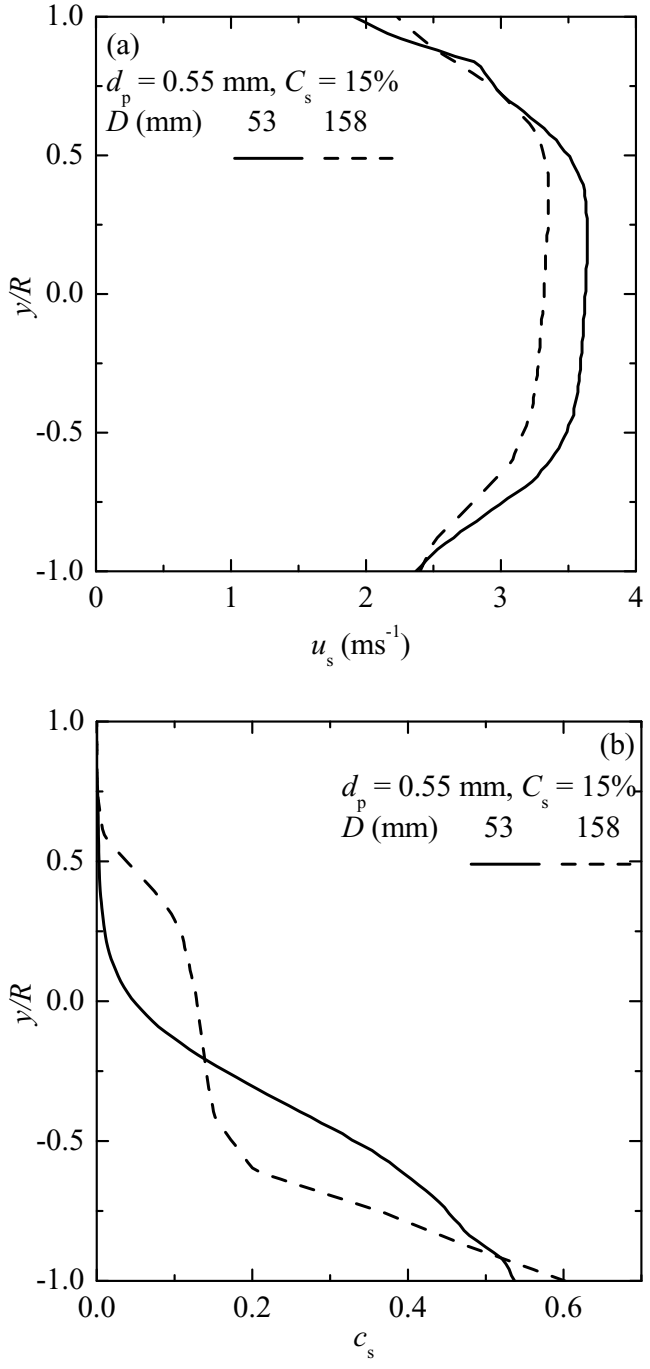

Figure 6.19: Pipe diameter effect on predicted u_s and c_s for 0.55 mm at c_s=15%.

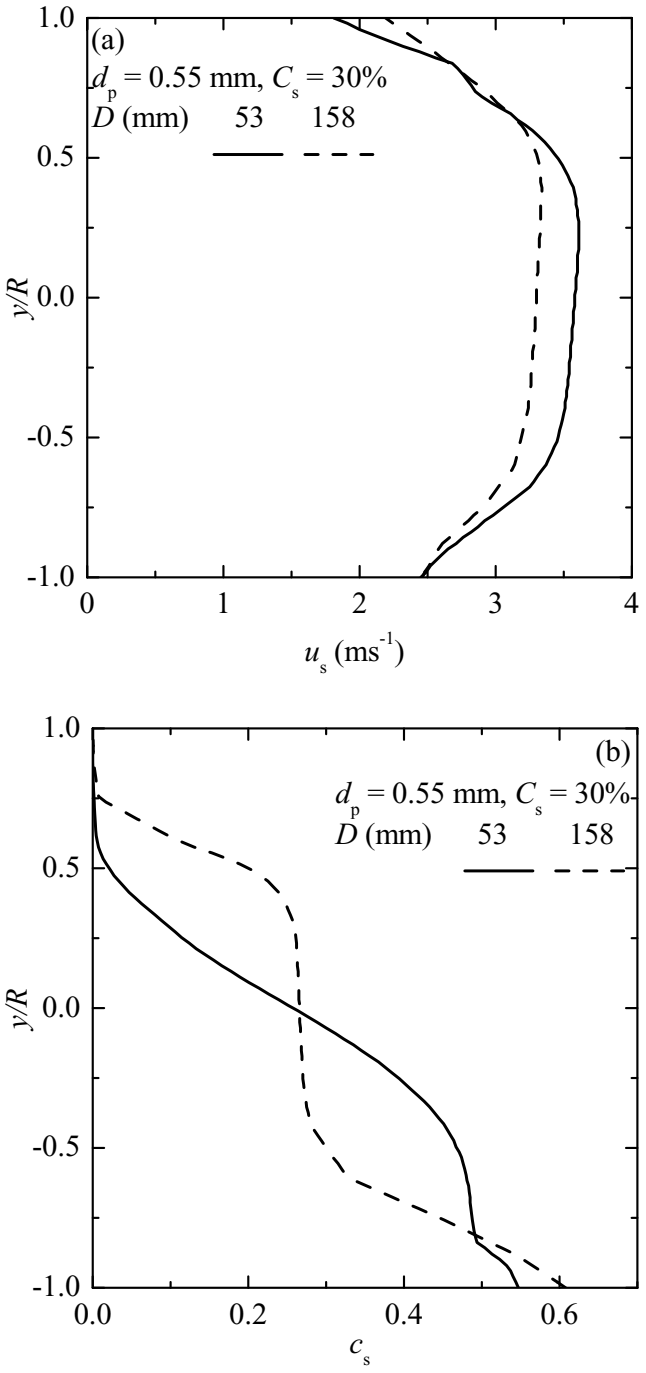

Figure 6.20: Pipe diameter effect on predicted u_s and c_s for 0.55 mm at c_s=30%.

phase stress implemented in the software were investigated. The flow simulations of 0.18 mm and 0.55 mm sand-water mixtures were performed in 53.2 mm, 158.3 mm, and 263 mm diameter pipes. Predictions using the models were compared to measured data. The simulations studied the effects of solids bulk concentration, particle diameter, and pipe diameter. The results showed that there is no significant difference between the solids-phase stress closure models available in ANSYS CFX-10. The case where the a solids-phase stress is not set active in the simulation (i.e. no solids stress model) leads to unrealistic solids concentration prediction, especially in the wall region. The mean velocity predictions fail to match the measured distributions. The calculated solids concentration profiles showed reasonable comparison with the experimental data in the central part of the pipe but failed to reproduce wall effects. The expected trend was obtained for the solids concentration field but the solids-phase velocity predictions were not encouraging. An overall conclusion is that the present models available in the software are not adequate for liquid-solid flow predictions and therefore, require further investigation.

CHAPTER 7

CONCLUSIONS AND RECOMMENDATIONS

In this chapter, the summary, contributions, and conclusions of the study are presented. In addition, recommendations for future work are identified.

7.1 Overall Summary

The present study involved experimental and numerical investigations of coarse-particle liquid-solid flows in pipes. The experimental study primarily involved pressure drop measurements in a 53 mm diameter vertical flow loop. Data was collected in both upward and downward flow sections. The liquid-phase was water and the solids-phase was glass beads with two diameters (0.5 mm and 2.0 mm). The solids-phase bulk concentration ranged between 0 and 45% and the mean mixture velocity was between approximately 2 and 5.5 $\mathrm{m\,s^{-1}}$. In addition, radial solids velocity distributions were measured using the conductivity probe in the upward flow section of the loop for several cases.

On the numerical side, flows of coarse particles at high concentrations in liquids in vertical and horizontal pipes were simulated using the two-fluid model. Following an extensive review of the literature, the constitutive relations required for closure of the two-fluid model governing equations were discussed in the context of the physical mechanisms present in the different flow regimes. For the vertical flow cases, investigations of the two-fluid model focused on the particle-particle interaction and the wall boundary condition. Solids-phase stress relations were used to model particle-particle interactions and investigate their effect on solids velocity, concentration, and turbulence predictions. Solids-phase wall boundary condition models were also investigated by testing their ability to predict frictional head

losses. The models were implemented in the commercial CFD package ANSYS-CFX using CFX-4.4 for the vertical flow simulations.

Three different model formulations for the solids-phase stress (the $k_s - \varepsilon_s$, $k_s - \varepsilon_s - T_s$, and $k_s - k_{fs}$ models) were investigated. One of the models requires a constant solids-phase viscosity to be specified. In this case, two distinct values were considered. The predictions were compared with available experimental solids velocity and concentration profiles taken from the studies of Sumner et al. (1990). Computations were performed for flows of two particle diameters (470 μm and 1700 μm) of sand with a material density of 2650 $\mathrm{kg\,m^{-3}}$. The solids-phase bulk concentrations were 10% and 30% for the 470 μm particles and 10% and 20% for the 1700 μm particles. All the flows simulated were at a mean velocity of approximately 3 $\mathrm{m\,s^{-1}}$. Solids-phase wall boundary condition formulations were also investigated for the prediction of frictional head loss in vertical liquid-solid pipe flows. Five models for the solids-phase wall boundary condition were tested and the results were compared to the experimental results of Shook and Bartosik (1994). For the simulations, the solids-phase bulk concentration ranged from 0 to 40% in intervals of 10% and the mean mixture velocity was nominally between 2 and 6 $\mathrm{m\,s^{-1}}$. The particles were PVC (material density 1400 $\mathrm{kg\,m^{-3}}$) and had a diameter of 3400 μm.

For horizontal flows, the simulations were performed using ANSYS CFX-10. The capability of the existing solids-phase stress models in the software to predict the flow of coarse-particle liquid-solid mixtures were investigated. The simulations were performed for three pipe diameters (53, 158, and 263 mm), two solids-phase bulk concentrations (15% and 30%), and two particle diameters (180 and 550 μm). The model results were compared to the experimental results of Gillies (1993). The simulations focussed on prediction of the solids velocity and concentration distributions.

7.2 Contributions

The main contributions of this study are summarized as follows:

1. A comprehensive review and analysis of two-fluid modelling of liquid-solid flows with application to coarse-particle slurry flows.

2. The first study to engage in the comparative evaluation of two-fluid models to predict coarse-particle flows with special attention on high solids-phase concentration.

3. Evaluation of various physically-based stress models for the two-fluid model to predict local distributions of solids velocity and concentration in liquid-solid slurry flows.

4. A study of wall boundary condition formulations in the context of the two-fluid model to predict frictional head losses for coarse-particle dense flows of liquid-solid mixtures.

5. An exploratory study of the solids stress closure models available in the commercial CFD software, ANSYS CFX.

6. Application of solids-phase stress models from the kinetic theory of granular flow to coarse-particle liquid-solid flows at solids-phase bulk concentration values higher than 10%.

7.3 Conclusions

The specific conclusions from the present study are outlined as follows:

7.3.1 Experimental work

1. The radial solids velocity profiles measured in the upward flow section of the loop showed steep velocity gradients near the wall. The profiles also indicated increased slip velocity in th upward flow section at lower velocities due to increase in the solids mean concentration. Data for the mean solids concentration in the flow loop sections was not obtained, due to problems with the measurement probe, for detailed analysis.

2. The magnitude of the measured pressure drop in both the upward and downward flow sections increases with increasing bulk velocity. The measured pressure drop

also exhibited a dependence on the solids bulk concentration by an upward shift in the value for the upward flow section and a downward shift in the value for the downward flow section. The dependence of the measured pressure drop on the solids bulk concentration is mainly attributed to the gravitational contribution to the total pressure drop. The effect of the gravitational pressure drop is more on the flow with the 0.5 mm glass beads compared to the flow with the 2.0 mm glass beads.

3. The wall shear stress was determined by subtracting the gravitational contribution from the measured pressure drop. For flow with the 0.5 mm glass beads at high bulk velocities in the upward flow section, the values of the wall shear stress were essentially similar for each concentration. At lower bulk velocities, the increase in the wall shear stresses for the flow with the 0.5 mm glass beads is more compared to higher velocities. For the large particle (2.0 mm glass beads), the observations were similar but the effect of concentration was much less in the upward test section.

4. In the downward flow section, the wall shear stress also increased as the bulk concentration was increased for the case of the flow with the 0.5 mm glass beads. The increase in the values of the wall shear stress is more at lower bulk velocities than at higher bulk velocities, and less compare to the upward flow section. The values of the wall shear stress for the flow of the 2.0 mm glass beads increased for all the bulk velocities investigated.

5. The increase is more pronounce in the upward flow section than in the downward flow section, and was attributed to the effect of different mean solids concentration values in the flow section.

6. In both test sections as well as for both particle sizes (i.e. the 0.5 mm and 2.0 mm glass beads), the wall shear stress does not depend on the bulk concentration below 10%.

7.3.2 Numerical work

7.3.2.1 Vertical flows: Comparison of solids-phase stress closures

1. For all three models for the solids stress tested, the solids velocity and concentration predictions were better for the smaller particles (470 μm) than the larger particles (1700 μm), irrespective of the solids-phase bulk concentrations considered.

2. The models gave poor predictions for the velocity and concentration profiles for flows with larger particles for all the concentrations investigated. The $k_{\mathrm{f}} - \varepsilon_{\mathrm{f}} - k_{\mathrm{s}} - \varepsilon_{\mathrm{s}} - T_{\mathrm{s}}$ model performed better in predicting the solids velocity. The models could not reproduce the experimental results of the solids concentration distributions for the 1700 μm particles.

3. The trends of the liquid-phase turbulence kinetic energy were similar to single-phase flow but the magnitudes were typically lower than for single phase flows for all the models investigated. Close to the wall of the pipe in the region where the solids-phase concentration is depleted, all the models predicted similar liquid-phase turbulence kinetic energy. The values of the liquid-phase turbulence kinetic energy for the liquid-solid flows were higher in than that predicted for the single-phase case.

4. The models produce increased peak values at the wall with increased solids-phase bulk concentration. For the smaller particles, the liquid-phase turbulence kinetic energy was attenuated with increase in solids bulk concentration for the $k_{\mathrm{f}} - \varepsilon_{\mathrm{f}} - k_{\mathrm{s}} - \varepsilon_{\mathrm{s}}$ and $k_{\mathrm{f}} - \varepsilon_{\mathrm{f}} - k_{\mathrm{s}} - \varepsilon_{\mathrm{s}} - T_{\mathrm{s}}$ models. The liquid-phase turbulence kinetic energy was enhanced for the $k_{\mathrm{f}} - \varepsilon_{\mathrm{f}} - k_{\mathrm{s}} - k_{\mathrm{fs}}$ model in the region towards the centre of the pipe. For the case of the larger particles, the liquid-phase turbulence kinetic energy was attenuated for all three models with no significant on the effect of concentration.

5. For each model, solids-phase turbulence kinetic energy was lower close to the wall and higher towards the centre of the pipe than that for the liquid phase. Increased in solids bulk concentration produced lower solids turbulence kinetic energy for all the models investigated. The values of solids-phase turbulence kinetic energy were higher for larger particles than for the smaller particles.

6. The solids-phase eddy viscosity was much larger than the liquid-phase eddy viscosity, and decreased with concentration and increased with particle size for the $k_{\mathrm{f}} - \varepsilon_{\mathrm{f}} - k_{\mathrm{s}} - \varepsilon_{\mathrm{s}}$ and $k_{\mathrm{f}} - \varepsilon_{\mathrm{f}} - k_{\mathrm{s}} - \varepsilon_{\mathrm{s}} - T_{\mathrm{s}}$ models. The solids-phase eddy viscosity predicted using the $k_{\mathrm{f}} - \varepsilon_{\mathrm{f}} - k_{\mathrm{s}} - k_{\mathrm{fs}}$ model was unique and different with a peak value close to the wall and lower values at the wall and at the centre of the pipe.

7. From the simulations results, the $k_{\mathrm{f}} - \varepsilon_{\mathrm{f}} - k_{\mathrm{s}} - \varepsilon_{\mathrm{s}} - T_{\mathrm{s}}$ model is considered the bestbetter s. The solids-phase eddy viscosity predicted using the $k_{\mathrm{f}} - \varepsilon_{\mathrm{f}} - k_{\mathrm{s}} - k_{\mathrm{fs}}$ model was unique and different with a peak value close to the wall and lower values at the wall and at the centre of the pipe.

7.3.2.2 Vertical flows: Pressure drop prediction

1. For the flow conditions investigated, neither the no-slip nor the free-slip is an appropriate boundary condition for the solids-phase. The free-slip wall boundary condition produced values of the frictional head loss that was lower than the measured data, including that for single-phase flow. The no-slip wall boundary condition predictions were between the measured data and that computed for the single-phase flow.

2. The wall boundary conditions of Ding and Lyczkowski (1992) and Bartosik (1996) were found to perform better at higher mean mixture velocities for the 10% solids mean concentration. They, however, did not reproduce the measured pressure drops.

3. From the present work, it is evident that an improved solids wall boundary condition formulation is required for accurate prediction of frictional head loss in liquid-solid two-phase vertical flows.

7.3.3 Horizontal flows

1. The simulation with three model options in ANSYS CFX-10 for the solids phase stress tensor (i.e. no modelling for the granular temperature, zero-equation and algebraic equilibrium models) and the so-called dispersed-phase zero equation model

for the solids-phase turbulence for the 180 μm and 550 μm sand-water slurries with produce similar results.

2. The characteristic flow features of horizontal flow of medium (180 μm particles) and coarse (550 μm particles) sand-water slurries can be qualitatively described using ANSYS CFX-10.

3. Comparing the predictions with experimental data, applying the kinetic theory of granular flows using an algebraic equilibrium model for the granular temperature for the solids-phase stress produced a more realistic distribution of solids-phase concentration than the solids velocity. The model fail to reproduce observed local distributions of the solids velocity.

4. The effect of solids-phase bulk concentration on solids velocity and concentration distributions exhibited the expected asymmetric characteristic of negatively buoyant solids flow in liquid. The local solids velocity in the upper part of the pipe at a solids-phase bulk concentration of 30% was slightly higher than that computed at 15% solids-phase bulk concentration. In the lower part of the pipe, they were essentially identical.

5. For flow in the 53 mm diameter pipe, the effect of particle diameter on the solids velocity and concentration distributions was mixed. The local velocity of the larger sand particles was lower than that of the smaller particles in the upper part of the pipe, while the lower part, it was much higher. The solids-phase concentration profiles showed a similar effect. In the lower part of the pipe, the values of the predicted concentration are higher than the measured values.

6. For the effect of pipe diameter, the solids velocity in the smaller pipe is higher than that of the larger pipe over almost the entire pipe cross-section. The value of the solids-phase concentration is higher in the lower half of both pipes, and lower in the upper region.

7.3.4 Recommendations

Based on the comparisons with experimental data as well as the comparative work on different models, the following recommendations are proposed:

1. The modelling of the unclosed terms in the two-fluid model should be explored in more detail.

2. The flow type investigated in this study is associated with complex physics, the understanding of which is far from complete. Microscopically, the flow is unsteady and the individual discrete particles of the solids-phase are in continuous motion. Presently, closure models based upon the kinetic theory of granular flows appear to provide some insight. Simulations in the context of discrete element simulation would provide further insight to understanding the dynamics involved. Such simulations would also aid in the development of better closure laws for the two-fluid model for dense flows.

3. Wall boundary conditions for the liquid and solids phases should each account for the other phase's effect in the model. For the case of flow in ducts of arbitrary geometry, the effect of solids concentration must be carefully considered in the wall boundary condition model. In addition, modification to existing wall boundary condition models for granular flows should carefully consider wall roughness effects where applicable.

4. As a requirement for two-fluid model validation, measurements of phasic variables like velocity and concentration as well as higher-order variables are needed.

5. To effectively implement and have full access to modify the models, an overall recommendation is that the models should be tested and developed using in-house programs where all model parameters and constants can be easily and completely verified.

6. Finally, extensive technical support and training from developers is strongly recommended when applying a commercial code such as CFX for the types of flow investigated in this study. This is because most commercial CFD codes have not been fully

tested for coarse particle slurry flows compared to single-phase or gas-liquid flows.

LIST OF REFERENCES

Abou-Arab, T. W. and Roco, M. C. (1990). Solid phase contribution in the two-phase turbulence kinetic energy equation. *Trans. ASME J. of Fluids Eng.*, 112:351–361.

Abu-Zaid, S. and Ahmadi, G. (1996). A rate dependent model for turbulent flows of dilute and dense two-phase solid-liquid mixtures. *Powder Technology*, 89:45–56.

Ahmadi, G. and Ma, D. (1990). A thermodynamical formulation for dispersed multiphase turbulent flows -I: Basic theory. *Int. J. Multiphase Flow*, 16(2):323–340.

Alajbegovic, A., Assad, A., Bonetto, F., and Lahey Jr., R. T. (1994). Phase distribution and turbulence structure for solid/fluid upflow in a pipe. *Int. J. Multiphase Flow*, 20(3):453–479.

Alajbegovic, A., Drew, D. A., and Lahey Jr., R. T. (1999). An analysis of phase distribution and turbulence in dispersed particle/liquid flows. *Chem. Eng. Comm.*, 174:85–133.

Anderson, T. B. and Jackson, R. A. (1967). A fluid mechanical description of fluidized beds: Equations of motion. *Ind. Eng. Chem. Fund.*, 6(4):527–539.

Bagnold, R. A. (1954). Experiments on a gravity-free dispersion of large solid spheres in a Newtonian fluid under shear. *Proc. R. Soc. London Ser. A*, 225(1160):49–63.

Bartosik, A. S. (1996). Modelling the Bagnold stress effects in vertical slurry flow. *J. Hydrol. Hydromech.*, 44(1):49–58.

Bartosik, A. S. and Shook, C. A. (1991). Prediction of slurry flow with non-uniform concentration distribution. In Taylor, C., Chin, J. H., and Homsy, G. M., editors, *Proceedings of the* 7^{th} *International Conference on Numerical Methods in Laminar and Turbulent Flow*, volume 7, Part 1, pages 277–287. Pineridge Press, Swansea, UK.

Bartosik, A. S. and Shook, C. A. (1995). Prediction of liquid-solid pipe flow using measured concentration distribution. *Particulate Sci. and Technology*, 13:85–104.

Benyahia, S., Syamlal, M., and O'Brien, T. J. (2005). Evaluation of boundary conditions used to model dilute, turbulent gas/solids flows in a pipe. *Powder Technology*, 156:62–72.

Bolio, E. J., Yasuna, J. A., and Sinclair, J. L. (1995). Dilute turbulent gas-solid flow in risers with particle-particle interaction. *AIChE J.*, 41(6):1375–1388.

Bouillard, J. X., Lyczkowski, R. W., and Gidaspow, D. (1989). Porosity distribution in a fluidised bed with an immersed obstacle. *AIChE J.*, 35:908–922.

Brennen, C. E. (2005). *Fundamentals of Multiphase Flows*. Cambridge University Press, New York.

Brown, N. P., Shook, C. A., Peters, J., and Eyre, D. (1983). A probe for point velocities in slurry flows. *Can. J. Chem. Eng.*, 61:597–602.

Burns, A. D., Frank, T., Hamill, I., and Shi, J.-M. (2004). The Favre averaged drag model for turbulent dispersion in Eulerian multi-phase flows. In Matsumoto, Y., Hishida, K., Tomiyama, A., Mishima, K., and Hosokawa, S., editors, *the 5th International Conference on Multiphase Flow*, Yokohama, Japan. Paper No. 392, Proceedings on CD.

Campbell, C. S. (1990). Rapid granular flows. *Ann. Rev. Fluid Mech.*, 22:57–92.

Cao, J. and Ahmadi, G. (1995). Gas-particle two-phase turbulent flow in a vertical duct. *Int. J. Multiphase Flow*, 21(6):1203–1228.

Cao, J. and Ahmadi, G. (2000). Gas-particle two-phase turbulent flow in horizontal and inclined ducts. *Int. J. Eng. Sci.*, 38:1961–1981.

Chapman, S. and Cowling, T. (1970). *The Mathematical Theory of Non-Uniform Gases*. Cambridge University Press, Cambridge, 3rd edition.

Charles, M. E. (1970). Transport of solids by pipelines. In *Proc. Hydrotransport 1 Conf.*, Cranfield, UK. Paper A3.

Churchill, S. W. (1977). Friction factor spans all fluid regimes. *Chem. Eng.*, 84(24):91–92.

Crowe, C. T. (1993). Research Needs in Fluid Engineering: Basic Research Needs in Fluid-Solid Multiphase Flows. *Trans. ASME J. of Fluids Eng.*, 115:341–342. Technical Forum.

Csanady, G. T. (1963). Turbulent diffusion of heavy particles in the atmosphere. *J. Atmos. Sci.*, 20:201–208.

Cundall, P. A. and Strack, O. D. L. (1979). A discrete numerical model for granular assemblies. *Geotechnique*, 29:47–65.

Daniel, S. M. (1965). *Flow of Suspensions in a Rectangular Channel*. PhD Thesis, Department of Mechanical Engineering, University of Saskatchewan, Saskatoon, Canada.

De Wilde, J., Marin, G. B., and Heynderickx, G. J. (2003). The effects abrupt T-outlets in a riser: 3D simulation using the kinetic theory of granular flow. *Powder Technology*, 58:877–885.

Deutsch, E. and Simonin, O. (1991). Large eddy simulation applied to the motion of particles in stationary homogeneous fluid turbulence. In *Turbulence Modifications in Multiphase Flows, ASME-FED, Vol. 110*.

Ding, J. and Gidaspow, D. (1990). A bubbling fluidization model using kinetic theory of granular flow. *AIChE J.*, 36:523–538.

Ding, J. and Lyczkowski, R. W. (1992). Three-dimensional kinetic theory modeling of hydrodynamics and erosion in fluidized beds. *Powder Technology*, 73:127–138.

Ding, J., Lyczkowski, R. W., Sha, W. T., Altobelli, S. A., and Fukushima, E. (1993). Numerical analysis of liquid-solids suspension velocity and concentrations obtained by NMR imaging. *Powder Technology*, 77:301–312.

Doron, P. and Barnea, D. (1993). A three-layer model for solid-liquid flow in horizontal pipes. *Int. J. Multiphase Flow*, 19:1029–1043.

Drew, D. and Passman, S. L. (1999). *Theory of Multicomponent Fluids*. Springer-Verlag, New York.

Drew, D. A. (1975). Turbulent sediment transport over a flat bottom using momentum balance. *J. Applied Mech.*, 42:38–44.

Drew, D. A. (1983). Mathematical modeling of two-phase flow. *Ann. Rev. Fluid Mech.*, 15:161–191.

Drew, D. A. and Lahey, R. T. (1993). Analytical modeling of multiphase flow. In Roco, M., editor, *in Particulate Two-Phase Flow*, pages 510–566. Butterworth-Heinemann.

Dudukovic, M. P. (2000). Opaque multiphase reactors: Experimentation, modeling and troubleshooting. *Oil & Gas Science and Technology - Rev. IFP*, 55(2):135–158.

Durand, R. and Condolios, E. (1952). Experimental study of the hydraulic transport of coal and solid materials in pipes. In *Colloquial of Hydraulic Transport of Coal*, pages 39–55, National Coal Board, (UK). Paper IV.

Eldighidy, S. M., Chen, R. Y., and Comparin, R. A. (1977). Deposition of suspensions in the entrance of a channel. *Trans. ASME J. of Fluids Eng.*, 99(2):365–370.

Elghobashi, S. E. (1991). Particle laden-turbulent flows: Direct simulation and closure models. *App. Sci. Res.*, 48(3-4):91–104.

Elghobashi, S. E. (1994). On predicting particle-laden turbulent flows. *App. Sci. Res.*, 52:309–329.

Elghobashi, S. E. and Abou-Arab, T. W. (1983). A two-equation turbulence model for two-phase flows. *Phys. Fluids*, 26(4):931–938.

Enwald, H., Peirano, E., and Almsted, A.-E. (1996). Eulerian two-phase flow theory applied to fluidization. *Int. J. Multiphase Flow*, 22(Suppl.):21–66.

Ergun, S. (1952). Fluid flow through packed columns. *Chem. Eng. Prog.*, 48:89–94.

Ferré, A. L. and Shook, C. A. (1998). Coarse particle wall friction in vertical slurry flows. *Part. Sci. Tech.*, 16:125–133.

Fessler, J. R. and Eaton, J. K. (1999). Turbulence modification by particles in a backward-facing step flow. *J. Fluid Mech.*, 394:97–117.

Garside, J. and Al-Dibouni, M. R. (1977). Velocity-voidage relationships for fluidization and sedimentation. *I & EC Process Des. Dev.*, 16:206–214.

Gidaspow, D. (1994). *Multiphase Flow and Fluidization: Continuum and Kinetic Theory Descriptions*. Academic Press, Boston.

Gillies, R. G. (1993). *Pipeline Flow of Coarse Particle Slurries*. PhD Thesis, Department of Chemical Engineering, University of Saskatchewan, Saskatoon, Canada.

Gillies, R. G., Hill, K. B., McKibben, M. J., and Shook, C. A. (1999). Solids transport by laminar Newtonian flows. *Powder Tech.*, 104:269–277.

Gillies, R. G., Husband, W. H. W., and Small, M. (1984). Some experimental methods for coarse coal slurries. In *9th Int. Conf. on Hydraulic Transport of Solids in Pipes*, Rome, Italy.

Gillies, R. G., Husband, W. H. W., and Small, M. (1985). A study of conditions arising in horizontal coarse slurry short distance pipelining practice. Technical report, Saskatchewan Research Council Report. R-833-2-85.

Gillies, R. G. and Shook, C. A. (1994). Concentration distributions of sand slurries in horizontal pipe flows. *Part. Sci. Tech.*, 12:45–69.

Gillies, R. G. and Shook, C. A. (2000). Modelling high concentration settling slurry flows. *Can. J. Chem. Eng.*, 78:709–716.

Gillies, R. G., Shook, C. A., and Wilson, K. C. (1991). An improved two-layer model for horizontal slurry pipeline flow. *Can. J. Chem. Eng.*, 69:173–178.

Gillies, R. G., Shook, C. A., and Xu, J. (2004). Modelling heterogeneous slurry flows at high velocities. *Can. J. Chem. Eng.*, 82:1060–1065.

Gómez, L. C. and Milioli, F. E. (2001). A parametric study of gas-solid flow in the riser of a circulating fluidized bed through continuous Eulerian modelling. In Taylor, C., Chin, J. H., and Homsy, G. M., editors, *Proceedings of the* 2^{nd} *International Conference on Computational Heat and Mass Transfer*, volume 7, Part 1, pages 277–287. COPPE/UFRJ - Federal University of Rio de Janeiro, Brazil.

Gore, R. A. and Crowe, C. T. (1989). Effect of particle size on modulating turbulent intensity. *Int. J. Multiphase Flow*, 15(2):279–285.

Greimann, B. P. and Holly, J. F. M. (2001). Two-phase flow analysis of concentrated profiles. *J. Hydr. Engrg., ASCE*, 127:753–762.

Greimann, B. P., Muste, M., and Holly, J. F. M. (1999). Two-phase formulation of suspended sediment transport. *J. Hydr. Res.*, 37(4):479–500.

Hadinoto, K. and Curtis, J. S. (2004). Effect of interstitial fluid on particle-particle interactions in the kinetic theory approach of dilute turbulent fluid-particle flow simulation. In Matsumoto, Y., Hishida, K., Tomiyama, A., Mishima, K., and Hosokawa, S., editors, *the 5th International Conference on Multiphase Flow*, Yokohama, Japan. Proceedings on CD.

Hanes, D. M. and Inman, D. L. (1985). Observations of rapidly flowing granular-fluid materials. *J. Fluid Mech.*, 150:357–380.

Hetsroni, G. (1989). Particle-turbulence interaction. *Int. J. Multiphase Flow*, 15(5):735–746.

Howard, G. W. (1939). Transportation of sand and gravel in four inch pipes. *Trans. ASCE.*, 104:1334–1348.

Hrenya, C. M. and Sinclair, J. L. (1997). Effects of particle-phase turbulence in gas-solid flows. *AIChE J.*, 43(4):853–869.

Hsu, F.-L., Turian, R. M., and Ma, T.-W. (1989). Flow of noncolloidal slurries in pipelines. *AIChE Journal*, 35(3):429–442.

Hsu, T.-J., Jenkins, J. T., and Liu, P. L.-F. (2003). On two-phase sediment transport: Dilute flow. *J. Geophys. Res.*, 108(C3):2(1)–2(14). 3057, doi:10.1029/2001JC001276.

Hsu, T.-J., Jenkins, J. T., and Liu, P. L.-F. (2004). On two-phase sediment transport: Sheet flow of massive particles. In *Proceedings of the Royal Society of London, Series A*, volume 460 (2048), pages 2223–2250.

Hui, K., Haff, P. K., and Ungar, J. E. (1984). Boundary conditions for high-shear grain flows. *J. Fluid Mech.*, 145:223–233.

Hwang, G.-J. and Shen, H. H. (1993). Fluctuation energy equations for turbulent fluid-solid flows. *Int. J. Multiphase Flow*, 19(5):887–895.

Ishii, M. (1975). *Thermo-fluid Dynamic Theory of Two-phase Flow*. Eyrolles, Paris.

Ishii, M. and Mishima, K. (1984). Two-fluid model and hydrodynamic constitutive relations. *Nuclear Engineering and Design*, 82:107–126.

Jackson, R. (1983). Some mathematical and physical aspects of continuum models for the motion of granular materials. In Meyer, R. E., editor, *In Theory of Dispersed Multiphase Flow*, pages 291–337. New York: Academic. Publication No. 49.

Jackson, R. (1997). Locally averaged equations of motion for a mixture of identical spherical particles and a Newtonian fluid. *Chem. Eng. Sci.*, 52(15):2457–2469.

Jackson, R. (1998). Erratum: Locally averaged equations of motion for a mixture of identical spherical particles and a Newtonian fluid. *Chem. Eng. Sci.*, 53:1955.

Jenike, A. W. and Shield, R. T. (1959). On the plastic flow of coulomb solids beyond original failure. *ASME J. Appl. Mech.*, 26:599–602.

Jenkins, J. T. and Louge, M. Y. (1997). On the flux of fluctuating energy in a collisional grain flow at a flat frictional wall. *Phy. Fluids*, 9(10):2835–2840.

Jenkins, J. T. and Richman, M. (1985). Grad's 13-moment system for dense gas of inelastic spheres. *Arch. Rat. Mech. Anal.*, 87:355–377.

Jenkins, J. T. and Richman, M. W. (1986). Boundary conditions for plane flows of smooth identical, rough, inelastic, circular disks. *J. Fluid Mech.*, 171:53–69.

Jenkins, J. T. and Savage, S. B. (1983). A theory for the rapid flow of identical, smooth, nearly elastic, spherical particles. *J. Fluid Mech.*, 130:187–202.

Johnson, P. C. and Jackson, R. (1987). Frictional-collisional constitutive relations for granular materials, with application to plane shearing flows. *J. Fluid Mech.*, 176:67–93.

Johnson, P. C., Nott, P., and Jackson, R. (1990). Frictional-collisional equations of motion for particles flows and their applications to chutes. *J. Fluid Mech.*, 210:501–535.

Joseph, D. D. and Lundgren, T. S. (1990). Ensemble averaged and mixture theory equations for incompressible fluid-particle suspensions. *Int. J. Multiphase Flow*, 16(1):35–42.

Kiger, K. T. and Pan, C. (2000). PIV technique for the simultaneous measurement of dilute two-phase flows. *J. Fluids Eng.*, 122:811–818.

Kleinstreuer, C. (2003). *Two-Phase Flow: Theory and Applications*. Taylor & Francis, New York; London.

Krampa-Morlu, F. N., Bergstrom, D. J., Bugg, J. D., Sanders, R. S., and Schaan, J. (2004). Numerical simulation of dense coarse particle slurry flows in a vertical pipe. In Matsumoto, Y., Hishida, K., Tomiyama, A., Mishima, K., and Hosokawa, S., editors, *the 5th International Conference on Multiphase Flow*, Yokohama, Japan. Proceedings on CD.

Krampa-Morlu, F. N., Yerrumshetty, A. K., Bergstrom, D. J., Bugg, J. D., Sanders, R. S., and Schaan, J. (2006). A study of turbulence modulation models for fluid-particle flows using a two-fluid model. In Hanjalić, K., Nagano, Y., and Jakirlić, S., editors, *Proc. of the symposium on Turbulence, Heat and Mass Transfer*, September 25-26, 2006, Dubrovnik, Croatia.

Lee, S. L. and Durst, F. (1982). On the motion of turbulent duct flows. *Int. J. Multiphase Flow*, 19(5):125–146.

Liljegren, L. M. and Vlachos, N. S. (1983). Laser velocimetry measurements in a horizontal gas-solid pipe flow. *Expts. Fluids*, 9(4):205–212.

Ling, J., Lin, C. X., and Ebadian, M. A. (2002). Numerical investigations of double-species slurry flow in a straight pipe entrance. In *Proc. IMECE2002, ASME International Mechanical Engineering Congress & Exposition*, New Orleans, Louisiana.

Lipsett, M. G. (2004). Oil sands extraction research needs and opportunities. *Can. J. Chem. Eng.*, 82:626–627.

Louge, M., Mastorakos, E., and Jenkins, J. T. (1991). The role of particle collisions in pneumatic transport. *J. Fluid Mech.*, 231:345–359.

Louge, M. Y. (1994). Computer simulations of rapid granular flows of spheres interacting with a flat, frictional boundary. *Phy. Fluids*, 6(7):2253–2269.

Lucas, G. P., Cory, J. C., and Waterfall, R. C. (2000). A six-electrode local probe for measuring solids velocity and volume fraction profiles in solids-water flows. *Meas. Sci. Technol*, 11:1498–509.

Lun, C. and Savage, S. (1986). The effects of an impact velocity dependant coefficient of restitution on stresses developed by sheared granular materials. *Acta Mechanica.*, 63:15–44.

Lun, C., Savage, S., Jefferey, D., and Chepurniy, N. (1984). Kinetic theory for granular flow: Inelastic particles in Coutte flow and slightly inelastic particles in a general flow-field. *J. Fluid Mech.*, 140:223–256.

Makkawi, Y. and Ocone, R. (2006). A model for gas-solid flow in a horizontal duct with a smooth merge of rapid-intermediate-dense flows. *Chem. Eng. Sci.*, 61:4271–4281.

Matousek, V. (2002). Pressure drops and flow patterns in sand-mixture pipes. *Experimental Thermal and Fluid Science*, 26:693–702.

McKibben, M. J. (1992). *Wall Erosion in Slurry Pipelines*. PhD Thesis, Department of Chemical Engineering, University of Saskatchewan, Saskatoon, Canada.

Miller, A. and Gidaspow, D. (1992). Dense, vertical gas-solid flow in a pipe. *AIChE Journal*, 38:1801–1815.

Monin, A. S. and Yaglom, A. M. (1971). *Statistical Fluid Mechanics: Mechanics of Turbulence*, volume 1. The MIT Press, Cambridge.

Nasr-El-Din, H., Shook, C. A., and Colwell, J. (1986). A conductivity probe for measuring local concentrations in slurry systems. *Int. J. Multiphase Flow*, 13(5):365–378.

Nasr-El-Din, H., Shook, C. A., and Colwell, J. (1987). The lateral variation of solids concentration in horizontal slurry pipeline flow. *Int. J. Multiphase Flow*, 13(5):661–669.

Newitt, D. M., Richardson, J. F., Abbott, M., and Turtle, R. B. (1955). Hydraulic conveying of solids in horizontal pipes. *Trans. Inst. Chem. Engrs.*, 33(2):93–113.

Newitt, D. M., Richardson, J. F., and Gliddon, B. J. (1961). Hydraulic conveying of solids in vertical pipes. *Trans. Inst. Chem. Engrs.*, 39:93–100.

Peirano, E. and Leckner, B. (1998). Fundamentals of turbulent gas-solid flows applied to circulating fluidized bed combustion. *Prog. Energy Combust. Sci.*, 24:259–296.

Pope, S. B. (2000). *Turbulent Flows*. Cambridge University Press.

Ren, W. M., Ghiaasiaan, S. M., and Abel-Khalik, S. I. (1994). GT3F: an implicit finite difference computer code for transient three-dimensional three-phase flow, Part I: governing equations and solution scheme. *Numerical Heat Transfer*, 25:1–20.

Richardson, J. F. and Zaki, W. N. (1954). Sedimentation and fluidization: Part I. *Trans. Inst. Chem. Eng.*, 32:35–52.

Richman, M. W. (1988). Boundary conditions based upon a modified Maxwellian velocity distribution for flows of identical, smooth, nearly elastic spheres. *Acta Mechanica*, 75:227–240.

Rizk, M. A. and Elghobashi, S. E. (1989). A two-equation turbulence model for dispersed dilute confined two-phase flows. *Int. J. Multiphase Flow*, 15(1):119–133.

Roco, M. C. (1990). One equation turbulence modeling of incompressible mixtures. In Cheremisinoff, N. P., editor, *Encyclopedia of Fluid Mechanics*, volume 10, chapter 1, pages 1–68. Gulf. Pub. Co., New Jersey.

Roco, M. C. (1997). Particulate Science and Technology: A New Beginning. *Powder Technology*, 15:81–83.

Roco, M. C. and Balakrishnan, N. (1985). Multi-dimensional flow analysis of solid-liquid mixtures. *J. of Rheology*, 29(4):431–456.

Roco, M. C. and Shook, C. A. (1983). Modeling of slurry flow: The effect of particle size. *Can. J. Chem. Eng.*, 61:494–503.

Roco, M. C. and Shook, C. A. (1984). A model for turbulent slurry flow. *J. of Pipelines*, 4(1):3–13.

Roco, M. C. and Shook, C. A. (1985). Turbulent flow of incompressible mixtures. *Trans. ASME J. of Fluids Eng.*, 107:224–231.

Savage, S. B. (1983). Granular flows at high shear rates. In Meyer, R. E., editor, *In Theory of Dispersed Multiphase Flow*, pages 339–358. New York: Academic. Publication No. 49.

Savage, S. B. (1998). Analysis of slow high-concentration flows of granular materials. *J. Fluid Mech.*, 377:1–26.

Savage, S. B. and Jeffrey, D. J. (1981). The stress tensor in a granular flow at high shear rates. *J. Fluid Mech.*, 110:255–272.

Schaeffer, D. G. (1987). Instability in the evolution equations describing incompressible granular flow. *J. Differ. Equ.*, 66:19–50.

Schergevitch, P. (2006). Calibration of 2-inch foxboro flowmeter (M-213326-B) with foxboro transmitter (E96S-IA). Technical report, Saskatchewan Research Council.

Schiller, L. and Naumann, A. (1933). A drag coefficient correlation. *VDI-Zeitschrift*, 77:318–320.

Shook, C. A. and Bartosik, A. S. (1994). Particle-wall stresses in vertical slurry flows. *Powder Technology*, 81:117–124.

Shook, C. A., Gillies, R. G., and Sanders, R. S. (2002). *Pipeline Hydrotransport with Applications in the Oil Sand Industry*. SRC Publication No. 11508-1E02.

Shook, C. A. and Roco, M. C. (1991). *Slurry Flows: Principles and Practice*. Butterworth-Heinemann, Stoneham, MA.

Simonin, O. (1996). Continuum modelling of dispersed two-phase flows. Combustion and turbulence in two-phase flows, 47 pages, Von Karman Institute of Fluid Dynamics Lecture Series. Von Karman Institute of Fluid Dynamics Lecture Series, 47 pages.

Sinclair, J. L. and Jackson, R. (1989). Gas-particle flow in a vertical pipe with particle-particle interactions. *AIChE J.*, 35:1473–1486.

Sommerfeld, M. (1992). Modelling of particle-wall collisions in confined gas-particle flows. *Int. J. Multiphase Flow*, 18(6):905–926.

Soo, S. L. (1967). *Fluid Dynamics of Multiphase Systems*. Blaidesll, Waltham.

Squires, K. D. and Eaton, J. K. (1991). Measurements of particle dispersion obtained from direct numerical simulation of isotropic turbulence. *J. Fluid Mech.*, 226:1–35.

Squires, K. D. and Eaton, J. K. (1994). Effect of selective modification of turbulence on two-equation models for particle-laden turbulent flows. *ASME J. Fluids Eng.*, 5:778–784.

Srivastava, A. and Sundaresan, S. (2003). Analysis of a frictional-kinetic model for gas-particle flow. *Powder Technology*, 129:72–85.

Sumner, R. J. (1992). *Concentration Variations and Their Effects in Flowing Slurries and Emulsions*. PhD Thesis, Department of Chemical Engineering, University of Saskatchewan, Saskatoon, Canada.

Sumner, R. J., McKibben, M. J., and Shook, C. A. (1990). Concentration and velocity distributions in turbulent vertical slurry flows. *Ecoulements Solide-Liquide*, 2(2):33–42.

Sun, B. and Gidaspow, D. (1999). Computation of circulating fluidized bed riser flow for the fluidization VIII: benchmark test. *Ind. Eng. Chem. Res.*, 38:787–792.

Syamlal, M. (1990). *DOE Tech. Rep.* Morgantown Energy Technology Center. Tech. Note.

Syamlal, M., Rogers, W., and O'Brien, T. J. (1993). *Mfix Documentation Theory Guide*. U.S. Dept. of Energy, Office of Fossil Energy. Tech. Note.

Tardos, G. I., McNamara, S., and Talu, I. (2003). Slow and intermediate flow of a frictional bulk powder in couette geometry. *Powder Tech.*, 131:23–39.

Troshko, A. A. and Hassan, Y. A. (2001). Law of the wall for two-phase turbulent boundary layers. *Int. J. Heat Mass Trans.*, 44:781–875.

Tsuji, Y. (2000). Activities in discrete particle simulation in Japan. *Powder Technology*, 113:278–286.

Tsuji, Y. and Morikawa, Y. (1982). LDV measurements of an air-solid two-phase flow in a horizontal pipe. *J. Fluid Mech.*, 120:358–409.

Tsuji, Y., Morikawa, Y., and Shiomi, H. (1984). LDV measurements of an air-solid two-phase flow in a vertical pipe. *J. Fluid Mech.*, 139:417–434.

Tsuo, Y. P. and Gidaspow, D. (1990). Computation of flow patterns in circulating fluidized beds. *AIChE J.*, 36:886–896.

Turian, R. M. and Yuan, T. F. (1977). Flow of slurries in pipelines. *AIChE J.*, 23:232–242.

van Wachem, B. G. M. and Almstedt, A. E. (2003). Methods for multiphase computational fluid dynamics. *Chem. Eng. Sci.*, 96:81–98.

van Wachem, B. G. M., Schouton, J. C., van den Bleek, C. M., Krishna, R., and Sinclair, J. L. (2001). Comparative analysis of CFD models of dense gas-solid systems. *AIChE J.*, 47(5):1035–1051.

Wani, G. A., Mani, B. P., Suba, R. D., and Sarkar, M. K. (1983). Studies on hold-up and pressure gradient in hydraulic conveying of settling slurries through horizontal pipes. *J. Pipelines*, 3:215–222.

Wani, G. A., Sarkar, M. K., and Pitchumani, B. (1982). Pressure drop prediction in multi-size particle transportation through horizontal pipes. *J. Pipelines*, 3:23–33.

Wasp, E. J., Kenny, J. P., and Gandhi, R. L. (1977). *Solid-Liquid Flow Slurry Pipeline Transportation*. Rockport, Mass.: Trans Tech. publications.

Wen, C. Y. and Yu, Y. H. (1966). Mechanics of fluidization. *Chem. Eng. Prog. Symp. Ser.*, 62:100–111.

Whitaker, S. (1969). Advances in the theory of fluid motion in porous media. *Ind. Eng. Chem.*, 61(12):14–28.

Whitaker, S. (1973). The transport equations for multi-phase systems. *Chem. Eng. Sci.*, 28(1):139–147.

Wilcox, D. C. (2002). *Turbulence Modeling for CFD*. DCW Industries, La Canada, CA, 2nd edition.

Wilson, K. C. and Pugh, F. J. (1995). Real and virtual interfaces in slurry flows. In *Proceedings of the* 8^{th} *International Conference on Transport and Sedimentation of Solid Particles*, volume Paper A4, pages 1–8. Prague, Czech Republic.

Wilson, K. C. and Sellgren, A. (2003). Interaction of particles and near-wall lift in slurry pipelines. *J. Hydraul. Engr.*, 129(1):73–76.

Wilson, K. C., Sellgren, A., and Addie, G. R. (2000). Near-wall fluid lift of particles in slurry pipelines. In Sobota, J., editor, *Proceedings of the* 10^{th} *International Conference on Transport and Sedimentation of Solid Particles*, pages 435–444. Wroclaw, Poland.

Wilson, K. C., Streat, M., and Bantin, R. A. (1972). Slip-model correlation for dense two-phase flow. In *Proc. Hydrotransport 6 Conference*, volume Paper A1, pages 1–12. BHRA Fluid Engineering, Cranfield, UK.

Wilson, W. E. (1942). Mechanics of flow with noncolloidal, inert solids. *Trans. ASCE.*, 107:1576–1594.

Yasuna, Y. A., Moyer, H. R., Elliot, S., and Sinclair, J. L. (1995). Quantitative predictions of gas-particle flow in a vertical pipe with particle-particle interactions. *Powder Technology*, 84:23–34.

Zeng, Z., Zhou, L., and Zhang, J. (2005). A two-scale second-order moment two-phase turbulence model for simulating dense gas-particle flows. *Acta Mech. Sinica*, 21:425–429.

Zhang, Y. and Reese, J. M. (2001). Particle-gas turbulence interactions in a kinetic theory approach to granular flows. *Int. J. Multiphase Flow*, 27:1945–1964.

Zhang, Y. and Reese, J. M. (2003a). The drag force in two-fluid models of gas-solid flows. *Chem. Eng. Sci.*, 58:1641–1644.

Zhang, Y. and Reese, J. M. (2003b). Gas turbulence modulation in a two-fluid model for gas-solid flows. *AIChE Journal*, 49(12):3048–3065.

Zisselmar, R. and Molerus, O. (1986). Investigation of solid-liquid pipe flow with regard to turbulence modification. *The Chemical Engineering Journal*, 18:233–239.

APPENDIX A

ELECTROMAGNETIC FLOW METER CALIBRATION

This appendix describes the calibration procedure for the electromagnetic flow meter used to measure the bulk velocity in the pipeline in this thesis. The calibration was performed and documented by Schergevitch (2006). The description provided in this appendix is an edited version.

A.1 Sampling Drum

In the electromagnetic flow meter calibration, a drum was needed for sample collection. A calibration of the height versus volume of a drum to be used for sample collection was done. The height of the drum, from the inside of the bottom to the top lip, was measured to be 33.375 inches. A mark was placed on the lip of the drum where the measurement was made to ensure that all future measurements were taken at the same position. The drum was placed on a floor scale. The weight of the empty drum was zeroed on the scale. Water was incrementally added to the drum. For each addition, the weight and temperature of the water were taken. The water temperature was used to determine density, which was used in the conversion of mass to volume.

A.2 Volumetric Calibration of Sampling Drum

A height versus volume calibration of the drum employed was performed and the results are shown in Figure A.1. The height of the drum was measured to be 84.77 cm from the inside of the bottom to the top lip. A mark was placed on the lip of the drum where the measurement was made to ensure that all future measurements were taken at the same position. The drum was placed on a floor scale and the weight of the empty drum was zeroed on the scale. Water was then incrementally added to the drum and the weight and temperature of the water were recorded. The water temperature was used to determine density, which was subsequently used to determine the volume.

A.3 Calibration Setup and Procedure

A Linatex 3×2 pump with a Reeves variable-speed drive was used to provide flow for the calibrations. The suction side of the pump was connected to a conical bottomed tank equipped with a mixer. The Foxboro Electromagnetic Flowmeter was installed on the pump discharge line in a horizontal orientation with 54-inches of straight piping before the flow

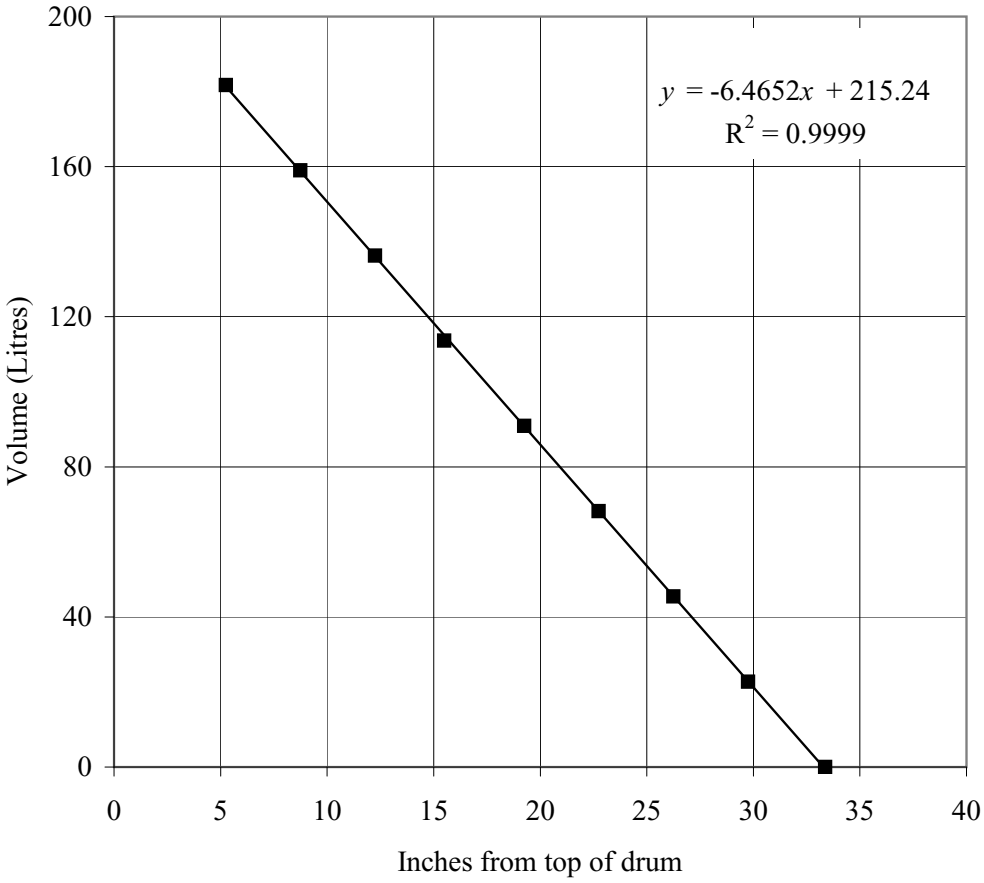

Figure A.1: Sampling drum calibration.

meter. A 2-inch flexible hose, of sufficient length to reach the top of the tank, was connected to the discharge side of the flow meter. The output of the flow meter transmitter was connected to the Saskatchewan Research Council data acquisition system. The pump was set to provide the required flow, with the slurry (or water) being re-circulated back into the supply tank. When ready, the flow was diverted to the sampling drum, and the sampling time and the output voltage reading from the flow meter transmitter were then measured. After the level of the sample in the drum was noted, the contents were returned to the supply tank. This measurement was used to calculate the sample volume (see Figure A.1). This procedure was repeated for several flow rates.

A.4 Calibration with Slurry and Water

1160 Litres of slurry made up of 403 kg of 30/50 sand ($d_{50} = 500$ μm) and water was prepared in the supply tank. The mixer was set such that adequate mixing was provided while ensuring minimum air entrainment. The procedure described above was performed for four flow rates and the output values were recorded. For these four sets of data, the solids concentration flowing through the flow meter was not accounted for. To consider the effect of solids concentration, additional data for five flow rate settings were obtained where the level of the solids in the sample drum for each case was measured as well as the level of the total sample collected. This measurement allowed the solids concentration in the slurry flowing through the meter to be measured. The settled solids in the drum were assumed to have a concentration of 62% by volume. With this value, which was assumed to be the concentration at maximum packing, and the total volume of the mixture, the solids concentration in the flowing mixtures was determined. The calibration data is plotted in terms of the flow rate as a function of the EMFM output voltage (Figure A.2). Solids concentrations of 20% and 40% by volume were used. After the calibration with the slurry, the system was flushed and replaced with an equal volume of water. The mixer was set to run at similar condition as during the calibration with the slurry. The procedure described above was repeated for several flow rates. As in the case of the slurry, the measured flow rate as a function of the output voltage from the MFM transmitter is shown in Figure A.2.

As shown in Figure A.2, the calibration lines for both water and the slurry are similar. Since, the flow rate through the EMFM is measured as the amount of the volume of the mixture passing through it for a known period of time interval, the flow rate is interpreted as that of the mixture in this thesis.

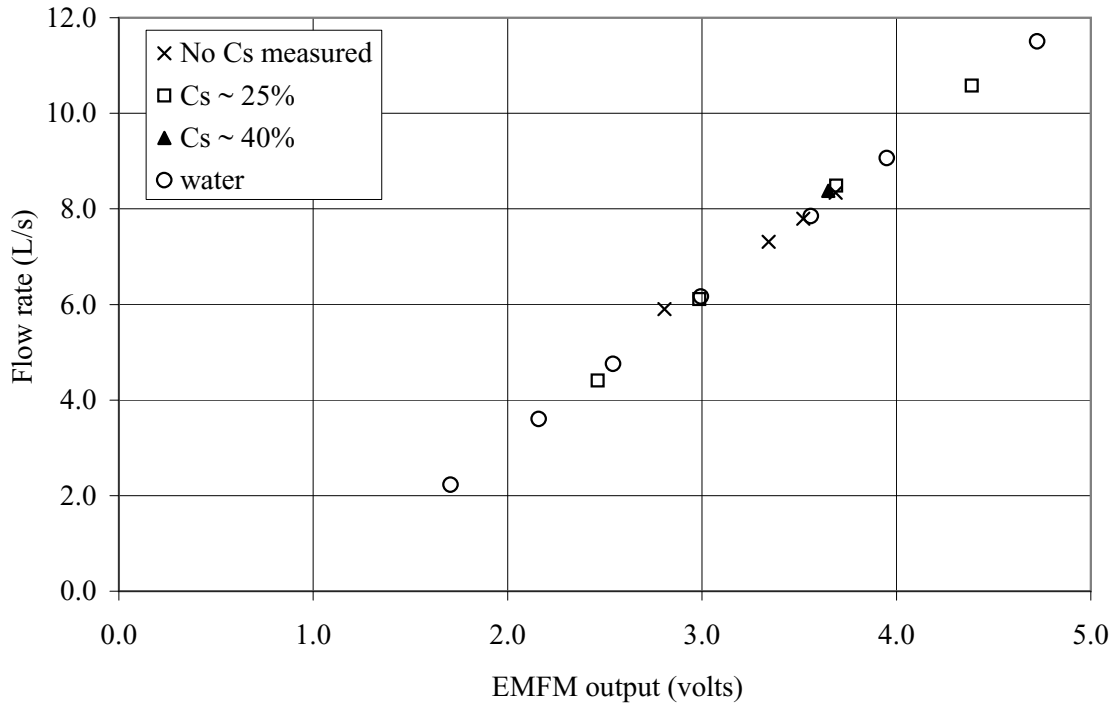

Figure A.2: Electromagnetic flow meter calibration data for water and water-sand slurry mixtures.

APPENDIX B

SOLIDS VELOCITY MEASURED WITH THE L-PROBE

In this appendix, additional solids velocity profiles for the upward flow of 0.5 mm and 2.0 mm glass beads at bulk concentrations between 5% and 45% in water are shown. The profiles for the 0.5 mm glass bead slurries are presented in Figures B.1 through B.3. The bulk velocity is denoted by V and U_{us} refers to the means solids velocity in the upward flow section in the figures. Those obtained for the 2.0 mm glass bead slurries are shown in Figure B.4. As noted in Chapter 3, the general trend of the profiles resembles those obtained in previous studies using similar probes. The solids velocity profiles for the 2.0 mm glass beads were not realistic. This can be seen in Figure B.4 where the velocity profile does not follow the expected trend near the wall.

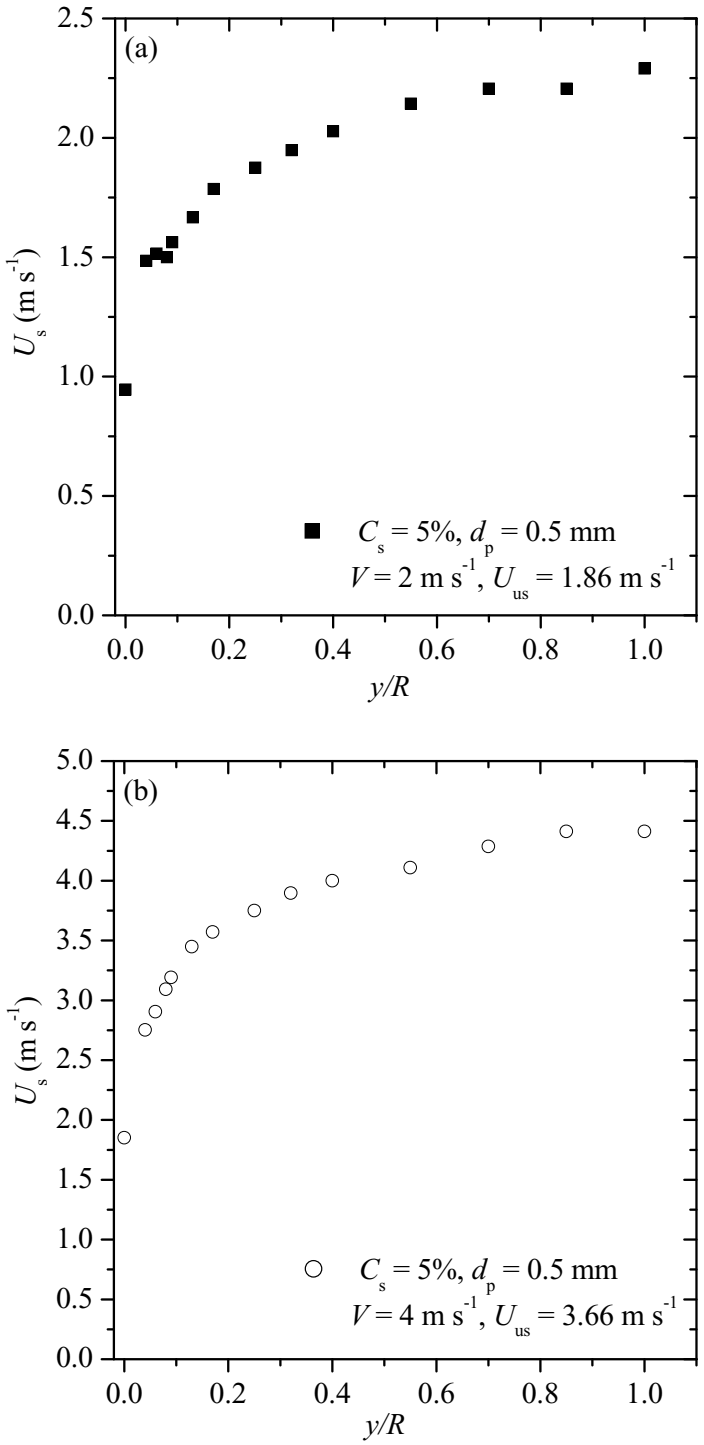

Figure B.1: Solids velocity profiles for vertical upward flow of 0.5 mm glass beads at bulk solids concentration of 5% in water: (a) bulk velocity = 2 m s^{-1}, and (b) bulk velocity = 4 m s^{-1}.

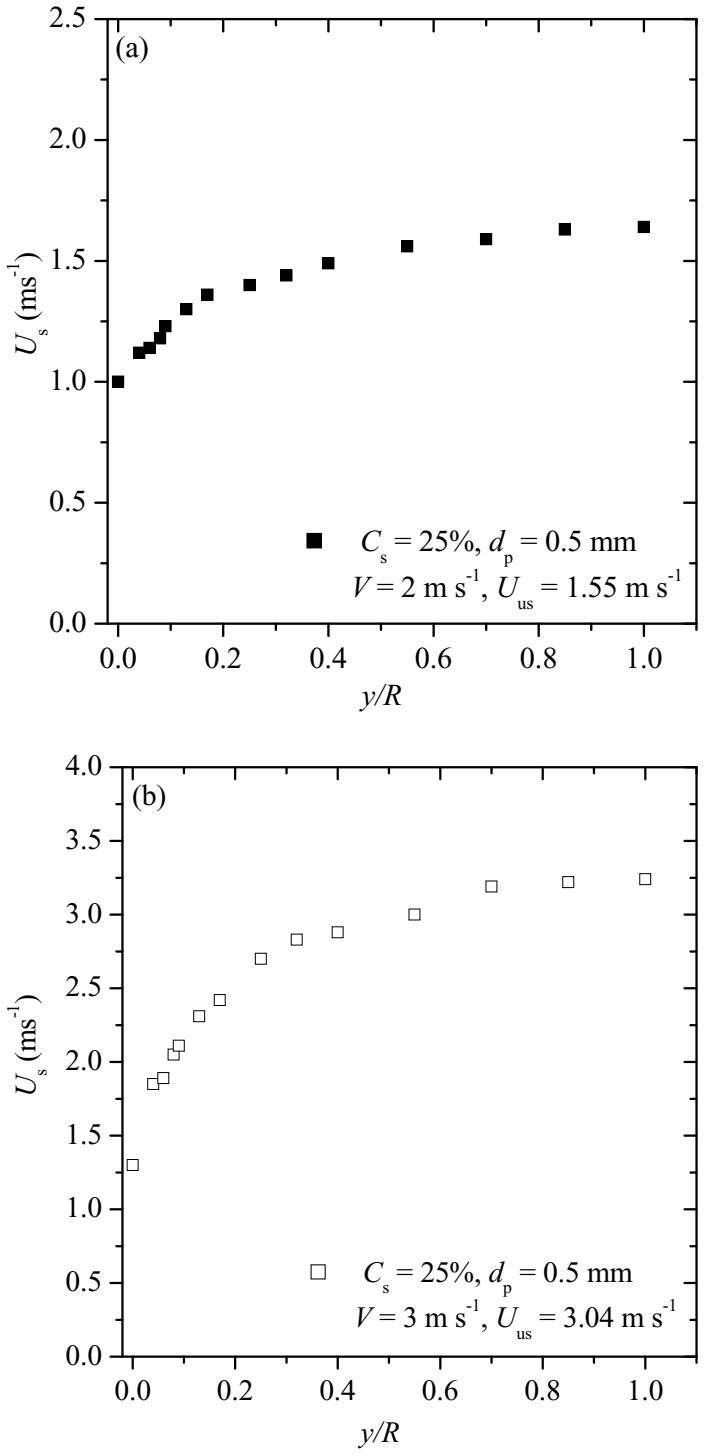

Figure B.2: Solids velocity profiles for vertical upward flow of 0.5 mm glass beads at bulk solids concentration of 25% in water: (a) bulk velocity = 2 m s^{-1}, and (b) bulk velocity = 3 m s^{-1}.

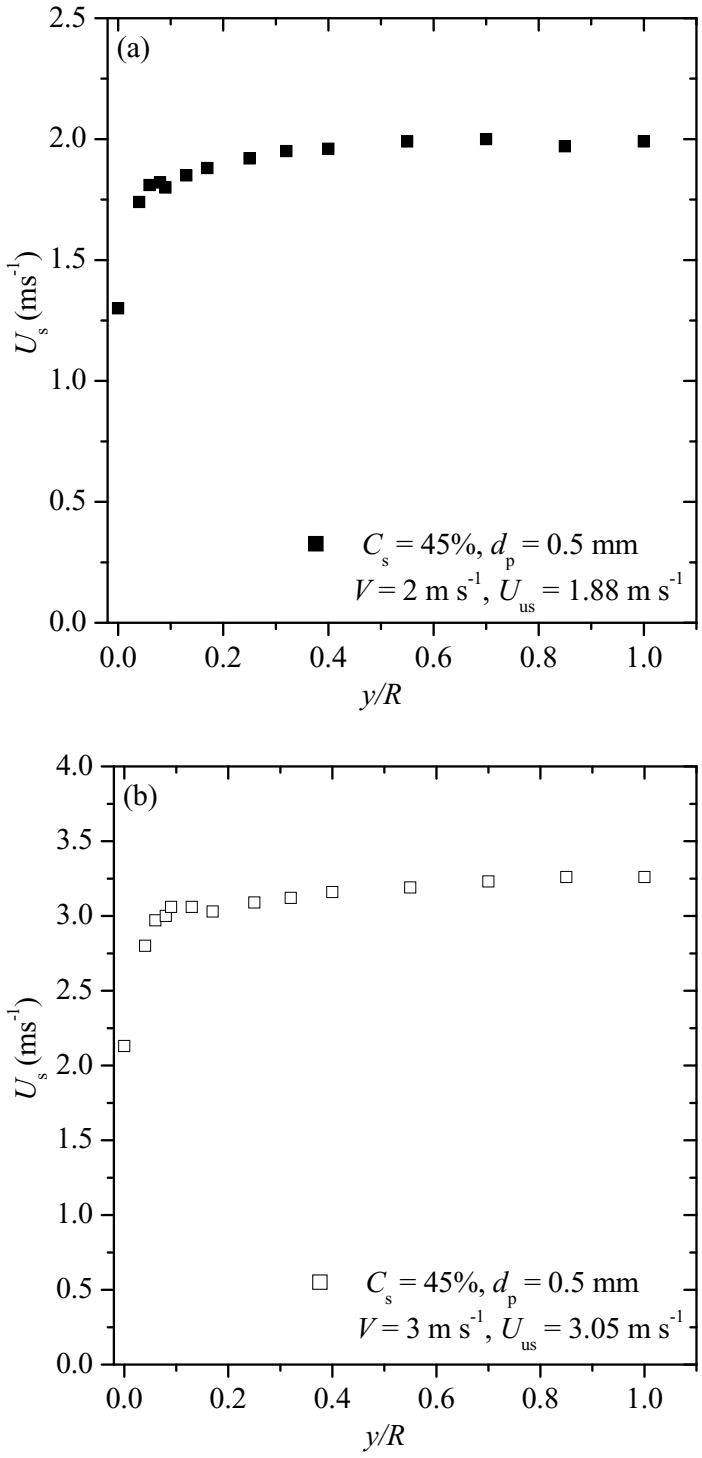

Figure B.3: Solids velocity profiles for vertical upward flow of 0.5 mm glass beads at bulk solids concentration of 45% in water: (a) bulk velocity = 2 m s^{-1} and (b) bulk velocity = 3 m s^{-1}.

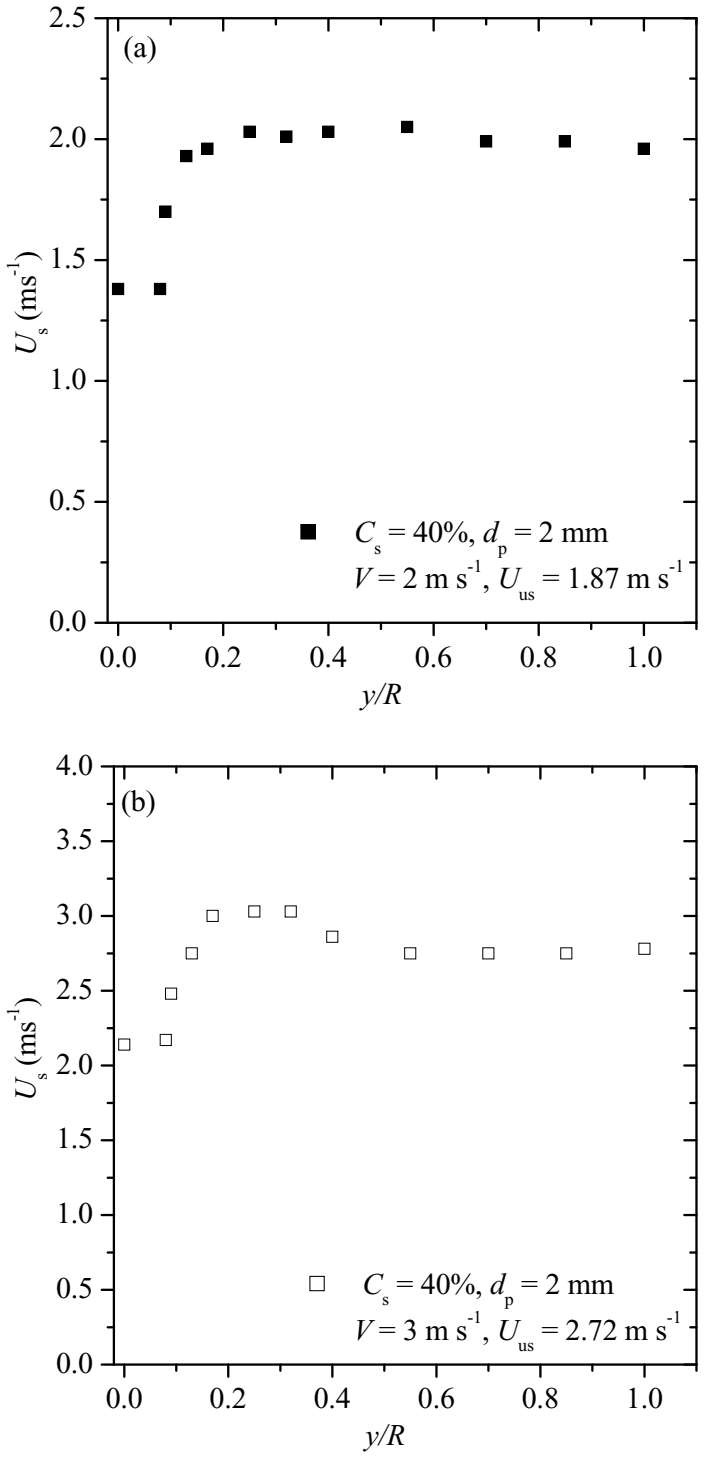

Figure B.4: Solids velocity profiles for vertical upward flow of 2.0 mm glass beads at bulk solids concentration of 40% in water: (a) bulk velocity = 2 m s^{-1}, and (b) bulk velocity = 3 m s^{-1}.

APPENDIX C

RAW PRESSURE DROP DATA

The measured pressure gradients are provided in this appendix. Tables C.1 through C.7 show the data for the 0.5 mm glass beads, and Tables C.8 through C.10 represents measured data for the 2.0 mm glass beads. In the tables, the total flowrate, which is used to calculate the bulk velocity, is measure with the Electromagnetic Flow Meter (EFM). The pressure gradients data in the upward and downward test sections are given by equations (3.6) and (3.7); the average pressure gradient corresponds to equation (3.8).

Table C.1: Pressure gradient data for flow 0.5 mm glass beads at 5% bulk solids concentration in water

Total Flowrate	**Downward Test Section**	**Upward Test Section**	**Temperature**	**Average dP/dz**	**Velocity**
(L/s)	(kPa/m)	(kPa/m)	(°C)	(kPa/m)	(m/s)
11.11	3.069	4.604	22.9	3.8365	5.02
10.15	2.492	4.038	22.9	3.265	4.58
8.96	1.865	3.370	22.9	2.6175	4.05
7.74	1.281	2.767	22.8	2.024	3.50
6.75	0.866	2.327	22.8	1.5965	3.05
5.52	0.414	1.835	22.8	1.1245	2.49
4.47	0.104	1.459	22.7	0.7815	2.02
4.04	0.000	1.306	22.7	0.653	1.82
3.49	-0.107	1.115	22.7	0.504	1.58
2.18	-0.191	0.644	22.7	0.2265	0.98

Table C.2: Pressure gradient data for flow of 0.5 mm glass beads at 25% bulk solids concentration in water

Total Flowrate	**Downward Test Section**	**Upward Test Section**	**Temperature**	**Average dP/dz**	**Velocity**
(L/s)	(kPa/m)	(kPa/m)	(°C)	(kPa/m)	(m/s)
9.78	-0.396	7.099	23.2	3.351	4.42
9.34	-0.648	6.850	22.8	3.101	4.22
8.89	-0.890	6.594	22.9	2.852	4.02
8.23	-1.228	6.253	22.9	2.513	3.72
7.74	-1.469	6.006	22.8	2.269	3.50
7.15	-1.741	5.731	22.9	1.995	3.23
6.69	-1.938	5.524	22.9	1.793	3.02
6.09	-2.182	5.271	22.8	1.545	2.75
5.62	-2.364	5.0756	22.8	1.356	2.54
4.97	-2.579	4.8214	22.8	1.121	2.24
4.40	-2.782	4.6091	22.8	0.914	1.99
3.47	-3.057	4.3541	22.8	0.649	1.56
2.75	-3.202	4.1573	22.9	0.478	1.24

Table C.3: Pressure gradient data for flow of 0.5 mm glass beads at 30% bulk solids concentration in water

Total Flowrate	**Downward Test Section**	**Upward Test Section**	**Temperature**	**Average dP/dz**	**Velocity**
(L/s)	(kPa/m)	(kPa/m)	(°C)	(kPa/m)	(m/s)
9.01	-1.292	7.480	26.5	3.094	4.07
8.27	-1.740	7.042	26.8	2.651	3.73
7.71	-2.033	6.739	26.7	2.353	3.48
7.23	-2.273	6.507	26.7	2.117	3.26
6.76	-2.489	6.291	26.6	1.901	3.05
6.05	-2.801	5.979	26.5	1.589	2.73
5.61	-2.985	5.805	26.3	1.410	2.53
4.92	-3.253	5.566	26.3	1.157	2.22
4.41	-3.443	5.434	26.2	0.996	1.99
3.92	-3.615	5.335	26.2	0.860	1.77
3.38	-3.779	5.229	26.2	0.725	1.53

Table C.4: Pressure gradient data for flow of 0.5 mm glass beads at 35% bulk solids concentration in water

Total Flowrate	**Downward Test Section**	**Upward Test Section**	**Temperature**	**Average dP/dz**	**Velocity**
(L/s)	(kPa/m)	(kPa/m)	(°C)	(kPa/m)	(m/s)
8.36	-2.310	7.601	27.7	2.646	3.78
7.77	-2.633	7.322	27.8	2.345	3.51
7.18	-2.940	7.057	27.8	2.059	3.24
6.68	-3.180	6.862	27.7	1.841	3.02
6.04	-3.456	6.663	27.6	1.604	2.73
5.46	-3.692	6.526	27.5	1.417	2.47
4.96	-3.881	6.428	27.4	1.274	2.24
4.41	-4.071	6.334	27.4	1.132	1.99
3.85	-4.255	6.238	27.3	0.992	1.74
3.38	-4.384	6.147	27.3	0.882	1.53

Table C.5: Pressure gradient data for flow of 0.5 mm glass beads at 40% bulk solids concentration in water

Total Flowrate	**Downward Test Section**	**Upward Test Section**	**Temperature**	**Average dP/dz**	**Velocity**
(L/s)	(kPa/m)	(kPa/m)	(°C)	(kPa/m)	(m/s)
7.59	-3.380	7.923	28.6	2.272	3.43
7.22	-3.553	7.815	28.7	2.131	3.26
6.68	-3.779	7.708	28.7	1.965	3.02
6.09	-4.001	7.581	28.6	1.790	2.75
5.59	-4.201	7.480	28.5	1.640	2.52
4.97	-4.446	7.363	28.4	1.459	2.24
4.55	-4.623	7.291	28.3	1.334	2.05
3.95	-4.781	7.177	28.2	1.198	1.78
3.41	-4.894	7.095	28.2	1.101	1.54
2.98	-4.977	7.063	28.2	1.043	1.35

Table C.6: Pressure gradient data for flow of 0.5 mm glass beads at 45% bulk solids concentration in water

Total Flowrate	**Downward Test Section**	**Upward Test Section**	**Temperature**	**Average dP/dz**	**Velocity**
(L/s)	(kPa/m)	(kPa/m)	(°C)	(kPa/m)	(m/s)
7.46	-4.135	8.843	22.7	2.354	3.37
7.20	-4.250	8.734	22.6	2.242	3.25
6.69	-4.444	8.599	22.6	2.078	3.02
6.09	-4.664	8.456	22.6	1.896	2.75
5.51	-4.815	8.344	22.5	1.765	2.49
4.94	-4.949	8.217	22.5	1.634	2.23
4.47	-5.118	8.137	22.5	1.510	2.02
3.87	-5.353	8.085	22.5	1.366	1.75
3.36	-5.539	8.037	22.5	1.249	1.52
2.75	-5.745	8.045	22.4	1.150	1.24

Table C.7: Pressure gradient data (repeat) for flow of 0.5 mm glass beads at 45% bulk solids concentration in water

Total Flowrate	**Downward Test Section**	**Upward Test Section**	**Temperature**	**Average dP/dz**	**Velocity**
(L/s)	(kPa/m)	(kPa/m)	(°C)	(kPa/m)	(m/s)
7.13	-4.165	8.652	22.9	2.244	3.22
7.18	-4.156	8.643	22.9	2.244	3.24
6.70	-4.381	8.507	22.9	2.063	3.02
6.72	-4.377	8.512	22.9	2.068	3.03
6.11	-4.615	8.358	22.8	1.872	2.76
6.09	-4.616	8.373	22.8	1.878	2.75
5.57	-4.762	8.250	22.8	1.744	2.52
5.58	-4.783	8.250	22.8	1.733	2.52
5.00	-4.958	8.125	22.8	1.584	2.26
5.00	-4.967	8.120	22.8	1.577	2.26
4.47	-5.101	8.020	22.8	1.460	2.02
4.47	-5.106	8.024	22.7	1.459	2.02

Table C.8: Pressure gradient data for flow of 2.0 mm glass beads at 5% bulk solids concentration in water

Total Flowrate	**Downward Test Section**	**Upward Test Section**	**Temperature**	**Average dP/dz**	**Velocity**
(L/s)	(kPa/m)	(kPa/m)	(°C)	(kPa/m)	(m/s)
7.59	-3.380	7.923	28.6	2.272	3.43
7.22	-3.553	7.815	28.7	2.131	3.26
6.68	-3.779	7.708	28.7	1.965	3.02
6.09	-4.001	7.581	28.6	1.790	2.75
5.59	-4.201	7.480	28.5	1.640	2.52
4.97	-4.446	7.363	28.4	1.459	2.24
4.55	-4.623	7.291	28.3	1.334	2.05
3.95	-4.781	7.177	28.2	1.198	1.78
3.41	-4.894	7.095	28.2	1.101	1.54
2.98	-4.977	7.063	28.2	1.043	1.35

Table C.9: Pressure gradient data for flow of 2.0 mm glass beads at 10% bulk solids concentration in water

Total Flowrate	**Downward Test Section**	**Upward Test Section**	**Temperature**	**Average dP/dz**	**Velocity**
(L/s)	(kPa/m)	(kPa/m)	(°C)	(kPa/m)	(m/s)
7.46	-4.135	8.843	22.7	2.354	3.37
7.20	-4.250	8.734	22.6	2.242	3.25
6.69	-4.444	8.599	22.6	2.078	3.02
6.09	-4.664	8.456	22.6	1.896	2.75
5.51	-4.815	8.344	22.5	1.765	2.49
4.94	-4.949	8.217	22.5	1.634	2.23
4.47	-5.118	8.137	22.5	1.510	2.02
3.87	-5.353	8.085	22.5	1.366	1.75
3.36	-5.539	8.037	22.5	1.249	1.52
2.75	-5.745	8.045	22.4	1.150	1.24

Table C.10: Pressure gradient data for flow of 2.0 mm glass beads at 40% bulk solids concentration in water

Total Flowrate	**Downward Test Section**	**Upward Test Section**	**Temperature**	**Average dP/dz**	**Velocity**
(L/s)	(kPa/m)	(kPa/m)	(°C)	(kPa/m)	(m/s)
7.13	-4.165	8.652	22.9	2.244	3.22
7.18	-4.156	8.643	22.9	2.244	3.24
6.70	-4.381	8.507	22.9	2.063	3.02
6.72	-4.377	8.512	22.9	2.068	3.03
6.11	-4.615	8.358	22.8	1.872	2.76
6.09	-4.616	8.373	22.8	1.878	2.75
5.57	-4.762	8.250	22.8	1.744	2.52
5.58	-4.783	8.250	22.8	1.733	2.52
5.00	-4.958	8.125	22.8	1.584	2.26
5.00	-4.967	8.120	22.8	1.577	2.26
4.47	-5.101	8.020	22.8	1.460	2.02
4.47	-5.106	8.024	22.7	1.459	2.02

APPENDIX D

AVERAGING TECHNIQUES

The definitions of the averaging techniques applied to develop governing equations of multiphase flows in the Eulerian-Eulerian formulation are given here. Consider a given field variable, φ, defined by the function $\varphi = \varphi(\mathbf{r}, t)$, which can be a scalar, vector or tensor of a phase being studied at a fixed point in space $\mathbf{r}$ at any time, t. The averaging processes are defined below:

1. The time average of $\varphi(\mathbf{r}, t)$ is defined by

$$\langle\varphi\rangle_t(\mathbf{r}, t) = \frac{1}{T}\int_{t-T/2}^{t+T/2} \varphi(\mathbf{r}, t)\mathrm{d}(\tau), \tag{D.1}$$

   where T is the averaging time scale.

2. The volume average is defined by

$$\langle\varphi\rangle_v(\mathbf{r}, t) = \frac{1}{V}\int_V \varphi(\mathbf{r}, t)\mathrm{d}V, \tag{D.2}$$

   where V is the averaging volume.

3. The ensemble average, defined by

$$\langle\varphi\rangle_e(\mathbf{r}, t) = \frac{1}{N}\sum_{n=1}^{N} \varphi_n(\mathbf{r}, t) \tag{D.3}$$

   is generally thought of as the most fundamental averaging process. In equations (D.3), $\varphi_n(\mathbf{r}, t)$ is the realization of $\varphi(\mathbf{r}, t)$ over all possible realizations N or Ω.

APPENDIX E

SAMPLE CFX-4.4 COMMAND FILE

In this appendix a sample of the input file use for CFX-4.4 simulations is provided. After creating a geometry to be used for the simulation, a case need to be generated and the file for that is called the *command file* in CFX-4.4. In the command file, one typically sets the parameters required for the numerics, specifies the type of geometry, selects the model(s) of interest, fluid properties, defines user-routine names, and sets inlet, outlet and wall boundary conditions. A sample of a command file is given below:

```
>>CFX4
    #CALC
      TI  = 1.0E-1;
      U1  = 2.58E+00;
      K1  = 3.0*(U1*TI)**2.0/2.0;
      E1  = 0.09**(3.0/4.0)*K1**(3.0/2.0)/(0.007*0.04);
      T2  = 1.0E-1;
      U2  = 2.58E+00;
      K2  = 3.0*(U2*TI)**2.0/2.0;
      GT2 = 3.0*K2/2.0;
      E2  = 0.09**(3.0/4.0)*K2**(3.0/2.0)/(0.007*0.04);
      CS2 = 0.087;
      CS1 = 1.0-CS2;
    #ENDCALC
  >>SET LIMITS
    TOTAL INTEGER WORK SPACE 10000000
    TOTAL CHARACTER WORK SPACE 500000
    TOTAL REAL WORK SPACE 17000000
  >>OPTIONS
    TWO DIMENSIONS
    CYLINDRICAL COORDINATES
    AXIS INCLUDED
    TURBULENT FLOW
    ISOTHERMAL FLOW
    INCOMPRESSIBLE FLOW
    STEADY STATE
    USER SCALAR EQUATIONS 24
```

```
28      NUMBER OF PHASES 2
29    >>USER FORTRAN
30      USRIPT
31      USRBF
32      USRVIS
33      USRDIF
34      USRSRC
35      USRWTM
36      USRPRT
37    >>VARIABLE NAMES
38      USER SCALAR1 'USRDCC GPRESS'
39      USER SCALAR2 'USRDCC BULKVIS'
40      USER SCALAR3 'USRDCC TAUXX'
41      USER SCALAR4 'USRDCC TAUXY'
42      USER SCALAR5 'USRDCC EXTAU'
43      USER SCALAR6 'USRDCC GAM'
44      USER SCALAR7 'USRDCC INTERF'
45      USER SCALAR8 'USRDCC UDRAG'
46      USER SCALAR9 'USRDCC USMUL'
47      USER SCALAR10 'USRDCC UMUSTURB'
48      USER SCALAR11 'USRDCC UDPDX'
49      USER SCALAR12 'USRDCC UDPDY'
50      USER SCALAR13 'USRDCC UDPDZ'
51      USER SCALAR14 'X SHEAR STRESS'
52      USER SCALAR15 'Y SHEAR STRESS'
53      USER SCALAR16 'USRDCC UMUFTURB'
54      USER SCALAR17 'USRDCC TSCLT'
55      USER SCALAR18 'USRDCC TSCLP'
56      USER SCALAR19 'USRDCC TSCLC'
57      USER SCALAR20 'USRDCC TSCLFS'
58      USER SCALAR21 'USRDCC UMUCT'
59      USER SCALAR22 'USRDCC UMUSC'
60      USER SCALAR23 'USRDCC UMUSH'
61      USER SCALAR24 'USRDCC UDRIFT'
62    >>PHASE NAMES
63      PHASE1 'WATER'
64      PHASE2 'SAND'
65  >>MODEL DATA
66    >>DIFFERENCING SCHEME
67      U VELOCITY 'HIGHER UPWIND'
68      V VELOCITY 'HIGHER UPWIND'
69      VOLUME FRACTION 'HYBRID'
70      K 'HYBRID'
71      EPSILON 'SUPERBEE'
72    >>RHIE CHOW SWITCH
```

```
 73      IMPROVED
 74 /*   >>SET INITIAL GUESS
 75      >>INPUT FROM FILE
 76        READ DUMP FILE
 77        UNFORMATTED   */
 78    >>TITLE
 79      PROBLEM TITLE  'UPWARD LIQUID-SOLID SLURRY FLOW'
 80    >>WALL TREATMENTS
 81      PHASE NAME  'WATER'
 82      NO SLIP
 83    >>WALL TREATMENTS
 84      PHASE NAME  'SAND'
 85      SLIP
 86    >>PHYSICAL PROPERTIES
 87      >>FLUID PARAMETERS
 88        PHASE NAME  'WATER'
 89        VISCOSITY  1.0000E-03
 90        DENSITY  9.9800E+02
 91      >>FLUID PARAMETERS
 92        PHASE NAME  'SAND'
 93        VISCOSITY  1.0000E-8
 94        DENSITY  2.650E+03
 95      >>MULTIPHASE PARAMETERS
 96        >>PHASE DESCRIPTION
 97          PHASE NAME  'WATER'
 98          LIQUID
 99          CONTINUOUS
100        >>PHASE DESCRIPTION
101          PHASE NAME  'SAND'
102          SOLID
103          DISPERSE
104          MEAN DIAMETER  470.0E-06
105 /*           MEAN DIAMETER  1700.0E-06*/
106        >>MULTIPHASE MODELS
107          >>MOMENTUM
108            INTER PHASE TRANSFER
109            SINCE
110            IPSAC
111      >>TURBULENCE PARAMETERS
112        >>TURBULENCE MODEL
113          PHASE NAME  'WATER'
114          TURBULENCE MODEL  'K-EPSILON'
115        >>TURBULENCE MODEL
116          PHASE NAME  'SAND'
117          TURBULENCE MODEL  'K-EPSILON'
```

```
118 >>SOLVER DATA
119   >>PROGRAM CONTROL
120     MAXIMUM NUMBER OF ITERATIONS 100
121     MASS SOURCE TOLERANCE 1.0000E-15
122     ITERATIONS OF TEMPERATURE AND SCALAR EQUATIONS 2
123     ITERATIONS OF TURBULENCE EQUATIONS 1
124     ITERATIONS OF VELOCITY AND PRESSURE EQUATIONS 1
125     ITERATIONS OF HYDRODYNAMIC EQUATIONS 1
126   >>PRESSURE CORRECTION
127     SIMPLEC
128     >>UNDER RELAXATION FACTORS
129     PHASE NAME 'WATER'
130     U VELOCITY 6.0000E-01
131     V VELOCITY 6.0000E-01
132     PRESSURE 1.0E+00
133     VOLUME FRACTION 4.5E-02
134     VISCOSITY 4.0000E-01
135     K 5.0000E-01
136     EPSILON 5.0000E-01
137   >>UNDER RELAXATION FACTORS
138     PHASE NAME 'SAND'
139     U VELOCITY 4.0000E-01
140     V VELOCITY 6.0000E-01
141     PRESSURE 1.0E+00
142     VOLUME FRACTION 4.5E-02
143     VISCOSITY 4.0000E-01
144     K 5.0000E-01
145     EPSILON 5.0000E-01
146 >>MODEL BOUNDARY CONDITIONS
147   >>INLET BOUNDARIES
148     PHASE NAME 'WATER'
149     PATCH NAME 'INLET1'
150 /* For  dp = 470 mic; U = 2.58 and Cr=0.087*/
151     NORMAL VELOCITY #U1
152     VOLUME FRACTION #CS1
153 /* For  dp = 470 mic; U = 2.62 and Cr=0.278
154     NORMAL VELOCITY #U1
155     VOLUME FRACTION #CS1*/
156 /* For  dp = 1700 mic; U = 2.77 and Cr=0.085
157     NORMAL VELOCITY #U1
158     VOLUME FRACTION #CS1*/
159 /* For  dp = 1700 mic; U = 2.89 and Cr=0.177
160     NORMAL VELOCITY #U1
161     VOLUME FRACTION #CS1*/
162 /* For  Daniel 1965: dp = 1700 mic;U = 1.5 and Cr=0.224
```

```
163       NORMAL VELOCITY #U1
164       VOLUME FRACTION #CS1*/
165       K #K1
166       EPSILON #E1
167     >>INLET BOUNDARIES
168       PHASE NAME 'SAND'
169       PATCH NAME 'INLET1'
170  /* For  dp = 470 mic; U = 2.58 and Cr=0.087*/
171       NORMAL VELOCITY #U2
172       VOLUME FRACTION #CS2
173  /* For  dp = 470 mic; U = 2.62 and Cr=0.278
174       NORMAL VELOCITY #U2
175       VOLUME FRACTION #CS2*/
176  /* For  dp = 1700 mic; U = 2.77 and Cr=0.085
177       NORMAL VELOCITY #U2
178       VOLUME FRACTION #CS2*/
179  /* For  dp = 1700 mic; U = 2.89 and Cr=0.177
180       NORMAL VELOCITY #U2
181       VOLUME FRACTION #CS2*/
182  /* For  Daniel 1965: dp = 1700 mic;U = 1.5 and Cr=0.224
183       NORMAL VELOCITY #U2
184       VOLUME FRACTION #CS2*/
185       K #K2
186       EPSILON #E2
187     >>WALL BOUNDARIES
188       PHASE NAME 'WATER'
189       PATCH NAME 'WALL1'
190     >>WALL BOUNDARIES
191       PHASE NAME 'SAND'
192       PATCH NAME 'WALL1'
193     >>WALL BOUNDARIES
194       PHASE NAME 'SAND'
195       PATCH NAME 'WALL1'
196  >>STOP
```

APPENDIX F

SOLIDS VELOCITY AND CONCENTRATION RESULTS IN 263 mm PIPE

This appendix contains contour plots of the solids-phase velocity and concentration of sand slurry flow in a 263 mm pipe.

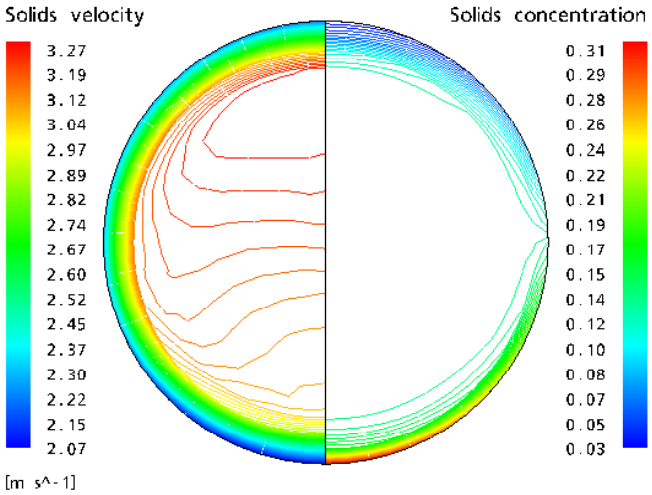

(a) Solids velocity and concentration at $C_{\mathrm{s}} = 15\%$

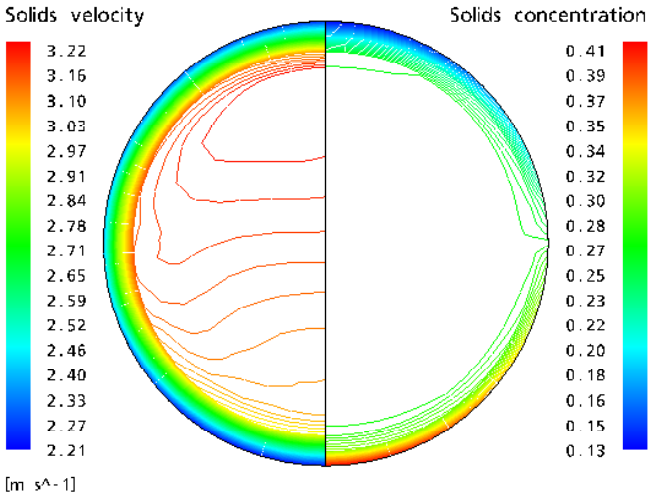

(b) Solids velocity and concentration at $C_{\mathrm{s}} = 30\%$

Figure F.1: Contour plots of solids velocity and concentration for 0.18 mm sand-in-water flow in 263 mm pipe.

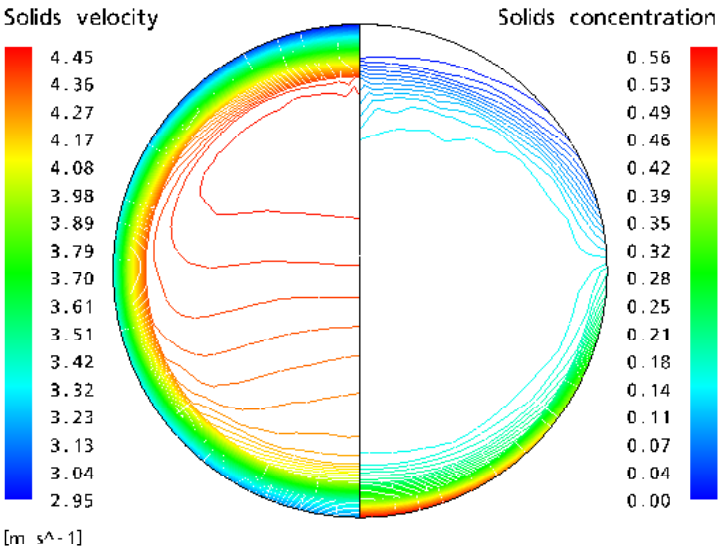

(a) Solids velocity and concentration at $C_s = 15\%$

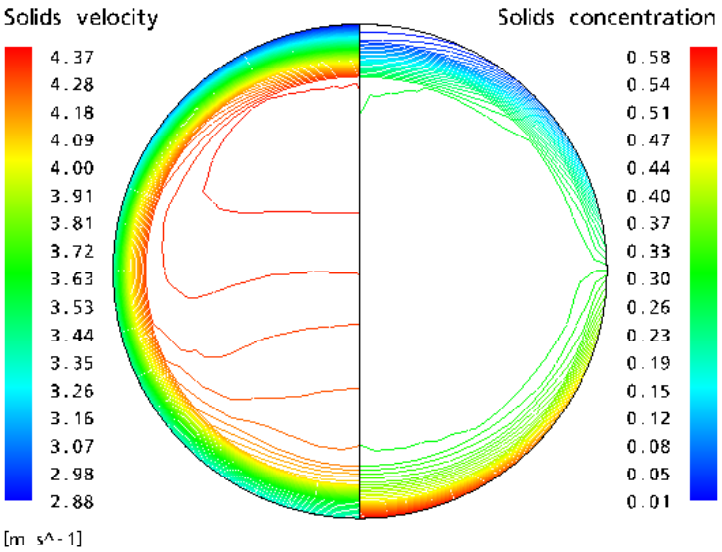

(b) Solids velocity and concentration at $C_s = 30\%$

Figure F.2: Contour plots of solids velocity and concentration for 0.55 mm sand-in-water flow in 263 mm pipe.